

UNIVERSITY OF OKLAHOMA
GRADUATE COLLEGE

PREDICTION OF RESERVOIR QUALITY WITH SEISMIC ATTRIBUTES IN
EOCENE SUBMARINE CONGLOMERATES (CALCLITHITES), MEXICO

A THESIS
SUBMITTED TO THE GRADUATE FACULTY
in partial fulfillment of the requirements for the
Degree of
MASTER OF SCIENCE

By
ARACELI SHANET ROMERO PELAEZ
Norman, Oklahoma
2012

PREDICTION OF RESERVOIR QUALITY WITH SEISMIC ATTRIBUTES IN
EOCENE SUBMARINE CONGLOMERATES (CALCLITHITES), MEXICO.

A THESIS APPROVED FOR THE
CONOCOPHILLIPS SCHOOL OF GEOLOGY AND GEOPHYSICS

BY

Dr. Kurt J. Marfurt, Chair

Dr. John J. Pigott

Dr. J. Timothy Kwiatkowski

© Copyright by ARACELI SHANET ROMERO PELAEZ 2012
All Rights Reserved.

To Antonio and América, the root of my strength.

To my mother Inés, my example of determination and persistence.

ACKNOWLEDGMENTS

I am very grateful with all who have made completion of my Master's degree at the University of Oklahoma possible.

Above all, I deeply thank my beloved husband Antonio for his invaluable help, motivation, extraordinary patience, and unconditional love through this journey. Without his love and support, I could not accomplish my degree at all. Infinite thanks to my daughter, América, for all her hugs and smiles that made me persist. With all my heart, thanks to my mother who always has encouraged me to be better and work hard to reach my goals.

I would like to express my special thanks and appreciation to my advisor, Dr. Kurt Marfurt, for his guidance, tutelage, and exceptional help in my thesis research. I am thankful for his trust and encouragement even before I came to the OU. I also want to thank my committee members, Dr. John Pigott and Dr. Tim Kwiatkowski for all their advice and discussion that were key to improving the quality of this thesis.

I would like to express my sincere gratitude to Petróleos Mexicanos (PEMEX) for providing the data and permission to pursue my Master's degree through the fellowship from "Fondo Sectorial CONACYT-SENER-Hidrocarburos".

I acknowledge all the people in PEMEX, CONACYT, BANOBRAS and SENER for their continuous assistance during this journey, especially José Antonio Escalera-Alcocer, Juan Arturo Hernández Carrera, Miguel Ángel Hernández-García, José Francisco Martínez-Mendoza, José Ramón Ramírez-Cuacenetl, Victor Valdivieso Ramos, Rafael Ramos-Palmeros, Pablo Arturo Gómez-Durán, Ana Rosa Parrilla-Puente, Erika Coral Carmona-Castañón and María Teresa Sánchez Serrano. I

particularly thank my PEMEX advisor, Ignacio Pereznegrón-Zarco, for his encouragement and positive feedback on my work.

I wish to extend my sincere thanks to my colleagues in PEMEX “Activo Integral Veracruz”, Ángel Mesa-Ríos, Angélica Martínez-Ordoñez, Carlos Flores-Romero, Rafael Muñoz-Vergara, Ricardo Domínguez-Ibarra, Ricardo Hernández-Martínez, Silvia Román-Vargas and Lorenzo Sánchez-Pérez for their previous work, advice and help in preparing the data.

Thanks to Schlumberger and Hampson & Russell for providing software to OU for use in research and education.

I acknowledge all members and sponsors of AASPI Consortium research program. Thanks to the CPSGG faculty, staff and fellow students who help me in different ways, especially Atish Roy, Oswaldo Davogustto, Paul Debapriya, Roderick Perez, Sumit Verma, and Yoryenis del Moro.

I am very grateful to my relatives and friends for their love, moral support and continuous encouragement; you are always in my heart. Special thanks to my Mexican friends in Norman who make me feel as home: Alejandro, Carlos, Erika, Hector, Monica, Paty, Sara, and Zairita. I will miss all of you.

TABLE OF CONTENTS

ACKNOWLEDGMENTS.....	<i>iv</i>
TABLE OF CONTENTS.....	<i>vi</i>
LIST OF FIGURES.....	<i>viii</i>
LIST OF TABLES.....	<i>xxii</i>
LIST OF SYMBOLS.....	<i>xxiii</i>
LIST OF ACRONYMS.....	<i>xxiv</i>
ABSTRACT.....	<i>xxvi</i>
CHAPTER I. INTRODUCTION.....	<i>1</i>
Problem statement.....	<i>3</i>
Scientific objectives.....	<i>4</i>
CHAPTER II. GEOLOGICAL SETTING.....	<i>5</i>
Regional geology.....	<i>5</i>
Geological and tectonic evolution.....	<i>8</i>
Characteristics of the field.....	<i>14</i>
CHAPTER III. MULTIATTRIBUTE ANALYSIS TO ASSIST STRUCTURAL INTERPRETATION.....	<i>21</i>
Acquisition parameters and processing sequence of the seismic survey.....	<i>23</i>
Poststack seismic data conditioning for structural interpretation.....	<i>27</i>
Recognition of structural patterns on geometric seismic attributes.....	<i>30</i>
Multiattribute analysis and structural interpretation attribute-assisted.....	<i>36</i>
Discussion and results.....	<i>44</i>

CHAPTER IV. SEISMIC INVERSION FOR ROCK PROPERTIES.....	46
Theoretical aspects of seismic inversion.....	48
Factors that control carbonate elastic properties.....	55
Previous studies of porosity prediction in carbonate reservoirs.....	59
Exploratory data analysis	62
Prestack data conditioning, well to seismic tie and wavelet extraction	78
Seismic inversion for reservoir properties	85
CHAPTER V. CORRELATION WITH PRODUCTION DATA	106
Field production data.....	106
Correlation of predicted volumes by PNN and production data	108
Correlation of seismic facies from GTM analysis and production data.....	112
CONCLUSIONS	116
REFERENCES.....	118
APPENDIX A: PETROGRAPHIC DESCRIPTION OF CORE SAMPLES	127
APPENDIX B: BIOSTRATIGRAPHIC DATA.....	147
APPENDIX C. STRUCTURE ORIENTED FILTERING.....	149

LIST OF FIGURES

Figure 1. Location of the area of study regarding the Mexican productive basins. (Modified from PEMEX, 2010).	3
Figure 2. Detail of the Veracruz Basin showing its boundaries and its two geological subdivisions: The Plataforma de Córdoba which is the buried tectonic front of the Sierra de Zongolica, and the Veracruz Tertiary Basin. The field of study (indicated by the red arrow) is located in the western margin of the buried tectonic front in Upper and Middle Eocene age Tertiary sediments. (Map courtesy of PEMEX E&P based on previous work by Prost and Aranda, 2001; Andreani et al., 2008; and Gutiérrez-Paredes et al., 2009).....	6
Figure 3. Structural cross-section through the Veracruz Basin consisting of the Plataforma de Córdoba and the Veracruz Tertiary Sub Basin. The Plataforma de Córdoba is a Cretaceous carbonate platform that was thrust towards the east, which currently constitutes the tectonic front of the Sierra de Zongolica. The Veracruz Tertiary Basin is a foreland basin developed at the foothills of the fold and thrust belt and is filled with Tertiary sandstones, shale and conglomerates.	8
Figure 4. Vertical section through the field with location shown on the inset time slice. The principal structure is a fault-propagation fold. The structural style correlates with the structural style of the buried tectonic front of the Plataforma de Córdoba. (Interpretation courtesy of PEMEX, E&P, Integral Veracruz Asset).	11
Figure 5. Tectonic evolution of the western margin of the Veracruz Basin (after Ferket et al., 2002). The basement is not shown because is not involved in the orogeny. Compression events started during Campanian (Ortuño-Arzate, et al., 2003).	12

Figure 6. Chronostratigraphic chart of the Veracruz basin, distinguishing the Plataforma de Córdoba, the buried tectonic front containing the Cretaceous oil and wet-gas fields of the basin, and the Tertiary Basin containing the studied field. (Modified from Ortuño-Arzate, et al., 2003 and Ferket et al., 2010, based on International Commission on Stratigraphy, 2010). The far right column summarizes the main geological events. FTB indicates fold and thrust belt. 13

Figure 7. Characteristics of the field and its base log showing the six Eocene units, of which five are productive while one is water bearing. (Data courtesy of PEMEX E&P). 14

Figure 8. Structural cross section through the field. EOC–10 and EOC–20 produce in the western portion of the structure; EOC–40 is water bearing and is distributed over the western portion of the anticline; EOC–30 and EOC–50 produce in the eastern flank (Hernández-Martínez, 2009).(Image is courtesy of PEMEX E&P). 15

Figure 9. Regional conceptual sedimentary model (Hernández-Martínez, 2009). (a) Isopach map of the sequence comprising the reservoir horizon EOC–10, contours every 50m. (b) Submarine fan fed by a canyon through a steep escarpment. (c) The analog depositional model for the field: a coarse-grained, sand-rich turbidite system (Bouma, 2000). This analogue model is the same for the Granite Wash deposits in Oklahoma and Texas (Mitchell, 2011). (Courtesy of PEMEX E& P). 17

Figure 10. Heterogeneity of the field at different scales (after Hernández-Martínez, 2009). (a) Well logs showing shale-sand-conglomerate layering. (b) Core with logs and facies distribution. Note high variability in less than 1 meter. (c) Thin sections illustrate variation in reservoir quality due to diagenetic processes, including dissolution, cementation and dolomitization. (Courtesy of PEMEX E&P) 19

Figure 11. Slabbed core of the most productive well (5 m). The darker intervals are oil-impregnated, which contrast with the lighter highly cemented zones. (Data courtesy of PEMEX E&P)..... 19

Figure 12. Petrographic analysis of units EOC–10, EOC–20, EOC–30, EOC–40 AND EOC–50. (a) Mineralogical composition from X-ray diffraction (XRD) analysis. (b) Clay minerals distribution normalized to 10% from XRD analysis. (c) Total components obtained by point counting analysis on thin sections. (d) Porosity normalized to 100% from point counting analysis. 20

Figure 13. Workflow for structural interpretation assisted with multiattribute analysis. The input is the seismic poststack amplitude volume conditioned trough structure-oriented filtering (SOF). Then I calculate similarity and attributes from the filtered volume to identify geological features on time slices. I cluster two or more attributes that associates with the same structural pattern (f. e. faults, relay ramps, transfer faults) Then, I use the clusters from multiattribute analysis to assist the structural interpretation. Correlation with production data is the maximum purpose to get a quantitative relation with seismic attributes. 22

Figure 14. Flowchart summarizing the steps in attribute-assisted structural interpretation. The multiattribute analysis phase consists in visually clustering attributes that highlight the same geological feature. 23

Figure 15. Fold map of the 3D seismic data available covering the field of study. The planned nominal fold was 35; the maximum fold for this crop is 40, the minimum fold is 22. Note that there are no low-fold values near the edges, since the data volume was cut out from a much larger mega-merge survey. (Data courtesy of PEMEX E&P)..... 24

Figure 16. PSTM processing sequence of the mega-merge data volume, which includes the 3D seismic survey covering the area of study. (Data courtesy of PEMEX E&P)..... 25

Figure 17. Vertical seismic slice through original seismic amplitude data (a), and its amplitude spectrum (b)..... 27

Figure 18. Time slices at $t=2.220s$ through (a) original seismic amplitude and (b) structured-oriented filtered amplitude volume. Corresponding time slices through coherence computed from the (c) original seismic amplitude and (d) SOF amplitude volume. Yellow block arrows indicate difference in fault edges while magenta arrows indicate differences in acquisition footprint. As desired, faults are sharpened and footprint is suppressed.....28

Figure 19. Vertical slices through seismic amplitude volumes (a) before and (b) after two iterations of SOF. (c) Rejected noise computed as the difference between (a) and (b). Location of line AA' shown in Figure 15. Block arrows indicate where the images are different.....29

Figure 20. Sign convention of curvature attribute (Chopra and Marfurt, 2010). 2D curvature, k , is the inverse of the radius of a circle, R , tangent to a surface. Positive values of k correspond to an anticline, negative values of k correspond to a syncline and zero values of k correspond to a flat or dipping plane.31

Figure 21. 3D curvature identification of my favorite fruits. For a quadratic surface, the two principal curvatures, $k_1 \geq k_2$ are orthogonal to each other, and represent the extreme most-positive and most-negative values. Note on my banana $k_1 > 0$ (anticlinal) and $k_2 < 0$ (synclinal) such that this part of the fruit is a saddle. For my guava I have $k_1 > k_2 > 0$, such that I have a dome. In my pitted avocado $k_2 < k_1 < 0$, such that I have a bowl. Finally, in my watermelon, $k_1 > k_2 = 0$, such that I have a ridge.....32

Figure 22. Drag along a reverse fault. San Rafael Reef, UT (After Fossen, 2010).....34

Figure 23. Vertical slice through seismic amplitude and time slices through (a) most negative principal curvature, k_1 , (b) most positive principal curvature, k_2 , and (c) Sobel filter similarity. Main unconformity, which separates Eocene carbonates from Miocene shale, indicated in red. Note the signature of the thrust fault on the three attribute time slices.35

Figure 24. (a) Clustering of seismic attributes sensitive to normal faults. (b) Low coherent lineaments bounded by flexures in k_1 and k_2 delineate normal faults with drag. 36

Figure 25. Clustering of seismic attributes sensitive to reverse faults. Low coherence areas around fault zones bounded by a positive flexure in k_1 , delineate reverse faults. For this data set, the k_1 lineament corresponds to the crest of the fault propagation fold, which has the same geometry as the drag along a reverse fault illustrated in Figure 23. 37

Figure 26. (a) Multiattribute display over the amplitude vertical slice AA' co-rendered with k_1 , k_2 and Sobel filter similarity. Yellow arrows indicate lineaments of k_1 and k_2 associated with faults that I interpret as drag; green arrows indicate curvature lineaments associated with folds and flexures. I interpret the low coherence area around reverse faults as damage zones illustrated in Fossen's diagram (b); the damage zone is the response of brittle deformation cause by faulting (Fossen, 2010). 39

Figure 27. (a) Multiattribute display along a time slice (at $t=2.420$ s) of k_1 co-rendered with k_2 and Sobel filter similarity. I associate low similarity lineaments bounded by both k_1 and k_2 curvatures as normal faults with drag. I interpret other perpendicular curvature anomalies as relay ramps or transfer faults at small scale. The block diagrams illustrates structural elements and curvature response of fault zones in carbonates rocks of the upper (b) Glen Rose formation and the (c) Del Rio, Buda, and Eagle Ford formation which I regard as analogues. (After Ferrill and Morris, 2008). 40

Figure 28. Vertical slice through seismic amplitude and horizon slice through shape index modulated by curvedness using a 2D color bar, where the hue indicates shape and lightness indicates the degree of deformation. Note that ridge- and dome-related patterns, defined by shape index attribute, correlate with blocks in between faults. 42

Figure 29. Amplitude vertical slice co-rendered with coherence and shape index. 43

Figure 30. Attribute-assisted structural interpretation. Using multiattribute analysis, I interpreted the structural framework of the field.....	43
Figure 31. Workflow for reservoir quality prediction using seismic inversion and exploratory data analysis. Exploratory data analysis (EDA) evaluates the feasibility of running seismic inversion. In this stage, the relationship between the elastic parameter and the reservoir property is found and later is used to transform the results from inverted elastic parameters to a desired reservoir property. The workflow shows three possible ways to obtain the reservoir property depending on the relationships obtained from EDA. (1) If there is no relationship, calculate the property using geostatistics or neural networks using just the well log data; (2) if there is a discrimination of desired property using only P-wave impedance, calculate property volume from poststack inversion and (3) if the discrimination improves using S-wave as well P-wave impedances, obtain the reservoir property from prestack inversion of migrated gathers.	47
Figure 32. (a) An example of a forward problem for exploration seismology, in which the convolutional model produces synthetic seismic traces. (b) An inverse problem, prestack seismic inversion, in which P- and S-wave parameters are estimated by inverting a linearized approximation of the Zoeppritz equations. (After Menke, 1984 and Meju, 1994).....	49
Figure 33. (a) At normal incidence there are two vertical wave components associated: a normal reflected and a vertical transmitted wave (Rai and Sondergeld, 2011). (b) In contrast, there are four wave components associated with an oblique incident P-wave at horizontal interface: P-wave reflected and P-wave transmitted; S-wave reflected and S-wave transmitted (Mavko et al., 2009). 53	
Figure 34. Porous carbonate frames exhibiting different elastic behavior (Eberli et al., 2003). (a) Intercrystalline porosity produced by dolomitization. This rock frame is weak and thus has low velocity. (b) Moldic porosity supported by precipitated cement which provides a stiff rock frame. Moldic porosity is less compressible due to the roundness of dissolved molds, which have an aspect ratio close to 1, and thus has high velocity.....	57

Figure 35. Velocity versus porosity plot for different carbonate rocks measured at 8 MPa effective pressure (Eberli et al., 2003). Moldic and intraframe porosity samples have higher velocity than the interparticle/crystalline and microporosity porosity types. The black curve represents the best exponential fit. Note that for the same porosity value, compressional velocity V_p varies accordingly to the pore type. 58

Figure 36. Representative thin section photographs of a nummulitic reservoir study by Marion and Jizba (1997). (a) Intraparticle porosity in nummulitic foraminifera. (b) Interparticle porosity. White arrows indicate porosity. 60

Figure 37. Calibrated rock physics model (Marion and Jizba, 1997). (a) Velocity–porosity relationship comparison between core measurements (dots) and rock physics model (solid line). (b) Velocity–impedance relationship. (c) Impedance–porosity relationship used to transform inverted seismic data to porosity. 61

Figure 38. (a) Acoustic impedance versus total porosity color-coded by water saturation (Bosch et al., 2010). Dots indicate measurements from well logs, the black curve indicates the calibrated petrophysical model and the gray band indicates plus and minus one standard deviation from the model. 61

Figure 39. Vertical slice through (a) acoustic impedance and (b) total porosity resulting from simultaneous seismic petrophysical inversion for a carbonate-clastic heavy oil field (Bosch et al., 2010). 62

Figure 40. Time structure map of the main unconformity that separates Miocene shale from Eocene calcilithites showing the distribution of sonic and density logs in the field of study. Red circles indicate wells with P-wave sonic, S-wave sonic and density logs. Green circles indicate wells with P-wave sonic and density logs but without S-wave sonic logs. 64

Figure 41. Vertical depth versus total porosity color-coded by well name for five reservoir units in the Eocene calcilithites. Note that for the same depth range, there is a wide range of porosity values. This response indicates that porosity is not depth dependent. 67

Figure 42. Vertical depth versus total porosity color-coded by bulk density (RHOB) for five reservoir units in the Eocene calcilithites. Although scattered, note that density increases as porosity decreases, independent of depth. 68

Figure 43. P-wave impedance versus total porosity color-coded by gamma ray (GR) for reservoir units EOC-10, EOC-20, EOC-30 and EOC-3. Note than red points, correlating to clean facies (color-coded by low GR), are scattered and present a wide range of impedance for the same porosity value. Red circle indicate shale layers cut by well 35. 69

Figure 44. P-wave impedance versus total porosity color-coded by bulk density (RHOB in g/cm^3) for reservoir units EOC-10, EOC-20, EOC-30 and EOC-3. The density decreases as porosity increases. This dependence is less evident in unit EOC-3. 70

Figure 45. Total porosity and clay volume discrimination for reservoir unit EOC-10 through crossplots of S-impedance versus P-impedance, V_P to V_S ratio versus P-impedance and $\mu\rho$ versus $\lambda\rho$. The left-hand crossplots are color-coded by total porosity while the right-hand crossplots are color-coded by clay volume. Red circles indicate clean facies while blue circles indicate high clay content. 72

Figure 46. Total porosity and clay volume discrimination for reservoir unit EOC-20 through crossplots of S-impedance versus P-impedance, V_P to V_S ratio versus P-impedance and $\mu\rho$ versus $\lambda\rho$. The left-hand crossplots are color-coded by total porosity (Φ_{Total}) while the right-hand crossplots are color-coded by clay volume (V_{clay}). Red circles indicate clean facies while blue circles indicate high clay content. 73

Figure 47. Total porosity and clay volume discrimination for reservoir unit EOC-30 through crossplots of S-impedance versus P-impedance, V_P to V_S ratio versus P-impedance and $\mu\rho$ versus $\lambda\rho$. The left-hand crossplots are color-coded by total porosity (Φ_{Total}) while the right-hand crossplots are color-coded by clay volume (V_{clay}). Red circles indicate clean facies while blue circles indicate high clay content. 74

Figure 48. Total porosity and clay volume discrimination for reservoir unit EOC–50 through crossplots of S-impedance versus P-impedance, V_P to V_S ratio versus P-impedance and $\mu\rho$ versus $\lambda\rho$. The left-hand crossplots are color-coded by total porosity (Φ_{Total}) while the right-hand crossplots are color-coded by clay volume (V_{clay}). Red circles indicate clean facies while blue circles indicate high clay content.	75
Figure 49. Total porosity and clay volume discrimination for reservoir unit EOC–3 through crossplots of S-impedance versus P-impedance, V_P to V_S ratio versus P-impedance and $\mu\rho$ versus $\lambda\rho$. The left-hand crossplots are color-coded by total porosity (Φ_{Total}) while the right-hand crossplots are color-coded by clay volume (V_{clay}). Red circles indicate clean facies while blue circles indicate high clay content.	76
Figure 50. Effective porosity indicators for reservoir unit EOC–50. (a) S-impedance versus P-impedance, (b) V_P to V_S ratio versus P-impedance, and (c) $\mu\rho$ versus $\lambda\rho$, all color-coded by effective porosity (Φ). Red circles indicate high effective porosity associated with clean facies.	77
Figure 51. Simple workflow for estimation of rock quality using prestack seismic inversion.	78
Figure 52. Workflow used for conditioning of prestack time migrated (PSTM) gathers for elastic seismic inversion.	79
Figure 53. Offset PSTM gathers: (a) Unconditioned gathers, (b) gathers after two iterations of prestack-SOF, (c) rejected noise computed as the difference between (a) and (b). Red arrows indicate the horizon that correlates with the main unconformity. The red arrow in the map indicates the position of the shown gathers.	81
Figure 54. Gathers in angle domain. (a) Angle gathers obtained from offset gathers after prestack-SOF. (b) Gathers in angle domain after trim statics processing. Note that reflectors have been flattened after trim statics. Red arrow indicates a reflector that exhibits a significant shift before and after trim statics. The red arrow in the map indicates the position of the shown gathers.	82

Figure 55. Amplitude spectra after stacking of (a) original PSTM gathers, (b) gathers after prestack-SOF and (c) final conditioned gathers after prestack SOF and trim statics. Note the increase in high frequencies with respect to the original stack.....	83
Figure 56. (a) Phase spectrum and (b) amplitude spectrum of the three seismic wavelets extracted over conditioned gathers for near, middle and far angles. Note the near angles have higher frequencies than far angles because of migration stretch.....	83
Figure 57. Well to seismic tie in a representative well for reservoir units EOC–20, EOC–10, and EOC–40. The crosscorrelation coefficient is 0.9.....	84
Figure 58. Well to seismic tie of a representative well of the eastern flank of the anticline containing the units EOC–50 and EOC–30. The crosscorrelation coefficient is 0.93.	84
Figure 59. Initial low frequency model for prestack simultaneous inversion overlapping traces of stacked conditioned gathers. The target window is defined by the main unconformity (pink horizon) and the deeper blue horizon which correlates with the base of unit EOC–3. The intermediate green horizon correlates with a sequence boundary that separates EOC-50 from EOC-30.....	86
Figure 60. Validation analysis of simultaneous inversion for the blind well R. The first three left-hand panes compare inverted with original and modeled impedance and density logs. The other three right-hand panes compare synthetic with original and the residual computed as the difference between them.....	87
Figure 61. Crosscorrelation coefficient of properties resulted from inversion.....	87
Figure 62. Inverted results versus original well logs. (a) P-impedance, (b) S-impedance. Gray lines indicated correlation of 1.0.....	87

Figure 63. Vertical slices through (a) P -wave impedance and (b) S-wave impedance resulting from model-based simultaneous inversion. The position of the vertical section is indicated by the red line in the map. The impedance calculated from well logs is represented by the inserted colored bar at well position.	88
Figure 64 Supervised probabilistic neural network workflow for rock property estimation. (Modified from Verma et al., 2012).	90
Figure 65. Structural cross section of wells B, K, L and N, productive in EOC-10. Top and base of reservoir unit EOC-10 is indicated by black lines.....	90
Figure 66. Horizons slices through (a) P-impedance, (b) $\lambda\rho$, (c) $\mu\rho$, and (d) coherent energy 10 ms below the top of EOC-10. Note that high coherent energy areas correlate with relatively high $\mu\rho$ and $\lambda\rho$. Correlation with Z_p is ambiguous. Elongated lineaments in all attributes correspond to normal faults indicated by white arrows.	92
Figure 67. a) Training and (b) validation of neural networks to estimate clay volume. The error is 0.027 with a correlation of 0.61 after validation. (c) crossplot of predicted porosity versus actual porosity at well position. The red line indicates correlation of 1.0.	93
Figure 68. Clay volume over cross section through wells R, Q, AD, and U. Line location is indicated in the inserted map	94
Figure 69. Horizons slices through (a) spectral magnitude component at 84Hz, (b) coherent energy, (c) inverted $\lambda\rho$ and (d) clay volume calculated with PNN. Note that high coherent energy areas correlate with low clay volume and relatively high $\lambda\rho$. Linear patterns oriented NE-SW correspond to normal faults. Those present low coherent energy which resulted in low clay volume estimation.	95
Figure 70. (a) Training and (b) validation of neural networks to estimate effective porosity. The error is 0.027 with a correlation of 0.61 after validation. (c) crossplot of predicted porosity versus actual porosity at well position. The red line indicates a correlation of 1.0.	96

Figure 71. Effective porosity cross section through wells R, Q, AD, and U. The inserted colored column at well position corresponds to effective porosity calculated from well logs. Note that the predicted volume underestimates the well property. Furthermore, the resolution of the predicted volume does not represent properly the vertical variation at finer well scale. The location of the cross section is indicated on the inserted map. 97

Figure 72. Vertical seismic section through (a) clay volume and (b) effective porosity. The black horizon correlates with the top of unit EOC-10 and the blue one with its base. Note in (a) that the clay content along reservoir unit does not vary significantly; the predominant facies have low clay content (warm colors). In contrast, the porosity varies more significantly along the unit. The reservoir unit EOC-10 is underlaid and overlaid by clay-rich facies (cold colors). 100

Figure 73. Mean distribution of the posterior probability projections of the reservoir zones (a) EOC-10 and (b) EOC-30) plotted in the 2D latent space. High density areas are represented by cold colors (magenta, blue, cyan). The arrows indicate the association of clusters delineated by polygons and high density areas. 102

Figure 74. Volume probe generated from classes selected on the crossplot of the mean distribution of the posterior probability function. Upper right- and left interpreter-generated color-coded polygons made in the 2D latent space identifying distinct clusters. Note that faults, indicated by white arrows, are also assigned to a class by the unsupervised algorithm. 103

Figure 75. Phantom horizon slice 10 ms below the top of the EOC-10 horizon through the (a) clay and (b) effective porosity volumes predicted from a supervised probabilistic neural networks, and (c) clusters along the top the top EOC-10 using an unsupervised generative topographic mapping (GTM) classification algorithm. 104

Figure 76. Phantom horizon slice 10 ms below the top of the EOC-30 horizon through the (a) clay and (b) effective porosity volumes predicted from a supervised probabilistic neural networks, and (c) clusters along the top the top EOC-30 using an unsupervised generative topographic mapping (GTM) classification algorithm..... 105

Figure 77. Total cumulative production per reservoir unit normalized to 100% for each type of hydrocarbon. Note that EOC-10 accounts for more than 50% of the total oil cumulative production. The second most productive unit, EOC-30, accounts for around 20% of the total oil production. EOC-50 has minor cumulative production. 107

Figure 78. Cumulative production for each reservoir unit normalized to 100%. Note that EOC-30 has the major water production (52%).The gas cumulative gas production do not vary significantly ranging from 5 to 8% of the total production in barrels of oil equivalent (BOE). 107

Figure 79. Phantom horizon slices 10 ms below EOC-10 through predicted (a) clay content and (b) effective porosity volumes, blended with bubble maps of the total average daily hydrocarbon production for the first seven months. Note that production is not linearly correlated with predicted clay content while higher production is not associated with the highest effective porosity areas. Blue dotted lines indicate the oil-water contact for the eastern fault block. The contour interval is 40 ms. 109

Figure 80. Phantom horizon slices 10 ms below EOC-30 through predicted (a) clay content and (b) effective porosity volumes, blended with bubble maps of the total average daily hydrocarbon production for the first seven months. Time structure contours are in ms. Note the low clay content over the unit. Elongated clay-richer zones are associated with normal faults. Higher production is not associated with the highest effective porosity areas. The established cut-off value of effective porosity is $\Phi \geq 9\%$ 111

Figure 81. Facies classification from GTM for reservoir unit EOC-10. (a) Seismic facies map 10 ms below top of EOC-10. Pie charts are proportional to daily average production for the first 7 month. (b) 3D view of the volume probe containing clustering from GTM analysis. Insert crossplots are generated directly in the 2D latent space. 113

Figure 82. Facies classification from GTM for reservoir unit EOC-30. (a) Seismic facies map 10 ms below top of EOC-30. Pie charts are proportional to daily average production for the first 7 months. (b) 3D view of the volume probe containing clustering from GTM analysis. Note that productive wells fall in orange seismic facies, except well AD which correspond brown seismic facies and happens to be the major water producing well in this unit. 115

LIST OF TABLES

Table 1. Acquisition parameters of the 3D seismic survey that covers the area of study. (Data courtesy of PEMEX E&P).....	26
Table 2. Summary of rock properties obtained with seismic inversion as a function of the data type inverted (Adapted from Barclay et al., 2008).	54
Table 3. Sonic and density logs available per well in the area of study.	65

LIST OF SYMBOLS

C	Curvedness
\mathbf{d}	Matrix representing the data
\mathbf{G}	Matrix of the linearized forward model
k_1	Most-positive principal curvature
k_2	Most-negative principal curvature
k_{max}	Maximum curvature
k_{min}	Minimum curvature
\mathbf{m}	Matrix of model parameters
P	Compressional
R	Reflection coefficient
s	Shape index
S	Shear
S_w	Water saturation
V_{clay}	Clay volume
V_P	P-wave velocity
V_P/V_S	P-wave velocity to S-wave velocity ratio
V_S	S-wave velocity
Z_P	P-wave impedance
Z_S	S-wave impedance
θ	Angle of incidence
μ	Shear modulus, second Lamé parameter
ν	Poisson's ratio
ρ	Density
Φ	Porosity
λ	Incompressibility, first Lamé parameter

LIST OF ACRONYMS

AAPG	American Association of Petroleum Geologists
AASPI	Attributed Assisted Seismic Processing & Interpretation
AI	Acoustic impedance
BANOBRAS	Banco Nacional de Obras y Servicios Públicos (National Works and Public Services Bank of Mexico)
BOE	Barrels of oil equivalent
CONACYT	Consejo Nacional de Ciencia y Tecnología (the National Council on Science and Technology of Mexico)
CPSGG	ConocoPhillips School of Geology & Geophysics
CSEG	Canadian Society of Exploration Geophysicists
E&P	Exploration and Production
EDA	Exploratory Data Analysis
EEI	Extended elastic impedance
EI	Elastic impedance
EUR	Expected ultimate recovery
FTB	Fold and thrust belt
GCSSEPM	Gulf Coast Section of the Society for Sedimentary Geology
GR	Gamma ray well log
GTM	Generative topographic mapping
ILD	Deep resistivity
ILM	Medium resistivity
mbsl	Meters below sea level
NE	Northeast
NPHI	Neutron porosity

NW	Northwest
OU	The University of Oklahoma
OWC	Oil-water contact
PCA	Principal component analysis
pdf	Probability density function
PEMEX	Petróleos Mexicanos, the Mexican national oil company
PNN	Probabilistic Neural Networks
PSTM	Prestack time migration
QC	Quality control
RHOB	Bulk density
RMS	Root mean square
SCAC	Surface consistent amplitude correction
SEG	Society of Exploration Geophysicists
SENER	Secretaría de Energía (Mexico Federal Government Ministry of Energy)
SMO	Sierra Madre Oriental
SOF	Structure-oriented filtering
SOM	Self organizing mapping
SW	Southwest
VTB	Veracruz Tertiary Basin
XRD	X-ray diffraction

ABSTRACT

The Veracruz Basin is PEMEX's second most productive non-associated gas basin with incipient oil production in both the Plataforma de Córdoba and the Tertiary foreland basin margin sub-provinces. My study focuses on an onshore oil field in the western boundary of the Veracruz Tertiary Basin, southern Mexico. The production comes from Eocene resedimented carbonates (calclithites) eroded from the Cretaceous limestones and dolomites of the tectonic front that were redeposited and buried in a slope environment.

The objective of this research is to develop a methodology using surface seismic data to map faults and discriminate changes in porosity, facies and thereby reservoir quality in order to better understand the observed reservoir compartmentalization seen by production. Prediction of reservoir quality and fault distribution is important in primary recovery and critical in planning a secondary recovery stage of the field.

I use volumetric coherence and curvature computed from data conditioned using structure-oriented filtering to delineate subtle structural patterns that are not evident on the original amplitude data. I find that reverse faults associated with fault-propagation folds are well delineated by curvature, and are surrounded by a low coherence area associated with damage zone. Other curvature anomalies are normal fault-related when they bracket low coherence patterns. The shape index attribute, which quantifies the deformation morphology of seismic reflectors, can be successfully used to delineate compartments.

I use prestack simultaneous inversion to delineate seismic facies and predict inter-well reservoir properties. I trained and validate with well data, a probabilistic

neural network to estimate porosity and clay content volume. I compared these results with my seismic facies obtained using generative topographic mapping, an unsupervised data driven clustering method. Production data shows that reservoir quality is qualitatively better discriminated by seismic facies from GTM analysis than by supervised neural networks.

CHAPTER I. INTRODUCTION

Reworked conglomerate reservoirs tend to be highly heterogeneous with a complex pore structure that is not only dependent on primary fabric but also on subsequent diagenetic processes. Although the Granite Wash of the Wichita Mountain from Oklahoma and the Texas panhandle is currently one of the hot plays in the Midcontinent of the USA, there is little scientific literature on resedimented deposits that serve as an analogue for this type of reservoir. This work will expand this data base by examining a carbonate wash oil field in the Veracruz Basin of Mexico.

Although an oil exporter, Mexico imports significant gas to meet growing industrial and household needs. The Veracruz Basin is the second most productive basin of non-associated Gas in Mexico following the Burgos Basin (Figure 1). The Tertiary target is of particular interest since the Veracruz Basin has primarily Mesozoic rather than Tertiary oil production (Martínez-Medrano et al., 2009; PEMEX, 2011). By better understanding this oil field, we may be able to extend the play concept to find similar areas along the unexplored eastern margin of the tectonic front of Veracruz Basin.

The field produces heavy oil that ranges from 16 to 22°API from Eocene carbonate conglomerates and sands (calclithites) that were eroded from the tectonic front of the Sierra Madre Oriental, and were redeposited and buried in a slope submarine environment. The field was discovered in 2001 with 2D seismic data. In 2003, a 1926 km² 3D seismic survey was acquired to characterize the structure prior to field development, which started in 2004 without an appraisal phase.

The PEMEX characterization team has used basic poststack seismic attributes, such as RMS amplitude, to distinguished shale from the calcareous reservoir. This

attribute has worked fine for that purpose but does not discriminate reservoir quality. To minimize risk due to reservoir heterogeneity, PEMEX's strategy contemplates deviated wells to penetrate more than one reservoir unit per well. As of December 2011, there were five exploratory wells, three of which encountered different reservoir levels in the Eocene calcilithites. There are also 25 development wells in the area, two of which are unproductive. In spite of these favorable economic results, the success is not considered complete since not all of the individual reservoir units penetrated were productive.

In this thesis, I will use high quality seismic data, sonic logs, production data, and seismic inversion to better predict reservoir quality between the wells.

I begin by reviewing the geological setting of the depositional and tectonic history of Veracruz Basin, followed by more detailed petrophysical analysis of the study area in Chapter II. Next in Chapter III, I use geometric attributes to support my structural interpretation. In Chapter IV, I use my petrophysical analysis to calibrate my seismic inversion to predict porosity and lithology. Finally, in Chapter V, I conclude with the correlation of estimated reservoir properties and seismic facies classification with production data. Appendix A includes petrographic descriptions of thin sections, results of X-ray diffraction analysis and point counting over core data. Appendix B presents biostratigraphic data. Appendix C reviews the structure-oriented filtering used in this work for data conditioning.



Figure 1. Location of the area of study regarding the Mexican productive basins. (Modified from PEMEX, 2010).

Problem statement

The field of study is little understood because of its structural and stratigraphical complexity. I therefore address two main problems:

- Lateral compartmentalization by faulting. Wells that are only 500 m apart or tag a structurally higher component of the same reservoir may not be productive.
- Lateral and vertical heterogeneity. The reservoir consisting of carbonates re-deposited in slope and basin floor environments are highly variable in distribution. Reservoir quality depends upon cementation, dissolution and dolomitization diagenetic processes. Nonproductive wells that target the same unit in the same fault block, drilled up dip, proves this variability in reservoir quality.

Scientific objectives

- Develop a seismic attribute-assisted workflow to define the fault system and predict the presence of faults at the limits of seismic resolution.
- Develop a methodology to predict the quality of reservoirs in the field, from surface seismic data calibrated by well log and production data.

CHAPTER II. GEOLOGICAL SETTING

Regional geology

Geologically, the field of study is situated in the Veracruz Basin, which is located in the southwestern Gulf of Mexico, between two oil prone basins: Tampico-Misantla in the north, and Salina del Istmo in the southeast (Figure 1) (Martínez-Medrano et al., 2009). The Sierra de Zongolica, a fold and thrust belt considered to be the southern extension of the Sierra Madre Oriental (SMO) (Eguiluz-de-Antuñano et al., 2000), marks the western limit of the Veracruz Basin (Prost and Aranda, 2001). The eastern boundaries are the volcanic Anegada and Los Tuxtlas complexes (Jennette et al., 2003; Andreani et al., 2008) while the Santa Ana high is a volcanic zone that defines the northern boundary (Cruz-Helú et al., 1977; Mossman and Viniegra, 1976). The southern boundaries are the metamorphic complexes of the Sierra de Juárez, the Mixtequita and the Sierra de Chiapas (Gutiérrez-Paredes et al., 2009). Figure 4 summarizes these boundaries.

There are two geological sub-provinces within the Veracruz basin: The “Plataforma de Córdoba” and the “Cuenca Terciaria de Veracruz” (PEMEX, 2010), the latter of which will be hereafter referred to as the Veracruz Tertiary Basin (VTB) (Figure 2). The Plataforma de Córdoba is a Cretaceous carbonate platform that was deformed into a series of eastward verging imbricate thrusts and folds (Figure 3) that currently constitutes the tectonic front of the Sierra de Zongolica (Prost and Aranda, 2001). The detachment of the buried front of the Plataforma de Córdoba is associated with Lower Cretaceous evaporites (Figure 3) (Eguiluz-de-Antuñano et al., 2000; Ortuño-Arzate et al., 2003). The Plataforma de Córdoba produces middle to heavy oil

and wet gas (PEMEX, 2010). The western edge of the platform is exposed in the Sierra de Zongolica (Morán-Zenteno, 1994) while the eastern part is buried under the VTB (Morán-Zenteno, 1994; Prost and Aranda, 2001; Ortuño-Arzate et al., 2003).

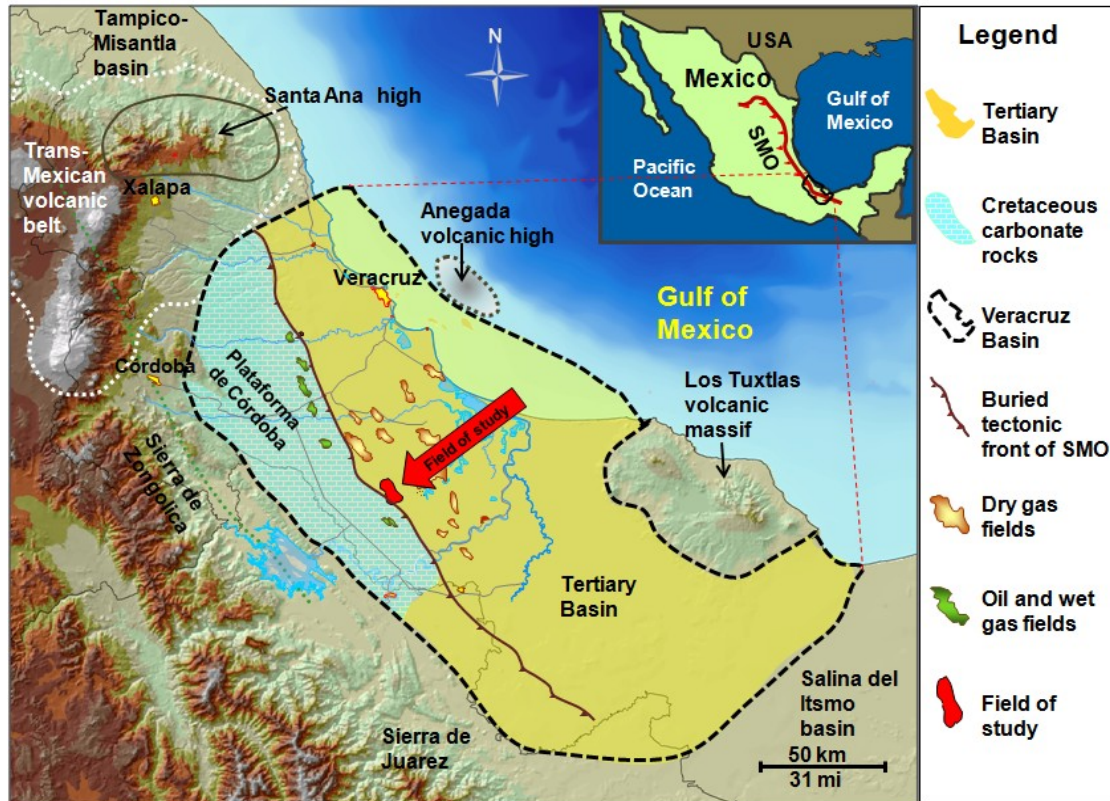


Figure 2. Detail of the Veracruz Basin showing its boundaries and its two geological subdivisions: The Plataforma de Córdoba which is the buried tectonic front of the Sierra de Zongolica, and the Veracruz Tertiary Basin. The field of study (indicated by the red arrow) is located in the western margin of the buried tectonic front in Upper and Middle Eocene age Tertiary sediments. (Map courtesy of PEMEX E&P based on previous work by Prost and Aranda, 2001; Andreani et al., 2008; and Gutiérrez-Paredes et al., 2009).

The Veracruz Tertiary Basin is a foreland basin (Prost and Aranda, 2001) developed at the foothills of the buried tectonic front, filled with sequences of shale, sands and conglomerates. The sediments come from a variety of sources: igneous

complexes (such as the Santa Anna high), metamorphic complexes (La Mixtequita, the Sierra de Juarez and Macizo de Chiapas), and carbonates from the Plataforma de Córdoba (PEMEX, 2010; Cruz-Helú et al., 1977). The VTB produces dry gas and a minor quantity of oil in the field of study located at its western margin (PEMEX, 2010). Biogenic gas is the major production from the Upper Miocene and Lower Pliocene reservoirs (Jennette et al., 2002). The production of non-associated gas makes the VTB the second most important basin for PEMEX after the Burgos Basin (PEMEX, 2010 and PEMEX, 2011). In this particular context, the field of study is at the eastern margin of the Plataforma de Córdoba, in the western margin of the VTB. Figure 3 shows a cross-section through the Veracruz Basin that illustrates the structural style of the Plataforma de Córdoba and the VTB.

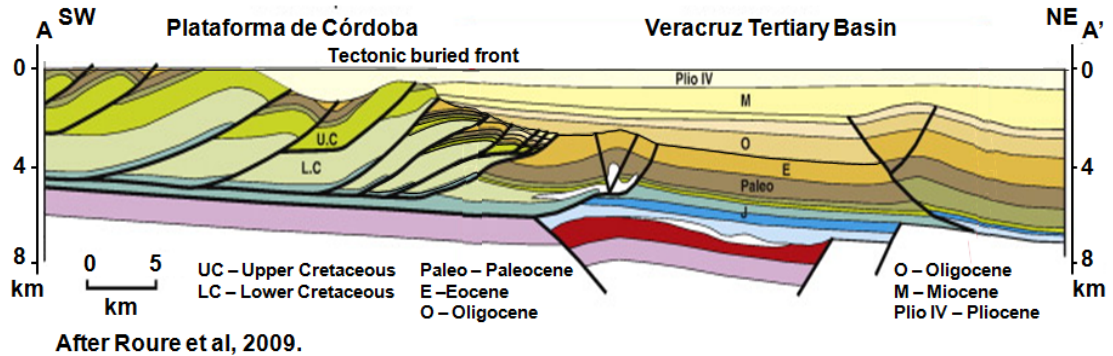
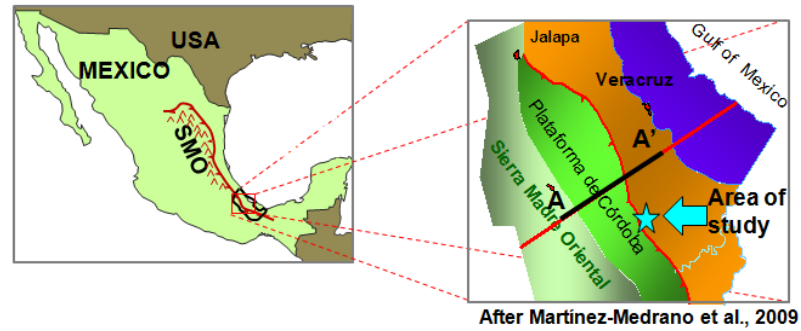


Figure 3. Structural cross-section through the Veracruz Basin consisting of the Plataforma de Córdoba and the Veracruz Tertiary Sub Basin. The Plataforma de Córdoba is a Cretaceous carbonate platform that was thrust towards the east, which currently constitutes the tectonic front of the Sierra de Zongolica. The Veracruz Tertiary Basin is a foreland basin developed at the foothills of the fold and thrust belt and is filled with Tertiary sandstones, shale and conglomerates.

Geological and tectonic evolution

The geological history of the study area is key to understanding the geometry and type of deposit of the field. A series of metamorphic rocks complexes, Late Carboniferous to Permian in age (Ortuño-Arzate et al., 2003), constitute the basement of the Sierra de Zongolica (Prost and Aranda, 2001). From Late Triassic to Middle Jurassic the area was subjected to continental rifting that generated a set of horsts and grabens (Magoon et al., 2001). Since Middle Jurassic (Magoon et al., 2001) to Late

Jurassic the Yucatan block moved southwards to its current position along a transform margin giving rise to the present day Gulf of Mexico (Prost and Aranda, 2001).

After the opening of the Gulf of Mexico, from Oxfordian to Early Cretaceous, there prevailed a passive margin (Magoon et al., 2001; Prost and Aranda, 2001) and slow post-rift thermal subsidence (Padilla-y-Sánchez, 2007) that favored carbonate sedimentation along a series of horsts aligned northwest (Prost and Aranda, 2001). From Early to Middle Cretaceous, several carbonate platforms such as the Plataforma de Tuxpan, the Plataforma de Orizaba, and the Plataforma de Córdoba (Roure et al., 2009) developed along the east coast of Mexico.

In Late Cretaceous, the Pacific Plate subducted under the west coast of Mexico causing the formation of the thrust and fold belt of the Sierra de Zongolica (Prost and Aranda, 2001) including its current front, the Plataforma de Córdoba (Guzmán and De Cserna, 1963). This orogeny, which was called Hidalgoan by Guzmán and De Cserna in 1963 (Gray and Lawton, 2011), took place from Late Cretaceous to Eocene forming the Sierra Madre Oriental, the Sierra de Coahuila and the Sierra de Zongolica (Padilla-y-Sánchez, 2007). The Hidalgoan orogeny is coincident in time with the Laramide orogeny in the United States (Gray et al., 2001; Gray and Lawton, 2011; Eguiluz-de-Antuñano et al., 2000) but is different in style (Gray et al., 2001; Gray and Lawton, 2011; Bird, 2002). The age of the orogeny in the Sierra de Zongolica has been discussed by several authors (Guzmán and De Cserna, 1963; Eguiluz-de-Antuñano et al., 2000, Mossman and Viniegra, 1976; Ortuño-Arzate et al., 2003; Padilla-y-Sánchez, 2007; Prost and Aranda, 2001; Roure et al., 2009); however, there is not full agreement in the duration of deformation, particularly when the last pulse deformed the front of the belt.

Ortuño-Arzate et al. (2003), Padilla-y- Sánchez (2007), and Guzmán and De Cserna (1963) state that the orogeny in Mexico lasted until Early Eocene. Guzmán and De Cserna (1963) point out that the major deformation occurred during Early Eocene. On the other hand, Mossman and Viniegra (1976) state that the major thrusting in the western margin of the belt took place during Middle Eocene. Both statements cast doubt for Eguiluz-de-Antuñano et al. (2000) who propose that the maximum compressional deformation was in Late Eocene with the tectonic front deformation extending until Late Eocene or even Oligocene, though the age is not well documented. 3D seismic data (Figure 4) show that the field of study has the same structural style as the buried thrust belt front of the Plataforma de Córdoba. Additionally, biostratigraphic data from 13 wells date the deposits as Middle Eocene and the upper reservoir as Late Eocene. These new data suggest that the orogeny is younger than stated in previous studies of the Basin. Ideally, palinspastic reconstruction based on the 3D seismic and biostratigraphic data of the development wells would address this ambiguity.

During Eocene time, the western portion of the Plataforma de Córdoba was uplifted, exposed and eroded during and after the orogeny, causing deposition of flysch sequences in the eastern margin of the front (Guzmán and De Cserna, 1963).

From Miocene to present, the basement started to subside and was tilted down to the east (Ortuño-Arzate et al., 2003). The Plataforma de Córdoba continued eroding from Miocene to Quaternary, with two stages of karstification (Ortuño-Arzate et al., 2003). In the Veracruz Tertiary Basin, there was inversion of normal basement faults and transpression during the Miocene (Ortuño-Arzate et al., 2003). The Miocene was also a period of significant sedimentation with increasing thickness toward the Gulf of

Mexico that give raise to gravitational collapse seen as growth and normal faulting in the eastern margin of the basin. Figure 5 shows the evolution of the western portion of the Veracruz Basin which is representative of the field studied. Figure 6 shows a chronostratigraphic chart of the exposed Plataforma de Córdoba, the buried front of the platform and the Veracruz Tertiary Basin. Because of erosion, the total thickness deposited during Eocene remains unknown (Cruz-Helú et al., 1977).

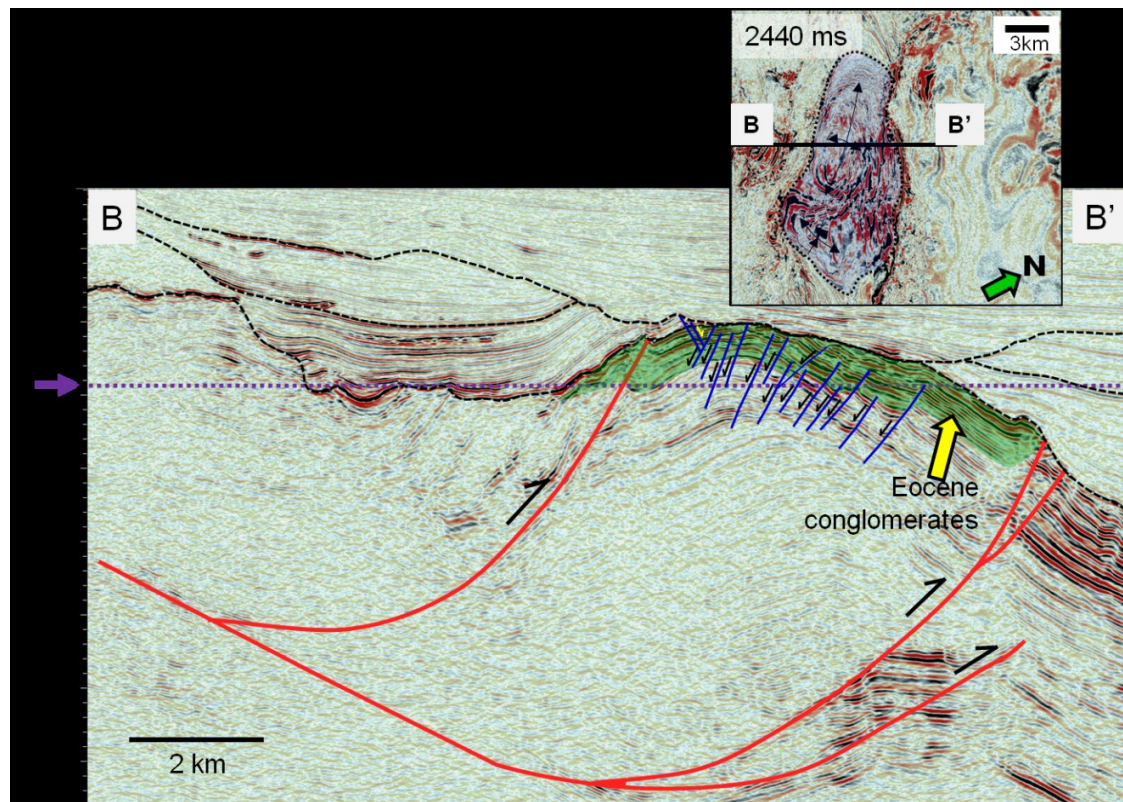


Figure 4. Vertical section through the field with location shown on the inset time slice. The principal structure is a fault-propagation fold. The structural style correlates with the structural style of the buried tectonic front of the Plataforma de Córdoba. (Interpretation courtesy of PEMEX, E&P, Integral Veracruz Asset).

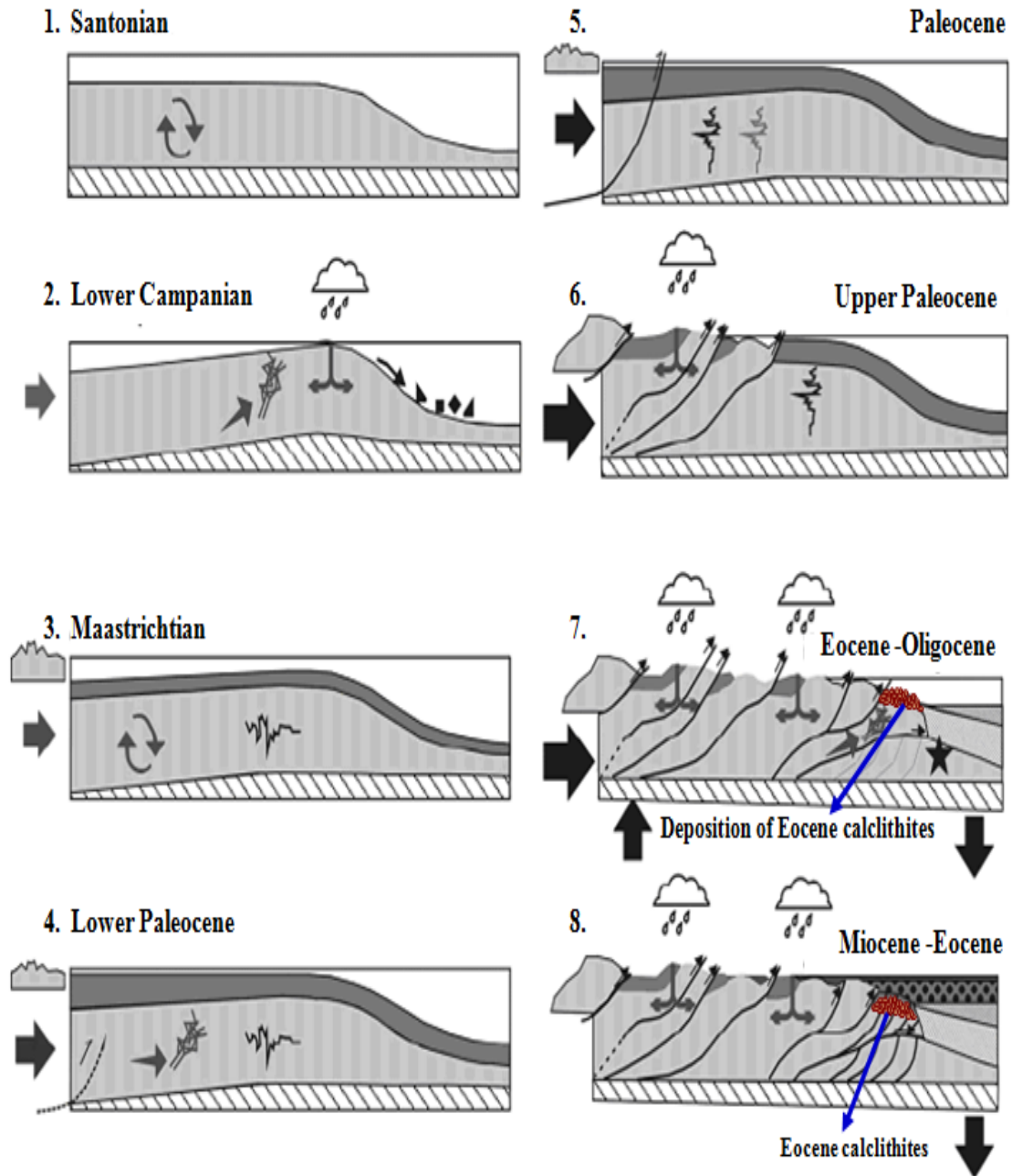


Figure 5. Tectonic evolution of the western margin of the Veracruz Basin (after Ferket et al., 2002). The basement is not shown because is not involved in the orogeny. Compression events started during Campanian (Ortuño-Arzate, et al., 2003).

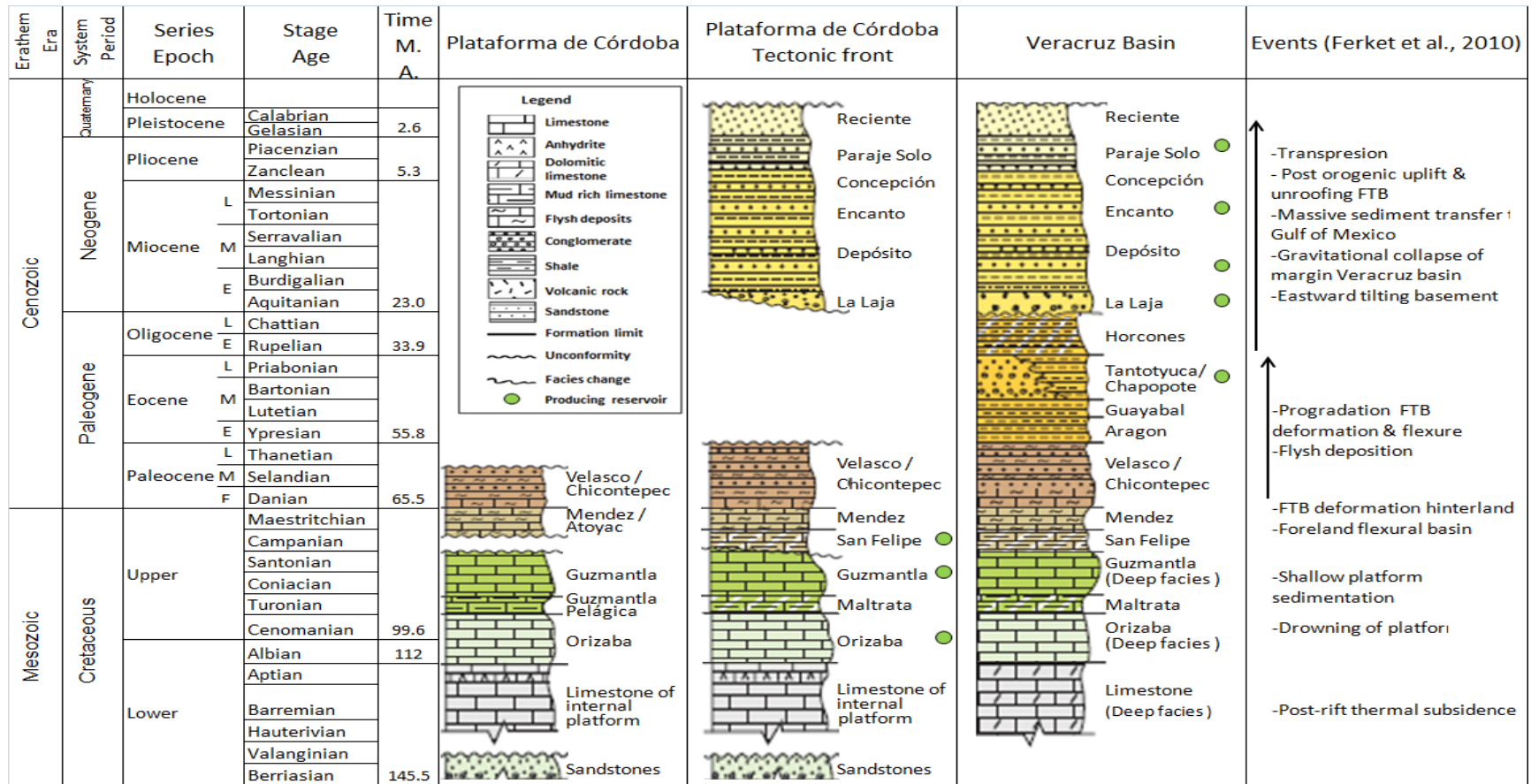


Figure 6. Chronostratigraphic chart of the Veracruz basin, distinguishing the Plataforma de Córdoba, the buried tectonic front containing the Cretaceous oil and wet-gas fields of the basin, and the Tertiary Basin containing the studied field. (Modified from Ortuño-Arzate, et al., 2003 and Ferket et al., 2010, based on International Commission on Stratigraphy, 2010). The far right column summarizes the main geological events. FTB indicates fold and thrust belt.

Characteristics of the field

The field is composed by five reservoirs vertically separated by impermeable shale layers, of which the older are Middle Eocene in age (EOC-3, EOC-10, EOC-20 and EOC-30) that produce an average weight of 22⁰ API oil. The youngest (EOC-50) produces heavy oil with weight of 16⁰ API. Figure 7 summarizes the characteristics of the field and shows the distinctive low gamma ray and high resistivity log response of the productive units. There is another correlated unit distributed over a restricted area along the crest of the structure, EOC-40, which is water-bearing (Figure 8). EOC-10, EOC-20 and EOC-3 produce in the top of the structure (Figure 8). In contrast, EOC-30 and EOC-50 are present only in the eastern flank of the anticline, where they produce 500 m down dip with respect to the crest of the structure. Figure 8 shows the distribution of the six units along a structural section of the field.

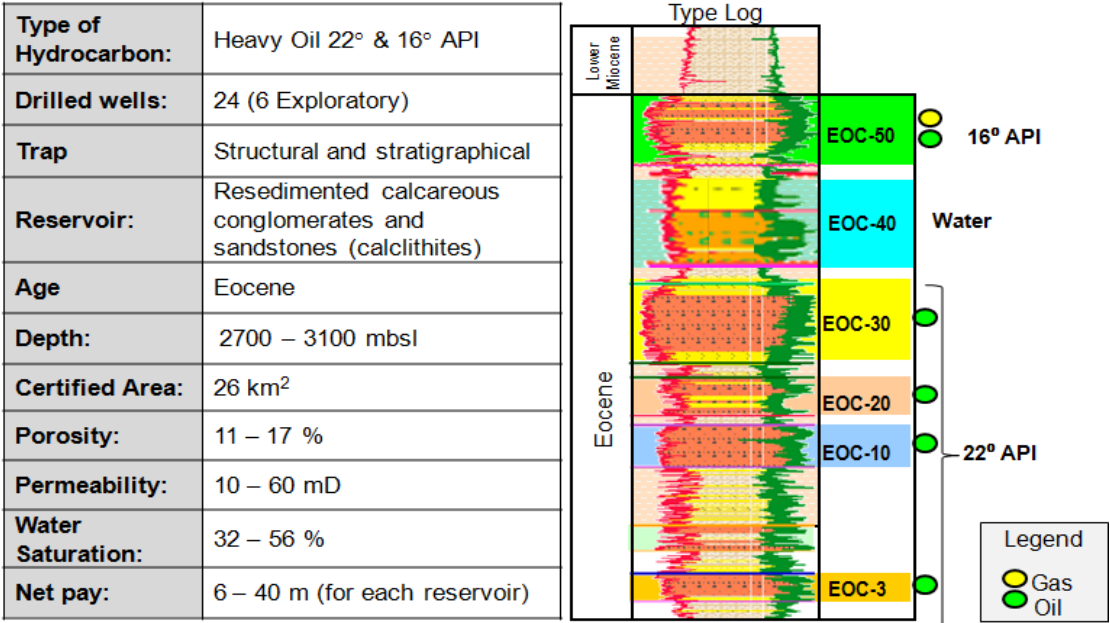


Figure 7. Characteristics of the field and its base log showing the six Eocene units, of which five are productive while one is water bearing. (Data courtesy of PEMEX E&P).

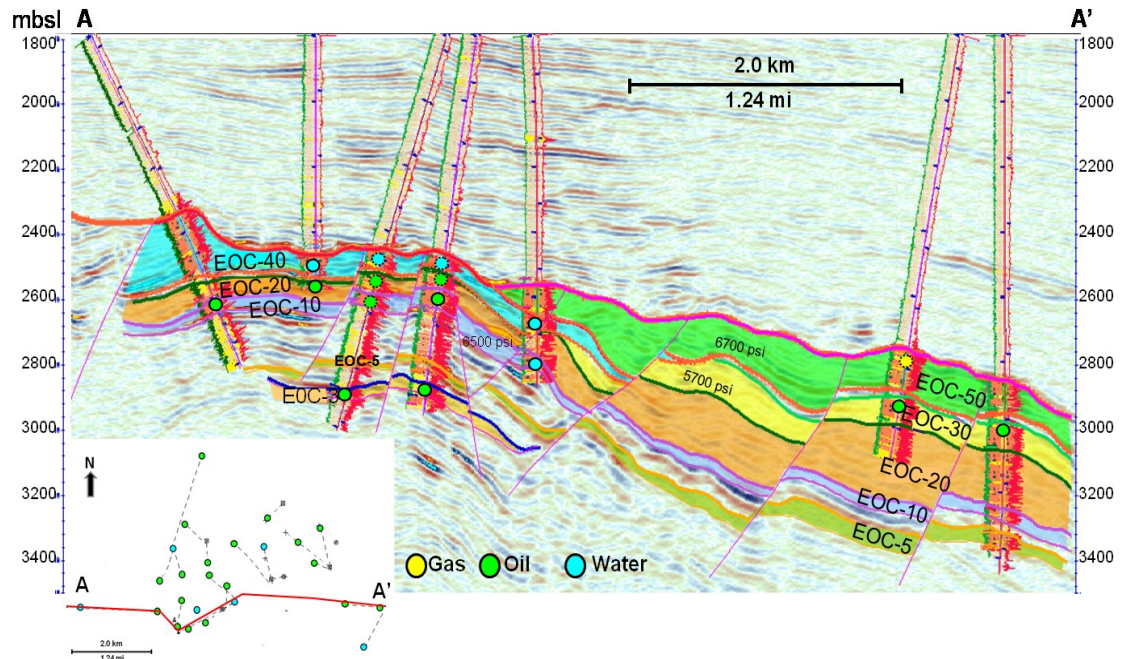


Figure 8. Structural cross section through the field. EOC-10 and EOC-20 produce in the western portion of the structure; EOC-40 is water bearing and is distributed over the western portion of the anticline; EOC-30 and EOC-50 produce in the eastern flank (Hernández-Martínez, 2009). (Image is courtesy of PEMEX E&P).

The primary structural element of the field of study is that of a fault-propagation fold with a secondary normal fault system which compartmentalizes the field (Figure 4). The trap has a strong structural component; however, lateral stratigraphic changes and pinch outs against the pre-Miocene unconformity control the entrapment as well. The seal of the upper reservoirs are Miocene shale deposits that unconformably overlay the Eocene reservoir units.

The reservoirs are primarily made up calcareous conglomerates and sands eroded from the Cretaceous Plataforma de Córdoba which were redeposited in Middle and Late Eocene. Therefore, a more appropriate term to describe these deposits is calcilithites, defined by Folk (1959) as terrigenous rocks that are made up more than

50% of carbonate fragments eroded from preexisting carbonate rocks. The Middle Eocene age is confirmed by the presence of foraminifera including *Turborotalia cerroazulensis frontosa*, *Morozovella spinulosa*, *Acarinina bullbrook*, *Morozovella lehneri*, *Truncorotaloides rohri*, *Truncorotaloides topilensis* in 12 wells (Betanzos-Gallifa et al., 2010). The age of the Late Eocene upper reservoir is dated by the presence of foraminifera *Turborotalia cerroazulensis*, *Hantkenina alabamensis*, and *Globigerinatheka semiinvoluta* reported on 3 wells (Betanzos-Gallifa et al., 2010). (Details of the biostratigraphic control are found in Appendix B).

Hernández-Martínez, (2009) propose the regional conceptual sedimentary model to be a slope and basin-floor fan, with distributary channels oriented Northwest-Southeast (Figure 9), very similar to the coarse-grain, sand-rich turbidite system described by Bouma (2000). This is the same depositional model of the Granite Wash, a major oil and gas play in Texas and Oklahoma (Mitchell, 2011).

Mossman and Viniegra (1976) state that during the Middle Eocene deep water depositional environments prevailed in the Veracruz Basin, which is in agreement with the bathyal environment reported by PEMEX paleontological analysis of benthic foraminifera in 13 wells of the area. The genesis of these calcilithites makes the reservoirs both laterally and vertically highly heterogeneous. This heterogeneity is observed at well log, core slab and thin section scales as seen in Figure 10. Note that thin sections 60 cm and 3.5 m apart present radical changes in porosity. One has good porosity due to dissolution and dolomitization, the second is partially cemented, and the third is fully cemented. This heterogeneity is a big issue in well placement proposals.

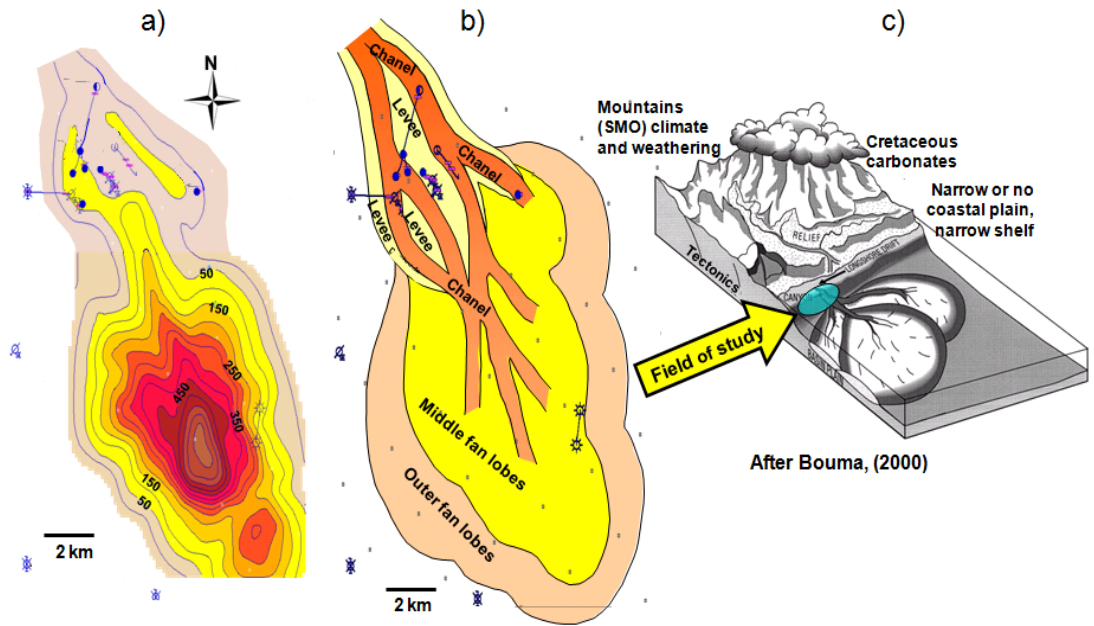


Figure 9. Regional conceptual sedimentary model (Hernández-Martínez, 2009). (a) Isopach map of the sequence comprising the reservoir horizon EOC-10, contours every 50m. (b) Submarine fan fed by a canyon through a steep escarpment. (c) The analog depositional model for the field: a coarse-grained, sand-rich turbidite system (Bouma, 2000). This analogue model is the same for the Granite Wash deposits in Oklahoma and Texas (Mitchell, 2011). (Courtesy of PEMEX E&P).

The facies of these Eocene calcilithites varies from breccias to conglomerates interbedded with poorly sorted calcareous sandstones and shale redeposited in slope and basin-floor environments. The calcilithites are rich in carbonate grains: skeletal grains with benthic foraminifera and red algae as the main components, limestone clasts that are subangular to rounded, and sand- to gravel-size, with textures varying from mudstone to grainstone. The main mineralogical component is calcite, 85% in average, followed by clay, quartz, dolomite and other minor components (ankerite, barite, pyrite, potassic feldspar, and gypsum) (Figure 13). By composition, these sediments can be defined as carbonates according to Tucker and Wright (2008). However, these

carbonates are not deposited in situ, but rather redeposited on fore-slope environments. The high calcite content reflects the source of the deposit which are the Cretaceous carbonates from the Plataforma de Córdoba. Reworked limestone clasts visible on core (Figure 11) and thin sections (Appendix A) confirm this re-sedimentation. These calcilithites are diagenetically altered providing secondary porosity, which is much more important than the primary porosity. The porosity for the pay zones ranges from 11 to 17%. Other than the high deformation associated with the orogeny and post-orogenic faulting, fracture porosity is statistically negligible in all the reservoir horizons contributing around 2% in average (Figure 12). However, the reservoir may be under-sampled, such that the recovered samples may not be fully representative of all reservoir facies. In particular, the porosity average from petrographic analysis falls below the porosity cut-off of productive areas. Figure 12 shows the average mineralogy and total components from petrographic analysis of calcilithites horizons EOC-10, EOC-20, EOC-30, EOC-40 and EOC-50. Core analysis of EOC-3 does is not available at this date.

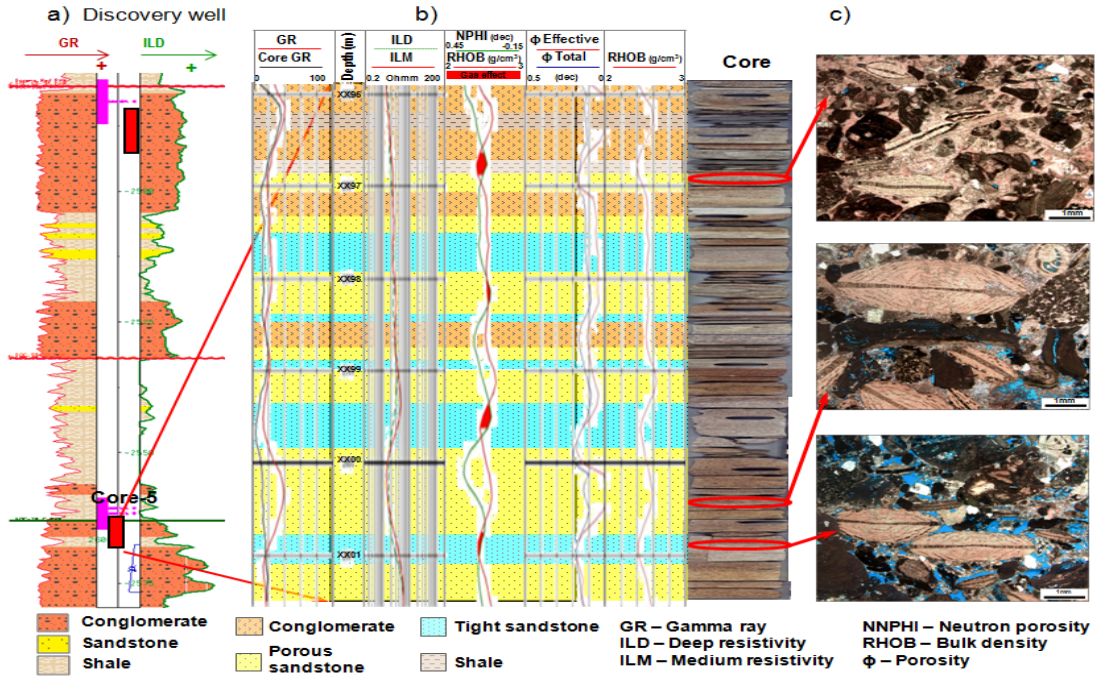


Figure 10. Heterogeneity of the field at different scales (after Hernández-Martínez, 2009). (a) Well logs showing shale-sand-conglomerate layering. (b) Core with logs and facies distribution. Note high variability in less than 1 meter. (c) Thin sections illustrate variation in reservoir quality due to diagenetic processes, including dissolution, cementation and dolomitization. (Courtesy of PEMEX E&P)

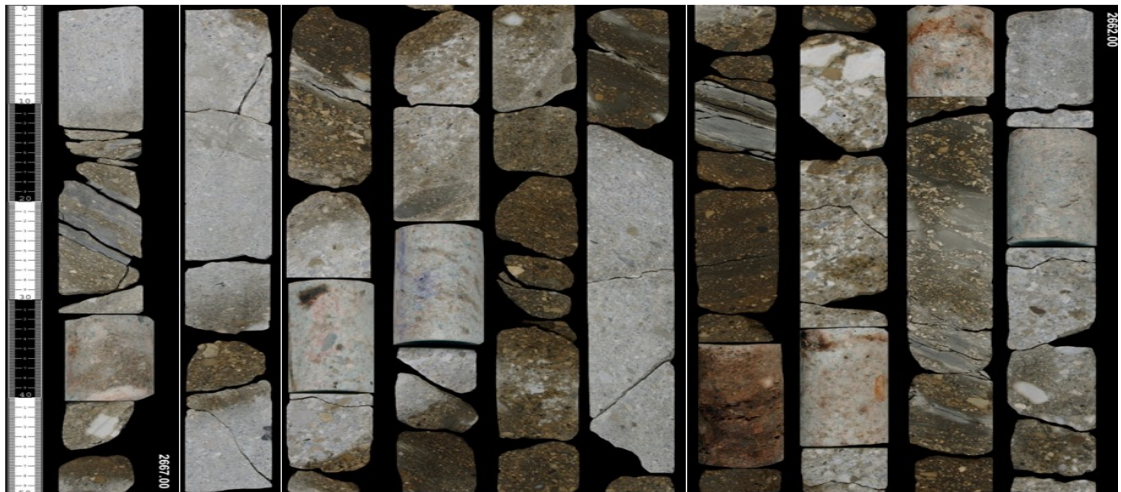


Figure 11. Slabbed core of the most productive well (5 m). The darker intervals are oil-impregnated, which contrast with the lighter highly cemented zones. (Data courtesy of PEMEX E&P).

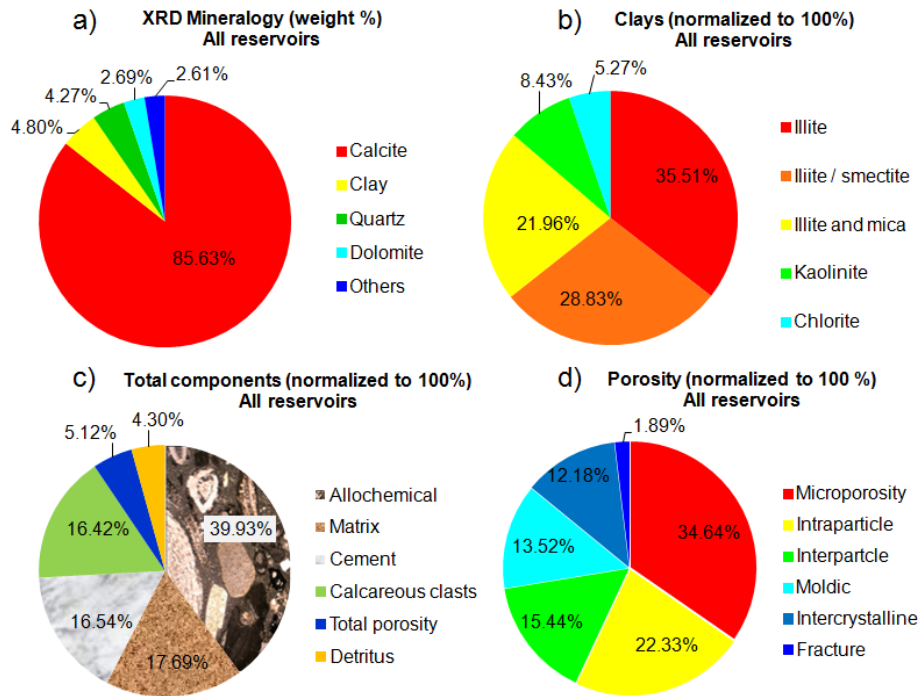


Figure 12. Petrographic analysis of units EOC-10, EOC-20, EOC-30, EOC-40 AND EOC-50. (a) Mineralogical composition from X-ray diffraction (XRD) analysis. (b) Clay minerals distribution normalized to 10% from XRD analysis. (c) Total components obtained by point counting analysis on thin sections. (d) Porosity normalized to 100% from point counting analysis.

CHAPTER III. MULTIATTRIBUTE ANALYSIS TO ASSIST STRUCTURAL INTERPRETATION

The lateral compartmentalization of the reservoir units caused by faulting is one of the major problems that affect the productivity of the field. An ideal structural reservoir characterization should consist of rapid and accurate detection of all faults from seismic data, including those that fall below seismic resolution. Multiattribute analysis of volumetric coherence and curvature computed from structure-oriented filtered (SOF) data enhance subtle structural patterns that are not easily correlated on the original amplitude data. Figure 13 shows a general workflow for structural interpretation attribute-assisted that could be applied in other compressional or extensional regimes. I simplified the workflow explained in Figure 13 resulting in flowchart shown in Figure 14.

My workflow begins with conditioning the poststack amplitude seismic data through structure-oriented filtering (SOF) to sharpen the edges of reflectors (Appendix C). Next, I calculate volumetric curvature and similarity attributes guided by the reflector dip computed from the structure-oriented filtered volume. Then, time slice by time slice, I correlate patterns with my tectonic deformation model. Next, I cluster attributes identified in the previous phase that are associated with the same geological feature. Finally, I use multiattribute analysis (visualization) to confirm my structural interpretation.

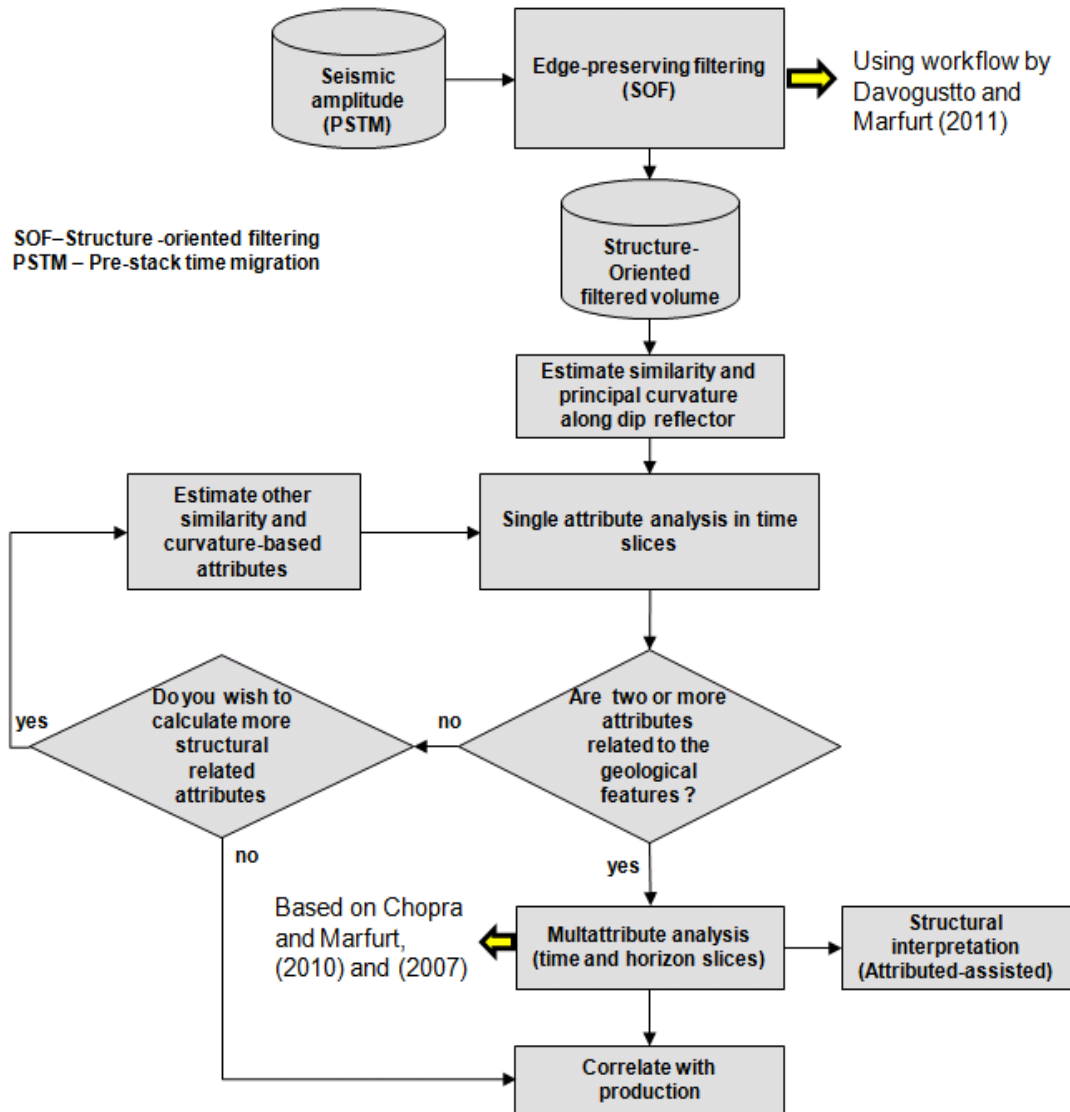


Figure 13. Workflow for structural interpretation assisted with multiattribute analysis. The input is the seismic poststack amplitude volume conditioned through structure-oriented filtering (SOF). Then I calculate similarity and attributes from the filtered volume to identify geological features on time slices. I cluster two or more attributes that associates with the same structural pattern (f. e. faults, relay ramps, transfer faults) Then, I use the clusters from multiattribute analysis to assist the structural interpretation. Correlation with production data is the maximum purpose to get a quantitative relation with seismic attributes.

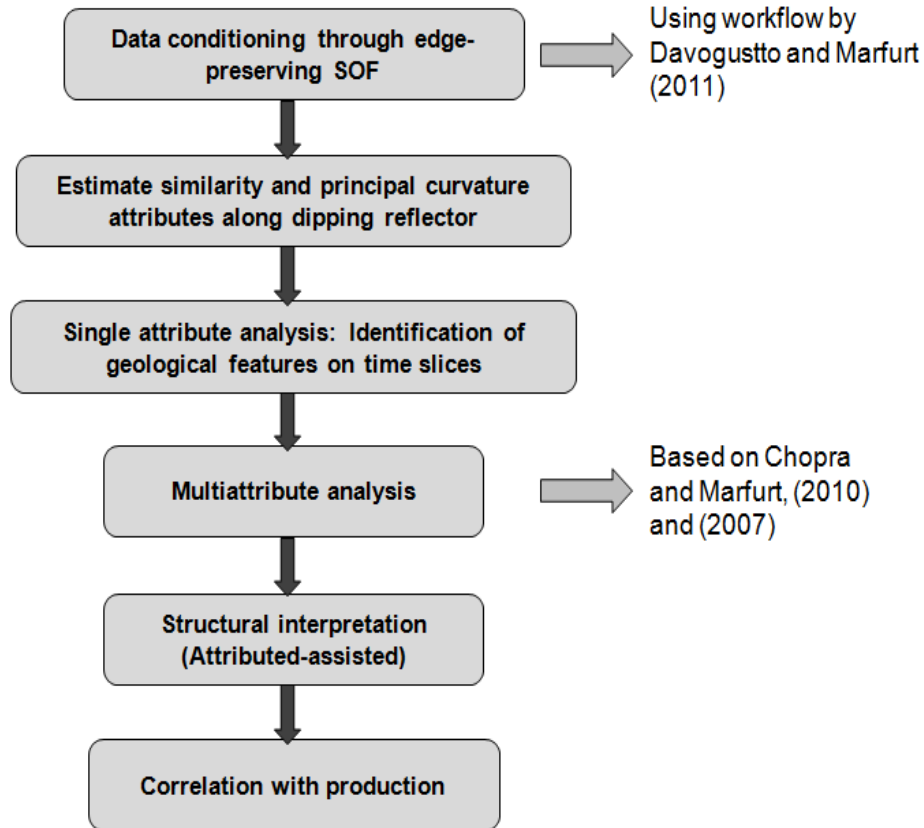


Figure 14. Flowchart summarizing the steps in attribute-assisted structural interpretation. The multiattribute analysis phase consists in visually clustering attributes that highlight the same geological feature.

Acquisition parameters and processing sequence of the seismic survey

In 2003, 1926 km² of 3D seismic data were acquired to illuminate the tectonic front of Sierra Madre Oriental including the area of study, as well as other gas fields in the Tertiary Veracruz Basin. The bin size of this seismic survey is 25 by 25 m with a nominal fold of 35 (Figure 15). The seismic source used was dynamite placed in shallow holes. Table 1 shows the acquisition parameters of the survey.

In 2004, the seismic survey covering the field of study was merged with six other seismic data volumes acquired with the same type of source forming a single “mega-merged” volume. The resulted mega-merged volume was imaged using a

Kirchhoff prestack time migration algorithm. The grid of the survey acquired over the area of interest formed the base for the merge process, in which the inlines (N62°E) are oriented perpendicular to the crosslines. Figure 16 shows the processing sequence of the mega- merged volume. This thesis work is based on 100 km² of PEMEX E&P's high quality prestack time migrated gathers and stacked volume cut out from the much larger mega-merge survey. Since the data are cut out, survey edge effects are minimal.

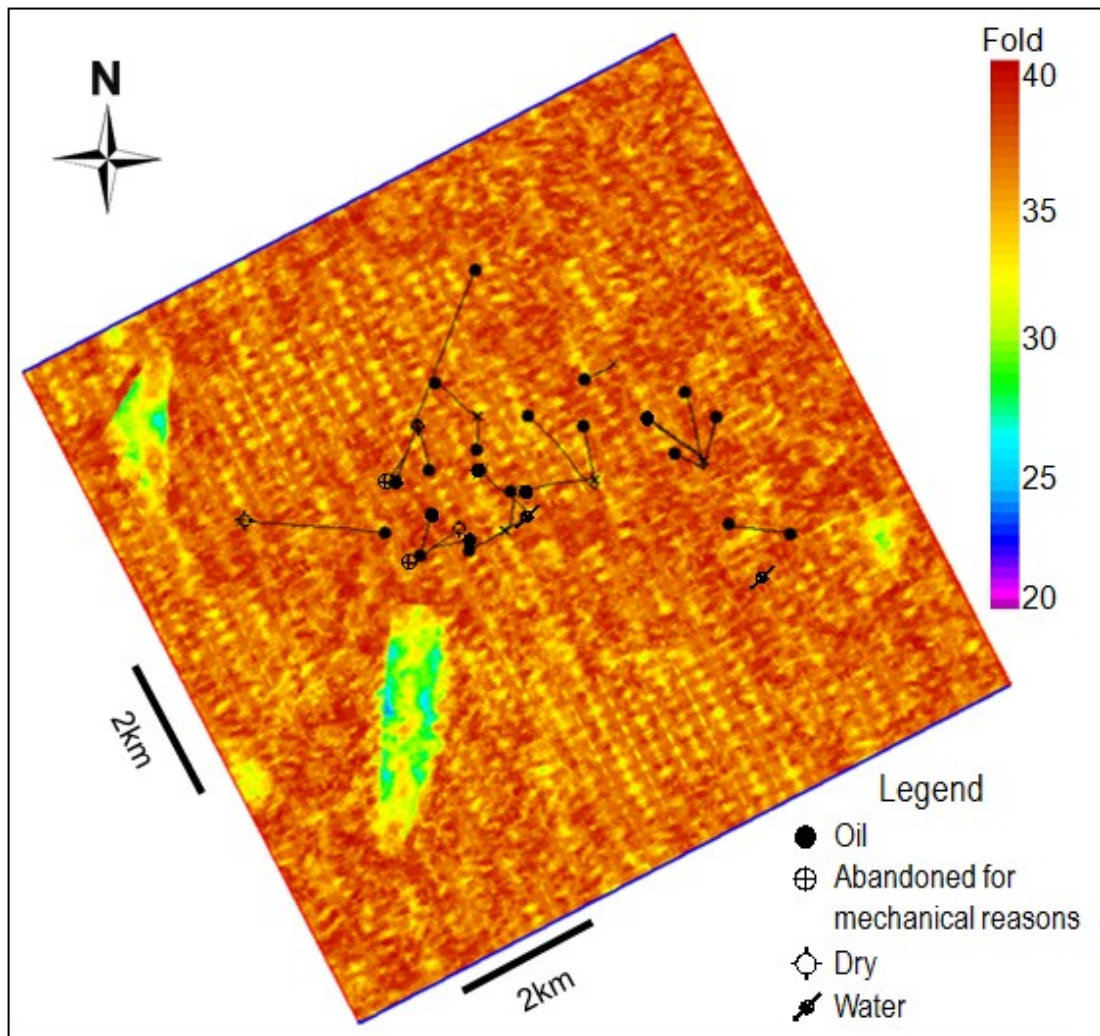


Figure 15. Fold map of the 3D seismic data available covering the field of study. The planned nominal fold was 35; the maximum fold for this crop is 40, the minimum fold is 22. Note that there are no low-fold values near the edges, since the data volume was cut out from a much larger mega-merge survey. (Data courtesy of PEMEX E&P).

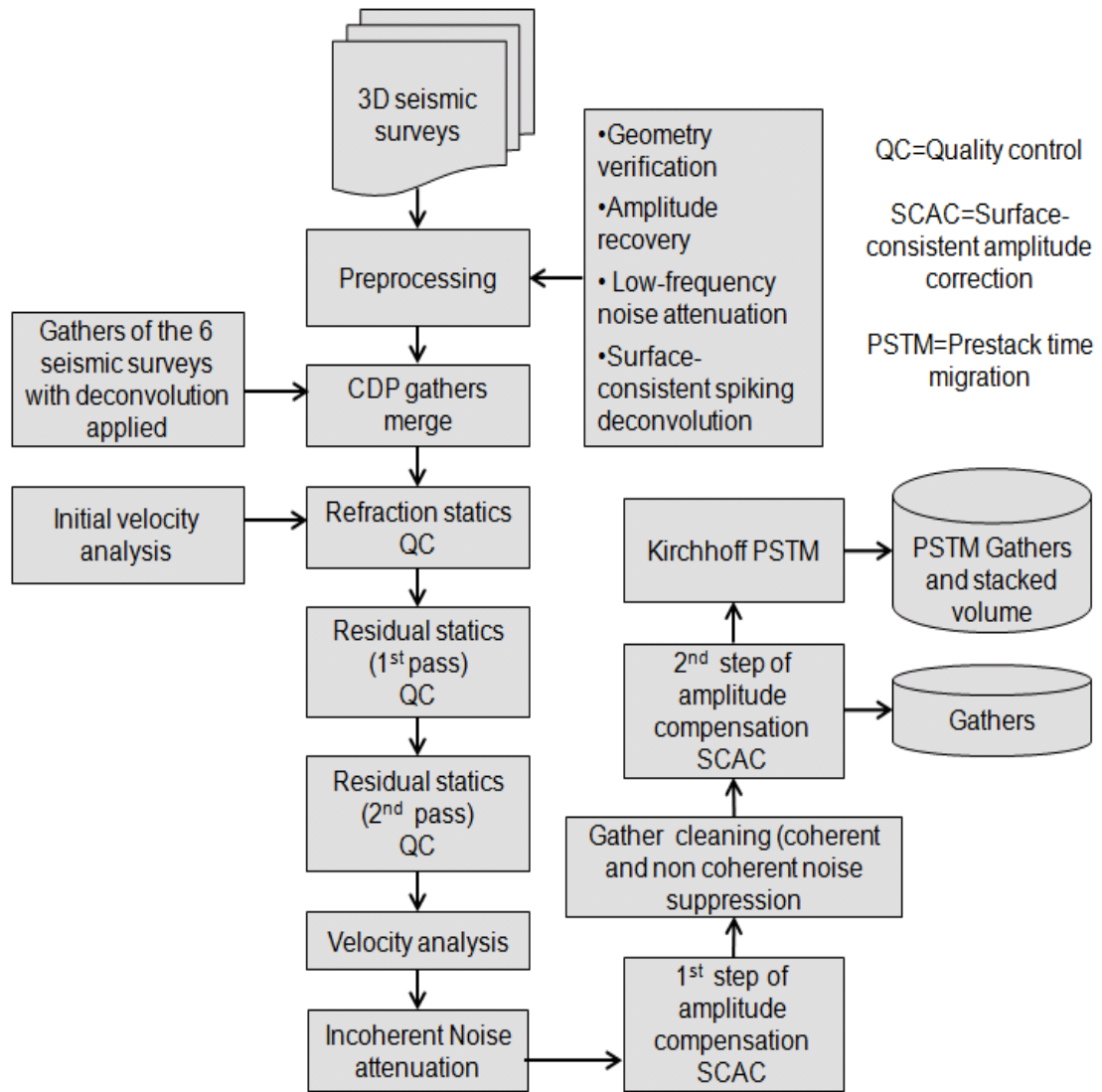


Figure 16. PSTM processing sequence of the mega-merge data volume, which includes the 3D seismic survey covering the area of study. (Data courtesy of PEMEX E&P).

Acquisition parameters	
Type of spread	bilateral symmetric
Source Type	Dynamite (Pentolite)
Receiver interval	50 m
Source interval	50 m
Receiver line spacing	400 m
Source line spacing	500 m
Bin size	25 by 25 m
Active lines	10
Number of active channels per receiver line	140
Number of total active channels per patch	1400
Maximum offset inline	3475
Maximum offset crossline	1975
Maximum offset (diagonal)	3997
Source array (per shot point)	Single hole, 15 to 25 m depth, charge of 1.5 to 3.0 kg of pentolite. Three wells, 12 m depth, charge of 1.0 kg of pentolite per well.
Number of shot points per salvo	8
Receiver array (per receiver point)	6 geophones separated 4.16 m. over 20.8 m
Recording parameters	
Sample rate	2 ms
Recording length	7 s
Nominal fold	35

Table 1. Acquisition parameters of the 3D seismic survey that covers the area of study. (Data courtesy of PEMEX E&P).

The dominant frequency at the target level of 2000-2500 ms is around 22 Hz. If I consider an interval velocity of 4000 m/s, then the seismic vertical resolution (tuning thickness) at the target level is around 45 m and the detection limit is around 6 m.

Figure 17 shows a representative vertical slice through the seismic amplitude data about the target unit along with its amplitude spectrum.

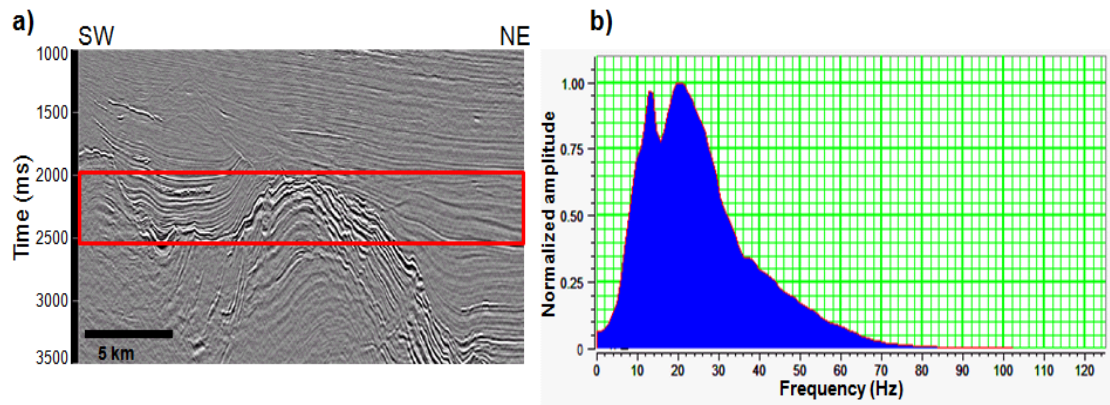


Figure 17. Vertical seismic slice through original seismic amplitude data (a), and its amplitude spectrum (b).

Poststack seismic data conditioning for structural interpretation

I used the stacked volume of the available PSTM which I conditioned for structural interpretation. The quality of the available poststack amplitude seismic data is relatively good. It suffers from acquisition footprint in the shallow area that heals with depth. Around the target zone (2000 to 2500 ms), the acquisition footprint is negligible. Footprint acquisition can masquerade the attribute response (Davogustto, 2011) for that reason it is very important apply an acquisition suppression process if it is strong at seismic target. For structural interpretation purposes, I conditioned the poststack seismic amplitude volume using the workflow suggested by Davogustto and Marfurt (2011) for structure-oriented filtering (SOF) along reflector dip, which helps to sharpen edges of reflectors and remove cross-cutting coherent and random noise (Chopra and Marfurt, 2007b). This filtering results in enhanced structural features on seismic attributes. To control quality, I compared coherence attributes extracted after each iteration of SOF.

Figures 18 and 19 show a representative time and vertical slices through the seismic amplitude and coherence volumes before and after two iterations of SOF. I include details of the SOF workflow in Appendix C.

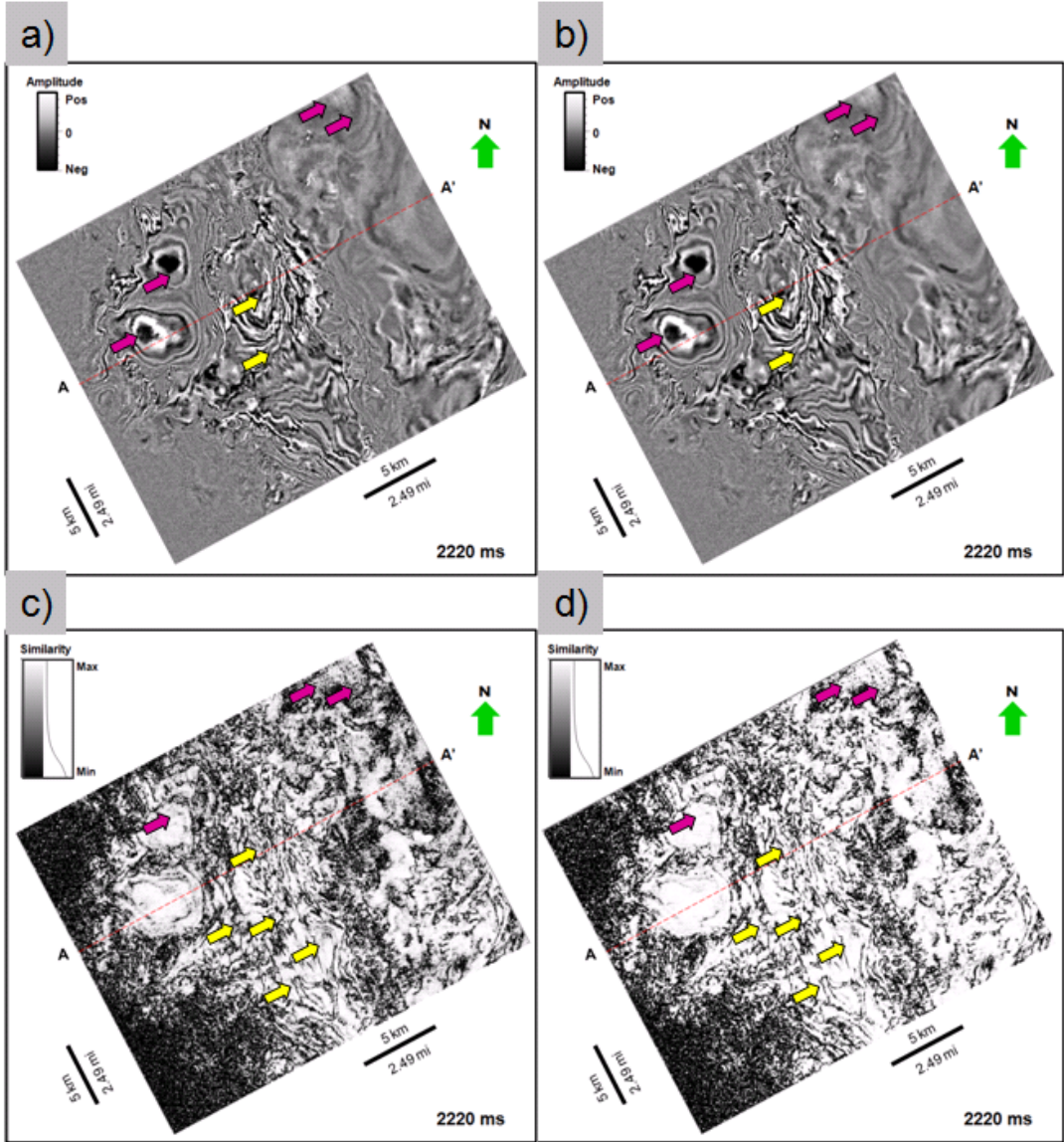


Figure 18. Time slices at $t=2.220$ s through (a) original seismic amplitude and (b) structured-oriented filtered amplitude volume. Corresponding time slices through coherence computed from the (c) original seismic amplitude and (d) SOF amplitude volume. Yellow block arrows indicate difference in fault edges while magenta arrows indicate differences in acquisition footprint. As desired, faults are sharpened and footprint is suppressed.

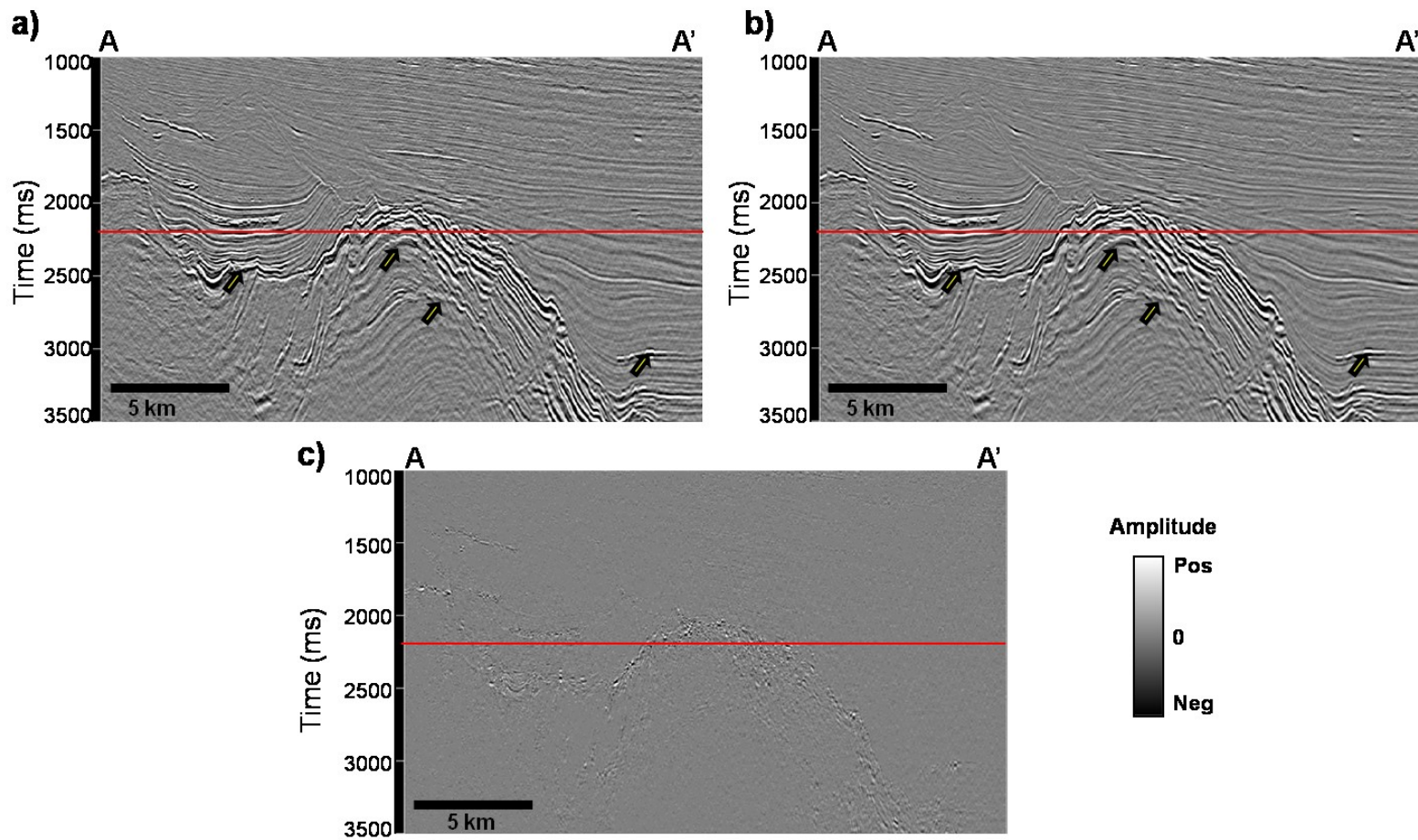


Figure 19. Vertical slices through seismic amplitude volumes (a) before and (b) after two iterations of SOF. (c) Rejected noise computed as the difference between (a) and (b). Location of line AA' shown in Figure 15. Block arrows indicate where the images are different.

Recognition of structural patterns on geometric seismic attributes

Once the poststack amplitude seismic data are conditioned, I use volumetric estimates of coherence and curvature computed along dip to identify the attribute expression of structural features.

Coherence is a measured of the lateral continuity of the seismic reflector shape (Chopra and Marfurt, 2007b) and measures how similar one trace or group of traces is from their surroundings. Areas with high coherence indicate continuous reflections and are plotted as white. Areas with low coherence often indicate faulted or fractured areas, channel edges, collapse features, mass transport complexes, and other discontinuities and are plotted as gray or black. I use coherence to delineate faults. Faults are not planes but zones of high deformation (Fossen, 2010); if the faulted material is brittle, as the calcilithites of this case study, I expect to have a damage zone around the fault, which I anticipate will appear as a low coherence area rather than a narrow low coherence lineament.

Curvature expresses the amount of flexure of reflectors; it is defined as the inverse of the radius of a circle that touches tangentially a given curve. (Chopra and Marfurt, 2007a). By convention, 2D curvature is positive for convex features (anticlines), is negative for concave shapes (synclines), and is zero for planar surfaces (Chopra and Marfurt, 2010). (Figure 20).

2D curvature is insufficient to describe a body in 3D space because one needs at least two curvatures to describe it. In general, more than two curvatures can be tangent to a quadratic surface (Blumentritt et al., 2006). The most-positive and most-negative principal curvatures, k_1 and k_2 , correspond to eigenvalues of a quadratic surface. The

maximum curvature, k_{max} , corresponds to the circle with smallest radius tangent to the quadratic surface (Chopra and Marfurt, 2010). The minimum curvature, k_{min} , corresponds to the circle with the largest radius tangent to the quadratic surface and will always be perpendicular to k_{max} . Relating k_{min} and k_{max} to k_1 and k_2 where $k_1 \geq k_2$,

$$k_{max} = \begin{cases} k_1, & \text{if } |k_1| \geq |k_2| \\ k_2, & \text{if } |k_1| < |k_2| \end{cases} \quad (1)$$

$$k_{min} = \begin{cases} k_2, & \text{if } |k_1| \geq |k_2| \\ k_1, & \text{if } |k_1| < |k_2| \end{cases} \quad (2)$$

The definition of k_{min} and k_{max} are based on eigenvalue analysis. Intuitively, many geoscientists think that k_{max} should be numerically larger than k_{min} in signed value, such that we have almost 50% of the commercial software defining maximum and minimum curvature one way, and 50% the other way. To avoid this confusion in notation, Chopra and Marfurt, (2010) use the most-positive and most-negative principal curvatures.

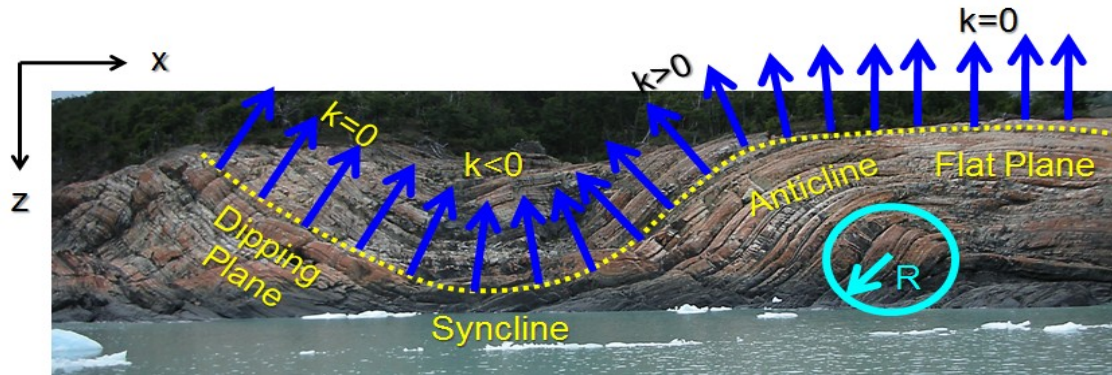


Figure 20. Sign convention of curvature attribute (Chopra and Marfurt, 2010). 2D curvature, k , is the inverse of the radius of a circle, R , tangent to a surface. Positive values of k correspond to an anticline, negative values of k correspond to a syncline and zero values of k correspond to a flat or dipping plane.

Figure 21 illustrates how most-positive principal curvature, k_1 , and most-negative principal curvature, k_2 , define a fruit in tridimensional space. The most-positive principal curvature, k_1 , represents the tightest curve along the tightest axis of the fruit while the most-negative principal curvature, k_2 , represents the curve along the most elongated axis of the fruit. Note that k_1 is always perpendicular to k_2 and greater in signed value than k_2 . Both principal curvatures can be positive (defining a dome) or negative (defining a bowl) (Chopra and Marfurt, 2007a). In general the greater the absolute value of curvature, the greater the deformation along that axis.

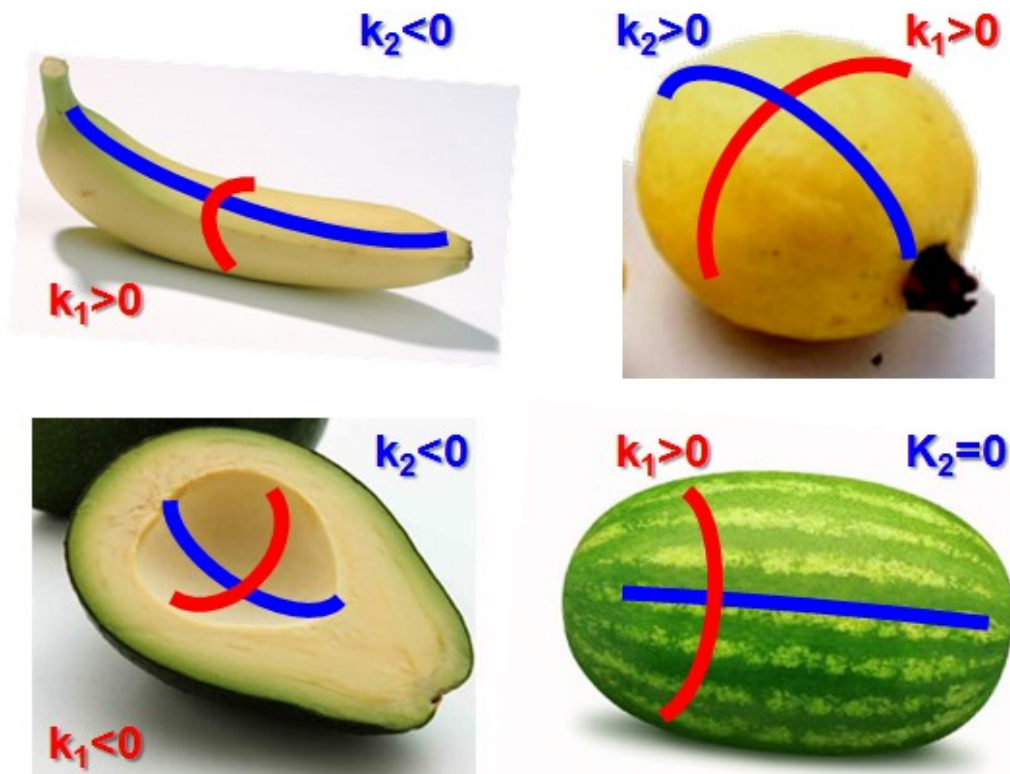


Figure 21. 3D curvature identification of my favorite fruits. For a quadratic surface, the two principal curvatures, $k_1 \geq k_2$ are orthogonal to each other, and represent the extreme most-positive and most-negative values. Note on my banana $k_1 > 0$ (anticlinal) and $k_2 < 0$ (synclinal) such that this part of the fruit is a saddle. For my guava I have $k_1 > k_2 > 0$, such that I have a dome. In my pitted avocado $k_2 < k_1 < 0$, such that I have a bowl. Finally, in my watermelon, $k_1 > k_2 = 0$, such that I have a ridge.

Al-Dossary and Marfurt (2006) showed how 3D curvature can be computed from volumetric estimates of dip and azimuth, thereby generating volumetric estimates of curvature independent from horizon interpretation. Volumetric curvature attributes are sensitive to folds, conjugate faults and fault drag that appear as a fold, edges of compacted channels, collapse features, carbonate buildups and other smoothly deformed features, including velocity pull-up and push-down artifacts (Chopra and Marfurt, 2007b). Reverse faults can develop drag (Fossen, 2010), which will be sensed by curvature attributes. Figure 22 shows an example of drag along a reverse fault in an outcrop of the San Rafael Reef, Utah. The drag along reverse and normal faults is the result of deformation of ductile horizons while faulting (Fossen, 2010). If I calculate the curvature along the drag, I will expect a positive curvature response on a 2D vertical slice.

In my workflow, I analyzed time slices through k_1 , k_2 , and coherence attributes individually to identify the attribute response of different structural elements of the tectonically deformed volume (Figure 23). I chose time slices rather than horizon slices because the thickness of the reservoir and seal units vary along the anticline; some of them thicken toward the lows, while other thin or even pinch out against the unconformity. Additionally, some faults have large offsets which can introduce errors in horizon interpretation across different fault blocks. I observed that some of the curvature lineaments (k_1 and k_2) are associated with faults, and other with folds or local synclines. Note in Figure 23c that normal faults present low coherence. In contrast, reverse faults are not well delineating by coherence, but rather appear as a low coherence area rather than as a plane.

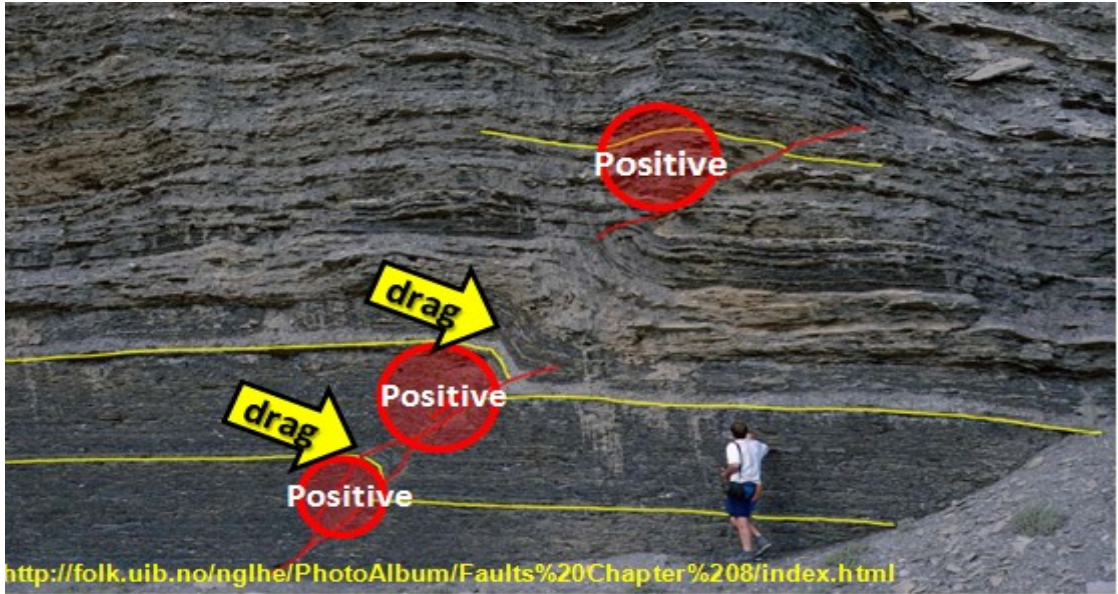


Figure 22. Drag along a reverse fault. San Rafael Reef, UT (After Fossen, 2010)

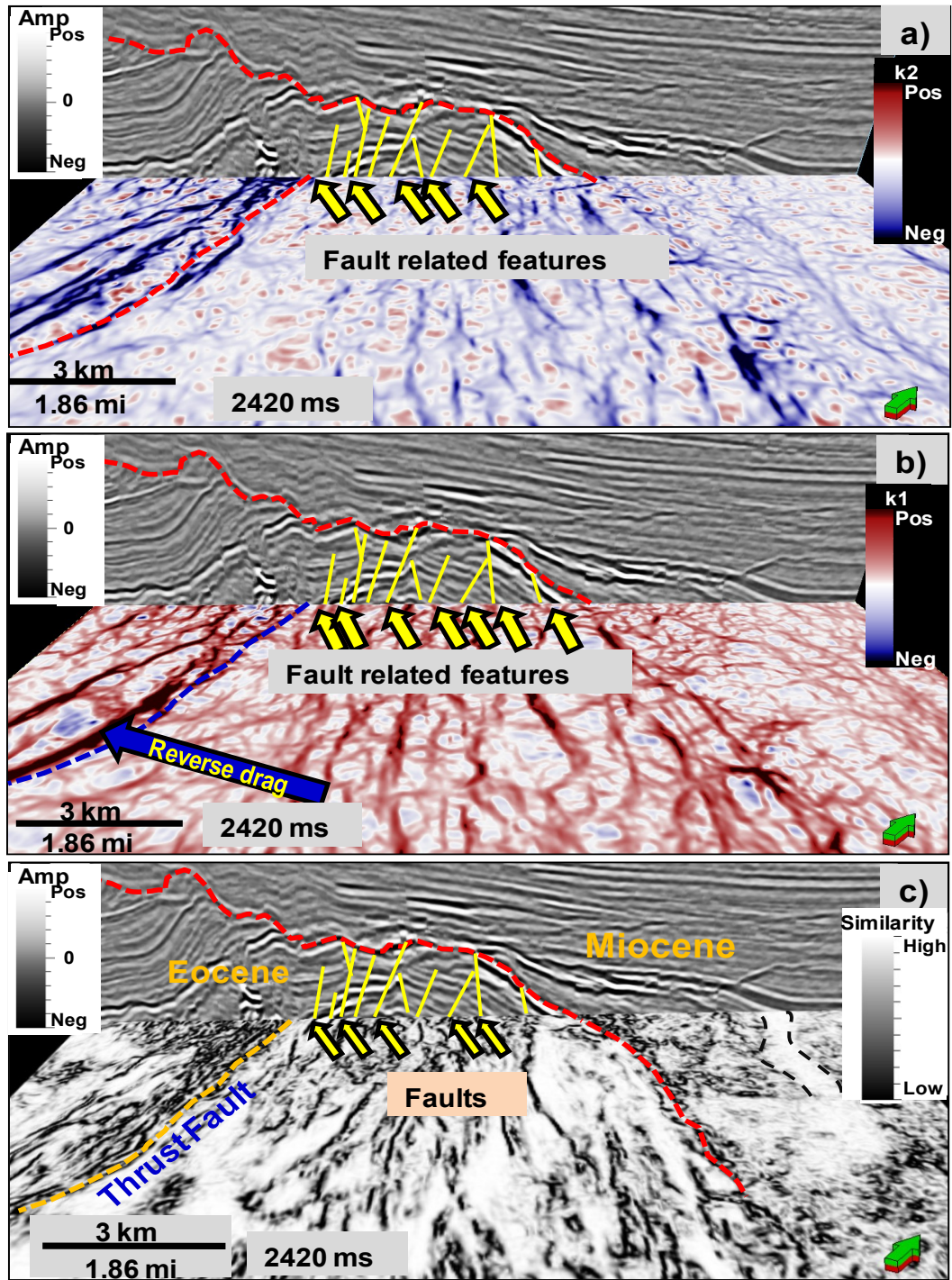


Figure 23. Vertical slice through seismic amplitude and time slices through (a) most negative principal curvature, k_1 , (b) most positive principal curvature, k_2 , and (c) Sobel filter similarity. Main unconformity, which separates Eocene carbonates from Miocene shale, indicated in red. Note the signature of the thrust fault on the three attribute time slices.

Multiattribute analysis and structural interpretation attribute-assisted

Once I identified the attribute response of structural features on single attribute displays, I visually clustered attributes sensitive to the same structural element.

First, I examined normal fault-related anomalies. From the previous analysis on single attributes, I found that both curvature and coherence attributes are sensitive to normal faults in my data. There are strong low-coherence lineaments delineating normal faults, with k_1 anomalies corresponding to the foot wall and k_2 anomalies corresponding to the hanging wall bracketing the coherence anomaly between them (Figure 24). I correlate the curvature response associated with faulting, with drag/drape geometry along both sides of the fault.

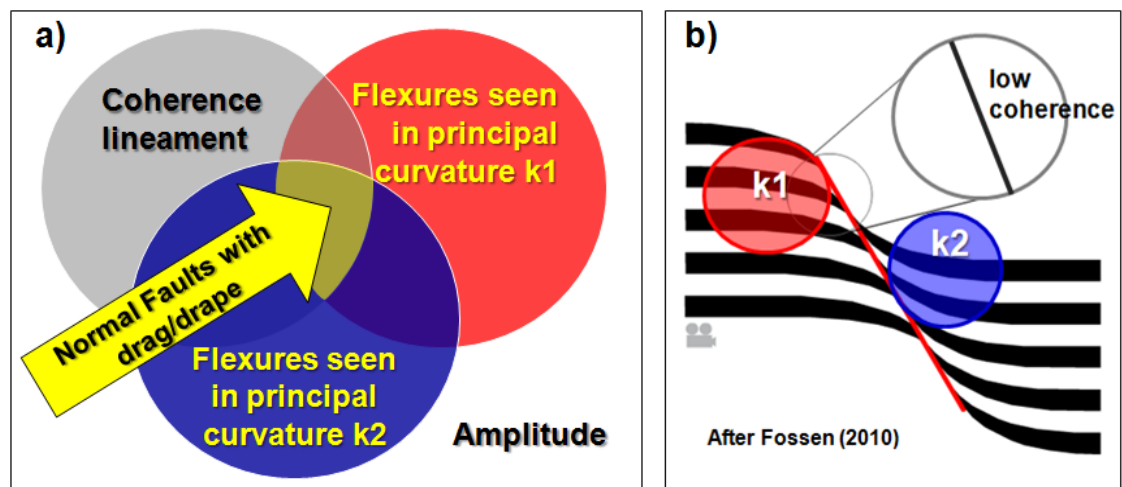


Figure 24. (a) Clustering of seismic attributes sensitive to normal faults. (b) Low coherent lineaments bounded by flexures in k_1 and k_2 delineate normal faults with drag.

In contrast to normal faults, reverse faults are not well delineated by coherence attributes. Rather, the west reverse fault is represented by a relatively low coherence area or zone (Figure 23c). On the other hand, there is a strong lineament of most positive curvature along the west thrust fault of the field (Figure 23b). Using my

previous single attribute analysis, I clustered curvature and coherence attributes to enhance the appearance of reverse faults (Figure 25a). The most positive curvature lineament is the response of the crest of the most western fault-propagation fold. The geometry of the crest is similar to the drag along the reverse fault showed in the Fossen's (2010) outcrop example (Figure 22) at a different scale. Thus, I expect a similar curvature response in the crest of the fault-propagation fold (Figure 25b).

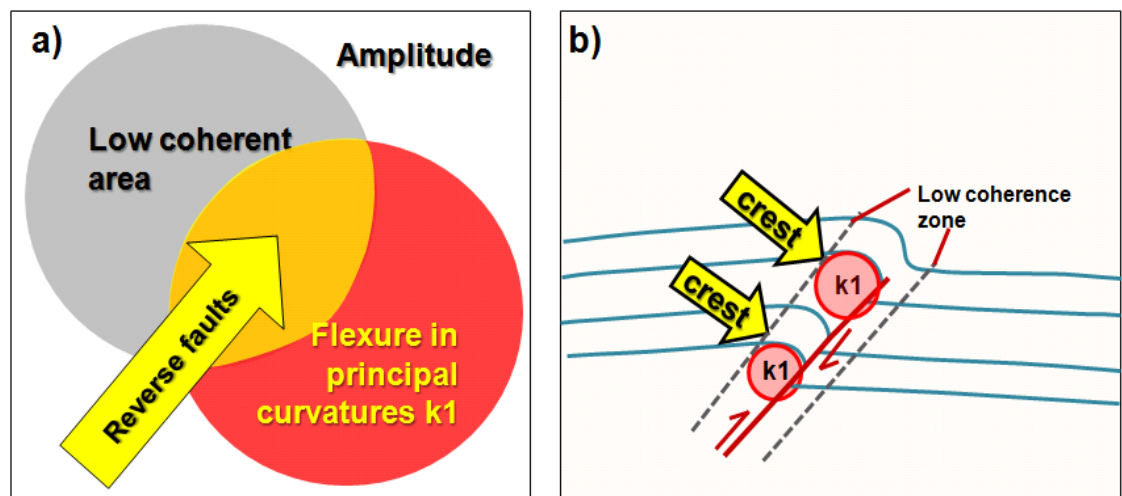


Figure 25. Clustering of seismic attributes sensitive to reverse faults. Low coherence areas around fault zones bounded by a positive flexure in k_1 , delineate reverse faults. For this data set, the k_1 lineament corresponds to the crest of the fault propagation fold, which has the same geometry as the drag along a reverse fault illustrated in Figure 23.

I use multiattribute display over time and vertical slices to emulate previous clustering. Figures 26a and 27a are amplitude vertical and time slices respectively co-rendered with k_1 , k_2 , and coherence.

Note that I interpreted the low coherence lineaments are bound by both most-positive and most-negative curvature anomalies, indicating normal faults with drag. I interpret this drag to indicate ductile deformation of the impermeable shale layers that separate the calcilithites reservoirs.

I extended the concept of the damage zone illustrated in Figure 26b to delineate the reverse faults in my dataset. Note in multiattribute display (Figures 26a and 27a) how the low coherent area associated with the damage zone of reverse faults of the field follow the most positive curvature lineament orientation. This clustering of attributes helps to delineate reverse fault planes better than just using amplitude or a single attribute display.

There are other perpendicular curvature lineaments seen on time slices (Figure 27a) that may correspond to relay ramps or transfer faults at smaller scales than usually documented. The relay ramps and transfer faults accommodate the deformation of the secondary normal fault system of the fault-propagation fold, especially in the crest. The relay ramps can be only identified in map view, and are difficult to see on vertical cross-sections. I use the structural components associated with a fault zone in carbonate sequences of upper Glen Rose formation (Figure 27b.) and Eagle Ford formation (Figure 27c) of Ferrill and Morris (2008) as analogues. The analogue models (Figure 27b and figure 27c) show the geometry of relay ramps and transfer faults at a larger scale.

According to Fossen (2010) “transfer faults are oriented normal to the overlapping faults and exhibit substantial strike-slip movement in extensional and contractional settings”.

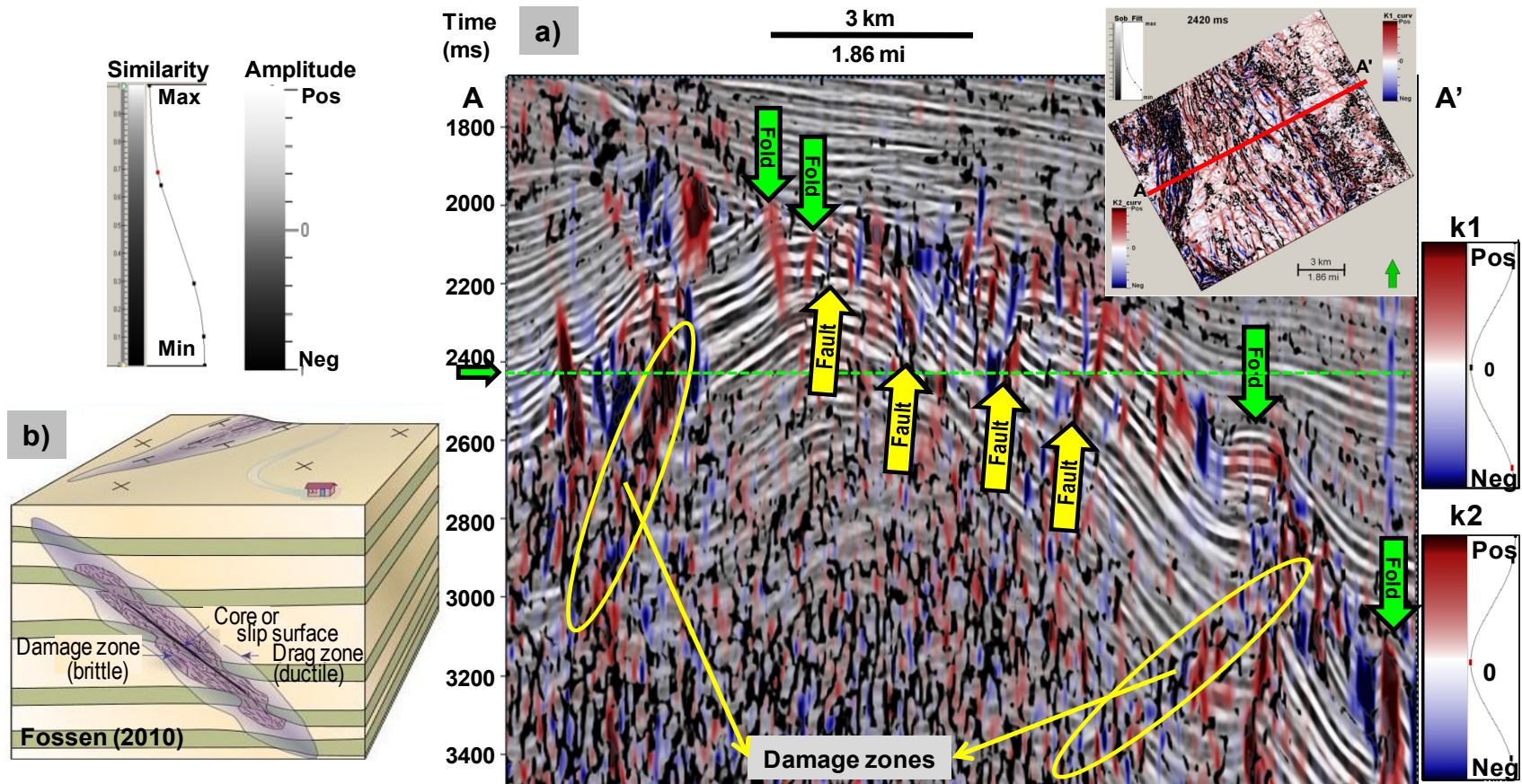


Figure 26. (a) Multiattribute display over the amplitude vertical slice AA' co-rendered with k_1 , k_2 and Sobel filter similarity. Yellow arrows indicate lineaments of k_1 and k_2 associated with faults that I interpret as drag; green arrows indicate curvature lineaments associated with folds and flexures. I interpret the low coherence area around reverse faults as damage zones illustrated in Fossen's diagram (b); the damage zone is the response of brittle deformation cause by faulting (Fossen, 2010).

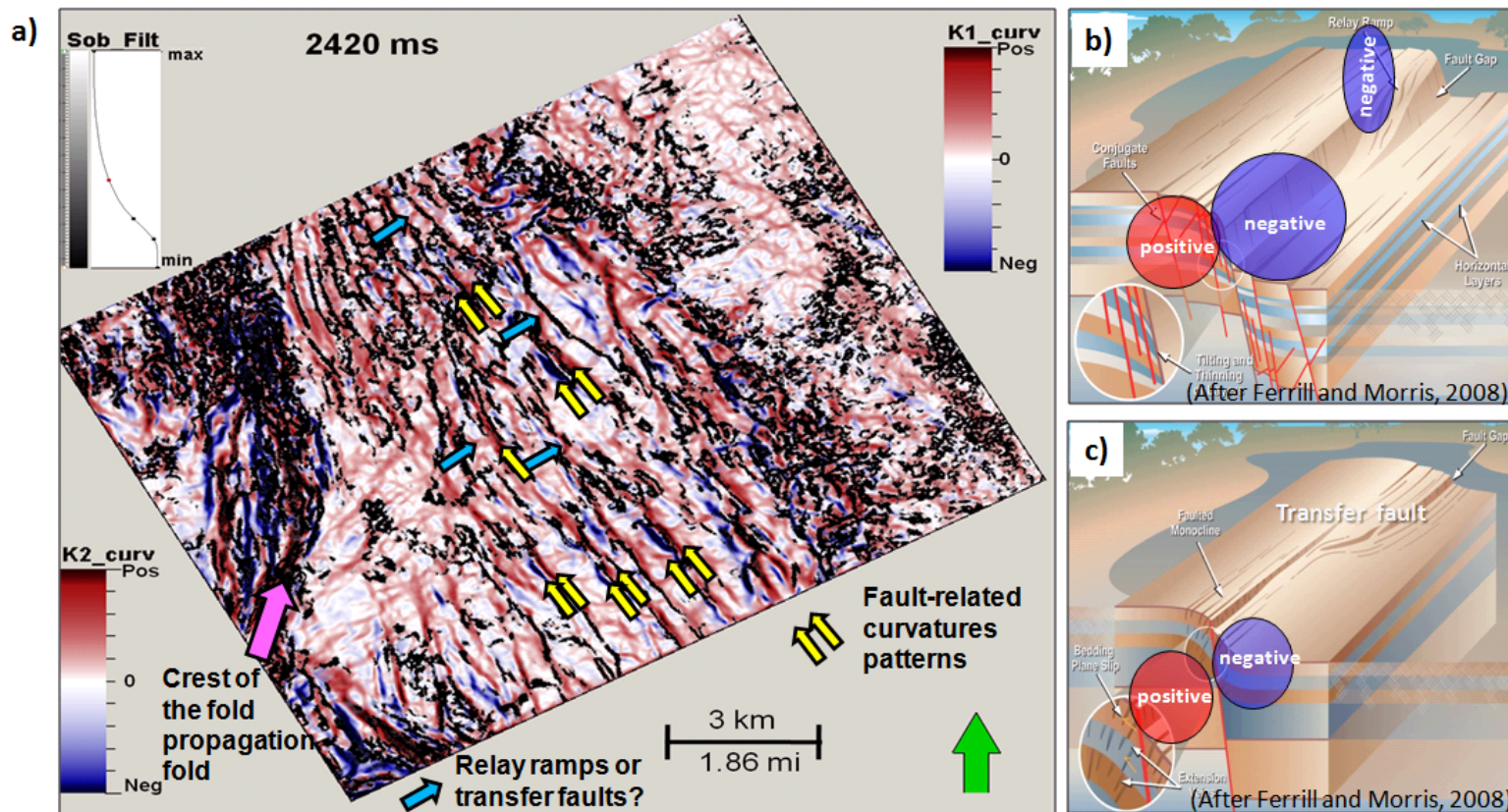


Figure 27. (a) Multiattribute display along a time slice (at $t=2.420$ s) of k_1 co-rendered with k_2 and Sobel filter similarity. I associate low similarity lineaments bounded by both k_1 and k_2 curvatures as normal faults with drag. I interpret other perpendicular curvature anomalies as relay ramps or transfer faults at small scale. The block diagrams illustrate structural elements and curvature response of fault zones in carbonate rocks of the upper (b) Glen Rose formation and the (c) Del Rio, Buda, and Eagle Ford formation which I regard as analogues. (After Ferrill and Morris, 2008).

Regarding compartmentalization, I found that there is a good correlation between ridge- and dome-like features defined by shape index, and blocks in between faults (Figure 28). Shape index, s , defines the type of deformation, while curvedness, C , defines the degree of deformation:

$$s = \frac{2}{\pi} \tan^{-1} \left(\frac{k_1}{k_2} \right), \quad (3)$$

$$C = (k_1^2 + k_2^2)^{1/2}. \quad (4)$$

The shape index, s , defines a bowl-like feature for $s=1$, a ridge-like if $s=0.5$, a saddle for $s=0$, a valley if $s=-0.5$, a bowl if $s=-1$ (Chopra and Marfurt, 2007b). Examining Figure 28, shape index is modulated by curvedness using a 2D color bar, where hue indicates the morphology of reflector determined by the shape index, and lightness indicates the amount of deformation defined by curvedness.

Figure 29 shows an amplitude vertical slice co-rendered with coherence and the shape index attribute. Note how the elongated patterns defined by the shape index visually correlate with blocks separated by normal faults. This correlation is good in the south part of the area where the normal faults are mostly parallel to each other and are oriented NE-SW (Figure 30). In the crest of anticline, the shape index is dominated by the local domal relief.

Previous multiattribute analysis served to assist the structural interpretation and define the structural framework of the field. The methodology for fault interpretation contemplates multiattribute displays of amplitude time and vertical slices, co-rendered with coherence, and principal curvatures k_1 and k_2 (Figure 30). I interpreted and correlated my faults using time slices. After that, I extended the fault interpretation over

vertical sections, which I used for quality control, adjusting my interpretation as appropriate.

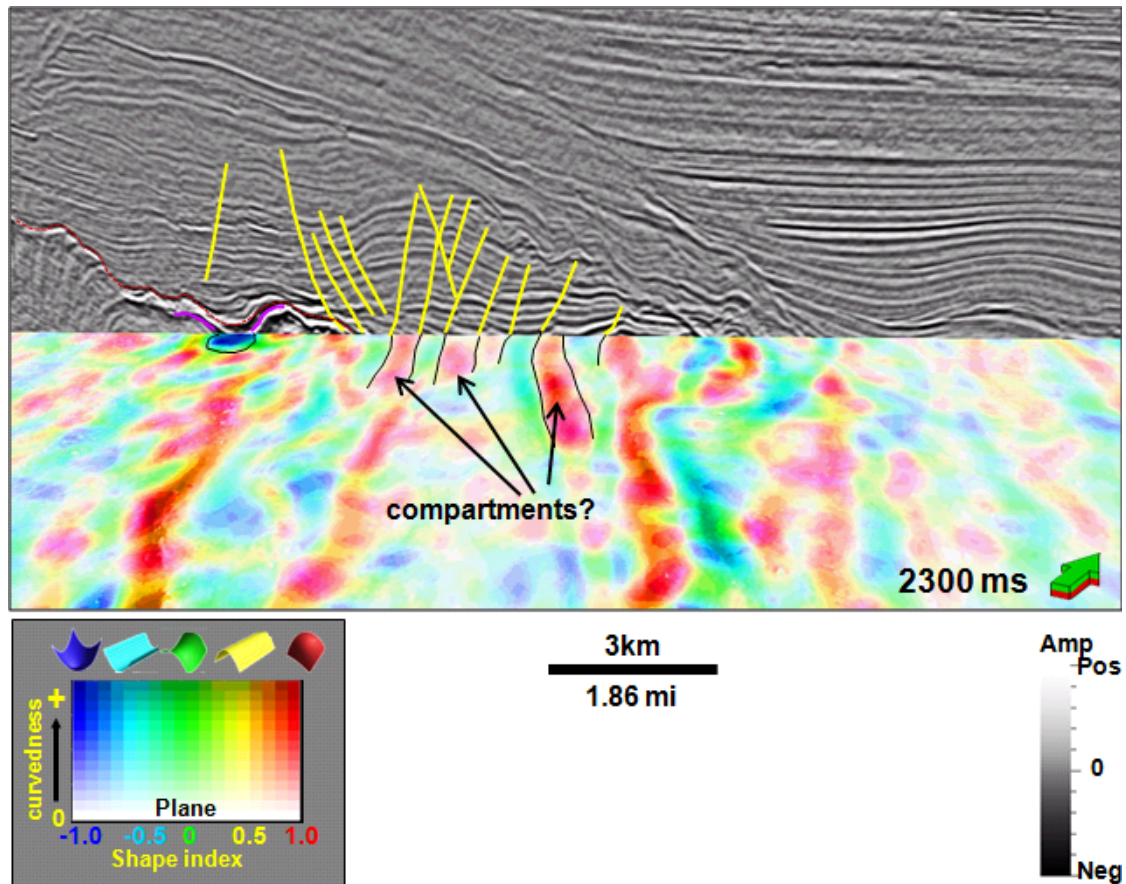


Figure 28. Vertical slice through seismic amplitude and horizon slice through shape index modulated by curvedness using a 2D color bar, where the hue indicates shape and lightness indicates the degree of deformation. Note that ridge- and dome-related patterns, defined by shape index attribute, correlate with blocks in between faults.

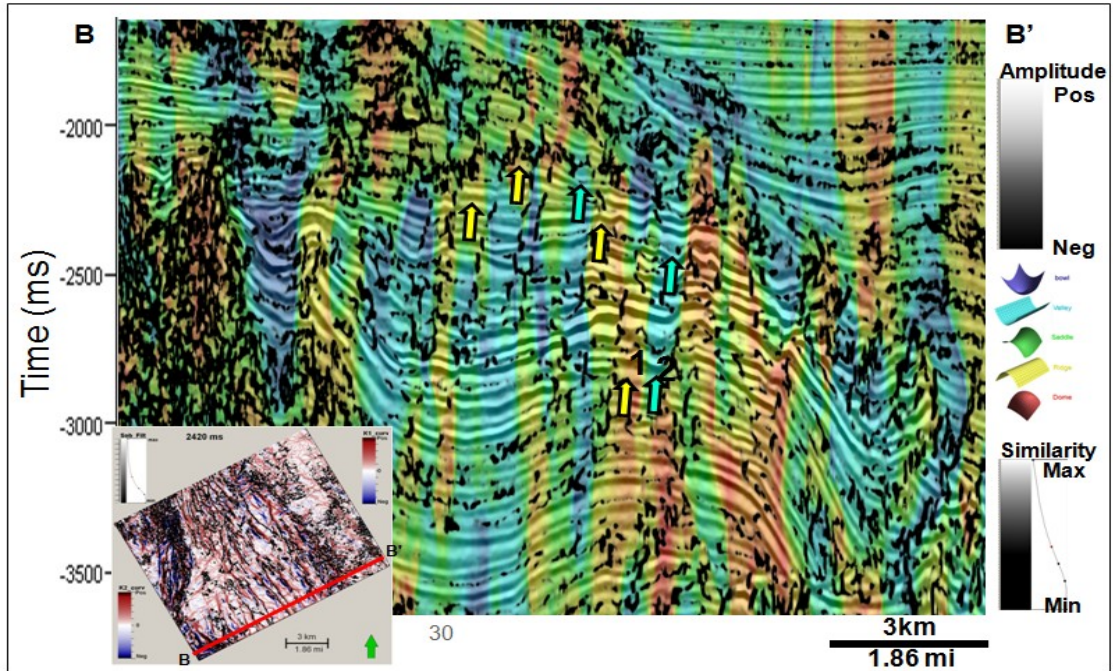


Figure 29. Amplitude vertical slice co-rendered with coherence and shape index.

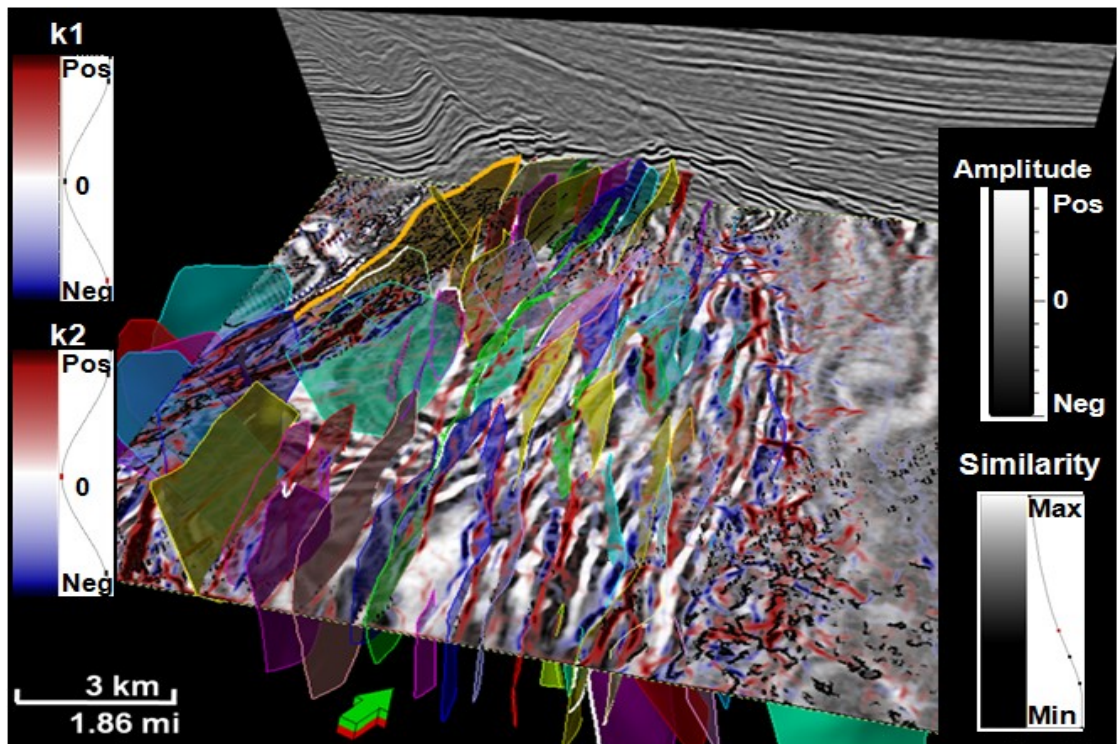


Figure 30. Attribute-assisted structural interpretation. Using multiattribute analysis, I interpreted the structural framework of the field.

Discussion and results

Multiattribute analysis can accelerate interpretation in structurally complex areas, as the example presented in this work along the tectonic front of the Sierra Madre Oriental, in the southeastern Mexico. This methodology can be applied to assist structural interpretation in other highly deformed terrenes. Although I apply this workflow to a development project data set, I consider this methodology would be more beneficial when it is applied to exploratory areas, appraisal projects or for areas with recently-acquired seismic data.

Attribute anomalies, are a function of the type of faults as well as the strength (brittle vs. ductile) and thickness of the rock units. Understanding the tectonic deformation model of the area and access to relevant outcrop or carefully analyzed seismic analogues is critical to correlating the individual attribute responses into a consistent multiattribute image.

Clustering associates independent attributes that are sensitive to components of the same geological feature. For my field, normal faults present curvature anomalies (k_1 and k_2) map drag or drape about a low coherence lineament that is aligned with the fault discontinuity. Reverse faults are not well delineated by coherence attributes, but are well delineated by curvature. The crest of the fault-propagation fold or the drag along reverse fault is expressed by a strong lineament of most positive curvature.

The attribute response of relay ramps is poorly documented. It is difficult to distinguish the ramp on cross sections, but they are easily seen on map views of attribute volumes. In this study, the relay ramps and transfer zones helps to accommodate deformation in a small scale.

The shape index attribute, which quantifies the deformation morphology of seismic reflectors, defined elongated shapes that correlate with blocks delineated by normal faults. This correlation can be successfully used to delineate individual reservoir compartments if production and pressure data support the lack of communication along faults.

Future work should focus on correlating this interpretation with well data to obtain a quantitative correlation with production or expected ultimate recovery (EUR).

CHAPTER IV. SEISMIC INVERSION FOR ROCK PROPERTIES

In hydrocarbon exploration and development, knowledge about the distribution of reservoir properties (porosity, lithology, net to gross, thickness, permeability and saturation) is important in optimizing recovery, reducing risk on well placement and confidently calculating the original hydrocarbon in place. For more mature fields, subsurface properties knowledge is critical in implementing an optimum secondary recovery stage. In either case, a workflow that infers inter-well reservoir properties will aid economic success, which is the ultimate objective of every project.

Chapter II showed that the field of study is vertically and laterally highly variable in distribution and quality. Although some wells target the same unit in the same block, up dip, wells may be nonproductive while down dip wells may be productive, indicating the need to predict inter-well reservoir quality. I hypothesize that porosity is one of the major controllers of reservoir quality.

I will use seismic inversion to estimate a porosity volume using the workflow described in Figure 31. The first step, exploratory data analysis, relates elastic properties measured in the wells to desired reservoir properties such as lithology, porosity and saturation. If this relationship is absent, there is little value in pursuing poststack or prestack seismic inversion. If P-wave impedances efficiently discriminate the desired property, then poststack seismic inversion may be sufficient. However if such discrimination requires S-wave related properties such S-wave impedance, P-wave velocity to S-wave velocity ratio, $\lambda\rho$, $\mu\rho$, or Poisson's ratio, then prestack seismic inversion is necessary.

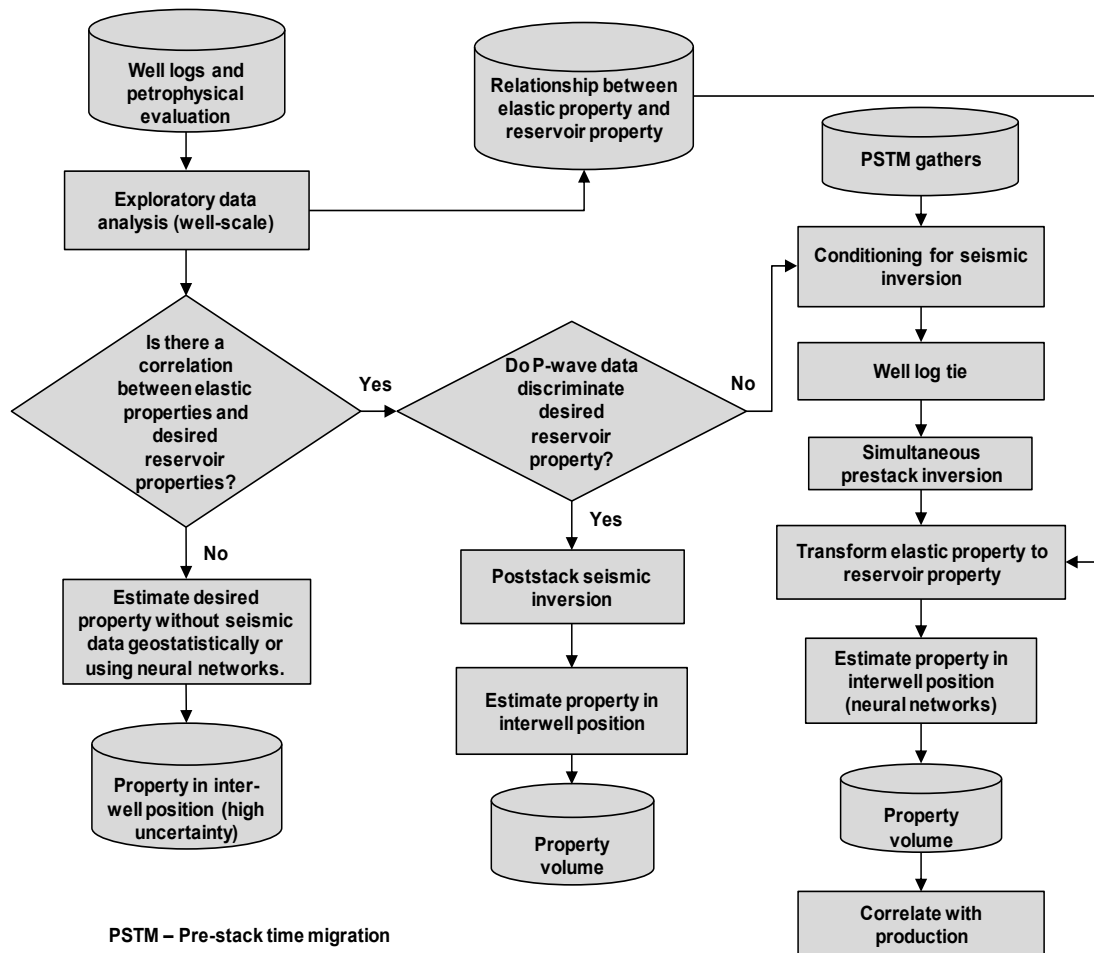


Figure 31. Workflow for reservoir quality prediction using seismic inversion and exploratory data analysis. Exploratory data analysis (EDA) evaluates the feasibility of running seismic inversion. In this stage, the relationship between the elastic parameter and the reservoir property is found and later is used to transform the results from inverted elastic parameters to a desired reservoir property. The workflow shows three possible ways to obtain the reservoir property depending on the relationships obtained from EDA. (1) If there is no relationship, calculate the property using geostatistics or neural networks using just the well log data; (2) if there is a discrimination of desired property using only P-wave impedance, calculate property volume from poststack inversion and (3) if the discrimination improves using S-wave as well P-wave impedances, obtain the reservoir property from prestack inversion of migrated gathers.

Theoretical aspects of seismic inversion

Ideally, elastic and reservoir properties should be related to each other using a calibrated rock physics model built from core and log data (Bosch et al., 2010), that accounts for all parameters that control the seismic response (Marion and Jizba, 1997) such as porosity, pore shape, mineralogy, fluid type, saturation, pressure and temperature (Wang, 1997). In the absence of a rock physics model, one can statistically estimate a linear regression from well log cross plots of elastic properties with reservoir properties. Once this relationship is validated with wells not used in the regression, we can extend the relationship to the seismic volume using geostatistical methods or trained neural networks (Bosch et al., 2010; Barclay et al., 2008).

Menke (1984) defines inverse theory as a set of mathematical techniques that allow obtaining properties (“model parameters”) of the physical world from field or lab measurements called “data”. The inverse problem is the opposite of the forward problem (Menke, 1984), in which one uses a hypothetical model, or series of equations or laws to estimate the theoretical response of known model parameters (Figure 32a). In the inverse problem, one estimates the model parameters that satisfied the observed data by applying a model or mathematical relationships (Figure 32b). The model or equations relates (linearly or non-linearly) the model parameters to the data (Menke, 1984). The goal of inversion is to minimize an objective function, which usually is the difference between the estimated data and the observed data (Bosch et al., 2010). The classic minimization method is based on least-squares using an iterative conjugate gradient method. More robust “global minimization” methods include simulated

annealing, genetic algorithms, and Monte Carlo and random search using geostatistical analysis (Chopra and Marfurt, 2007b).

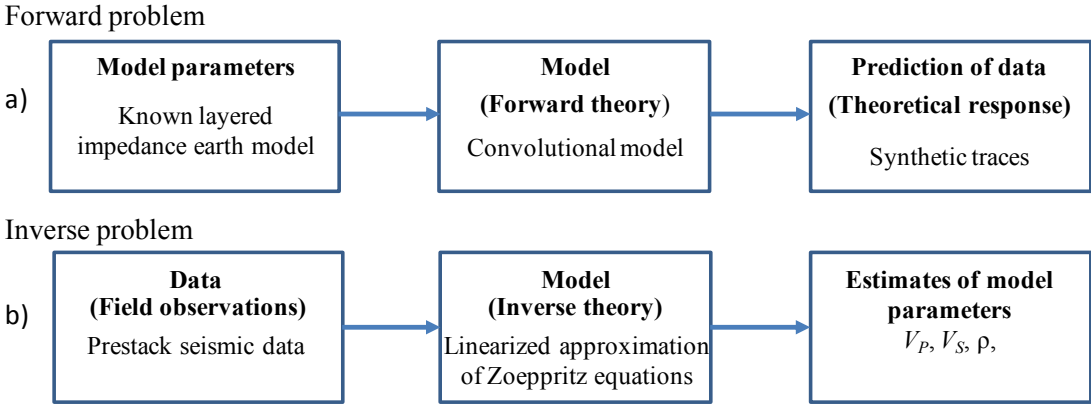


Figure 32. (a) An example of a forward problem for exploration seismology, in which the convolutional model produces synthetic seismic traces. (b) An inverse problem, prestack seismic inversion, in which P- and S-wave parameters are estimated by inverting a linearized approximation of the Zoeppritz equations. (After Menke, 1984 and Meju, 1994).

Most geophysical model parameters are described by nonlinear equations (Meju, 1994). In order to simplify the inverse problem we form local approximations. Hjelt (1992) describes three methods of linearization including rearrangement of nonlinear variables, transformation of variables, (such as log-log graphs providing a linear relationship), and Taylor series approximations.

Such linearization gives rise to a simple inverse problem represented by a linear matrix equation

$$\mathbf{Gm}=\mathbf{d}, \tag{5}$$

where \mathbf{m} is the vector representing the model parameters, \mathbf{d} is the vector representing the data, and \mathbf{G} is the matrix representing the linearized forward modeling problem.

Multiplying both sides of equation 5 by \mathbf{G}^T , we obtain the normal equations and solve for \mathbf{m} .

$$\mathbf{m} = (\mathbf{G}^T \mathbf{G})^{-1} \mathbf{G}^T \mathbf{d}, \quad (6)$$

where the superscripts T denote the transpose and -1 denotes the matrix inverse.

Given an estimate of errors in the measured data, commonly defined by its covariance matrix, one can estimate the errors in the predicted parameters, \mathbf{m} . For instance shear impedance, Z_s , is poorly estimated with offset-limited data, with accuracy increasing as farther offsets are included. In principle, density can be estimated if data are acquired beyond 45°; however, data errors of inaccurate moveout, migration stretch, and decreased signal to noise ratio counteract the improved theoretical resolution.

The 3D seismic reflection method provides the broadest coverage of recorded subsurface information in the form of travel time and amplitude. Both of these measurements can be inverted independently (Barclay et al., 2008). Travel time is inverted for depth conversion or seismic imaging using a velocity model (Barclay et al., 2008); amplitude is inverted to obtain elastic properties of the media that can be converted to reservoir properties such porosity, lithology, saturation and permeability using a mathematical relationship. Hereafter I use seismic inversion to refer aspects related specifically to amplitude inversion.

One of the assumptions of the seismic inversion method is that the recorded amplitude is a function of the reflection coefficient at each interface in the subsurface. To validate this assumption, the data processing sequence should preserve relative amplitudes (Yilmaz, 2001). The reflection coefficient is dependent upon the impedance

contrast between two layers. Impedance is the product of velocity and density. More specifically, P-wave impedance (Z_P) is the product of P-wave velocity (V_P) and density (ρ)

$$Z_P = V_P \cdot \rho ; \quad (7)$$

Z_P is also referred as acoustic impedance (AI), where the P-wave is the compressional or primary wave. Similarly, S-wave impedance (Z_S) is the product of S-wave velocity (V_S) and ρ ,

$$Z_S = V_S \cdot \rho, \quad (8)$$

where S-wave is the shear or secondary wave.

When a pure P- or S-wave strikes normally a planar interface between two layers, part of the energy is reflected normally to the surface while the rest is transmitted through the interface (Figure 33a) with no mode conversion (Mavko et al., 2009). For this case, the reflection coefficient (R_0) at the interface is the ratio of the differences of impedances to the sum of them:

$$R_0 = \frac{V_{n+1}\rho_{n+1} - V_n\rho_n}{V_{n+1}\rho_{n+1} + V_n\rho_n} \quad (9)$$

At non-normal incidence, a P-wave decomposes into four waves: a P-wave transmitted and a P-wave reflected, an S-wave transmitted and an S-wave reflected (Figure 33b). The nonlinear Zoeppritz equations describe the amplitudes of reflected and transmitted P- and S-wave components as a function of angle (Shue, 1985). Aki and Richards provided a linearized approximation of the Zoeppritz equations assuming small contrasts along the interface and angles smaller than critical in which reflectivity is a function of changes of V_P , V_S and ρ (Mavko et al., 2009; Shue, 1985):

$$R(\theta) \approx \frac{1}{2} \left(1 - 4 \frac{V_S^2}{V_P^2} \sin^2 \theta \right) \frac{\Delta\rho}{\rho} + \frac{\sec^2 \theta}{2} \frac{\Delta V_P}{V_P} \frac{-4V_S^2}{V_P^2} \sin^2 \theta \frac{\Delta V_S}{V_S}, \quad (10)$$

where:

$$\Delta V_P = (V_{P2} - V_{P1}), \quad (11)$$

$$V_P = (V_{P2} + V_{P1})/2, \quad (12)$$

$$\Delta V_S = (V_{S2} - V_{S1}), \quad (13)$$

$$V_S = (V_{S2} + V_{S1})/2, \quad (14)$$

$$\Delta \rho = (\rho_2 - \rho_1), \quad (15)$$

where θ is the average angle of incidence and transmission

$$\theta = (\theta_2 + \theta_1)/2, \quad (16)$$

defined by Snell's law

$$\frac{\sin \theta_1}{V_1} = \frac{\sin \theta_2}{V_2}. \quad (17)$$

Aki and Richards's approximations served as the inspiration for other approximations for different parameterizations: Shue (1985) Z_P and Poisson's ratio (ν), Connolly (1999) elastic impedance (EI) in terms of V_P , V_S and ρ , Goodway (2001) $\lambda\rho - \mu\rho$, Gray (2002) λ and μ , Whitcombe et al. (2002) extended elastic impedance (EEI), and Hampson and Russell (2005) Z_P , Z_S and ρ . Whatever the parameterization, the linearized Zoeppritz approximations are amenable to inversion using a variant of equation 6.

The stacking process simulates normal incidence propagation. Consequently, one can only estimate P-wave impedance (Z_P) from inversion of poststack P-wave seismic data. Similarly, one can invert poststack S-wave seismic data to estimate S-wave Impedance (Z_S) (Avseth et al., 2010). To maintain the assumption of vertical incidence, the poststack seismic data needs to be migrated (Yilmaz, 2001). Poststack

seismic inversion is not recommended in areas where seismic amplitude significantly varies with offset.

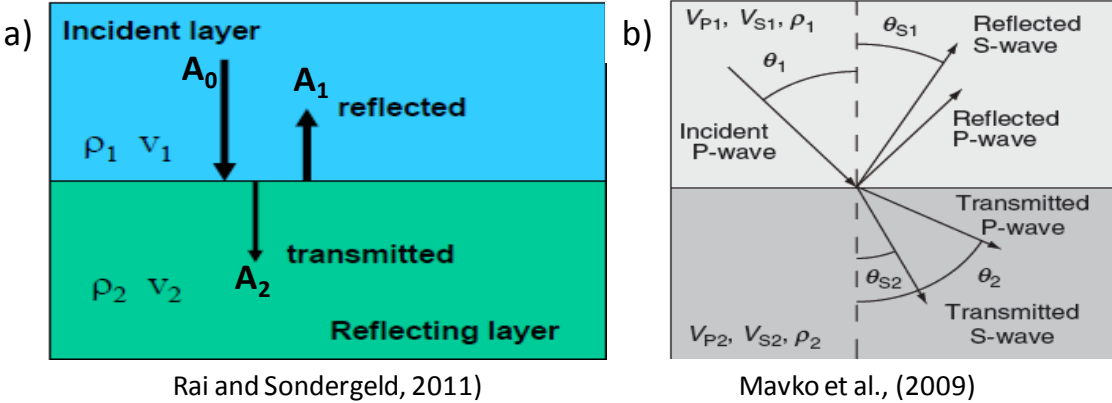


Figure 33. (a) At normal incidence there are two vertical wave components associated: a normal reflected and a vertical transmitted wave (Rai and Sondergeld, 2011). (b) In contrast, there are four wave components associated with an oblique incident P-wave at horizontal interface: P-wave reflected and P-wave transmitted; S-wave reflected and S-wave transmitted (Mavko et al., 2009).

More than one rock type, with different reservoir quality and saturation, can have the same P-wave impedance value. P-wave impedance represents the total effect of lithology, fluid and porosity (Russell and Hampson, 2006). Consequently, it is difficult to separate the effect of these factors having only measurements of Z_P . To distinguish rocks types with the same Z_P but different lithology, porosity, or saturation, it is advisable to introduce S-wave related properties. Adding S-wave information reduces the uncertainty in discriminating reservoir from non-reservoir rock. Pure S-wave and converted wave multicomponent seismic surveys are limited; consequently, to derive P-wave and S-wave properties when there is only P-wave data available, we need to invert prestack gathers with offset information which carry implicit S-wave information (Avseth et al., 2010). Thus, one can invert prestack seismic data for density,

P-wave and S-wave related properties. Table 2 summarizes which elastic properties could be generated depending on the type of seismic data inverted.

A common and powerful quality control of the inverted results is the blind test (Barclay et al., 2008; Pendrel, 2006), in which one or more wells are excluded from the inversion (“blind wells”), after which the inverted elastic parameter is compared with the same parameter computed from the excluded well logs. If the results are similar, the algorithm works properly, if not, the process updates iteratively until the difference falls below a threshold. This process does not end when results are reasonable. Ideally, we should update the model incorporating new information as soon as it is acquired throughout the life of the exploration, development or monitoring stage (Pendrel, 2006).

The best practice is to use a calibrated rock physics model that takes into account variation of elastic properties with variation of pore type, pore shape, changes in frequency, and changes in fluid. Ideally, the calibration should be done with controlled core measurements of elastic moduli, porosity, and density of the matrix for both dry and saturated samples. Unfortunately, no one has yet published a rock physics model for carbonate wash facies.

Data type	Rock properties
Full-stack P-wave	Z_P
Full-stack S-wave	Z_S
Pre-stack P-wave	$Z_P, Z_S, V_P/V_S, \lambda\rho, \mu\rho, \lambda/\mu, \lambda, \mu, \nu$ and ρ

Table 2. Summary of rock properties obtained with seismic inversion as a function of the data type inverted (Adapted from Barclay et al., 2008).

Factors that control carbonate elastic properties

Carbonates bear important quantities of hydrocarbons around the world; although they represent only 20% of sedimentary rocks in the Earth's crust, and 50% of the proven hydrocarbon reserves (Palaz and Marfurt, 1997). Tucker and Wright, (2008) define carbonates as "rocks that contain more than 50% of carbonate minerals; volumetrically the most important are calcite, dolomite and aragonite". Indeed, the low stability of these mineral components is what makes carbonates prone to suffer diagenesis in contrast to siliciclastics, which are much less affected. Diagenesis includes all the physical and chemical processes that modify sediments after deposition such as cementation, dissolution, mineral replacement, recrystallization chemical compaction and fracturing. (Scholle and Ulmer-Scholle, 2003). The type and order in which diagenetic processes occurred determine whether the reservoir quality diminishes or improves, carrying a consequent change in elastic and petrophysical properties. Because of diagenesis, carbonate rocks tend to have complicated porous structure that depends primarily upon their diagenetic history rather than upon the time of deposition or depth (Anselmetti and Eberli, 1997).

The reservoir units of my area of study are carbonate rocks by definition according to Tucker and Wright (2008), with an average mineral composition of 85% calcite and 3% dolomite. Although these carbonates rocks are allochthonous, eroded from the Cretaceous platform and redeposited in a slope environment during the Eocene, the reservoir quality depends upon their mineral composition, which makes the reservoir prone to diagenesis, just as the conventional carbonates deposited in situ. Appendix A summarizes the reservoir diagenesis from thin section analysis.

There are several factors that affect elastic carbonate rock properties such as pore type, mineralogy, porosity, saturation, pore fluid type, velocities in pore fluids, depth, pressure, and bulk density. Wang (1997) ran laboratory measurements on carbonate samples to evaluate how those factors affect seismic velocities. He noticed that compressibility of pores, which depends on aspect ratio (pore shape), inversely affects the velocity. The aspect ratio refers to the ratio of width to length of a pore, such that elliptical or crack-like pores have an aspect ratio <1 , while spherical pores have an aspect ratio of 1. The closer to 1 the pore aspect ratio, the harder to compress. For instance, a rock frame with intercrystalline (space between crystals of similar size) or interparticle porosity (space between any size and type of particles) have a relative low velocity because those pores are highly compressible due to their low aspect ratio. Intercrystalline and interparticle pores tend to be angular and irregular in shape, conferring a weak structure to the rock, and consequently a relative low velocity (Figure 34a). On the other hand, pores with aspect ratio closer to 1, such as moldic porosity, are less compressible. Moldic porosity provides a stiffer frame for the rock, thus its velocity is higher with respect to other porosity types (Figure 34b). Wang (1997) concluded that pore type and pore fluid compressibility variation are the main properties that account for velocity variation. These observations are also in agreement with Anselmetti and Eberli (1997) who conclude that pore structure is the primarily responsible for variation in velocities. Later on, Eberli et al. (2003) conducted several lab tests that show that velocity is higher for moldic and intraframe porosity, for a given porosity value, than microporosity, interparticle and intercrystalline porosity (Figure 35). These results support the velocity-porosity type dependence.

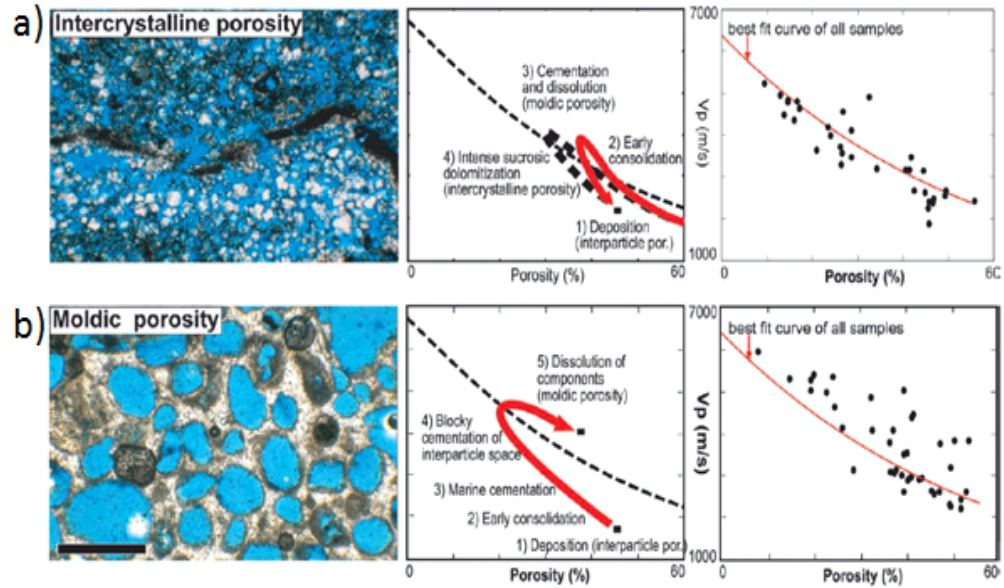


Figure 34. Porous carbonate frames exhibiting different elastic behavior (Eberli et al., 2003). (a) Intercrystalline porosity produced by dolomitization. This rock frame is weak and thus has low velocity. (b) Moldic porosity supported by precipitated cement which provides a stiff rock frame. Moldic porosity is less compressible due to the roundness of dissolved molds, which have an aspect ratio close to 1, and thus has high velocity

Anselmetti and Eberli (1997) studied 295 minicores from three locations, with different carbonate depositional environments and diagenetical history, to evaluate the effect of diagenesis with age and depth on thin sections. They analyzed core measurements under saturated conditions to explore seismic velocities dependence. They observed that porosity is neither age nor depth dependent, because porosity may be increased or decreased depending upon the stability of mineral composition and diagenetical history. Diagenesis affects sediments at any depth, including at the surface immediately after deposition. Anselmetti and Eberli (1997) and Eberli et al. (2003) state that diagenesis (cementation) in carbonates causes more significant porosity loss in comparison to mechanical compaction by overburden pressure. In siliciclastic sediments, mechanical compaction is the principal mechanism for porosity lost.

Velocity inversion is common in carbonates due to the non significant depth-porosity dependence (Anselmetti and Eberli , 1997).

Mineralogy exerts an important control of velocity changes when they have significant differences in elastic modulus Anselmetti and Eberli (1997). In this regard, Marion and Jizba (1997) showed that there is a significant difference in shear modulus of calcite and dolomite, while the difference in their bulk modulus is negligible. This difference in shear modulus also causes an important difference in their velocities. Such a difference provides the basis to use V_p , V_s , and impedance relations as lithology discriminator tools. One needs to take in mind that V_p and V_s are strongly dependent on pressure, under with V_p more affected than V_s , such that V_p to V_s ratio increases with pressure (Wang, 1997).

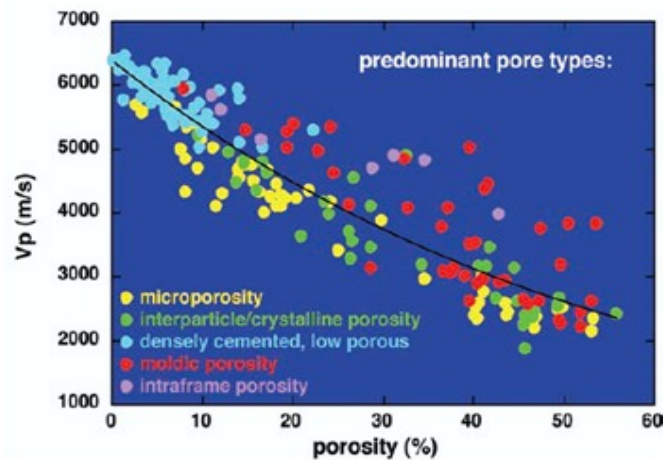


Figure 35. Velocity versus porosity plot for different carbonate rocks measured at 8 MPa effective pressure (Eberli et al., 2003). Moldic and intraframe porosity samples have higher velocity than the interparticle/crystalline and microporosity porosity types. The black curve represents the best exponential fit. Note that for the same porosity value, compressional velocity V_p varies accordingly to the pore type.

Previous studies of porosity prediction in carbonate reservoirs

Marion and Jizba (1997) studied a Tertiary carbonate oil field in which porosity was successfully predicted from poststack seismic inversion using a P-wave impedance-porosity relationship. The field they studied contained 30 drilled wells. The reservoir is made up nummulitic limestone with a dolomite content ranging from 0 to 30 %, with intraparticle (internal pores of particles or grains) and interparticle porosity (Figure 36). This carbonate field is highly heterogeneous, presenting a large variation in porosity, oil saturation, and thickness. A mixed structural and stratigraphical trap characterizes the field. The goal was to demarcate the reservoir and predict the distribution of reservoir properties. Note that these characteristics and problems are similar to my case study. Marion and Jizba (1997) successfully predicted porosity, Φ , from poststack model-based seismic inversion. They use blind wells to validate the resulted P-wave impedance volume. Then, using a relationship between Z_P and Φ (Figure 37) established with a rock physics model that evaluated the variation of velocity and impedance with variation in porosity, pore shape, mineralogy, fluid type, saturation, and frequency measurement, they converted impedance to porosity at each trace position. Blind wells proved a successfully porosity prediction, so the result was used with confidence to detect pay zones, which resulted larger than previously evaluated. All the results were in agreement with production data.

Bosch et al. (2010) show another example for a heavy oil field in carbonate and clastic sequences, in which porosity correlates with acoustic impedance (Figure 38). In this example, shale intervals have low acoustic impedance, corresponding to large total porosity. In contrast, the reservoir sand and carbonate layers exhibit high acoustic

impedance corresponding to lower total porosity values. P-wave data are insufficient to discriminate lithology in this field, but provide a good discrimination of porosity. The acoustic impedance to porosity relationship was used to run joint seismic and petrophysical inversion, in which the elastic parameter is determined simultaneously with the rock property to estimate porosity. Figure 39 shows the resulting porosity and acoustic impedance obtained from joint inversion. The correlation between P-wave impedance and porosity is common in several carbonate examples (as in Barclay et al., 2008; Bosh et al., 2010; Marion and Jizba, 1997; Wang, 1997), such that acoustic impedance derived from poststack seismic inversion could be transformed into porosity using the correlation between these properties. I use exploratory data analysis to determine whether this correlation is valid in my carbonate field. If so, I can predict porosity from poststack seismic inversion.

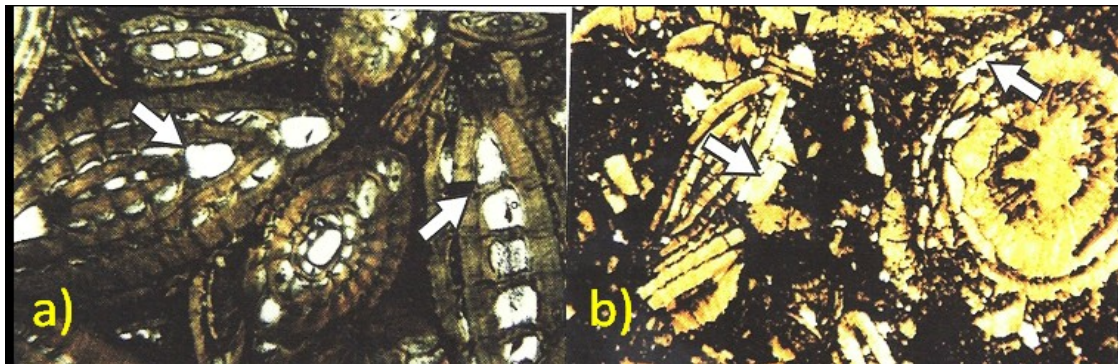


Figure 36. Representative thin section photographs of a nummulitic reservoir study by Marion and Jizba (1997). (a) Intraparticle porosity in nummulitic foraminifera. (b) Interparticle porosity. White arrows indicate porosity.

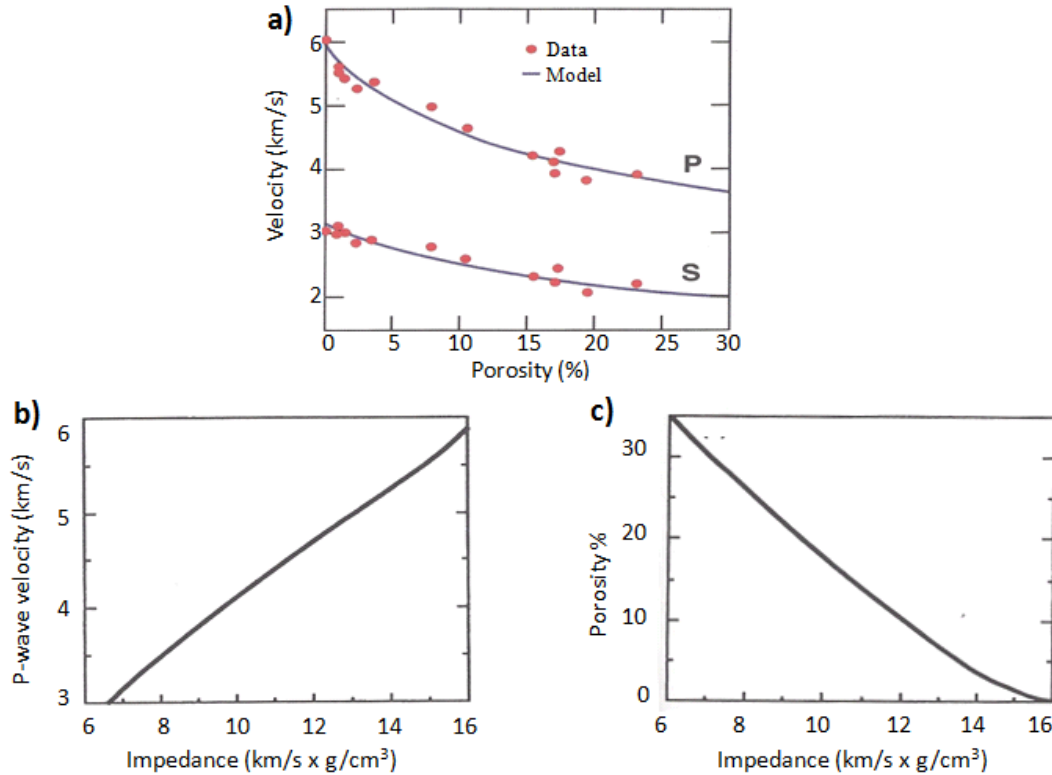


Figure 37. Calibrated rock physics model (Marion and Jizba, 1997). (a) Velocity–porosity relationship comparison between core measurements (dots) and rock physics model (solid line). (b) Velocity–impedance relationship. (c) Impedance–porosity relationship used to transform inverted seismic data to porosity.

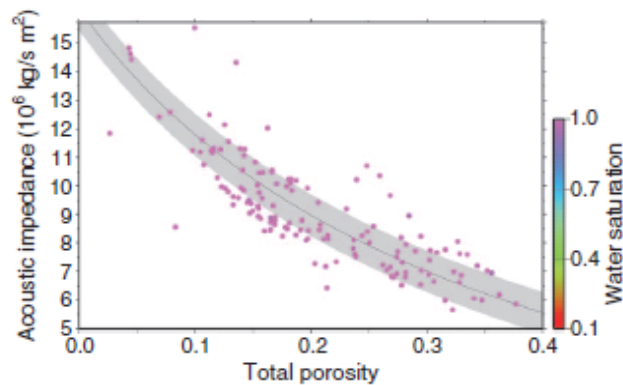


Figure 38. (a) Acoustic impedance versus total porosity color-coded by water saturation (Bosch et al., 2010). Dots indicate measurements from well logs, the black curve indicates the calibrated petrophysical model and the gray band indicates plus and minus one standard deviation from the model.

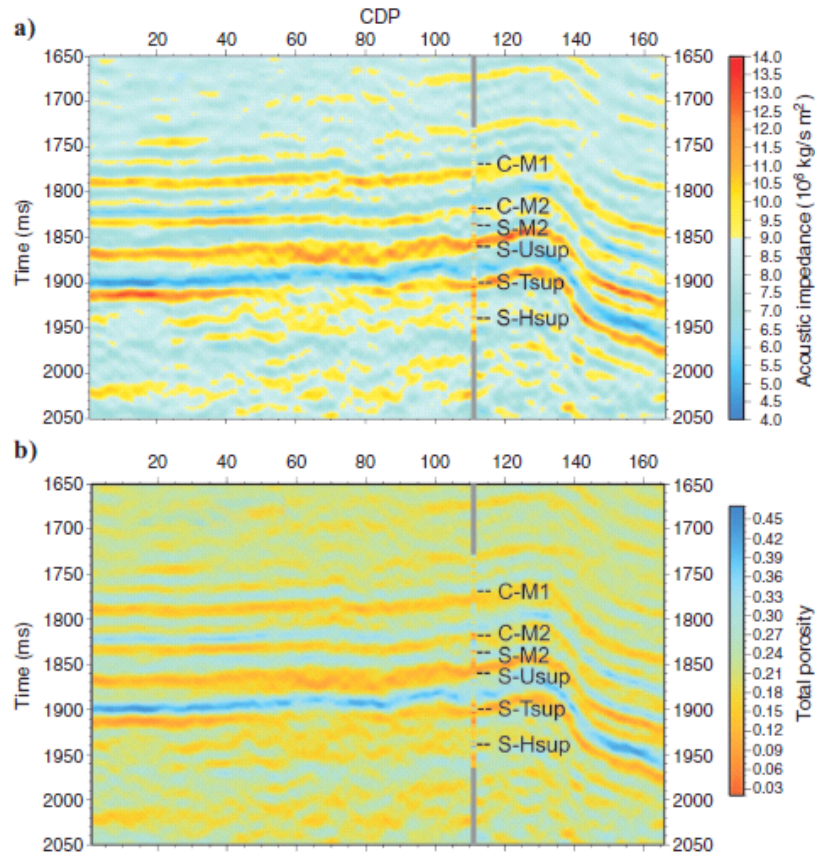


Figure 39. Vertical slice through (a) acoustic impedance and (b) total porosity resulting from simultaneous seismic petrophysical inversion for a carbonate-clastic heavy oil field (Bosch et al., 2010).

Exploratory data analysis

The main purpose of exploratory data analysis for seismic inversion concentrates in evaluating its feasibility. If inversion is viable, EDA assist in determining the type of inversion and parameters of inversion process. This analysis is commonly made through crossplots of well log and core data to determine the relationship between the desired rock property such water saturation, clay volume, permeability, lithology, or porosity, and the elastic property that could be obtained from seismic inversion such as P-wave impedance (Z_P), S-wave impedance (Z_S), V_P to V_S

ratio (V_P/V_S), Poisson's ratio (ν), $\lambda\rho$ and $\mu\rho$. If there is a high correlation between elastic and rock property, or the reservoir can be separate from an undesired background, then the seismic inversion is feasible and the relationship establish in this phase will be used to extend discriminate reservoir or desired property at seismic scale.

I evaluate the feasibility of predicting porosity, clay volume or saturation from seismic inversion through examination of well log data for five reservoir units EOC-10, EOC-20, EOC-30, EOC-50 and EOC-3. First, I investigate if my field presents a good correlation of porosity-acoustic impedance, as in Mario and Jizba's (1997) case study. If this correlation is high, then I would be able to transform Z_P , obtained from poststack seismic inversion into porosity at every trace position. Otherwise, I will explore further discrimination of my zones of interest incorporating S-wave related properties in addition to P-wave.

Before starting the analysis, I discarded anomalous values of sonic and density logs, reviewing the caliper log for quality control. Then, I converted P-wave and S-wave slowness (the inverse of velocity) from sonic logs to V_P and V_S respectively. I use these velocities and density logs to compute Z_P (Equation 7), Z_S (Equation 8), V_P/V_S , $\lambda\rho$ (Equation 18), and $\mu\rho$ (Equation 19).

$$\mu\rho = Z_S^2, \quad (18)$$

$$\lambda\rho = Z_P^2 - 2Z_S^2, \quad (19)$$

where μ is the shear modulus, λ is the second Lamé parameter, incompressibility, and ρ is density.

There are 32 drilled wells in the area from which 16 have P-wave sonic, S-wave sonic and density logs, while ten wells have just P-wave and density logs in the Eocene

reservoir units (Table 3). Figure 40 shows the well log distribution of the field overlapping the time structure map of the main unconformity that separates the Miocene shale from the Eocene calcilithites.

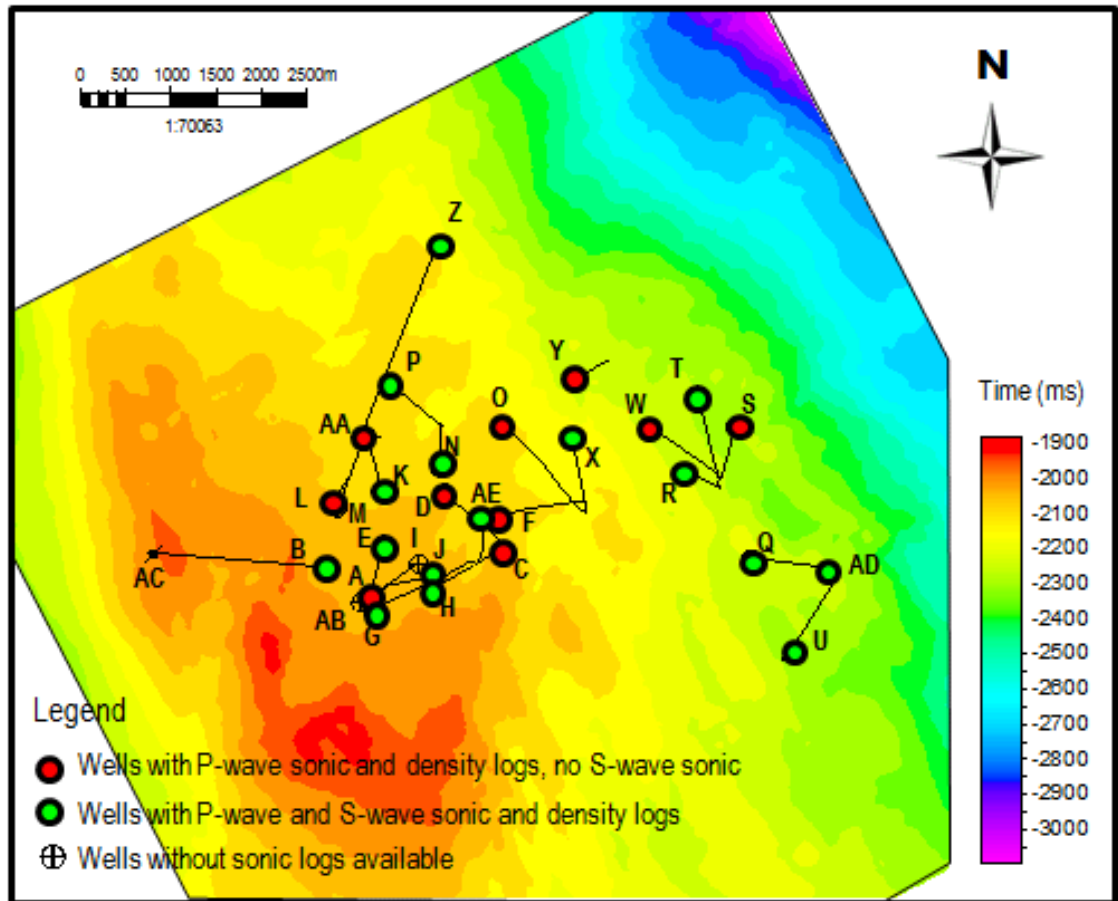


Figure 40. Time structure map of the main unconformity that separates Miocene shale from Eocene calcilithites showing the distribution of sonic and density logs in the field of study. Red circles indicate wells with P-wave sonic, S-wave sonic and density logs. Green circles indicate wells with P-wave sonic and density logs but without S-wave sonic logs.

Well	Status	Reservoir unit	Well logs		
			P-wave sonic	S-wave sonic	Bulk Density
A	Oil	EOC-20	x		x
B	Oil	EOC-10	x	x	x
C	Brine water	EOC-10	x		x
D	Oil	EOC-20 & EOC-10	x		x
E	Oil	EOC-20 & EOC-10	x	x	x
F	Oil	EOC-50	x		x
G	Oil	EOC-3 + EOC-10 + EOC-20	x	x	x
H	Oil	EOC-10 & EOC-20	x	x	x
I	Mechanical problems				
J	Oil	EOC-10	x	x	x
K	Oil	EOC-10	x	x	x
L	Mechanical problems		x		x
M	Oil	EOC-10			x
N	Oil	EOC-10	x	x	x
O	Oil	EOC-50	x		x
P	Oil	Miocene	x	x	x
Q	Oil & Gas	EOC-30 & EOC-50	x	x	x
R	Oil	EOC-30 & EOC-50	x	x	x
S	Oil	EOC-30 & EOC-50	x		x
T	Oil	EOC-30 & EOC-50	x	x	x
U	Brine water	EOC-30 & EOC-50	x	x	x
V	Mechanical problems				
W	Oil	EOC-30	x		x
X	Oil	EOC-50	x	x	x
Y	Oil	EOC-50	x		x
Z	Oil	Miocene	x	x	x
AA	Dry	EOC-10	x		x
AB	Mechanical problems				
AC	Brine water	EOC-10			
AD	Oil	EOC-30	x	x	x
AE	Oil	EOC-3	x	x	x

Table 3. Sonic and density logs available per well in the area of study.

Analyzing the dependence of porosity with depth and density, note in Figure 41 that there is a wide range of porosity for the same depth value. Although there is large difference in vertical depth among wells due to its structural position, porosity is not depth-dependent. These results are in agreement with Anselmetti and Eberli, (1997), who noted that porosity depends more on the diagenetic history rather than depth. Figure 42 shows that total porosity increases as density decreases for all the reservoirs, independently of structural position or depth.

Next, I search for a relationship between Z_P and porosity, clay volume, and water saturation to determine whether I can predict the correlated rock property using only P-wave information through poststack seismic inversion. I generated cross-plots of P-wave impedance versus total porosity for each of the five reservoirs, adding a third dimension using color-coded properties of gamma ray (Figure 43) and bulk density (Figure 44) to assist reservoir discrimination. Note that values are significantly scattered for the same value of impedance; there is a wide range of values in porosity and vice versa. There is no further discrimination with gamma ray (GR) as a third property, since shale and calcilithites present similar total porosity values (note the highly dispersed GR values along the plot). The discrimination is better when the third dimension is represented by bulk density (RHOB); a small range in density value corresponds to a small range in porosity with a wide range in acoustic impedance values. This behavior repeats in all the reservoir units. Unfortunately, density cannot be obtained from poststack seismic inversion, and can be difficult to estimate from inversion of prestack gathers for angles less than 45 degrees.

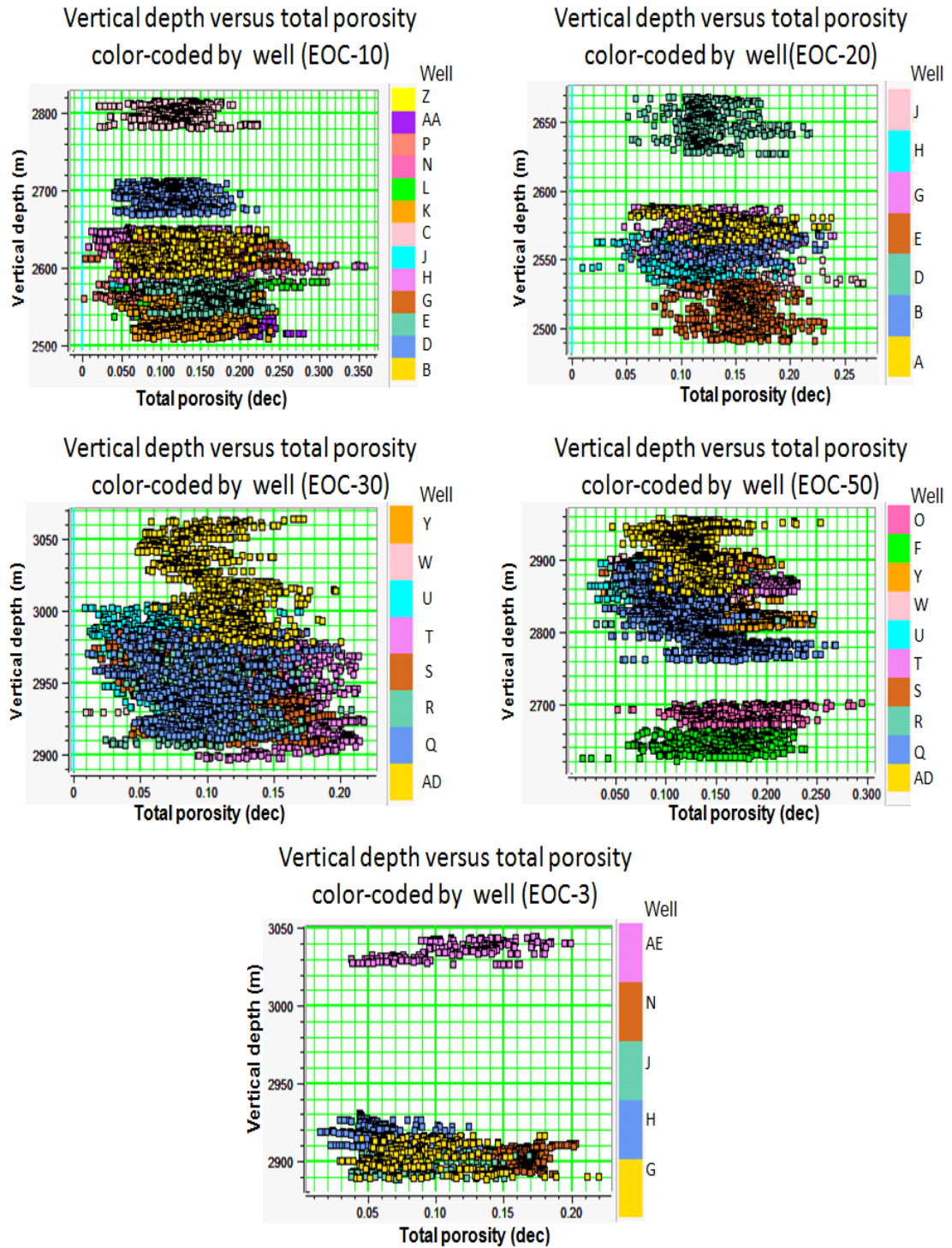


Figure 41. Vertical depth versus total porosity color-coded by well name for five reservoir units in the Eocene calcilithites. Note that for the same depth range, there is a wide range of porosity values. This response indicates that porosity is not depth dependent.

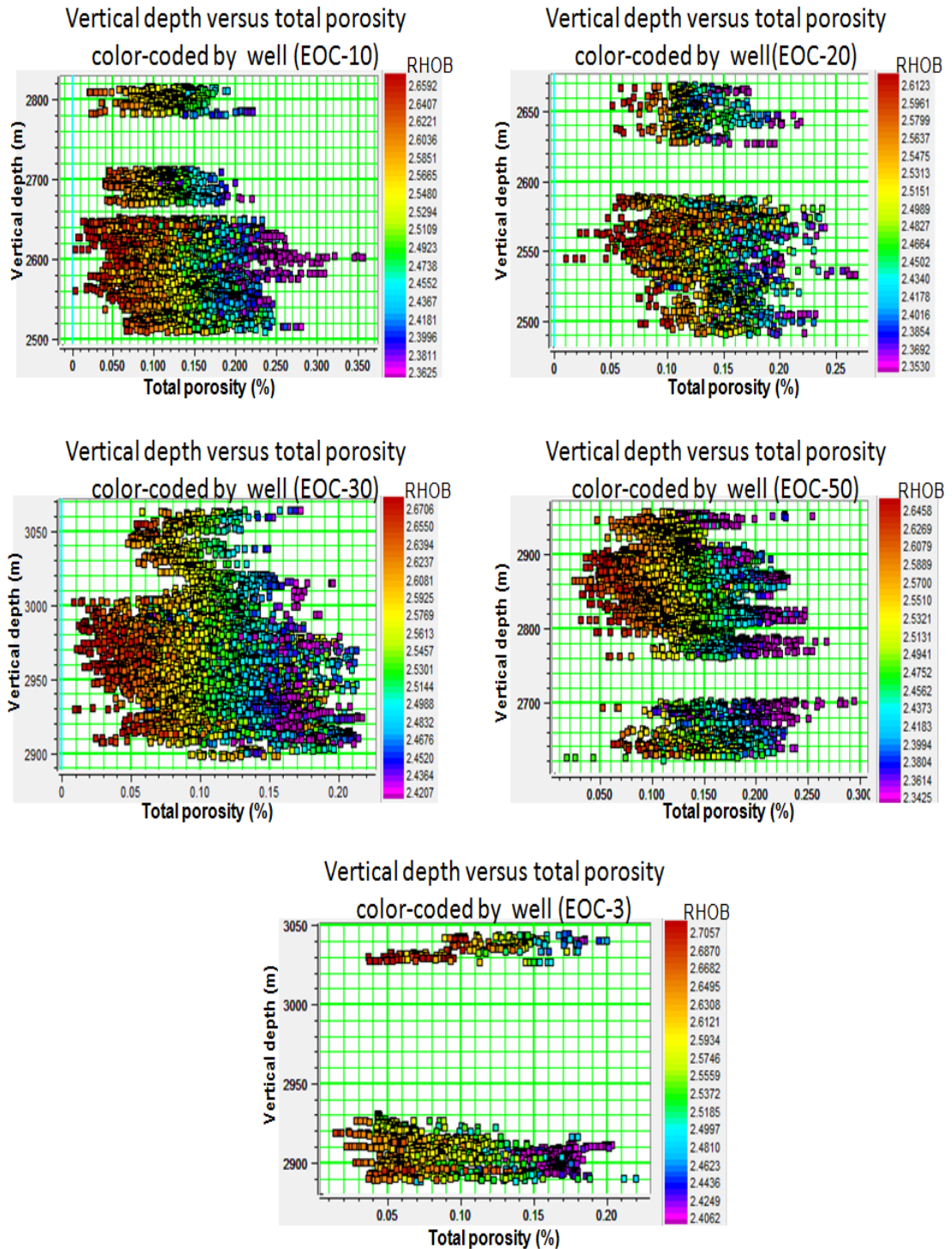


Figure 42. Vertical depth versus total porosity color-coded by bulk density (RHOB) for five reservoir units in the Eocene calcilithites. Although scattered, note that density increases as porosity decreases, independent of depth.

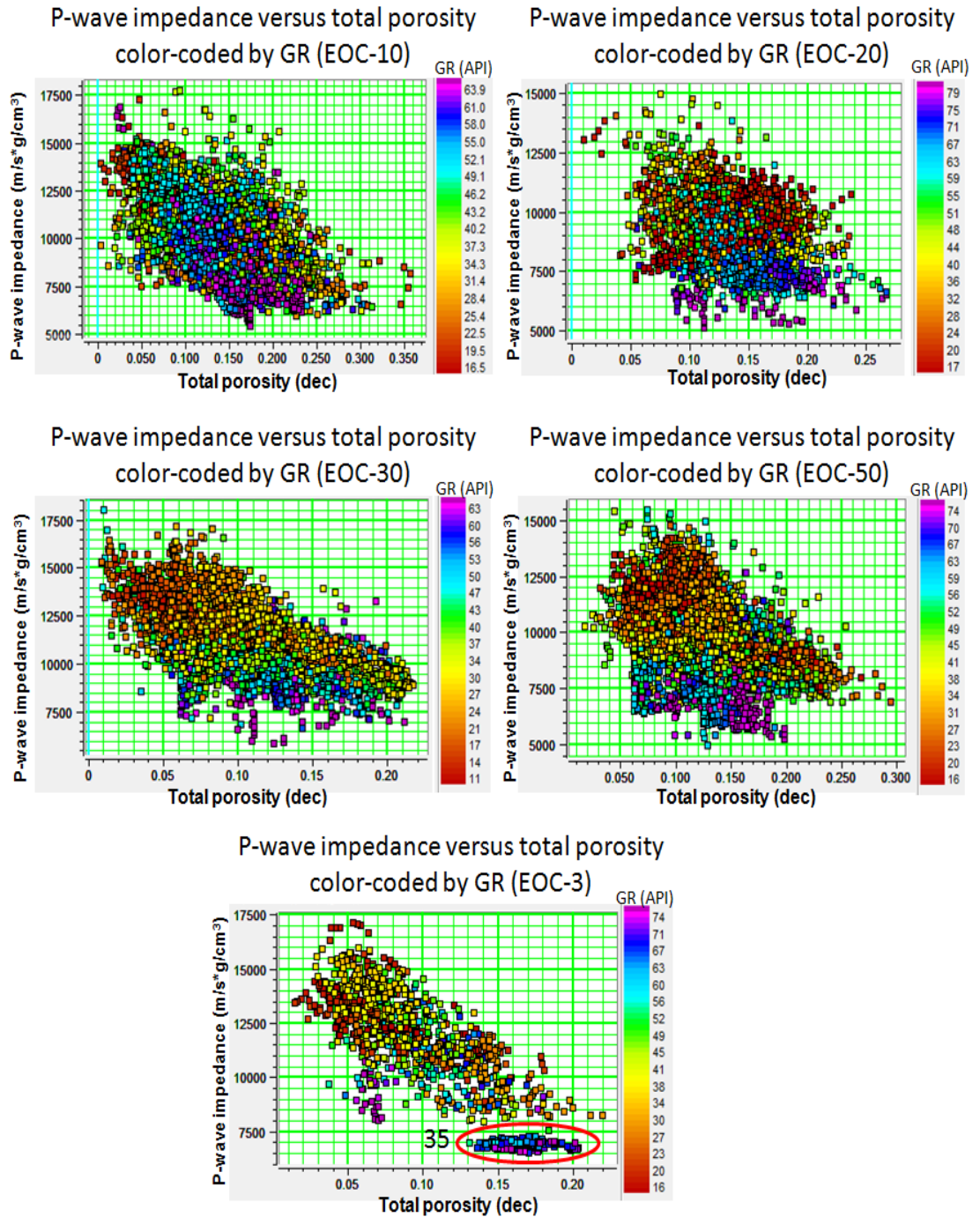


Figure 43. P-wave impedance versus total porosity color-coded by gamma ray (GR) for reservoir units EOC-10, EOC-20, EOC-30 and EOC-3. Note that red points, correlating to clean facies (color-coded by low GR), are scattered and present a wide range of impedance for the same porosity value. Red circle indicates shale layers cut by well 35.

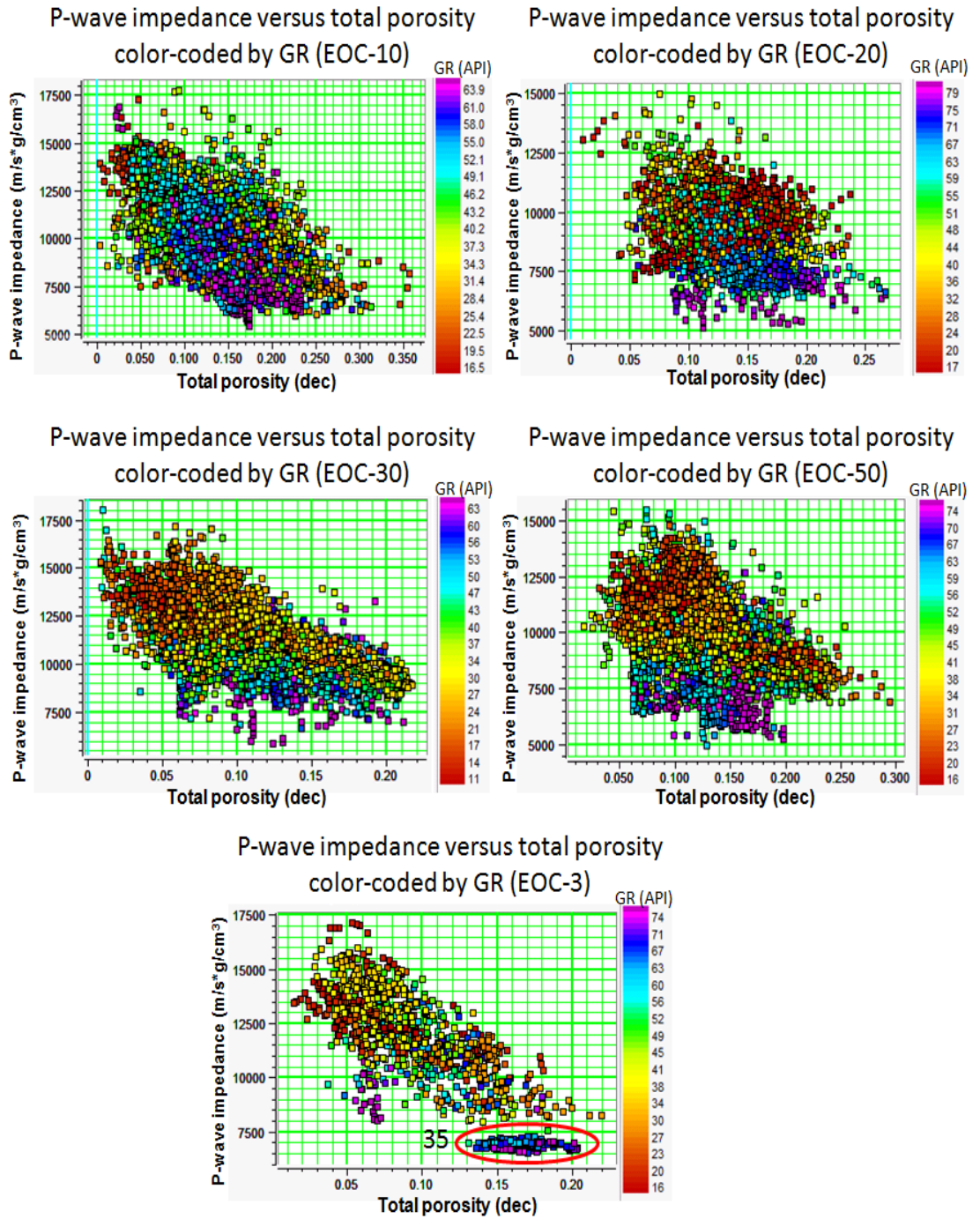


Figure 44. P-wave impedance versus total porosity color-coded by bulk density (RHO_B in g/cm^3) for reservoir units EOC-10, EOC-20, EOC-30 and EOC-3. The density decreases as porosity increases. This dependence is less evident in unit EOC-3.

Based on this exploratory data analysis, I conclude that P-wave impedance is insufficient either to estimate porosity or to discriminate shale from calcilithites in my field of study. For these reasons, poststack seismic inversion holds little value for reservoir porosity prediction in my area.

I therefore expand my analysis incorporating S-wave properties to better evaluate my reservoir. Figures 45 to 49 provide crossplots for EOC-10, EOC-20, EOC-30, EOC-50 and EOC-3 respectively. The left-hand crossplots are color-coded by total porosity and the right-hand ones are color-coded by clay volume. Note that clay-rich layers (indicated by red circles) tend to have high total porosity and low P-impedance, S-impedance, $\lambda\rho$ and $\mu\rho$ values. In contrast, the low total porosity clean facies are characterized by high P-impedance, S-impedance, $\lambda\rho$ and $\mu\rho$ values. Total porosity denotes the total pore space volume, including interconnected and isolated pores. Conventionally, clay-rich facies are considered to have high total porosity with isolated pores that result in low contribution to fluid flow. To exclude high porosity zones associated with clay-rich layers from high porosity zones associated with reservoir, it is necessary to identify facies with high clay content. For this reason, effective porosity, defined as interconnected pores that account for fluid flow, provides a most effective discrimination of reservoir. Figure 50 shows effective porosity discrimination for unit EOC-50. Both P-wave and S-wave properties are relative insensitive to water saturation.

The petrophysicist of the field has established minimum cut-off values of porosity $\Phi > 9\%$, water saturation $S_w > 60\%$ and clay volume $V_{clay} < 45\%$ for zones to be productive. Petrophysical properties used in this work were provided by PEMEX.

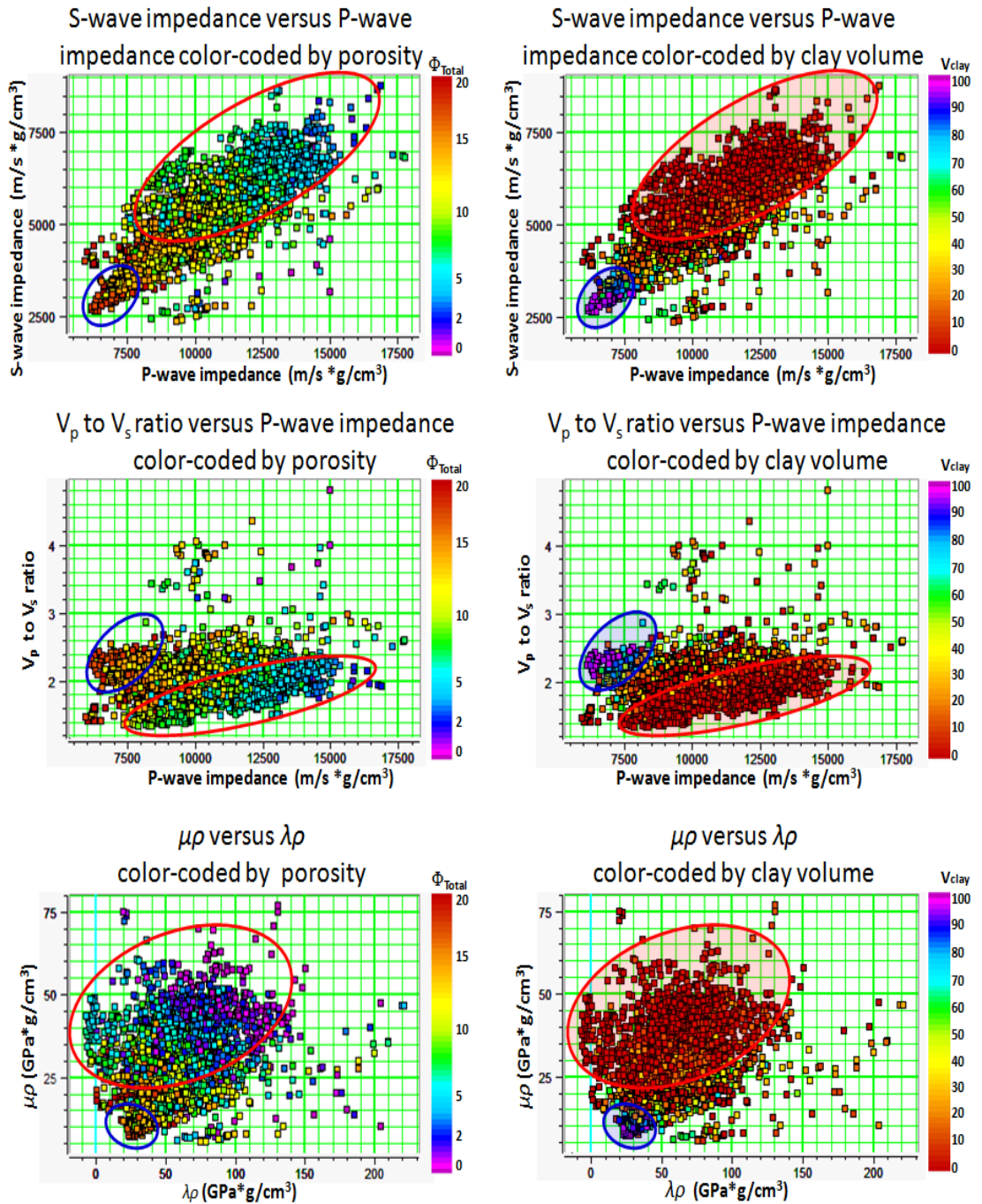


Figure 45. Total porosity and clay volume discrimination for reservoir unit EOC-10 through crossplots of S-impedance versus P-impedance, V_p to V_s ratio versus P-impedance and $\mu\rho$ versus $\lambda\rho$. The left-hand crossplots are color-coded by total porosity while the right-hand crossplots are color-coded by clay volume. Red circles indicate clean facies while blue circles indicate high clay content.

EOC-20

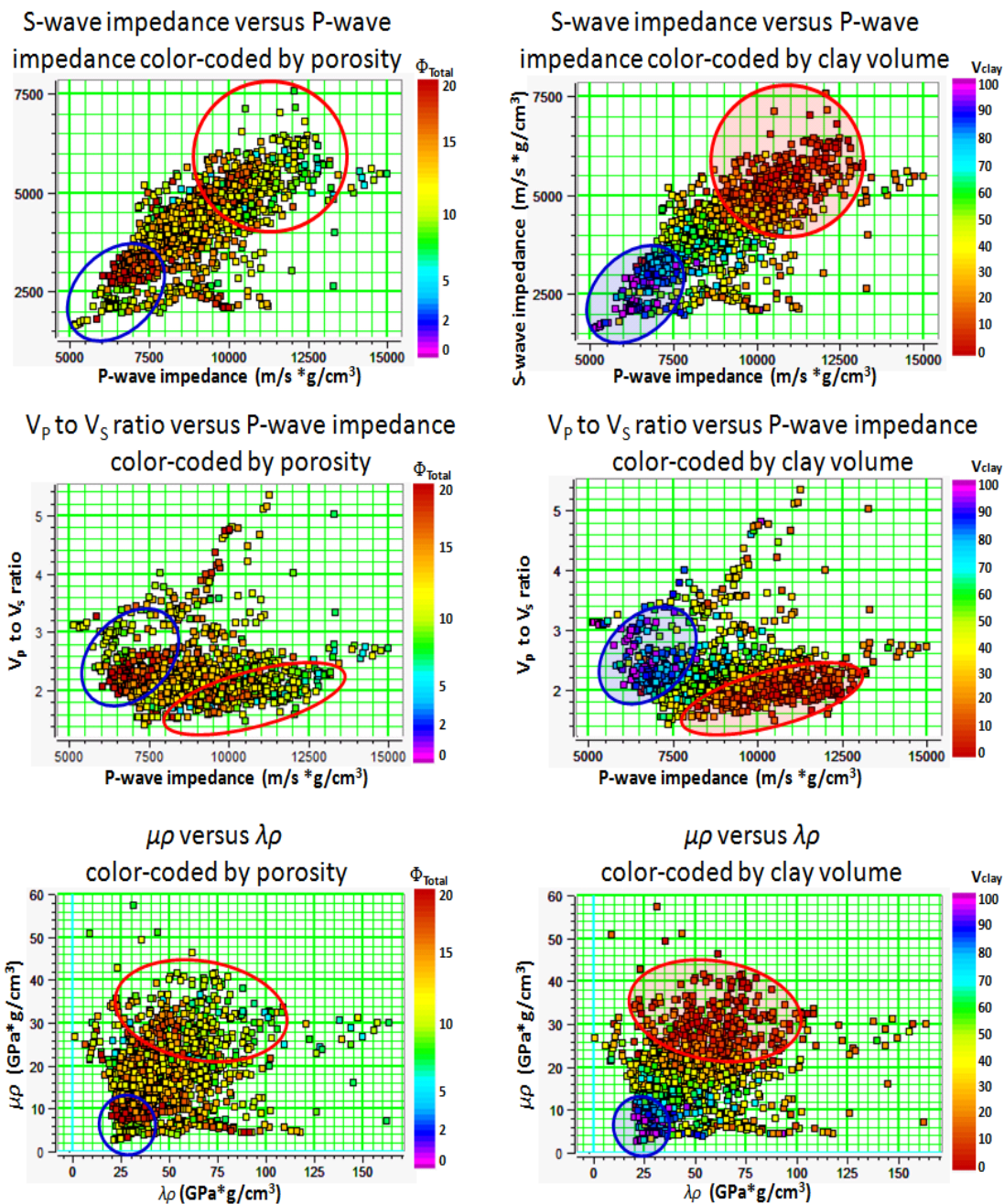


Figure 46. Total porosity and clay volume discrimination for reservoir unit EOC-20 through crossplots of S-impedance versus P-impedance, V_p to V_s ratio versus P-impedance and $\mu\rho$ versus $\lambda\rho$. The left-hand crossplots are color-coded by total porosity (Φ_{Total}) while the right-hand crossplots are color-coded by clay volume (V_{clay}). Red circles indicate clean facies while blue circles indicate high clay content.

EOC-30

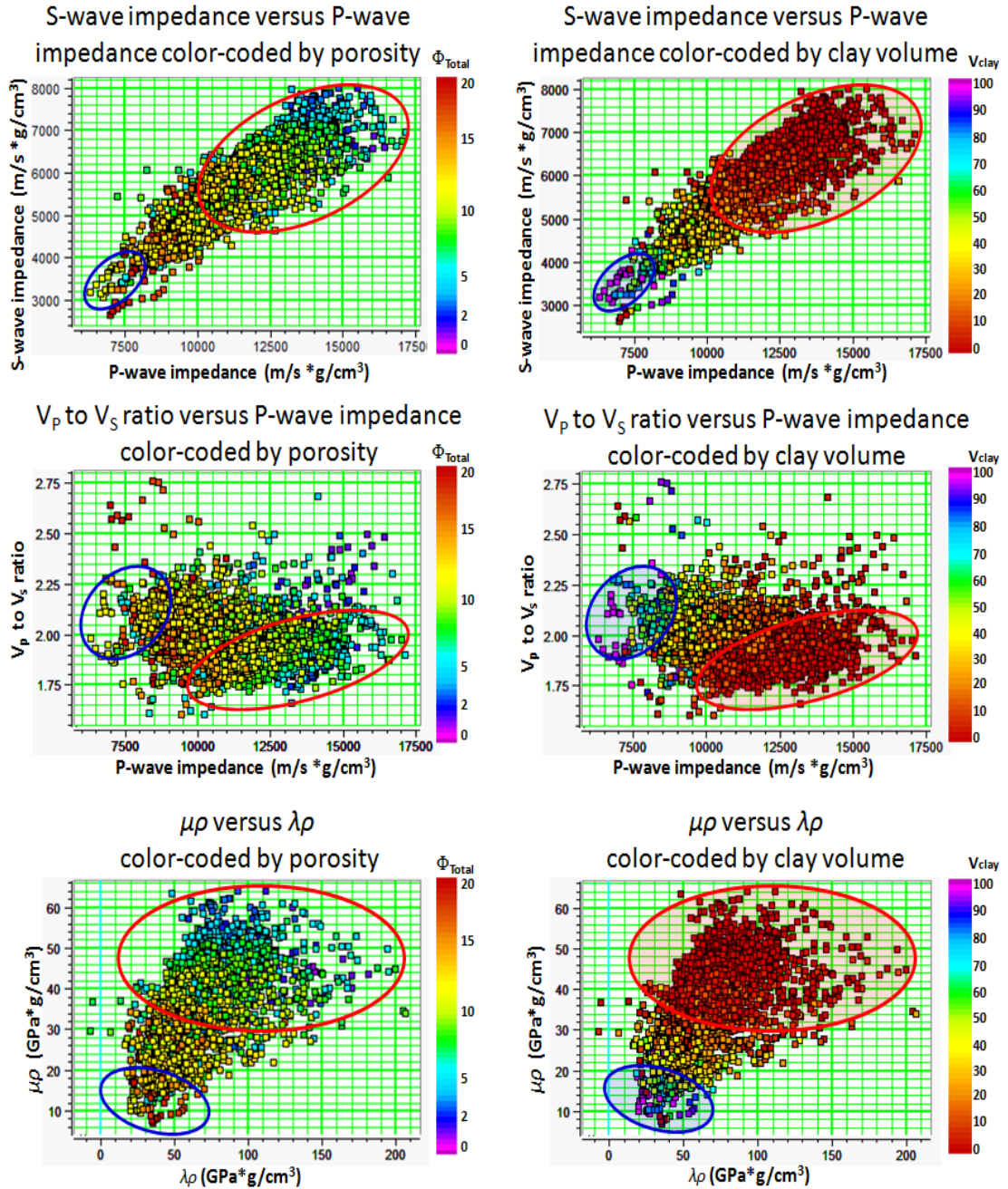


Figure 47. Total porosity and clay volume discrimination for reservoir unit EOC-30 through crossplots of S-impedance versus P-impedance, V_p to V_s ratio versus P-impedance and $\mu\rho$ versus $\lambda\rho$. The left-hand crossplots are color-coded by total porosity (Φ_{Total}) while the right-hand crossplots are color-coded by clay volume (V_{clay}). Red circles indicate clean facies while blue circles indicate high clay content.

EOC-50

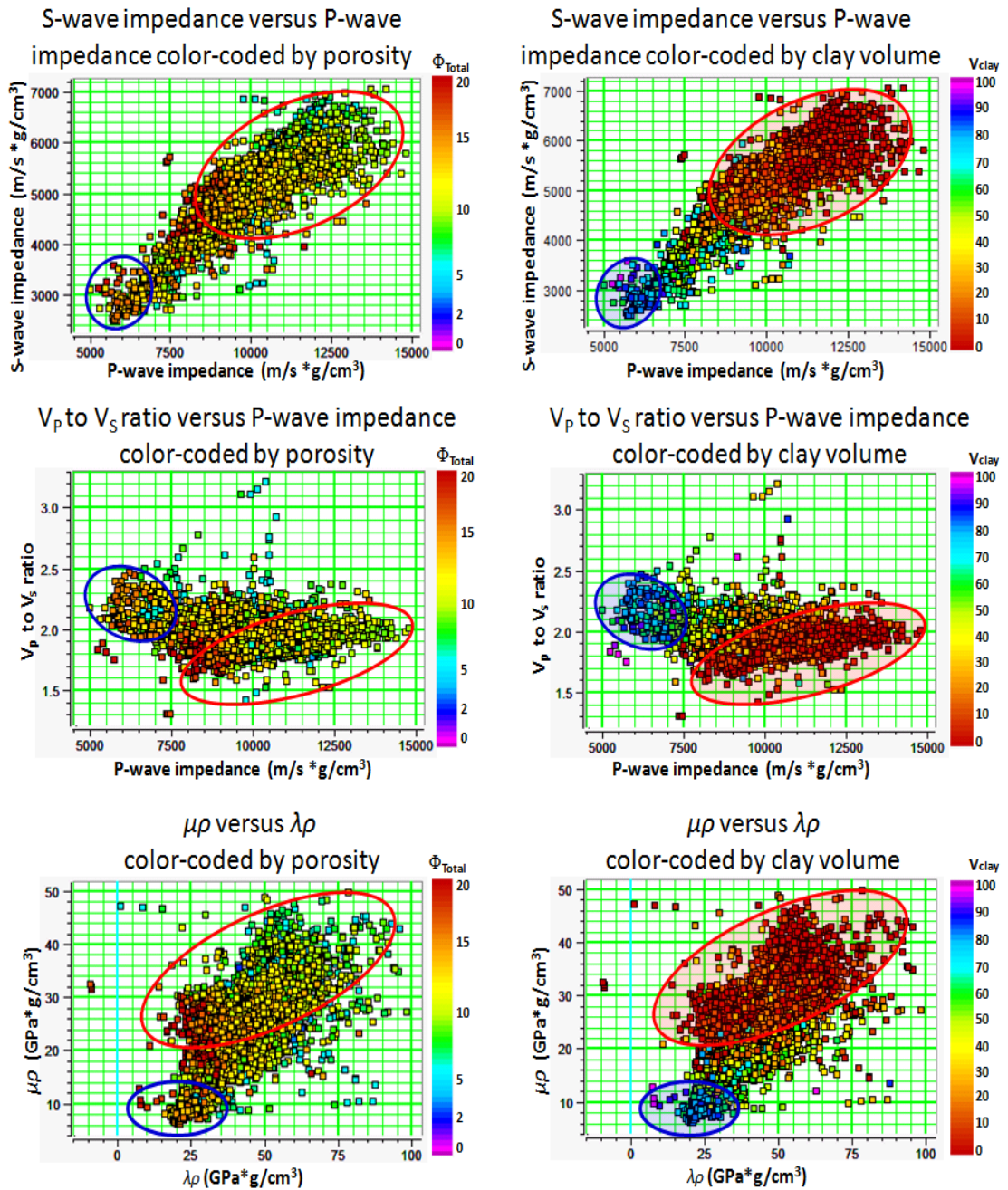


Figure 48. Total porosity and clay volume discrimination for reservoir unit EOC-50 through crossplots of S-impedance versus P-impedance, V_p to V_s ratio versus P-impedance and $\mu\rho$ versus $\lambda\rho$. The left-hand crossplots are color-coded by total porosity (Φ_{Total}) while the right-hand crossplots are color-coded by clay volume (V_{clay}). Red circles indicate clean facies while blue circles indicate high clay content.

EOC-3

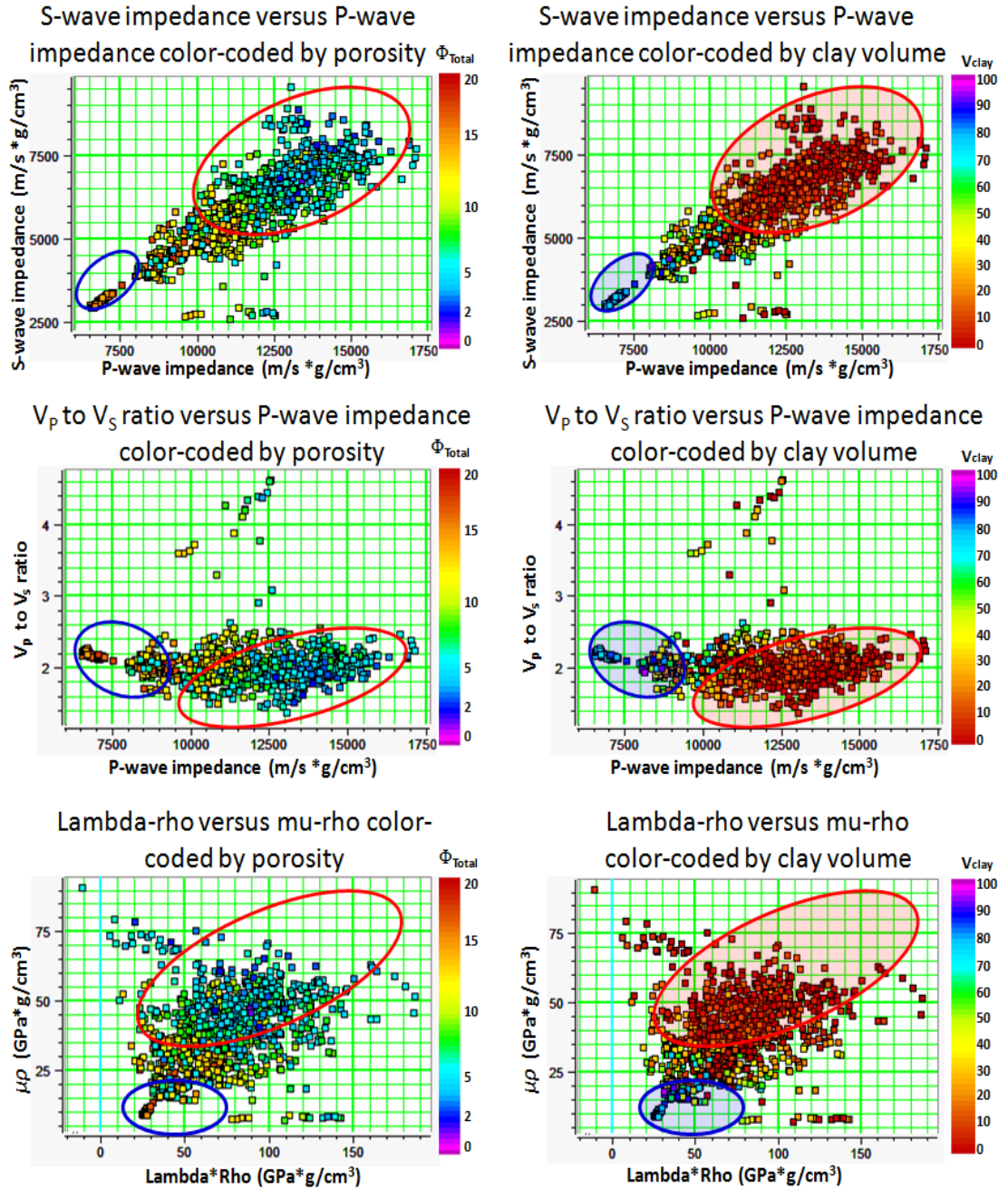


Figure 49. Total porosity and clay volume discrimination for reservoir unit EOC-3 through crossplots of S-impedance versus P-impedance, V_p to V_s ratio versus P-impedance and $\mu\rho$ versus $\lambda\rho$. The left-hand crossplots are color-coded by total porosity (Φ_{Total}) while the right-hand crossplots are color-coded by clay volume (V_{clay}). Red circles indicate clean facies while blue circles indicate high clay content.

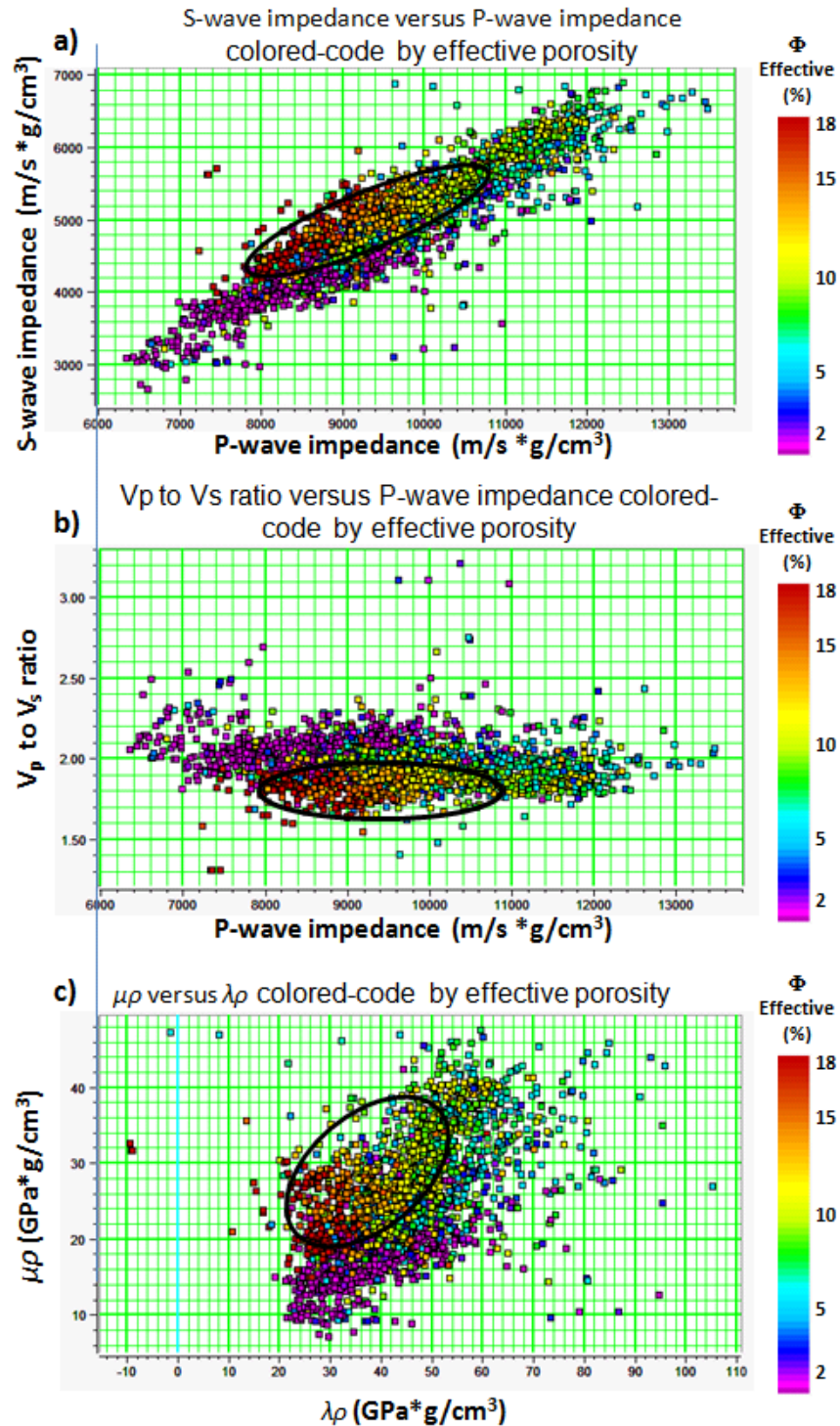


Figure 50. Effective porosity indicators for reservoir unit EOC-50. (a) S-impedance versus P-impedance, (b) V_P to V_S ratio versus P-impedance, and (c) $\mu\rho$ versus $\lambda\rho$, all color-coded by effective porosity (Φ). Red circles indicate high effective porosity associated with clean facies.

Prestack data conditioning, well to seismic tie and wavelet extraction

From exploratory data analysis of my well log measurements, I conclude that P-wave impedance is insufficient to discriminate porosity. Therefore, I run elastic inversion of prestack seismic gathers to predict reservoir heterogeneity following the flowchart shown in Figure 51, which is a simplification of the previous workflow shown in Figure 31.

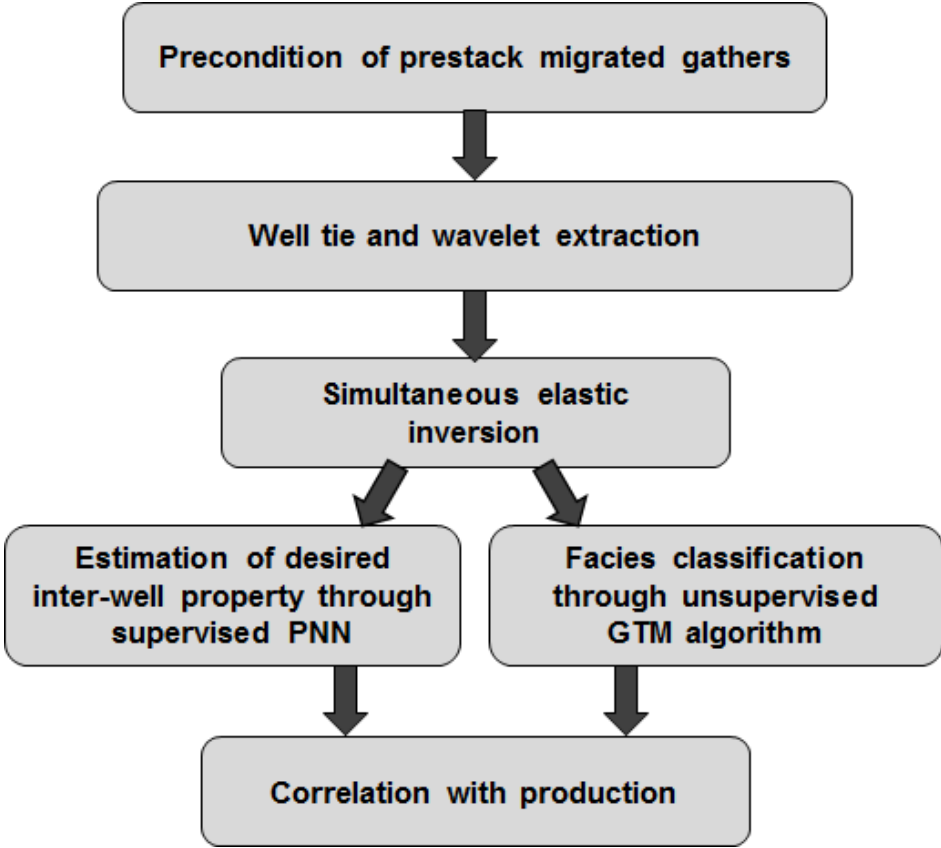


Figure 51. Simple workflow for estimation of rock quality using prestack seismic inversion.

The data available for seismic inversion consist of 10 km² of prestack time migrated common reflection point amplitude gathers after normal move-out (NMO) correction. The conditioning of seismic data for prestack seismic inversion has an

important influence on inverted results. Singleton (2011) states that conditioning workflows concentrate mainly on three aspects: gathers alignment, enhancement of signal to noise ratio, and recovery of frequency loss with distance (offset dependence). Singleton (2011) discusses the effects of data conditioning over inversion results. I concentrate in enhancement of signal to noise ratio and flattening of gathers. For that purpose, I conditioned the PSTM gathers for elastic seismic inversion using the flowchart shown in Figure 52.

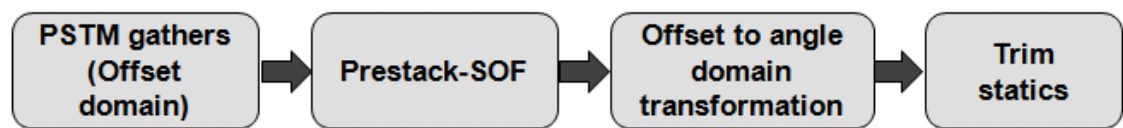


Figure 52. Workflow used for conditioning of prestack time migrated (PSTM) gathers for elastic seismic inversion.

First, I run two iterations of prestack-SOF using the workflow suggested by Davogustto et al. (2011) (Appendix C). SOF attenuates cross-cutting random and coherent noise while preserving amplitudes and enhancing signal to noise ratio (Zhang, 2010). Figure 53a shows the original CMP gathers; Figure 53b shows the CMP gathers, after two iterations of prestack-SOF; and Figure 53c shows the total rejected noise computed as the difference between unconditioned and SOF gathers.

After SOF, I convert the common reflection point gathers from offset to angle domain using the smoothed RMS migration velocity field. Finally, I applied trim statics to obtain flattened aligned gathers. Trim statics calculates an optimal shift by crosscorrelating a reference stacked volume with the gather traces to correct for miss alignment in time or residual moveout. I stack the prestack-SOF gathers to use that volume as my reference and I use a 350 ms window length from the main unconformity,

which separates the Miocene shale from the Eocene calcilithites for trim statics. Figure 54 shows the angle gathers before and after applying trim statics. Figure 55 shows the three amplitude spectra of the original amplitude stacked gathers, stacked gathers after prestack-SOF and the spectrum of the final stack of conditioned gathers after prestack SOF and trim statics from the zone of interest between 2000 and 2500 ms. Note the increase in high frequencies in the spectrum after prestack-SOF.

I extracted statistical wavelets for three angle ranges, from 0 to 15 (near angles), from 13 to 28 (middle angles) and from 26 to 40 degrees (far angles) in the zone of interest, 100 ms above the main unconformity and 150 ms below the lower boundary for inversion (Figure 56). I use these wavelets in well to seismic tie and simultaneous inversion.

I tie all available wells to the conditioned seismic data prior to model-based seismic inversion. The crosscorrelation coefficients range from 0.62 to 0.96. Most of the wells are deviated with an inclination angle ranging from 18° to 75°. The majority range between 35° to 45° deviation with displacements ranging from 800 to 2500 m from the surface location. Figure 57 shows the well to seismic tie of a representative well in the crest of the structure which contains reservoir units EOC-10, EOC-20 and the water-bearing unit EOC-40. Figure 58 illustrates the well to seismic tie for a representative well in the eastern flank of the field structure containing reservoir units EOC-30 and EOC-50. Note that the main unconformity that separates the Miocene shale from the Eocene calcilithites, as well as the top of each reservoir unit correlates with relatively high amplitude peak seismic response due to the contrast between the low impedance shale and the high impedance calcilithites.

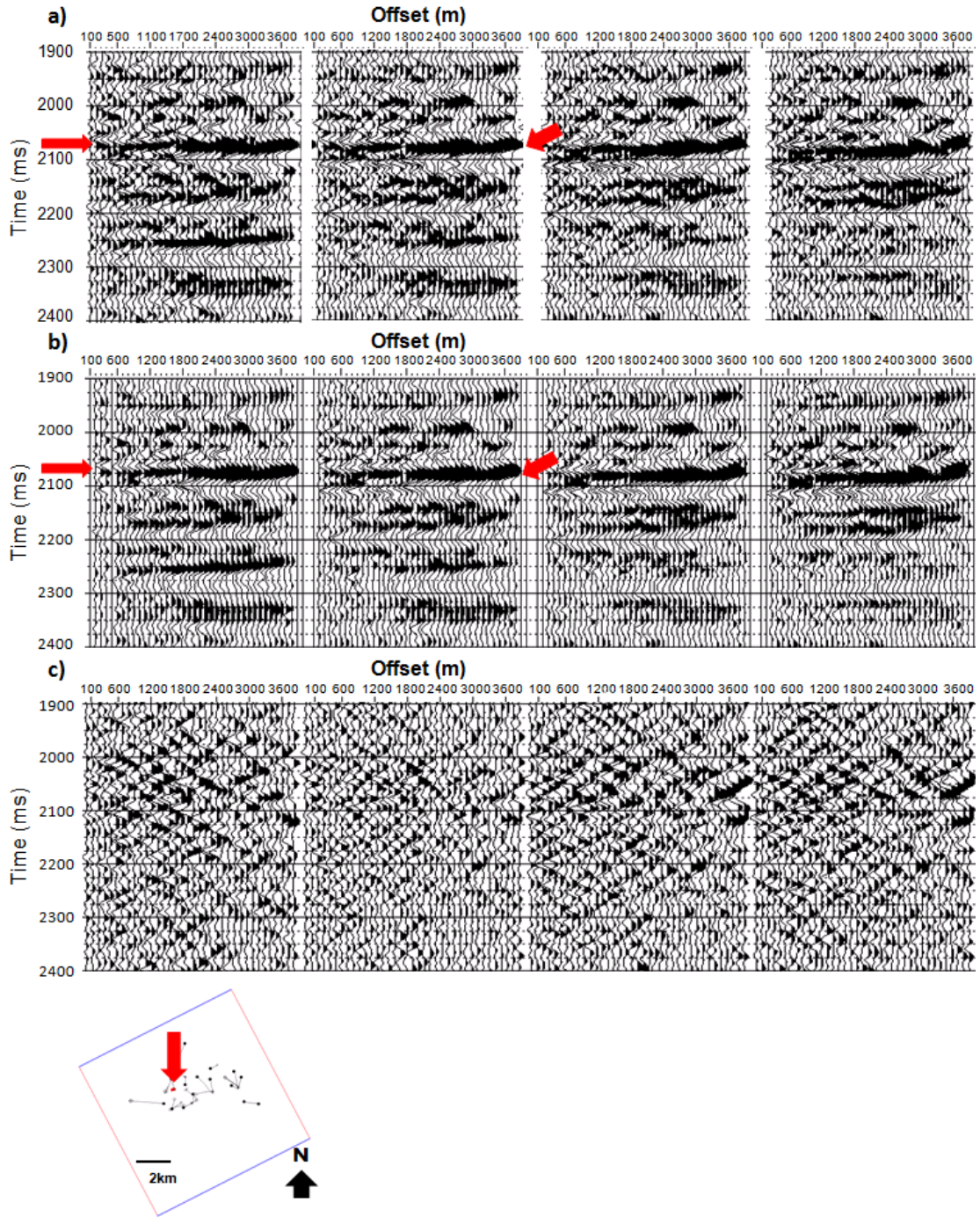


Figure 53. Offset PSTM gathers: (a) Unconditioned gathers, (b) gathers after two iterations of prestack-SOF, (c) rejected noise computed as the difference between (a) and (b). Red arrows indicate the horizon that correlates with the main unconformity. The red arrow in the map indicates the position of the shown gathers.

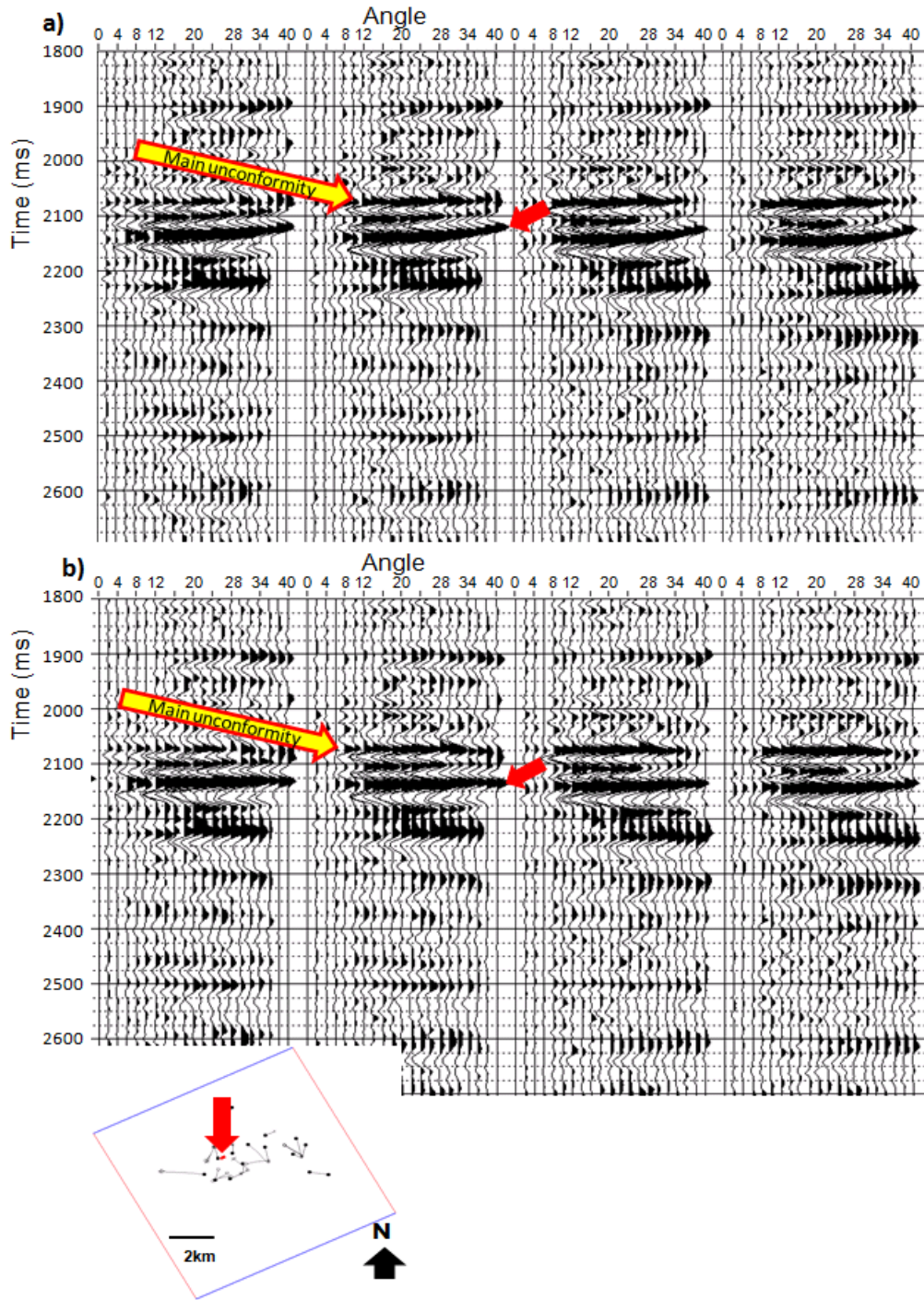


Figure 54. Gathers in angle domain. (a) Angle gathers obtained from offset gathers after prestack-SOF. (b) Gathers in angle domain after trim statics processing. Note that reflectors have been flattened after trim statics. Red arrow indicates a reflector that exhibits a significant shift before and after trim statics. The red arrow in the map indicates the position of the shown gathers.

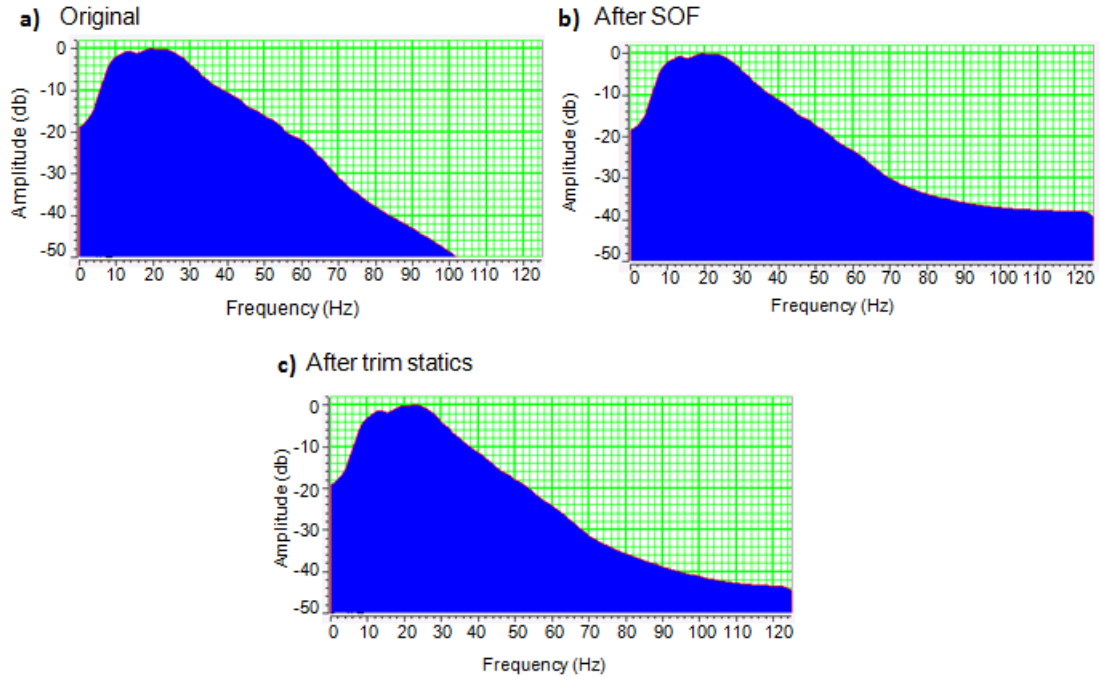


Figure 55. Amplitude spectra after stacking of (a) original PSTM gathers, (b) gathers after prestack-SOF and (c) final conditioned gathers after prestack SOF and trim statics. Note the increase in high frequencies with respect to the original stack.

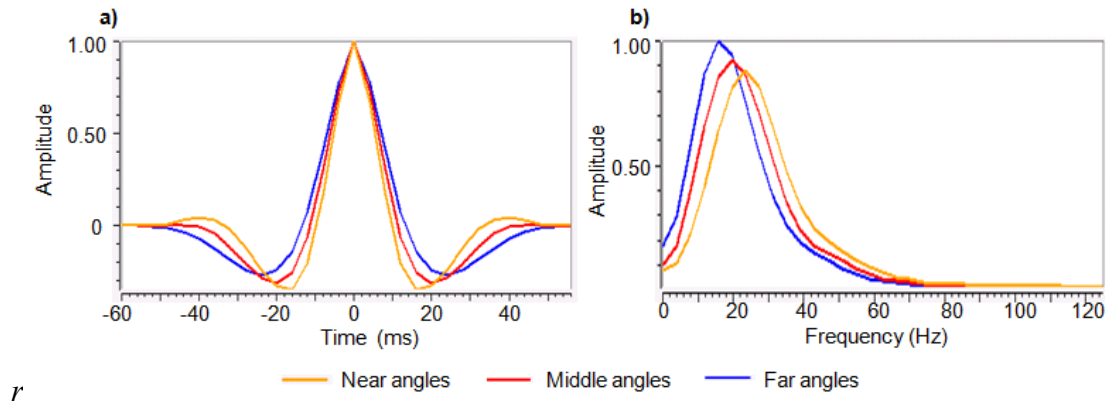


Figure 56. (a) Phase spectrum and (b) amplitude spectrum of the three seismic wavelets extracted over conditioned gathers for near, middle and far angles. Note the near angles have higher frequencies than far angles because of migration stretch.

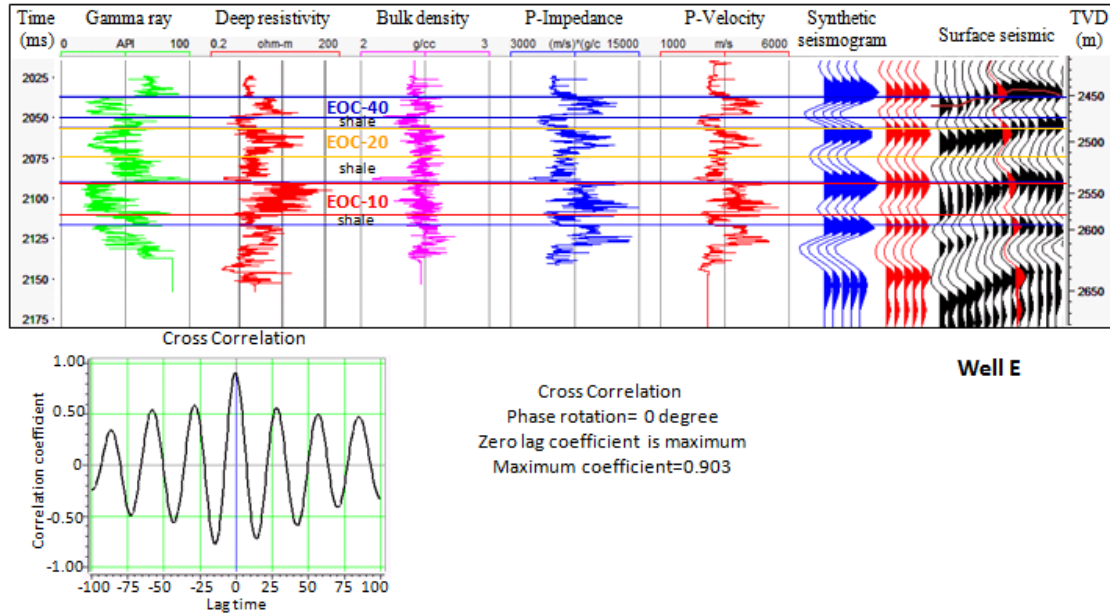


Figure 57. Well to seismic tie in a representative well for reservoir units EOC-20, EOC-10, and EOC-40. The crosscorrelation coefficient is 0.9.

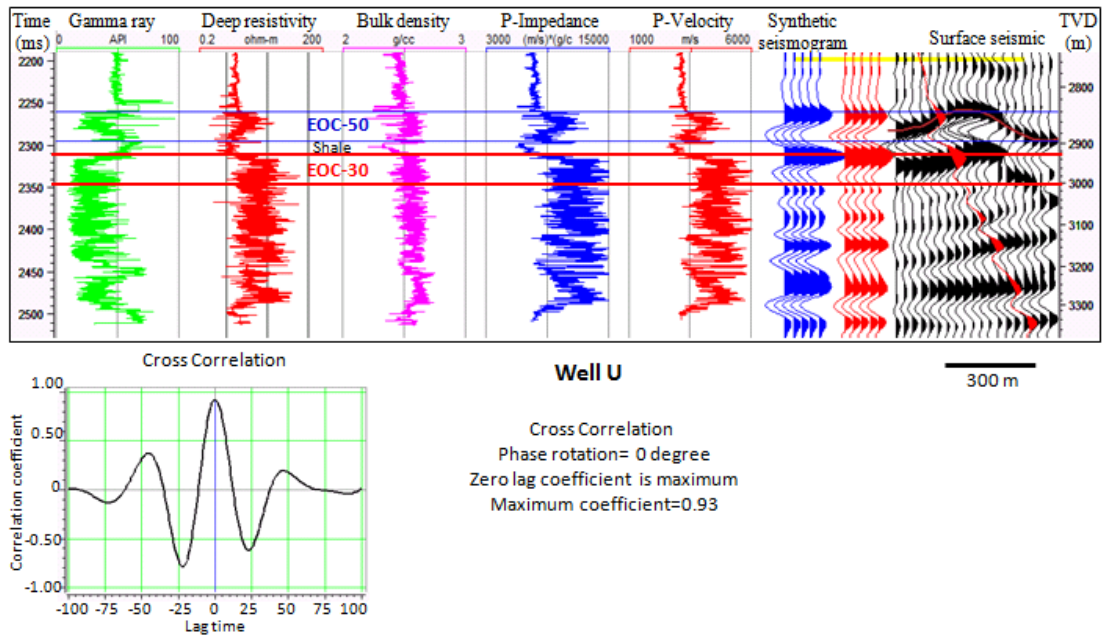


Figure 58. Well to seismic tie of a representative well of the eastern flank of the anticline containing the units EOC-50 and EOC-30. The crosscorrelation coefficient is 0.93.

Seismic inversion for reservoir properties

I computed \ model-based simultaneous seismic inversion of the preconditioned PSTM amplitude gathers from which I obtained P-wave impedance (Z_P), S-wave impedance (Z_S), and V_P to V_S ratio (V_P/V_S) volumes. Details of prestack simultaneous inversion can be found in Hampson and Russell, (2005).

In principle, the low frequency content is absent in amplitude seismic data (Russell and Hampson, 2006) and needs to be incorporated to the seismic inversion process from well logs to obtain absolute rather than relative inverted property values (Barclay et al., 2008; Latimer et al., 2000). I therefore built an initial low frequency model (Figure 59) from high-cut frequency filtered impedances and densities from 16 wells and three interpreted seismic horizons. The upper horizon correlates with the main unconformity that separates Miocene shale from Eocene calcilithites, and constitutes the upper boundary of the model and the inversion window; the intermediate horizon is a sequence boundary that separates Upper Eocene from Middle Eocene, EOC-50 from EOC-30 in the eastern flank; and the lower horizon correlates with the base of EOC-3 in the crest of the anticline. I did not add other interbedded reservoir horizons to constrain the initial model, since there is large uncertainty in the correlation from one fault block to another, in addition to their not being distributed over the whole area. In case of exploration areas where well data is scarce or absent, the low frequency component could be obtain from migration or processing velocities and regional gradients (Barclay et al., 2008).

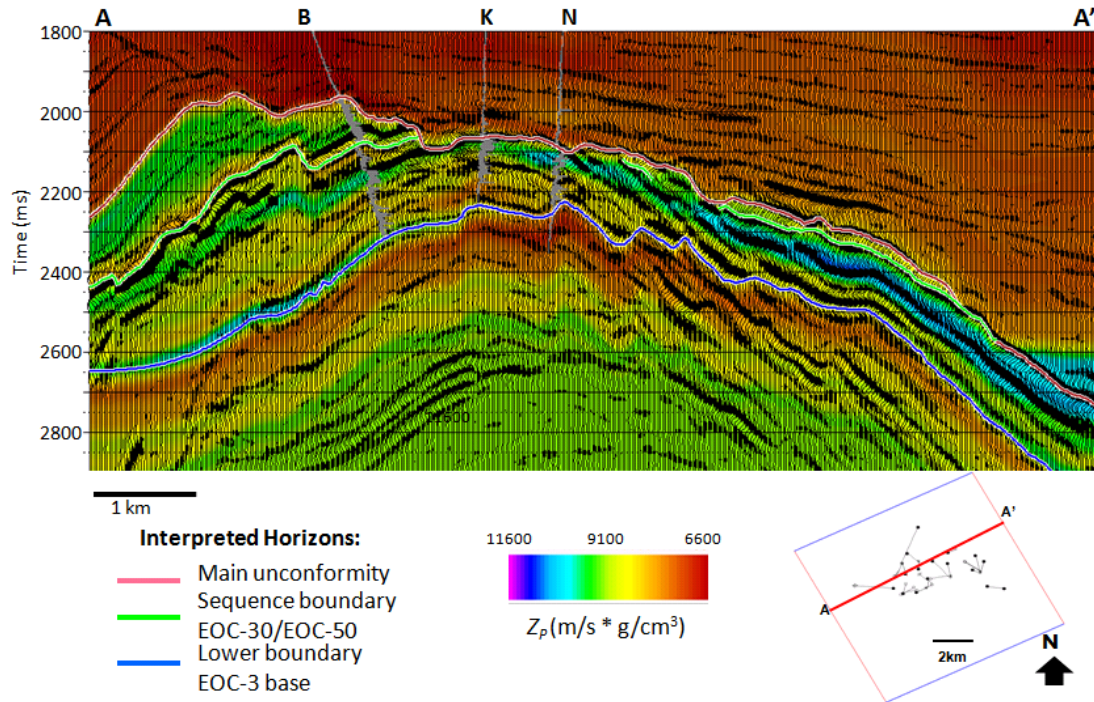


Figure 59. Initial low frequency model for prestack simultaneous inversion overlapping traces of stacked conditioned gathers. The target window is defined by the main unconformity (pink horizon) and the deeper blue horizon which correlates with the base of unit EOC-3. The intermediate green horizon correlates with a sequence boundary that separates EOC-50 from EOC-30.

I validate the simultaneous inversion using well R as a blind well. Figure 60 exhibits the inverted results for the blind well. The first three left panels compare inverted impedance and density with the measured and modeled logs for the target window. The far right panels compare the synthetic with the original gather and show the residual between them. As part of quality control, Figure 61 show crossplots of impedance obtained from seismic inversion versus calculated from wells. Figure 62 show the crosscorrelation coefficient for each well. Note the good correlation in Figure 63 between impedance obtained from well log and inverted impedance from inversion for well U, a well in the eastern flank of the field structure.

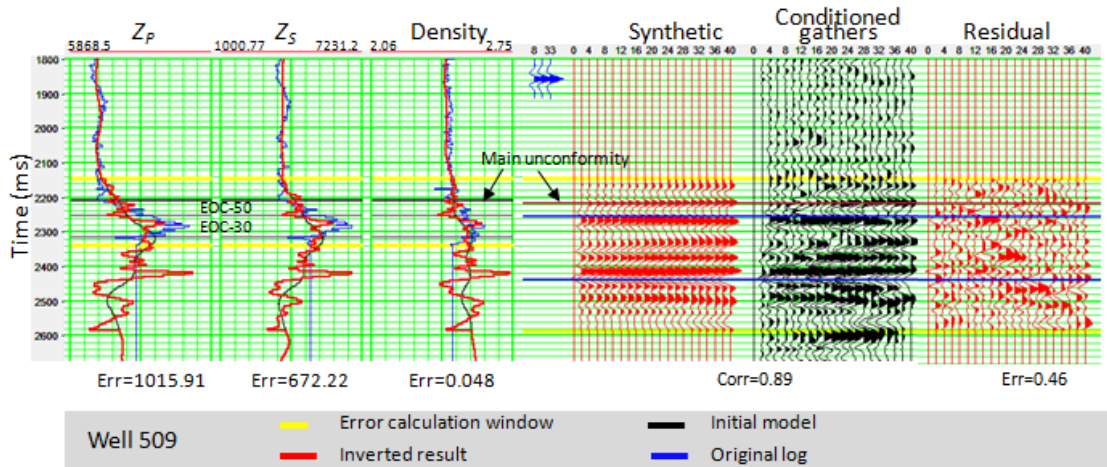


Figure 60. Validation analysis of simultaneous inversion for the blind well R. The first three left-hand panes compare inverted with original and modeled impedance and density logs. The other three right-hand panes compare synthetic with original and the residual computed as the difference between them.

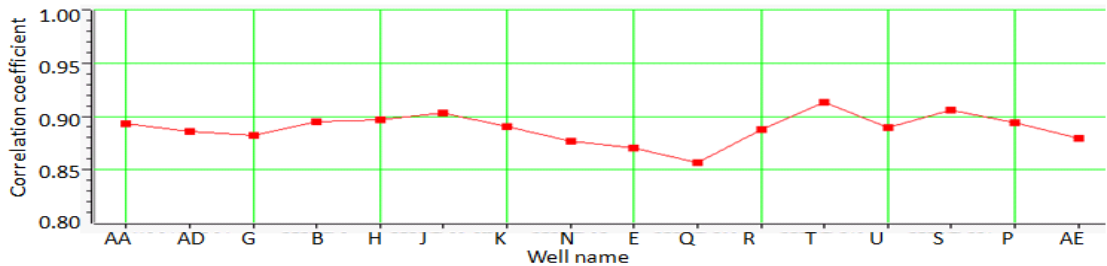


Figure 61. Crosscorrelation coefficient of properties resulted from inversion.

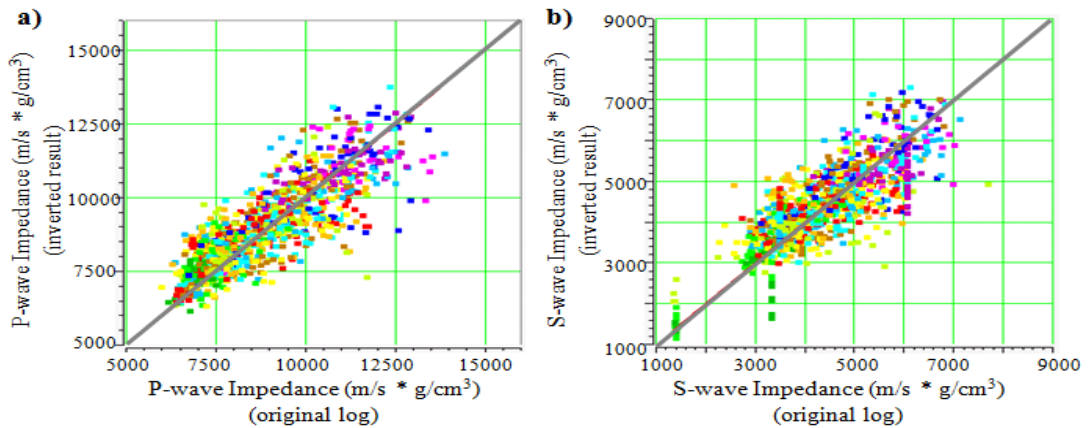


Figure 62. Inverted results versus original well logs. (a) P-impedance, (b) S-impedance. Gray lines indicated correlation of 1.0.

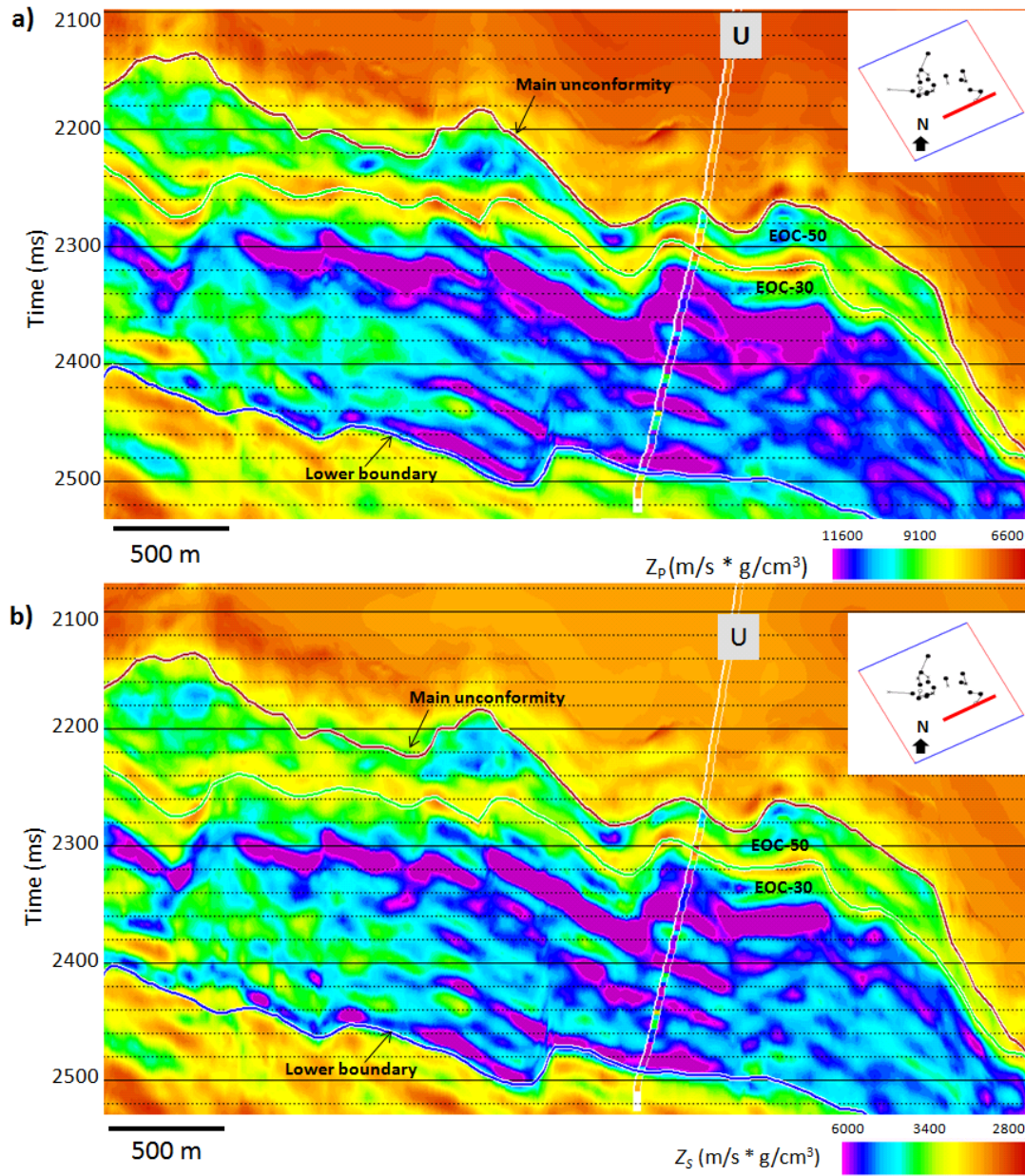


Figure 63. Vertical slices through (a) P -wave impedance and (b) S-wave impedance resulting from model-based simultaneous inversion. The position of the vertical section is indicated by the red line in the map. The impedance calculated from well logs is represented by the inserted colored bar at well position.

Once the inversion results were validated for all wells, I use my inverted impedance volumes to calculate volumetric values of $\lambda\rho$ and $\mu\rho$. Then, I used Z_P , Z_S ,

V_P/V_S , $\lambda\rho$ and $\mu\rho$ volumes as part of inputs to a supervised probabilistic neural network (PNN) to predict clay and porosity volumes, and generative topographic mapping (GTM), an unsupervised clustering algorithm, for facies classification. Figure 64 shows the PNN workflow for reservoir property volume estimation.

I initially include poststack seismic attributes such coherent energy, sensitive to changes in textural uniformity (Chopra and Marfurt, 2007b), and spectral magnitude components every 10 Hz from 8 to 88 Hz, sensitive to thin-bed tuning and stratigraphy. In addition, I include inverted prestack seismic attributes of Z_P , Z_S , V_P/V_S , $\lambda\rho$ and $\mu\rho$, sensitive to lithology and reservoir quality. First, I extract all attribute values at well position. Then, I used multilinear stepwise regression to calculate the optimum operator length and to choose which of the input attributes provide the major correlation and minor validation error with the target log. See Verma et al. (2012) for details. I excluded non-fit wells in this analysis. Next, I train my probabilistic neural network (PNN) with the operator length and attributes selected and I validate the trained PNN in wells not used in training. Finally, I apply the trained and validated PNN to calculate my target log as a 3D property.

Exploratory data analysis showed that in my area, clay-rich facies have the same high total porosity values as calcilithites zones. In contrast, the effective porosity is close to zero for clay-rich facies (Figure 65). For this reason, I first calculate the clay content, V_{clay} , to estimate effective porosity, such that high porosity values correlate with the better reservoir quality within calcilithites facies, excluding high porosity predictions associated with the shale zones.

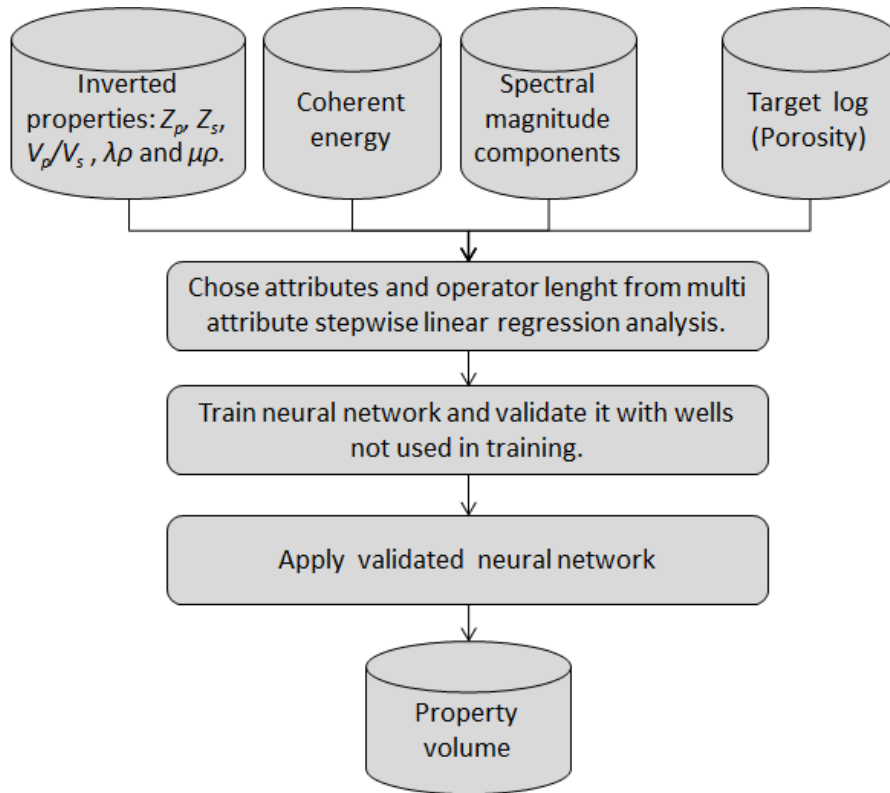


Figure 64 Supervised probabilistic neural network workflow for rock property estimation. (Modified from Verma et al., 2012).

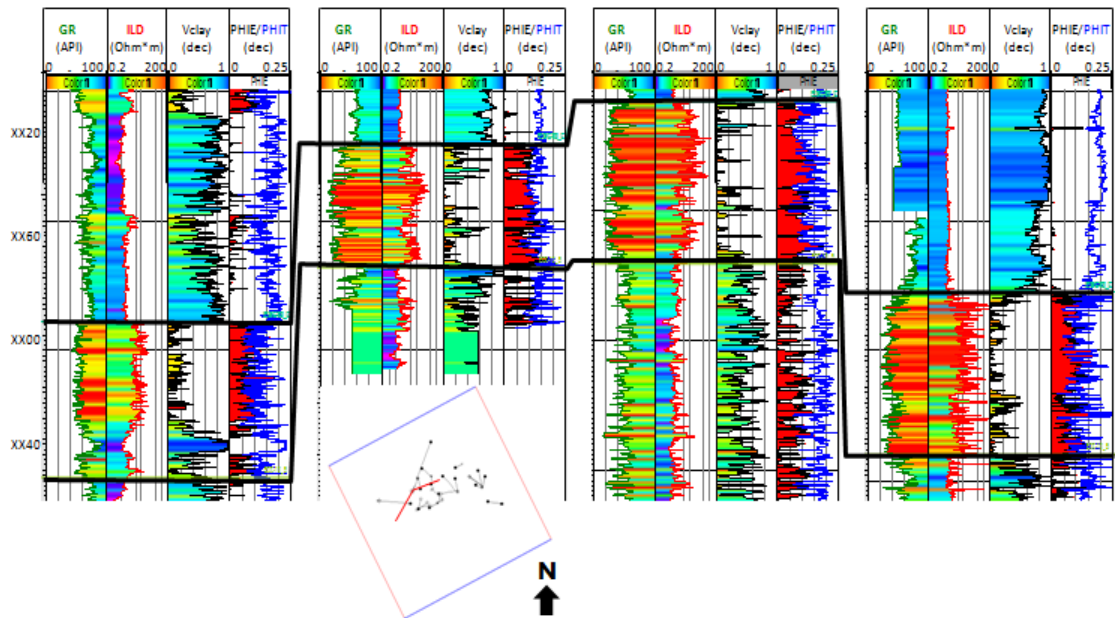


Figure 65. Structural cross section of wells B, K, L and N, productive in EOC-10. Top and base of reservoir unit EOC-10 is indicated by black lines.

For clay volume estimation, I used multilinear stepwise regression analysis to select four attributes: $1/Z_P$, $(\lambda\rho)^2$, $1/\mu\rho$, and coherent energy, which are then nonlinearly combined with an operator length of 5 ms to train my probabilistic neural network (PNN). The training error of the PNN was 0.12, with a validation error of 0.14. Clay content is expressed in decimals, where 0.0 indicates clean facies (0% clay) and 1.0 represents the dirtiest facies (100% clay). The correlation was 0.87. Figure 66 illustrates a horizons slice, 10 ms below top of EOC-10, through the Z_P , $\lambda\rho$, $\mu\rho$, and coherent energy, which were input volumes to the PNN clay volume prediction. Note that high coherent energy areas correlate with relatively high $\mu\rho$ and $\lambda\rho$. Figure 67 shows the training and validations results of PNN applied in well data and the crossplot of estimated versus original clay volume. Figure 68 exhibits a clay volume cross section through wells R, Q, AD and U. Note the good correlation between clay volume calculated from well logs and clay volume predicted by PNN.

To calculate the effective porosity I used the same workflow, incorporating the estimated clay volume as a fixed input attribute in the multilinear regression analysis. I trained and validate my PNN using an operator length of 6ms and the following four attributes: the square root of $\lambda\rho$, V_{clay} , the square root of the spectral magnitude component at 84 Hz and coherent energy. Z_P and Z_S attributes are implicit in $\lambda\rho$. My training error was 0.03 and my validation error was 0.027 with a correlation of 0.7. Figure 69 exhibits a phantom horizon 10 ms below the top of EOC-30, through the $\lambda\rho$, V_{clay} , spectral magnitude component at 84 Hz and coherent energy. Note that clean facies, indicated by warm colors in volume clay, correlates with high coherent energy and high $\lambda\rho$. Figure 70 shows the training and validations results of PNN applied in well

data, and the crossplot of estimated versus original porosity. Figure 71 is an effective porosity cross section through wells R, Q, AD and U. The inserted colored column at well position corresponds to the values from the logs.

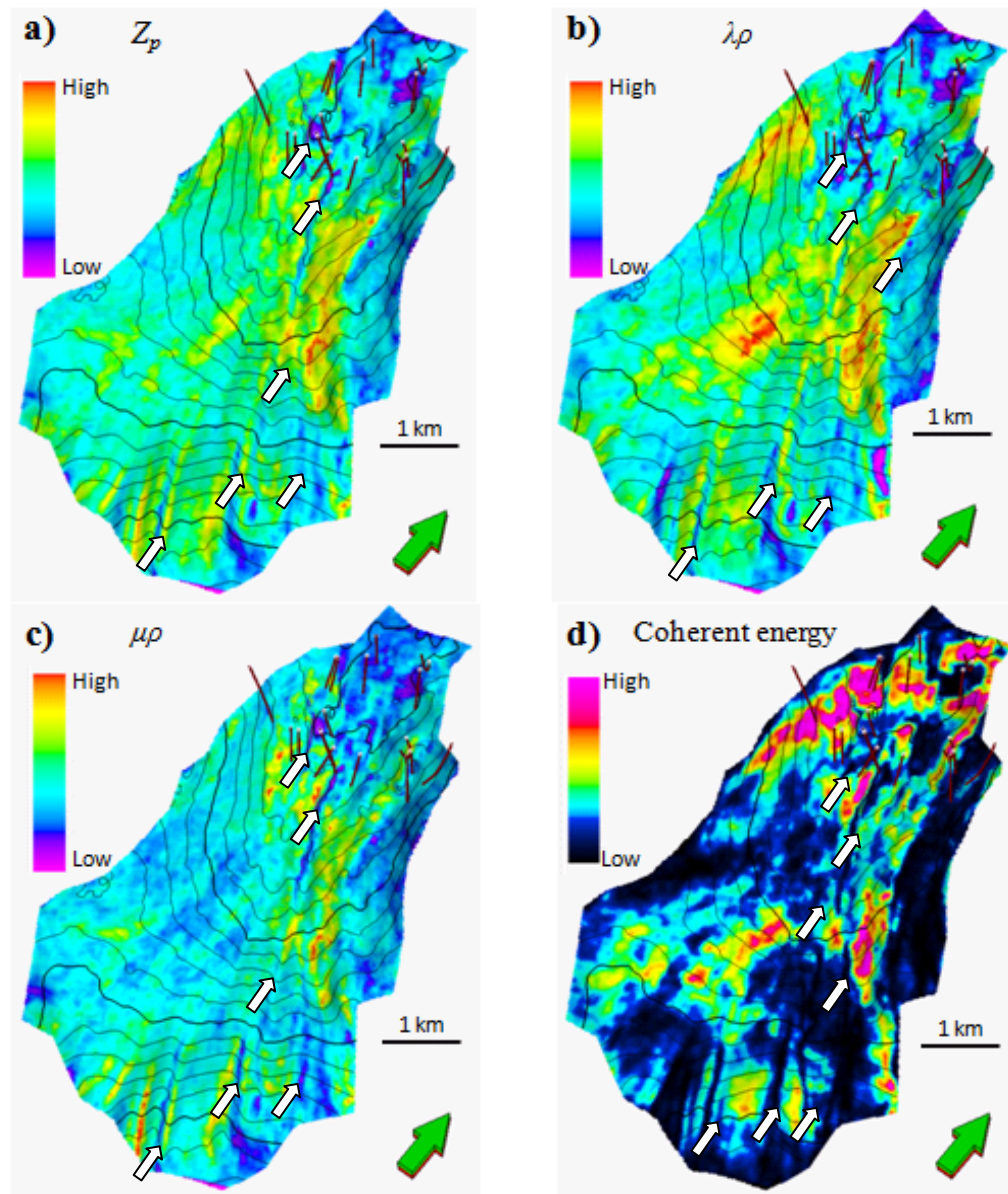
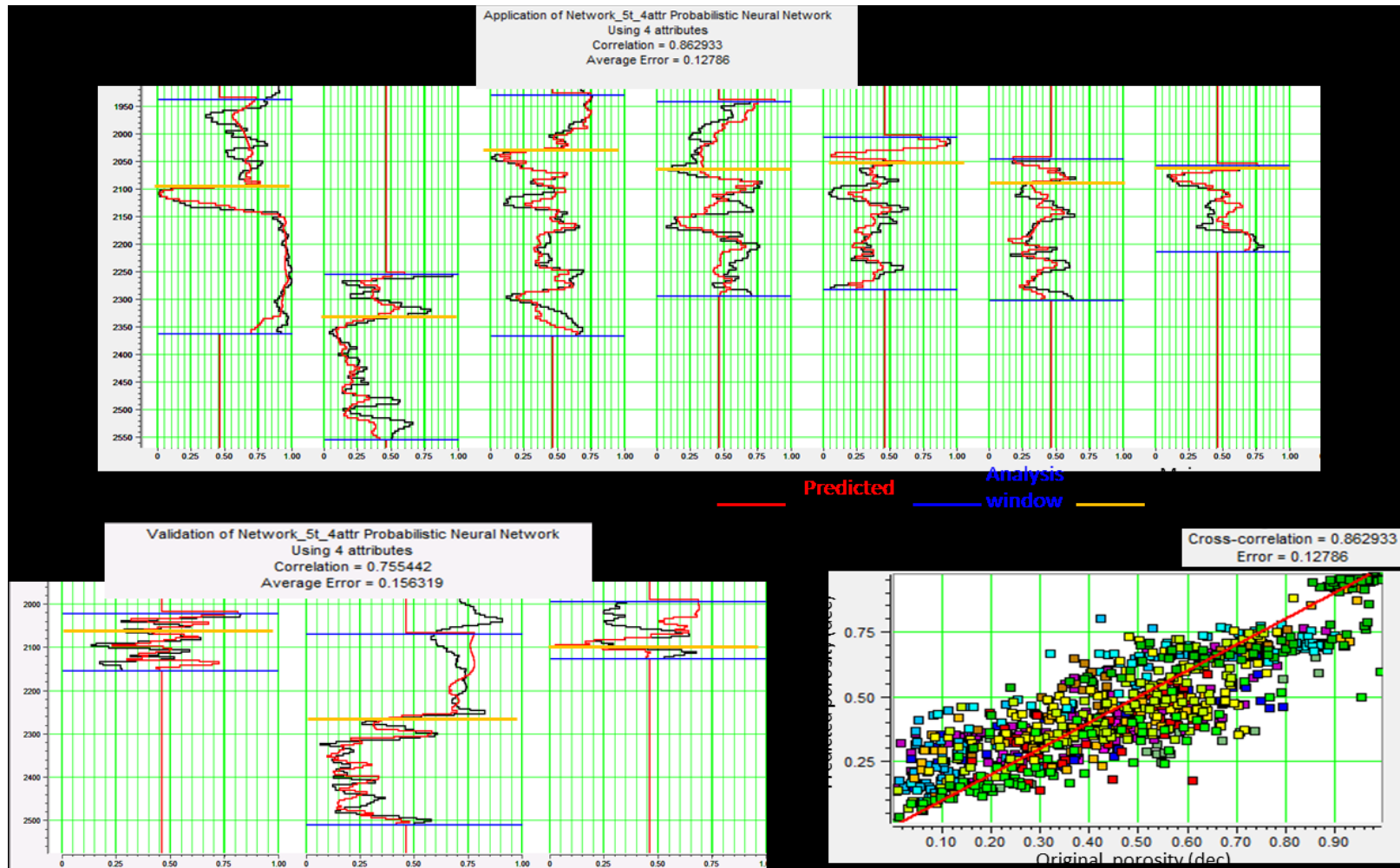


Figure 66. Horizons slices through (a) P-impedance, (b) $\lambda\rho$, (c) $\mu\rho$, and (d) coherent energy 10 ms below the top of EOC-10. Note that high coherent energy areas correlate with relatively high $\mu\rho$ and $\lambda\rho$. Correlation with Z_p is ambiguous. Elongated lineaments in all attributes correspond to normal faults indicated by white arrows.



93

Figure 67. a) Training and (b) validation of neural networks to estimate clay volume. The error is 0.027 with a correlation of 0.61 after validation. (c) crossplot of predicted porosity versus actual porosity at well position. The red line indicates correlation of 1.0.

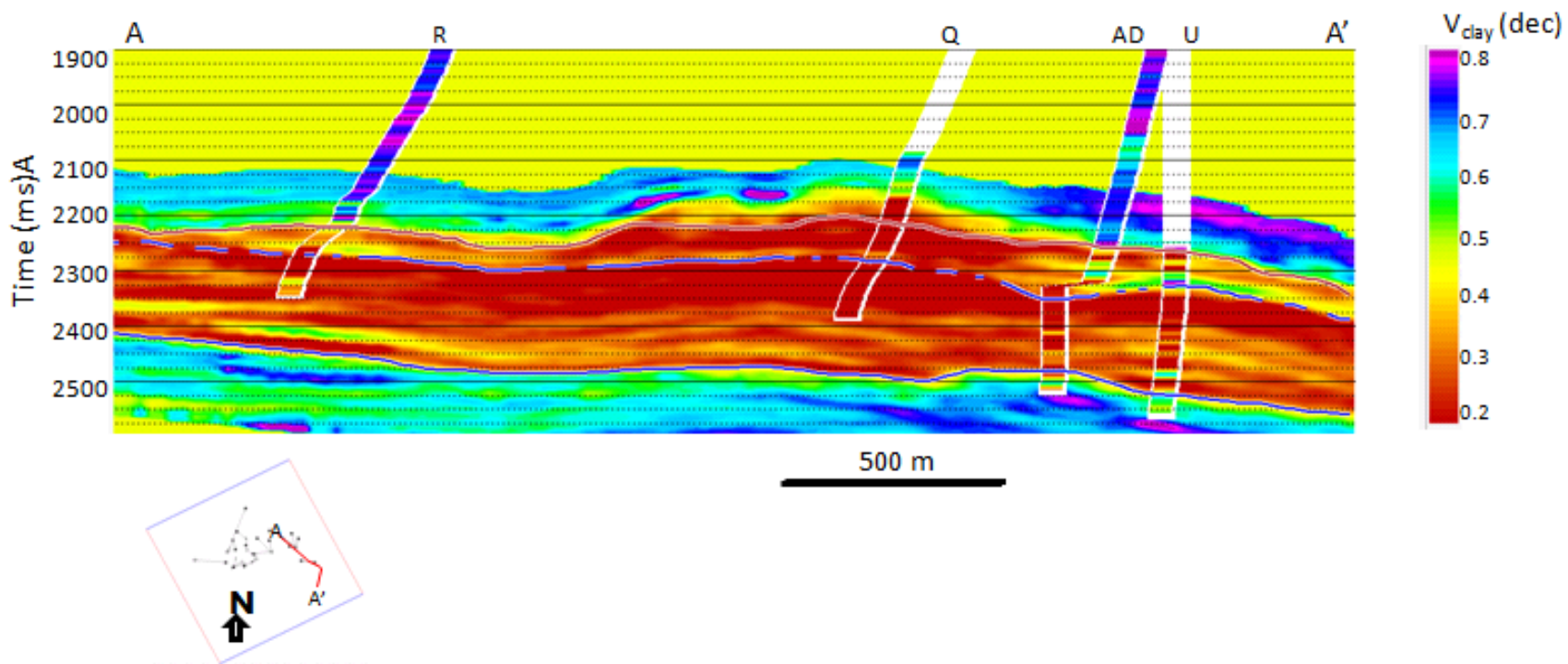


Figure 68. Clay volume over cross section through wells R, Q, AD, and U. Line location is indicated in the inserted map

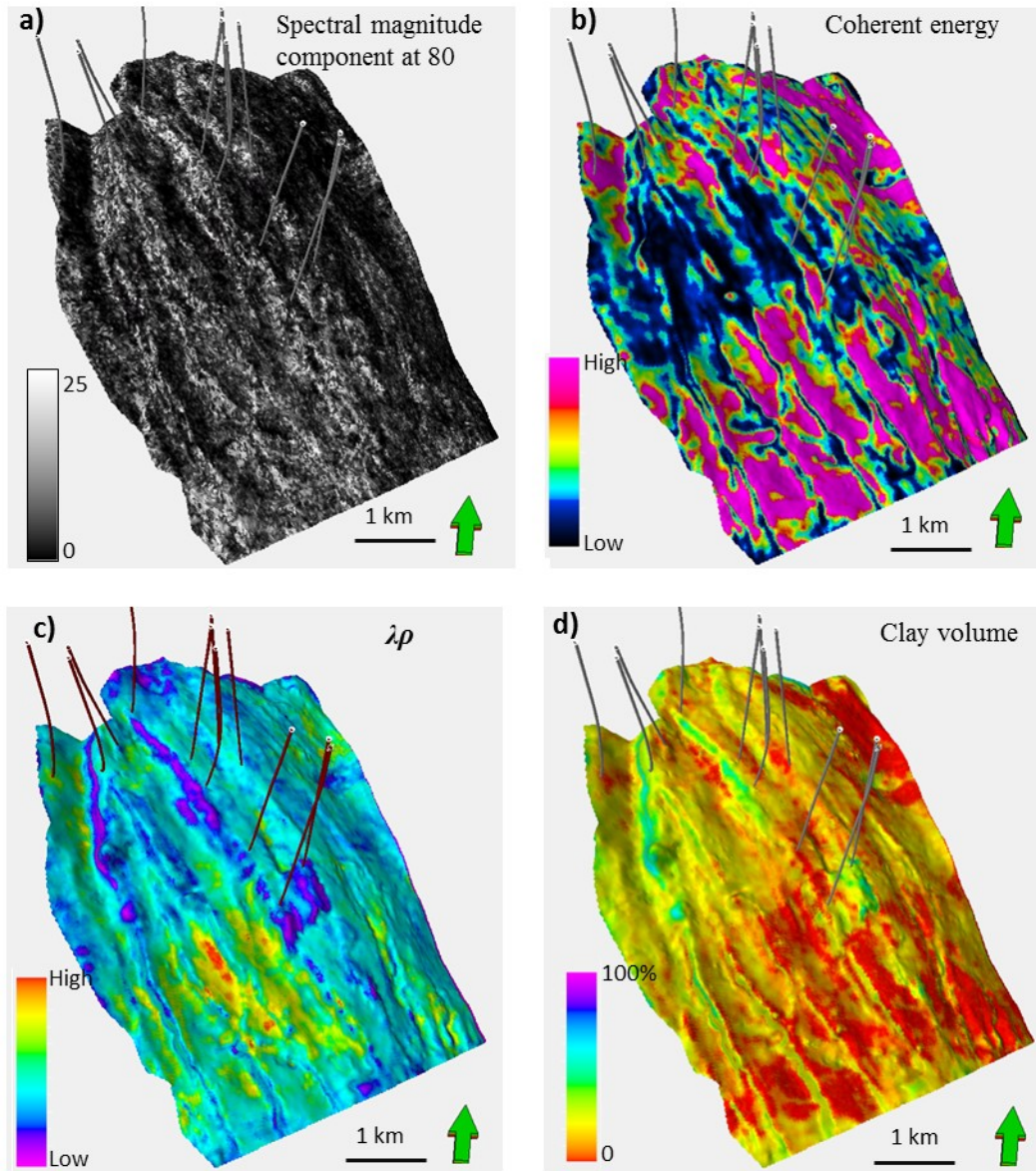


Figure 69. Horizons slices through (a) spectral magnitude component at 84Hz, (b) coherent energy, (c) inverted $\lambda\rho$ and (d) clay volume calculated with PNN. Note that high coherent energy areas correlate with low clay volume and relatively high $\lambda\rho$. Linear patterns oriented NE-SW correspond to normal faults. Those present low coherent energy which resulted in low clay volume estimation.

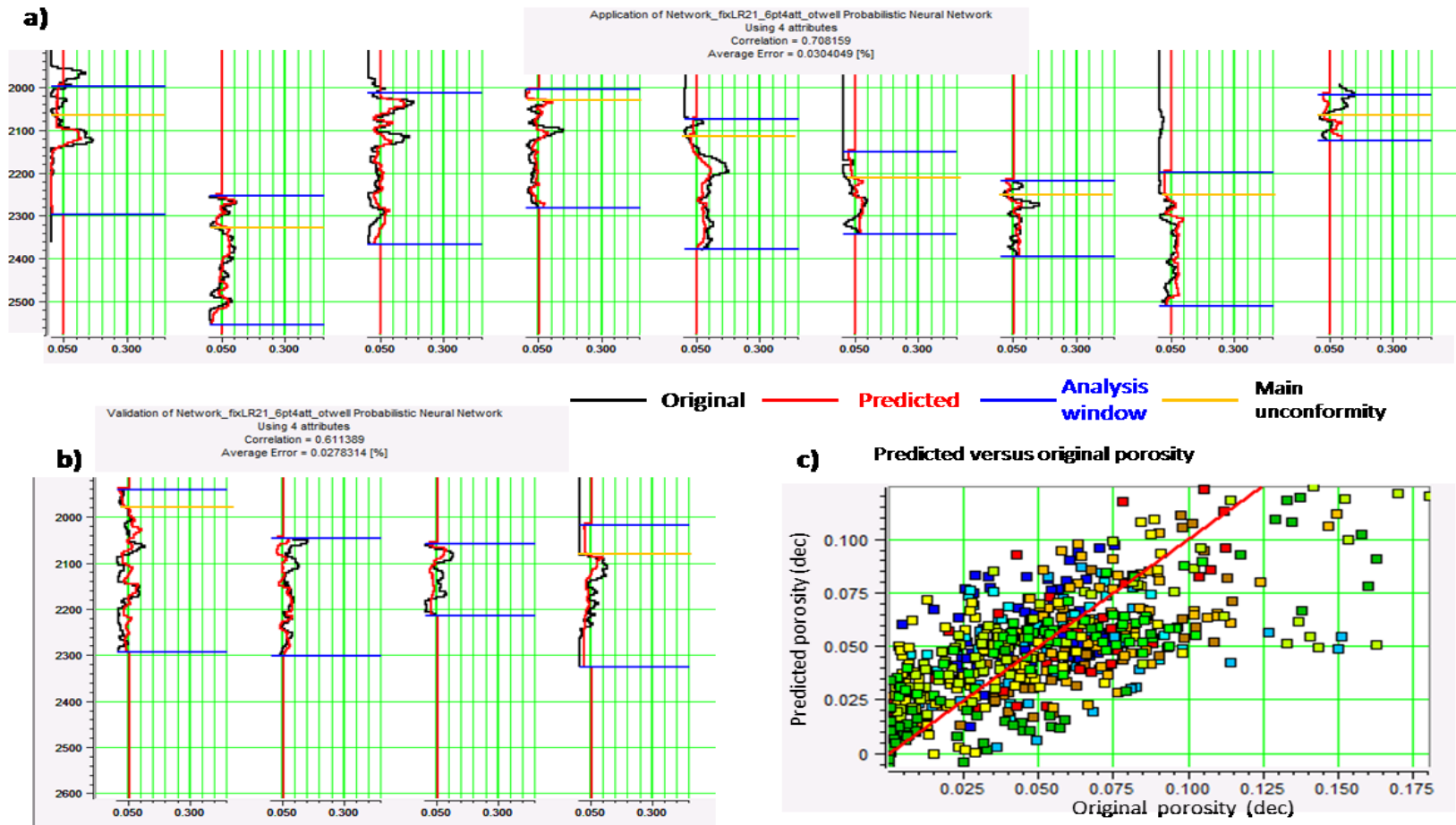


Figure 70. (a) Training and (b) validation of neural networks to estimate effective porosity. The error is 0.027 with a correlation of 0.61 after validation. (c) crossplot of predicted porosity versus actual porosity at well position. The red line indicates a correlation of 1.0.

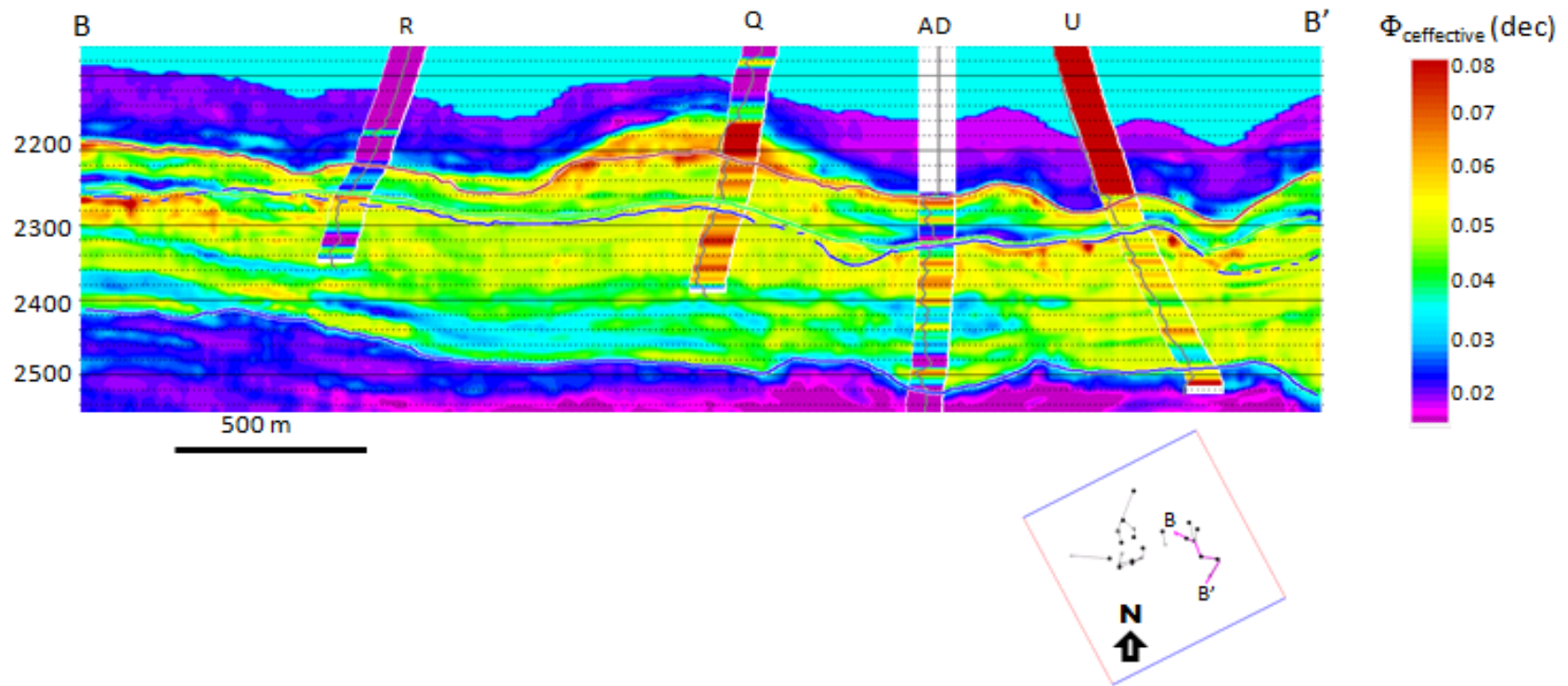


Figure 71. Effective porosity cross section through wells R, Q, AD, and U. The inserted colored column at well position corresponds to effective porosity calculated from well logs. Note that the predicted volume underestimates the well property. Furthermore, the resolution of the predicted volume does not represent properly the vertical variation at finer well scale. The location of the cross section is indicated on the inserted map.

Figure 72 shows predicted the clay volume, V_{clay} , and effective porosity cross sections through wells B, K, M and N at the crest of the structure to show the result for unit EOC-10. Note the good correlation of estimated clay volume with inserted gamma ray logs. Clay volume varies insignificantly within the reservoir unit EOC-10 since it was correlated based on the well log character of gamma ray, GR, and deep resistivity, ILD. The top and base of the unit is marked by a strong inflexion in GR curve toward low values and in ILD curve toward larger values (Figure 65). In contrast, effective porosity varies considerable within the lithostratigraphical unit.

Exploratory data analysis of well measurements showed that elastic parameters of Z_P , Z_S , V_P/V_S , $\lambda\rho$ and $\mu\rho$ can be successfully used to discriminate facies variation as a function of porosity and clay content. As an alternative method to PNN, I used generative topographic mapping (GTM) algorithm to discriminate seismic facies and better identify reservoir heterogeneity.

Classification analysis of several seismic attributes volumes can be possible by representing each attribute as an additional dimension, so the number of dimensions is equal to the number of desired attributes for analysis. The understanding of several dimensions may be difficult to understand and interpret. However, multi-dimension can be easily managed mathematically (Wallet et al., 2009), although it may be difficult to interpret and visualize. Latent space provides a simple and accurate mode to project D -dimensional data (for D attributes or D stratal slices) onto much more compact 1D or 2D latent spaces (Wallet et al., 2009). Furthermore, the clusters in latent spaces are ordered, such that can be effectively visualized by the use of color bars. Wallet et al. (2009) review three different algorithms to train the latent space for less-dimension

representation of data: self organizing mapping (SOM), generative topographic mapping (GTM), and diffusion mapping.

One of the weaknesses of SOM algorithm is the lack of convergence assurance. For that reason, GTM was created to overcome SOM flaws. Consequently, GTM is a more robust method to train the latent space (Roy et al., 2012; Wallet et al., 2009).

GTM represents the data volumes with a mixture of Gaussian distributions. The model parameters are determined by maximizing the likelihood of the data. (Wallet et al., 2012). The principal advantage of GTM over SOM is the iterative learning of latent space through the algorithm of expectation maximization (EM), which makes that the model always converge at local maxima onto the likelihood surface (Roy et al., 2012).

The GTM algorithm was run using software described by Roy et al. (2012), in which first, the data are normalized by subtracting off the mean and then dividing it by the standard deviation for each dimension (i.e. using the z-score algorithm). The model is then initialized using multi-attribute principal component analysis (PCA). Then, the latent space is trained iteratively using a subset of the normalized data to compute the model parameters, which are the locations of a suite of Gaussian probability distribution functions (pdfs) used to define the data. QC plots are examined after each iteration. After training, each data vector (suite of attributes at each voxel) is projected against the Gaussian pdfs, resulting in a posterior probability or “responsibility” value for each latent space location. Summing these probabilities gives us a mean projection of the data vector in the 2D latent space which typically form natural clusters (Roy et al., 2012).

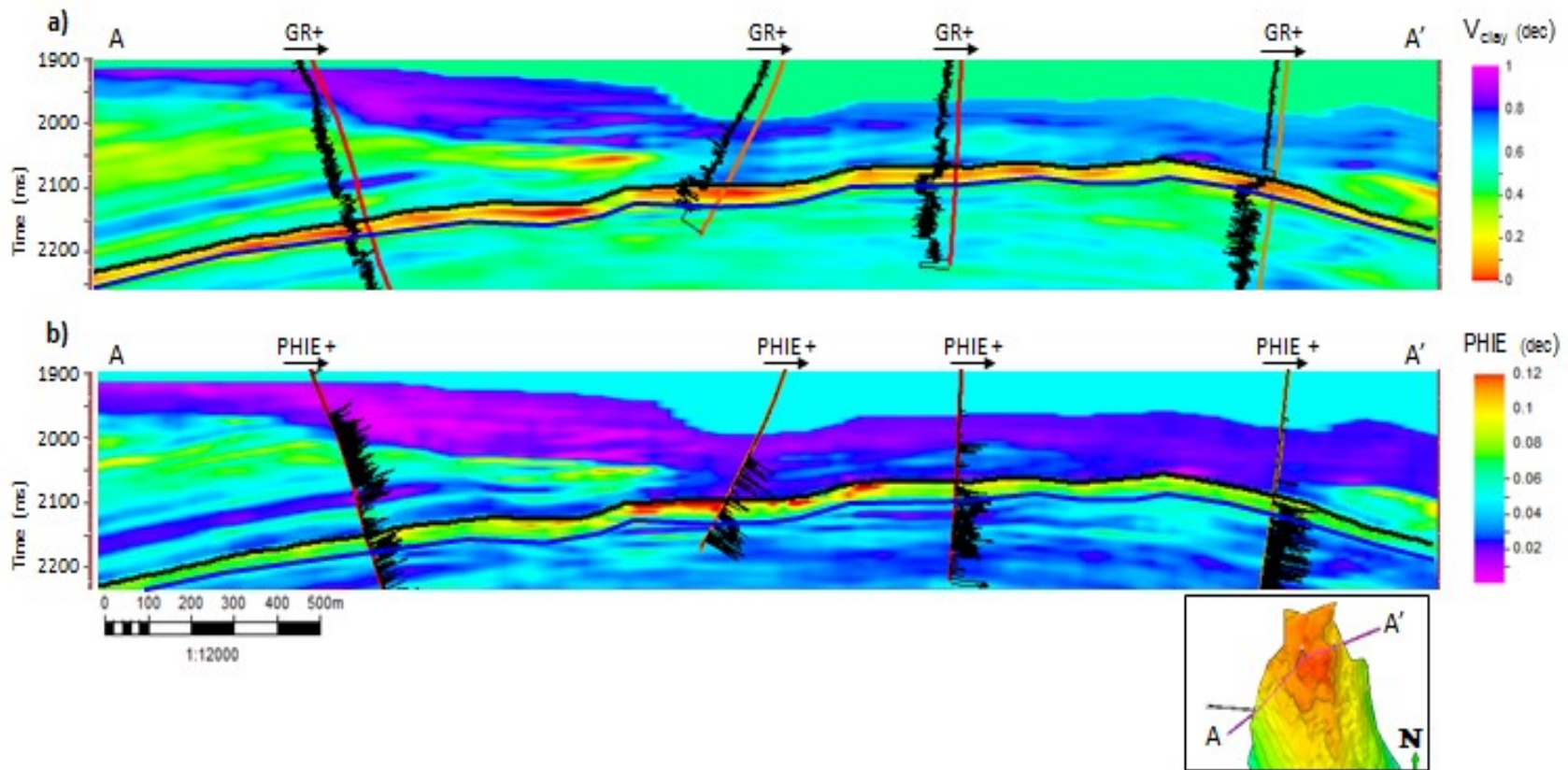


Figure 72. Vertical seismic section through (a) clay volume and (b) effective porosity. The black horizon correlates with the top of unit EOC-10 and the blue one with its base. Note in (a) that the clay content along reservoir unit does not vary significantly; the predominant facies have low clay content (warm colors). In contrast, the porosity varies more significantly along the unit. The reservoir unit EOC-10 is underlaid and overlaid by clay-rich facies (cold colors).

The inputs for GTM analysis in my area were the inverted property volumes Z_p , V_p/V_s , $\lambda\rho$ and $\mu\rho$, giving rise to a 4D data space.

Figure 73 show a 2D histogram (number of vectors that project to a given location in the latent space) of the GTM results for reservoir units EOC-10 and EOC-30 for classification analysis. EOC-10 and EOC-30 are the most productive units of the field. Both units are Middle Eocene with a 22 API oil production with a similar mineralogy content and porosity distribution (Appendix A). For that reason, clustering was done using the same criteria for both units. Once clusters have been defined around the high density areas in the density crossplots, seismic facies models for reservoir units EOC-30 and EOC-10 were created by generating a volume probe for 3D analysis. (Figure 74). The projected mean of the posterior probability is updated according to the selected window to generate the volume probe.

The seismic facies generated from unsupervised analysis of generative topographical maps (GTM).were visually correlated with reservoir property volumes calculated by supervised PNN. Figure 75 compares predicted effective porosity and clay volume to seismic facies for reservoir unit EOC-10. Similarly, Figure 76 compares results from both PNN and GTM methods for reservoir unit EOC-30. Note that pink and purple facies correlates with clay-rich areas. In addition, observe in EOC-30 that high porosity occurs in elongated patterns close to normal faults along hangingwalls.

Distribution of the mean posterior probability of the reservoir zones plotted in the 2D Latent space

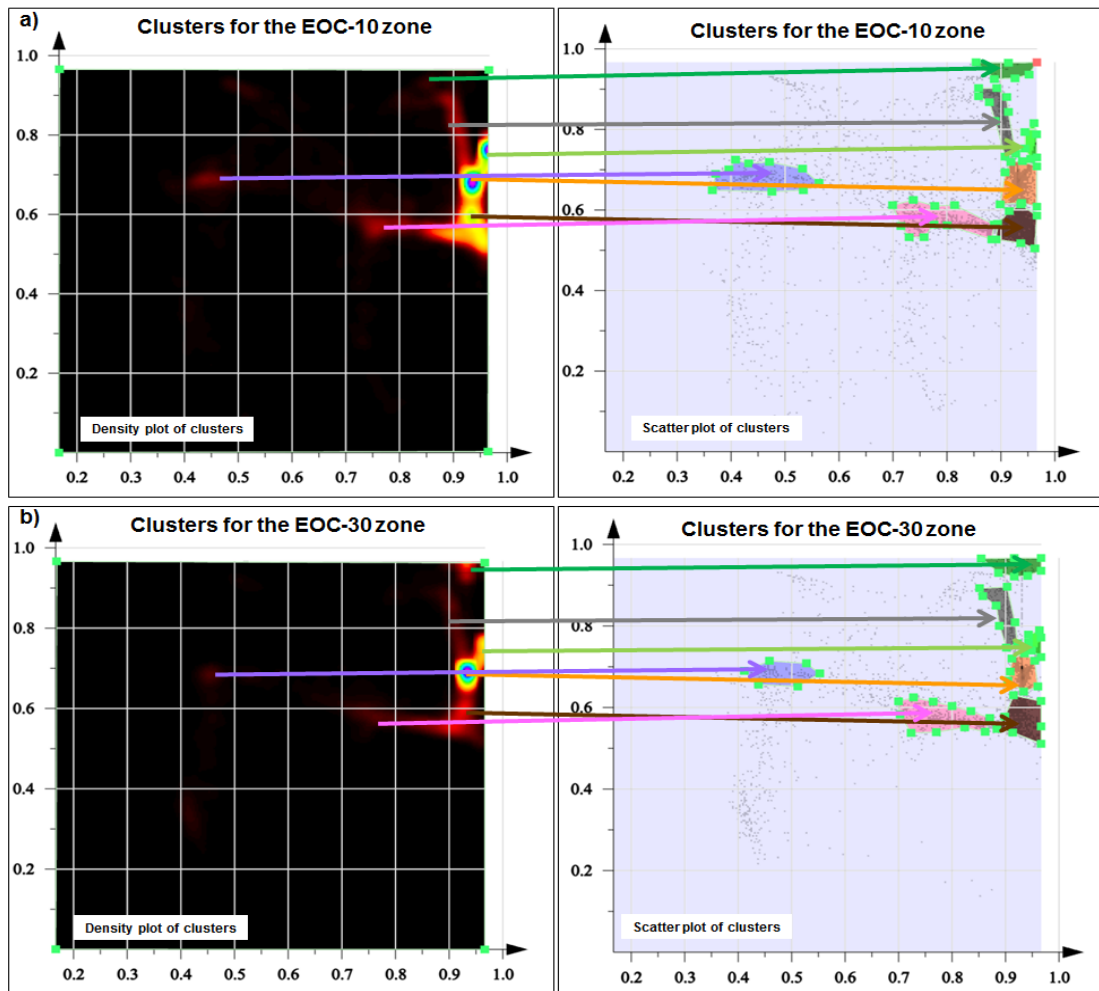


Figure 73. Mean distribution of the posterior probability projections of the reservoir zones (a) EOC-10 and (b) EOC-30) plotted in the 2D latent space. High density areas are represented by cold colors (magenta, blue, cyan). The arrows indicate the association of clusters delineated by polygons and high density areas.

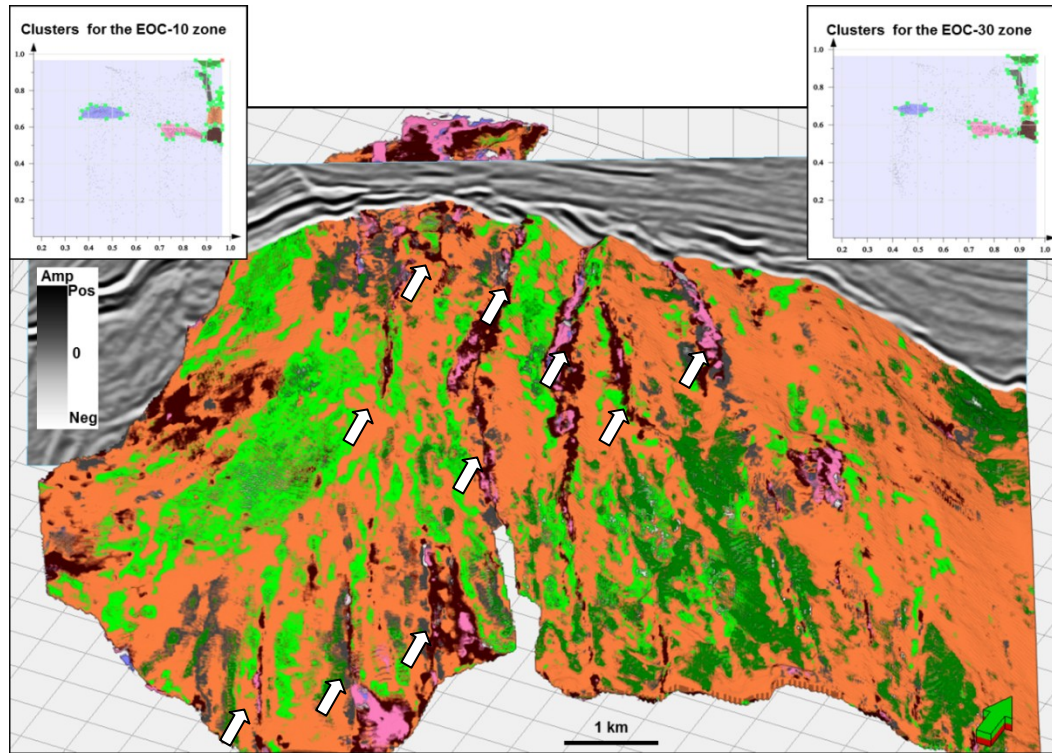


Figure 74. Volume probe generated from classes selected on the crossplot of the mean distribution of the posterior probability function. Upper right- and left interpreter-generated color-coded polygons made in the 2D latent space identifying distinct clusters. Note that faults, indicated by white arrows, are also assigned to a class by the unsupervised algorithm.

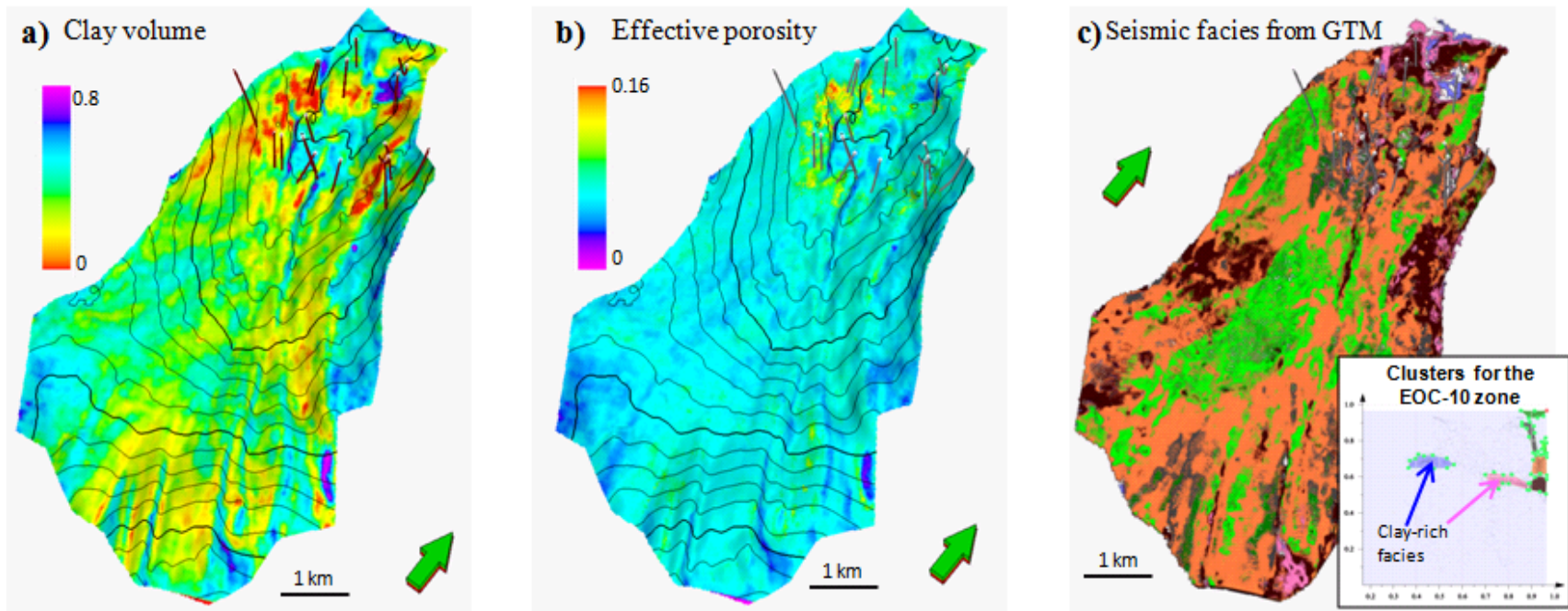


Figure 75. Phantom horizon slice 10 ms below the top of the EOC-10 horizon through the (a) clay and (b) effective porosity volumes predicted from a supervised probabilistic neural networks, and (c) clusters along the top the top EOC-10 using an unsupervised generative topographic mapping (GTM) classification algorithm.

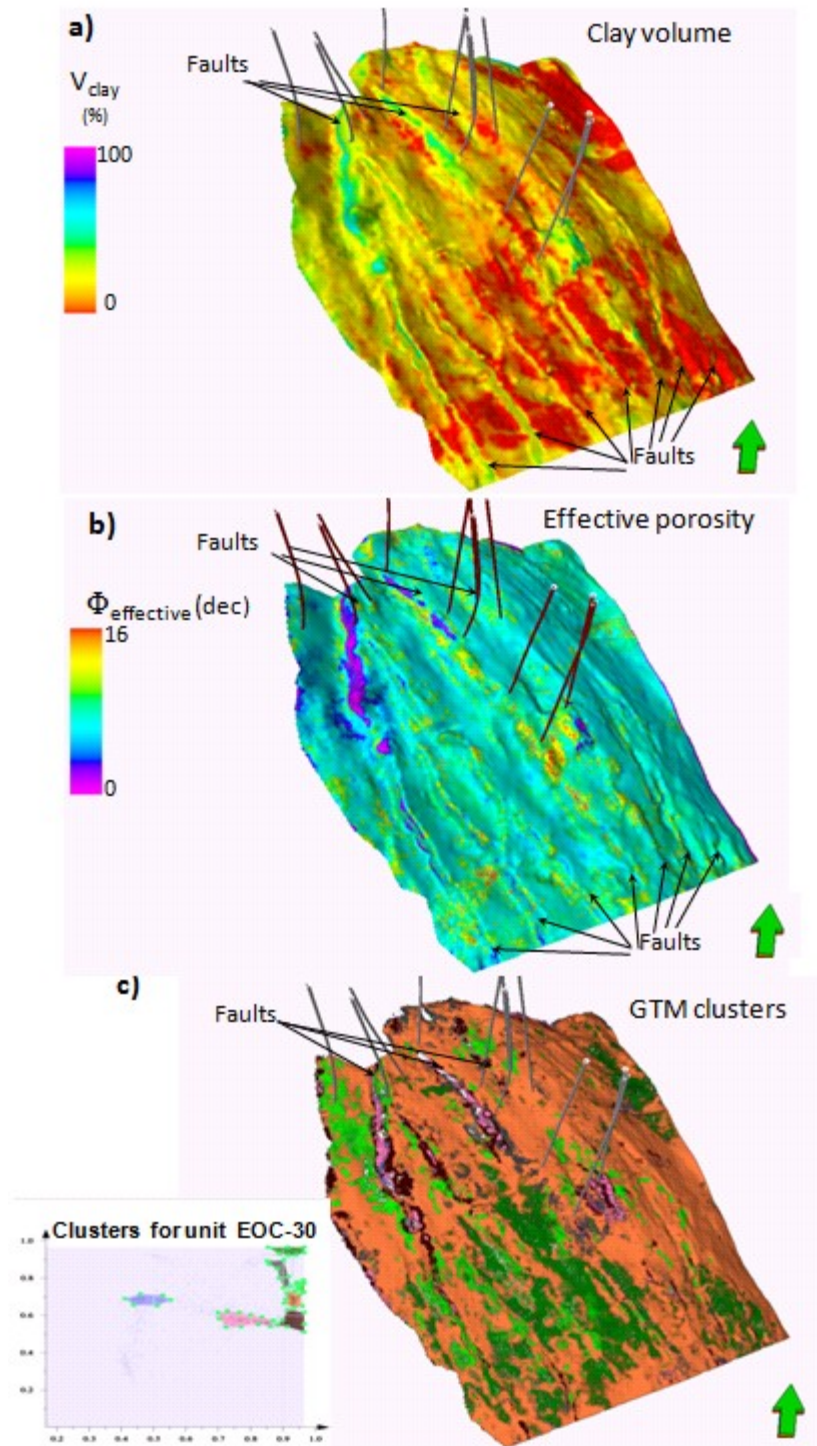


Figure 76. Phantom horizon slice 10 ms below the top of the EOC-30 horizon through the (a) clay and (b) effective porosity volumes predicted from a supervised probabilistic neural networks, and (c) clusters along the top the top EOC-30 using an unsupervised generative topographic mapping (GTM) classification algorithm.

CHAPTER V. CORRELATION WITH PRODUCTION DATA

Field production data

The production data available for my field consist of the monthly cumulative oil, water and gas production per well since the beginning of production. Ideally, the correlation of any estimated reservoir property should be made with the expected ultimate recovery (EUR) per well and reservoir unit. In the absence of EUR information, I used the first seven months cumulative production for wells with longer history, and total cumulative production for more recently productive wells to calculate an average daily production. To correlate available production data with my inverted results, I hypothesized that all wells were ideally drilled and exploited under similar conditions and that production is only a function of the reservoir quality. This hypothesis also implies that the decline factor and time of production will be equal for all the wells.

Figure 77 shows a graph with the total cumulative production normalized to 100% for each type of hydrocarbon. Note that EOC-10 and EOC-30 are the major producing units. EOC-50 has a smaller cumulative production which likely reflects the shorter production history, rather than the true productivity of unit.

Figure 78 shows the total cumulative production normalized to 100% for each reservoir unit. The gas production was converted from volume units to barrels of oil equivalent (BOE). 35% of the total cumulated production for EOC-10 is water. Cumulative water production of EOC-30 is 52% exceeding the cumulative oil production. The gas production does not vary significantly ranging from 5 to 8% of the total production.

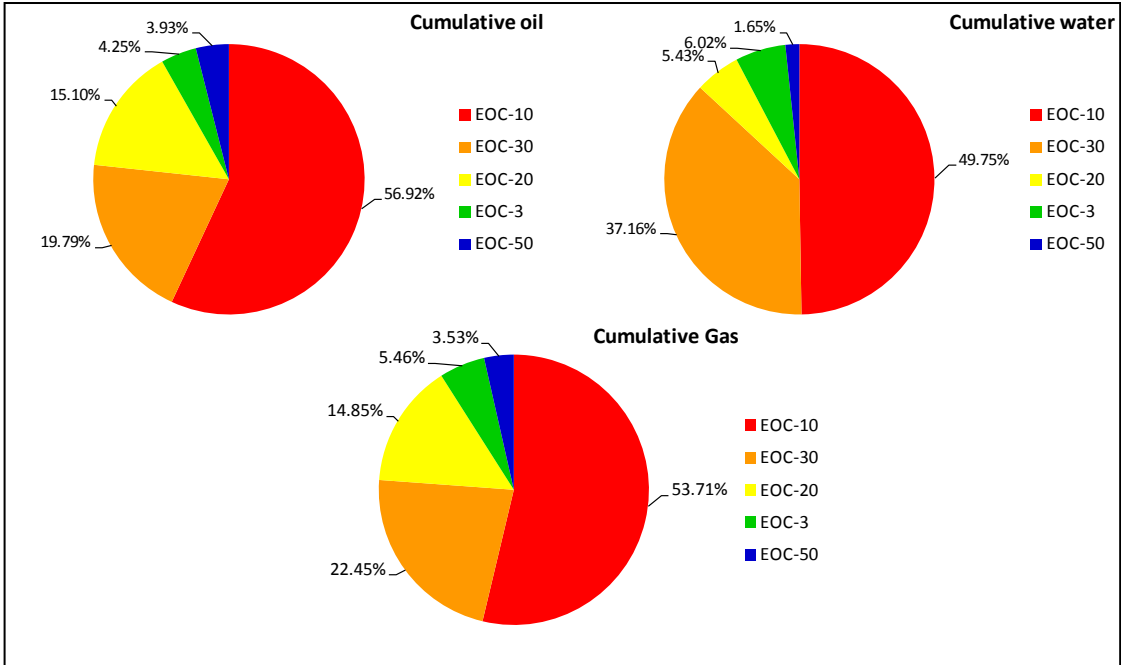


Figure 77. Total cumulative production per reservoir unit normalized to 100% for each type of hydrocarbon. Note that EOC-10 accounts for more than 50% of the total oil cumulative production. The second most productive unit, EOC-30, accounts for around 20% of the total oil production. EOC-50 has minor cumulative production.

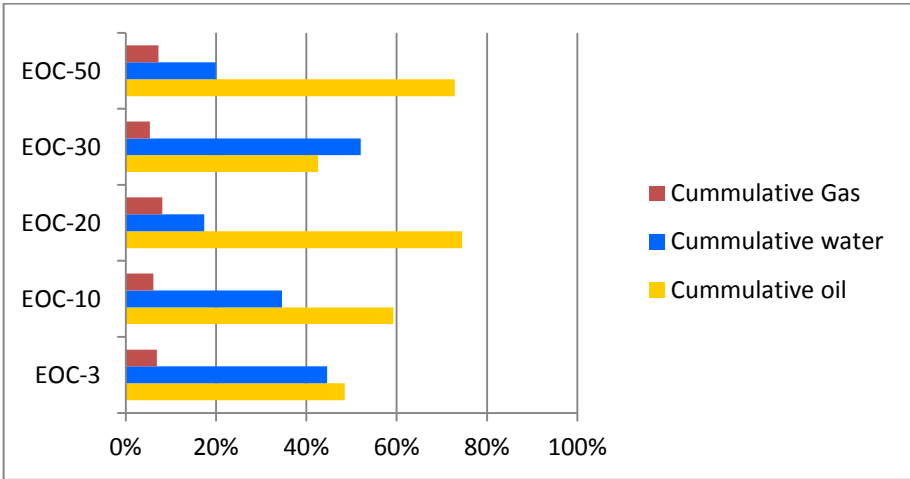


Figure 78. Cumulative production for each reservoir unit normalized to 100%. Note that EOC-30 has the major water production (52%). The gas cumulative gas production do not vary significantly ranging from 5 to 8% of the total production in barrels of oil equivalent (BOE).

Correlation of predicted volumes by PNN and production data

I validate the effectiveness in my estimated effective porosity and clay volume by correlating production data from the most productive units EOC-10, producing in the crest of the anticline, and EOC-30, producing in the eastern flank. For this analysis, I used phantom horizons 10 ms below the interpreted top to make sure that the horizon was within the reservoir.

Figure 79 shows a blended bubble map of EOC-10 production with phantom horizon slices through the predicted V_{clay} and effective porosity volumes obtained with PNN. The pie charts are proportional to the average daily production from the first seven months of production history, except for three wells with shorter production history. Both PNN predicted properties, clay volume and effective porosity, exhibit a low correlation with production rates.

Observe in Figure 79a that clean calcilithite zones with extremely low clay volume may produce less than wells with 10% to 25% of clay content. While there may not be a linear relationship between clay content and production, however, clay volume prediction can be used to identify some prospect areas between wells where the clay content is less than the cut-off value of 45% established for the field. Similarly note in Figure 78b that higher production is not associated with the highest effective porosity areas. The dry well in the NW part of the field has an effective porosity similar to other high productive wells.

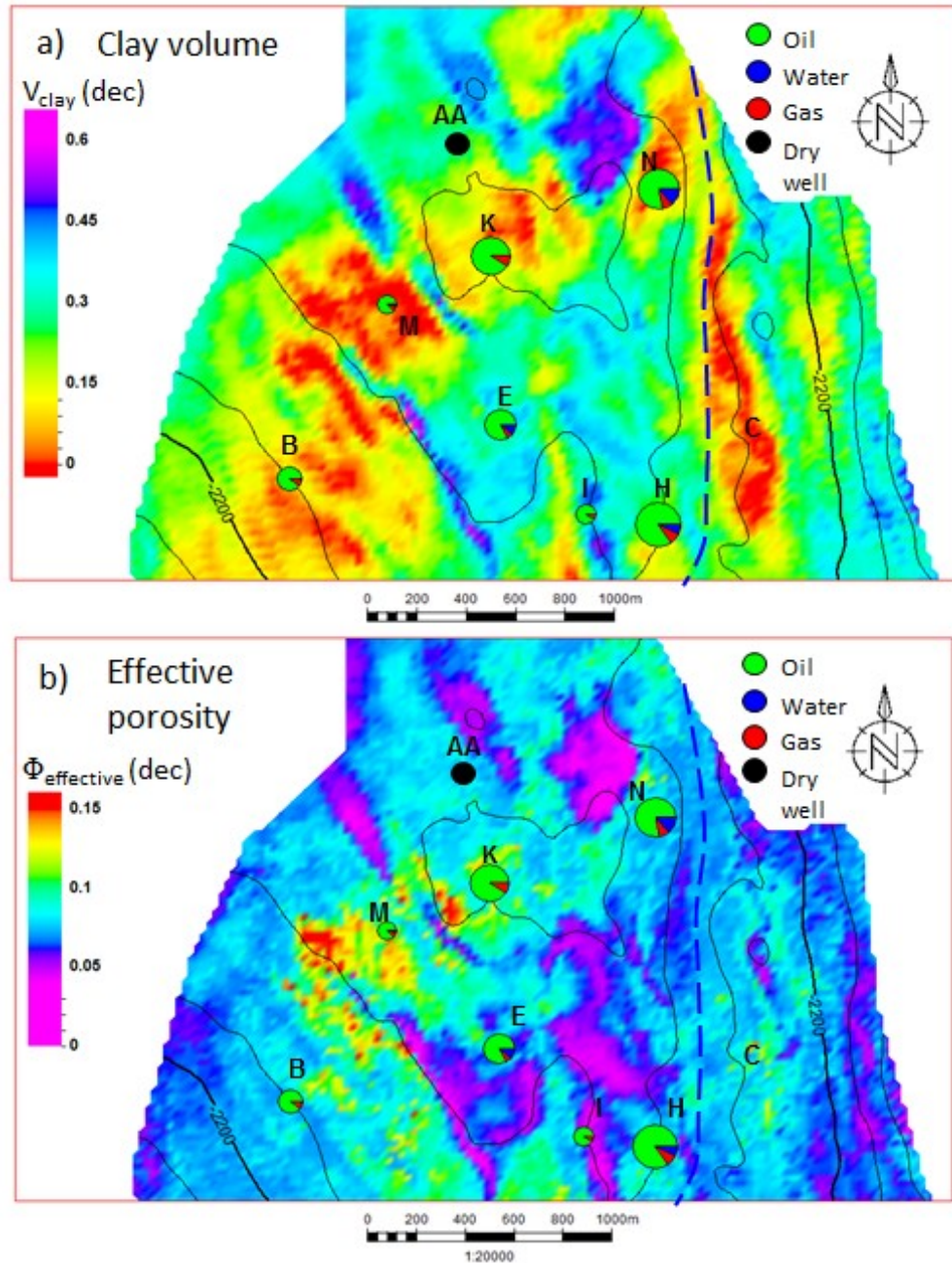


Figure 79. Phantom horizon slices 10 ms below EOC-10 through predicted (a) clay content and (b) effective porosity volumes, blended with bubble maps of the total average daily hydrocarbon production for the first seven months. Note that production is not linearly correlated with predicted clay content while higher production is not associated with the highest effective porosity areas. Blue dotted lines indicate the oil-water contact for the eastern fault block. The contour interval is 40 ms.

Oil-water contacts (OWC) for this field have been established primarily with pressure data, production tests and nuclear resonance magnetic logs. Conventional well logs such as resistivity do not provide an evident OWC response due to bearing hydrocarbon areas with high water saturation. PEMEX's team has identified at least one OWC for this unit established from the results of well C, which is indicated by a blue contour on both maps. Each compartment has a different original reservoir pressure and independent OWC, although many compartments have not yet been tested.

Figure 80 compares predicted clay volume and effective porosity for reservoir unit EOC-30. Note in Figure 80a that most of the unit area is associated with clean carbonate facies, with a clay volume less than 60%. Clay-rich areas correlate with normal faults. All productive wells were drilled in areas with a clay content around 20%. Observe in Figure 80a that productive units fall below the 9% cut-off value of effective porosity, which suggests that the effective volume porosity was underestimated. This underestimation may be the result from averaging thin shale/carbonate layers that fall below seismic resolution. This averaging smears subtle variations in effective porosity within economically important stratigraphic units. Furthermore, productivity does not linearly correlate with the predicted volume. The highest porosity zones have not been yet drilled. This high porosity zones may represent prospective areas, but reservoir compartmentalization needs to be established before condemning down dip areas for those blocks with a known OWC.

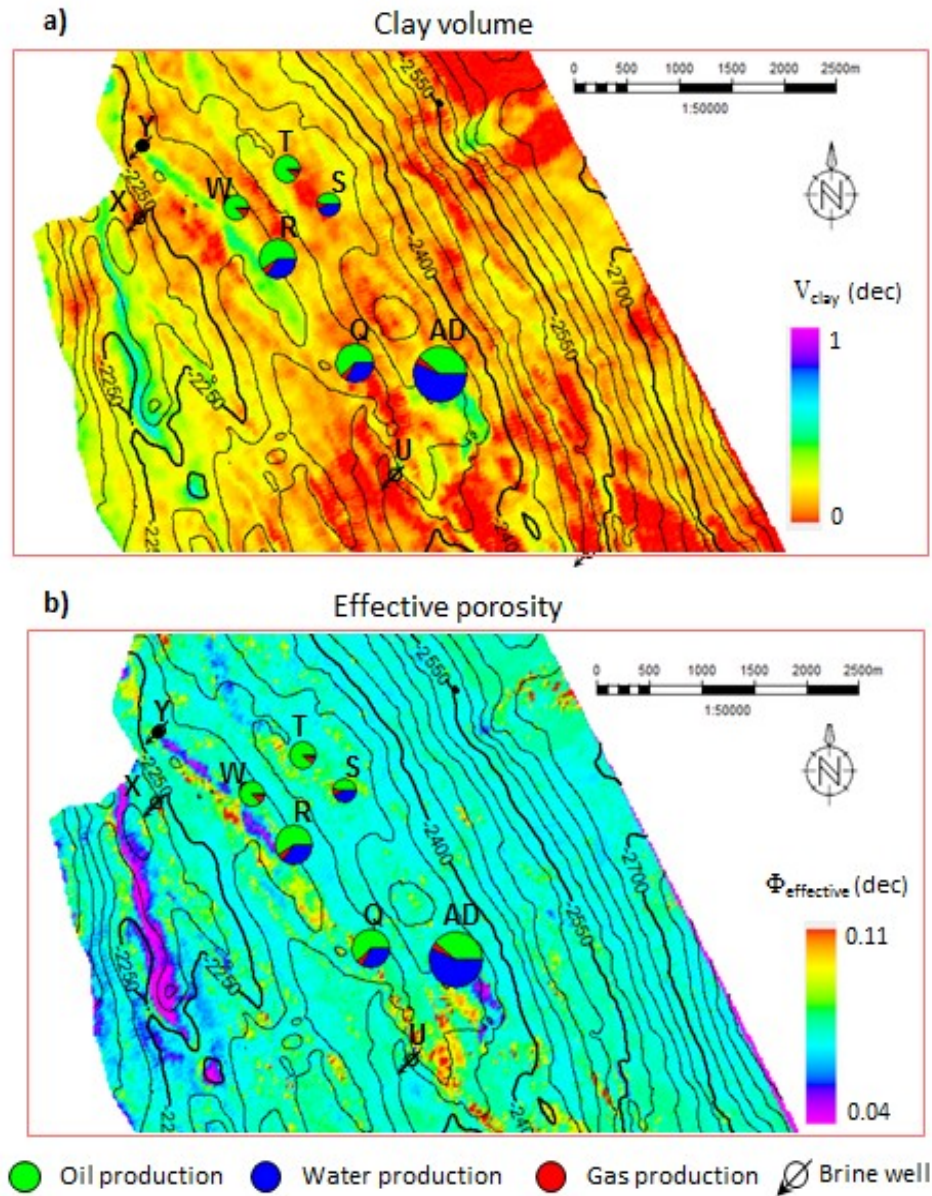


Figure 80. Phantom horizon slices 10 ms below EOC-30 through predicted (a) clay content and (b) effective porosity volumes, blended with bubble maps of the total average daily hydrocarbon production for the first seven months. Time structure contours are in ms. Note the low clay content over the unit. Elongated clay-richer zones are associated with normal faults. Higher production is not associated with the highest effective porosity areas. The established cut-off value of effective porosity is $\Phi \geq 9\%$.

Correlation of seismic facies from GTM analysis and production data

The low correlation of production data with PNN prediction of clay and effective porosity suggest that these are other (unknown) diagenetic or structural factors that control production. I therefore expand my correlation analysis to seismic facies identified by classification analysis of GTM results for reservoir units EOC-10 and EOC-30.

Rather than plotting the “class” of each voxel, I plot the voxels x and y coordinate projected onto the 2D latent space. Such a projection facilitates the use of crossplot tools. Figure 81a shows a horizon slice through the volume probe of the mean of the GTM posterior probability projections onto a 2D latent space for reservoir unit EOC-10. Figure 80b is a 3D view of the volume probe. Note that productive wells fall in light green facies and orange seismic facies. In contrast, brown facies correlates with poor reservoir quality. All wells falling in the orange facies are productive. Note that well C, which tested brine water, also falls into the orange facies, which is associated with good reservoir quality but below the OWC. Seismic facies classification does not provide saturation discrimination for the attributes provided.

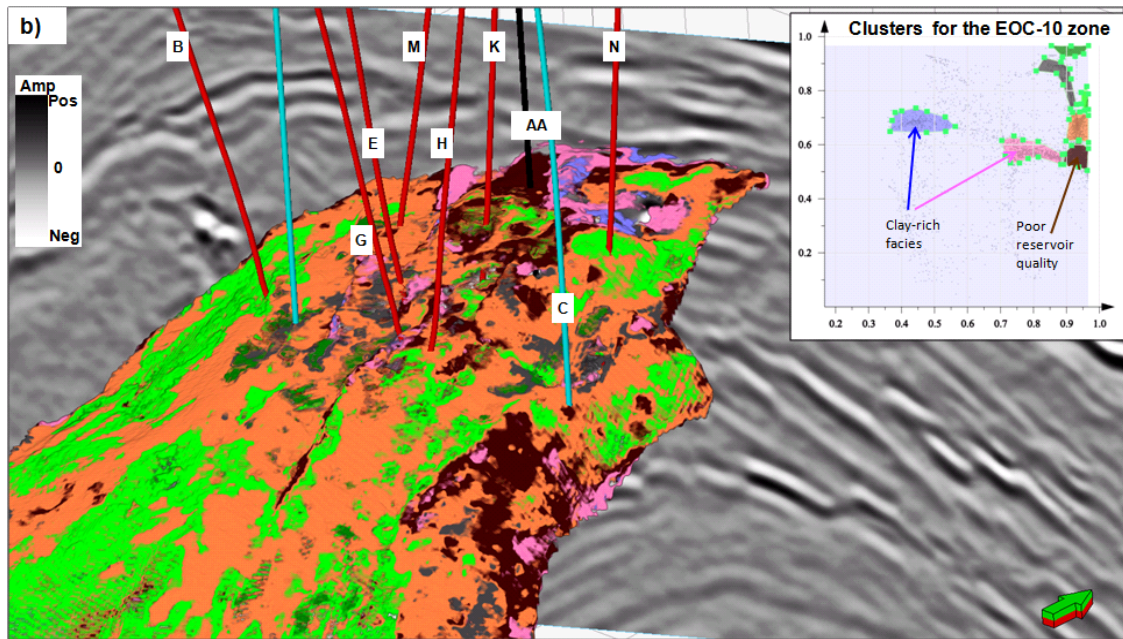
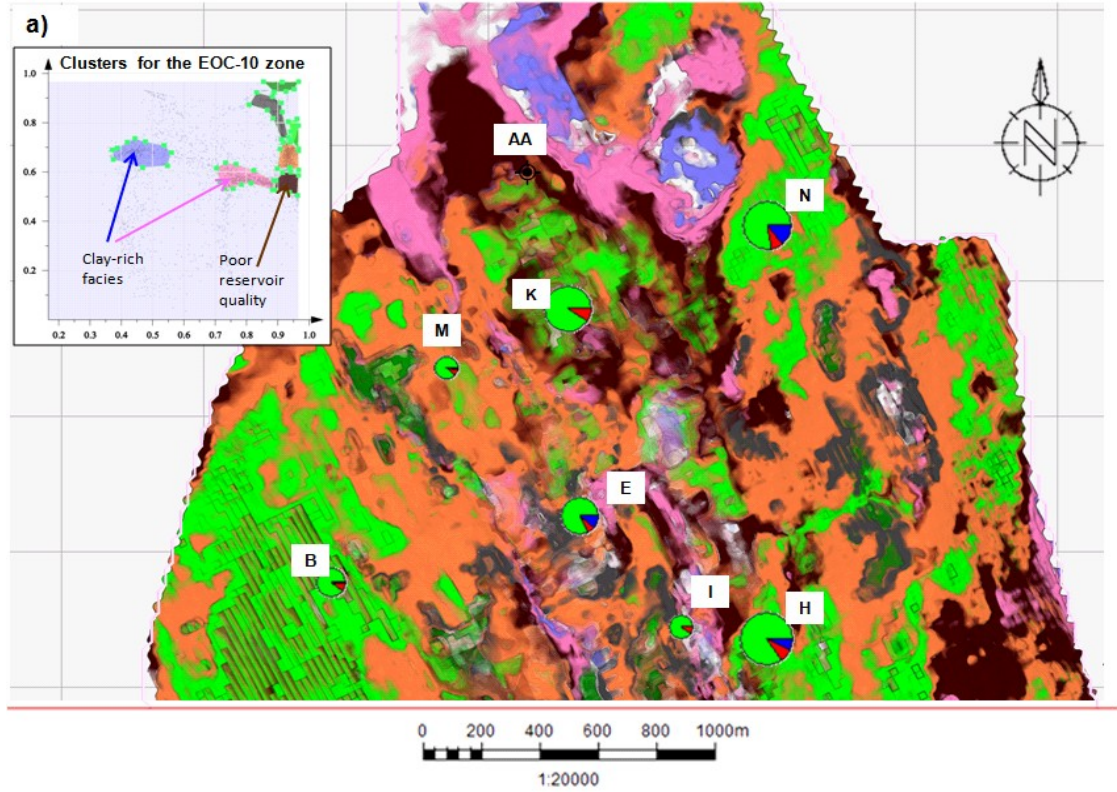


Figure 81. Facies classification from GTM for reservoir unit EOC-10. (a) Seismic facies map 10 ms below top of EOC-10. Pie charts are proportional to daily average production for the first 7 month. (b) 3D view of the volume probe containing clustering from GTM analysis. Insert crossplots are generated directly in the 2D latent space.

Next, I apply GTM to EOC-30, Figure 81 presents the correlation between seismic facies from GTM analysis and production data. Figure 81a is a horizon slice through the volume probe generated with the classes interpreted in the density crossplot of the mean of the posterior probability projections in 2D latent space for reservoir unit EOC-10 blended with the corresponding bubble map. Figure 81b is a 3D view of the volume probe generated with the clusters for this unit. Note that productive wells fall within the orange facies. The well with the major production of water, AD, falls into the brown facies, while well U, which tested brine water, falls along the boundary between the orange and brown facies, near the elongated brown-pink lineament southward. In addition, wells X and Y, which also tested brine water in this unit, fall into the orange facies. This confirms that the reservoir quality is good, since they have oil shows and water flow; seismic facies classification using these attributes does not differentiate fluid saturation.

These results show that GTM provides a more effective identification of reservoir variability than PNN.

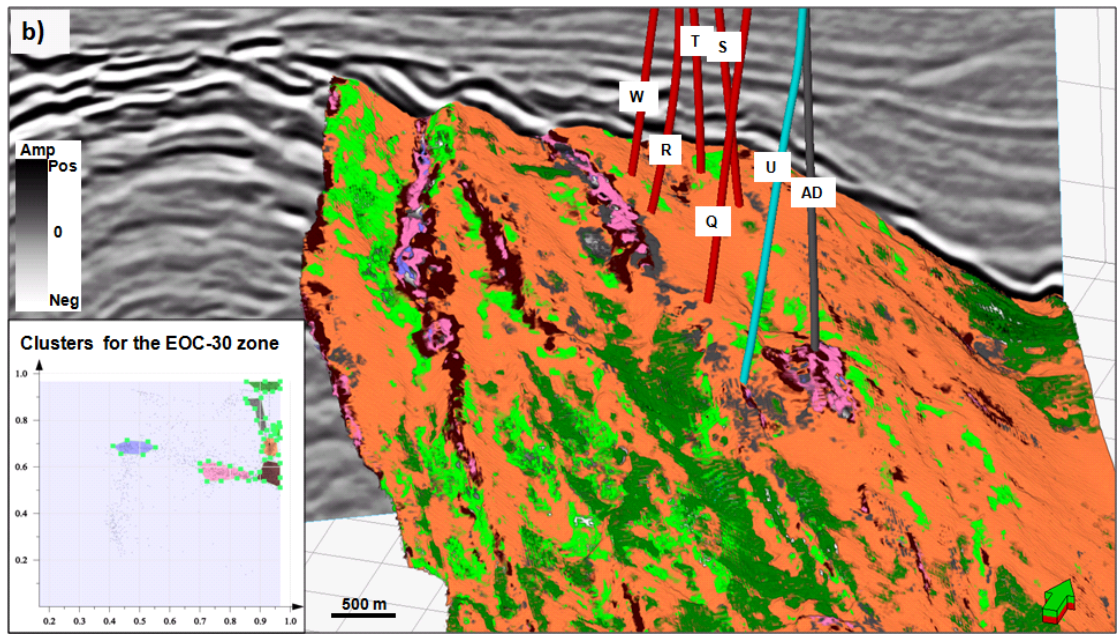
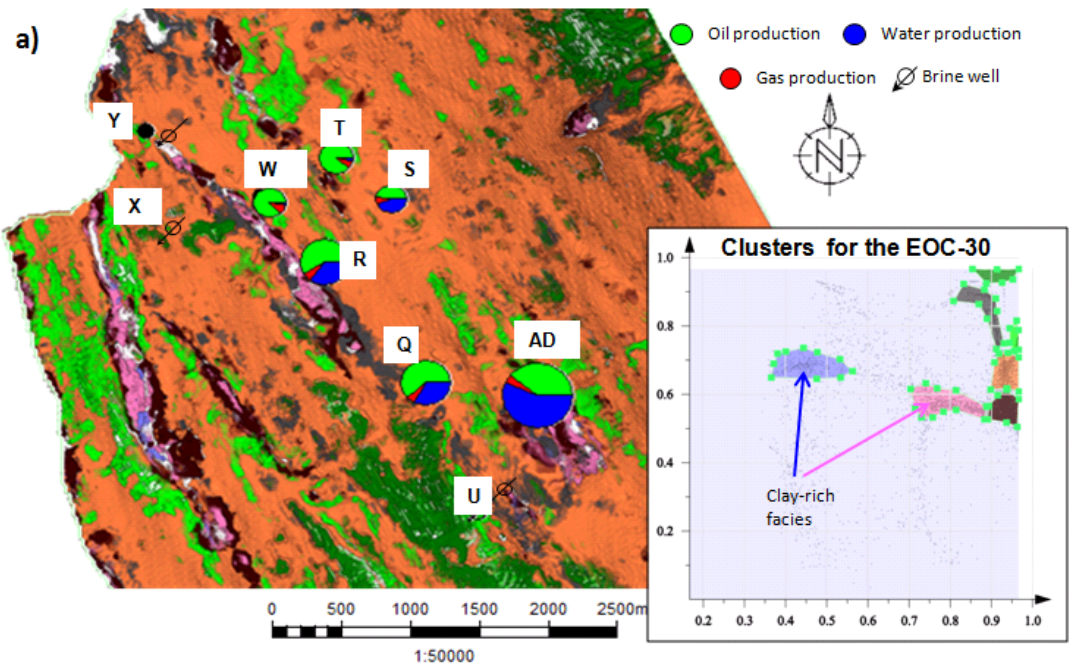


Figure 82. Facies classification from GTM for reservoir unit EOC-30. (a) Seismic facies map 10 ms below top of EOC-30. Pie charts are proportional to daily average production for the first 7 months. (b) 3D view of the volume probe containing clustering from GTM analysis. Note that productive wells fall in orange seismic facies, except well AD which correspond brown seismic facies and happens to be the major water producing well in this unit.

CONCLUSIONS

Multiattribute analysis coupled with an analogue tectonic deformation model provides a powerful method to assist structural interpretation in a structurally complex area along the tectonic front of the Sierra Madre Oriental, in the Veracruz Tertiary Basin, southeastern Mexico.

I applied structure-oriented filtering to condition my poststack seismic data for structural interpretation, and my prestack seismic gathers for simultaneous inversion. SOF enhances reflector edges while removes crosscutting coherent and random noise, preserving the amplitude for inversion analysis.

Porosity has been successfully predicted in many carbonates reservoir using just poststack seismic inversion. However, exploratory data analysis of my well measurements showed that P-impedance is insufficient to predict porosity of my carbonate wash facies. I therefore estimate S-related properties for a better discrimination through prestack simultaneous inversion.

In my area, clay-rich zones present high total porosity comparable to reservoir zones. The prestack inversion results were used in a supervised neural networks workflow to predict clay volume. I then used the clay prediction with $\lambda\rho$, spectral magnitude component at 80 Hz and coherent energy to predict effective porosity.

Well correlation shows that the clay volume was successfully predicted by a supervised neural network and can be used with confidence to identify clay-rich facies. In contrast, effective porosity was underestimated. This inaccuracy is linked to the resolution of the method which is insufficient to illuminate changes in porosity of the thin layered, interbedded cemented and porous calcilithites.

The prestack inversion volumes, Z_P , V_P/V_S , $\lambda\rho$ and $\mu\rho$, were inputs for a generative topographic mapping unsupervised clustering workflow. GTM seismic facies provided a more effective identification of reservoir heterogeneity, consistent with production data.

REFERENCES

- Al-Dossary S., and K. J. Marfurt, 2006, 3D volumetric multispectral estimates of reflector curvature and rotation, *Geophysics*, **71**, P41–P51, doi: 10.1190/1.2242449.
- Andreani L., C. Rangin, J. Martínez-Reyes, C. Le Roy, M. Aranda-García, X. Le Pichon, and R. Peterson-Rodríguez, 2008, The Neogene Veracruz fault: evidences for left-lateral slip along the southern Mexico block: *Bulletin de la Société Géologique de France*, **179**, 195–208, doi: 10.2113/gssgfbull.179.2.195.
- Anselmetti F. S., and G. P. Eberli, 1997, Sonic velocity in carbonate sediments and rocks, *in* H. Palaz, and K. J. Marfurt, eds., *Carbonate seismology: Society of Exploration Geophysicists, Geophysical developments no. 6*, 53–74.
- Avseth P., T. Mukerji, and G. Mavko, 2010, *Quantitative seismic interpretation applying rock physics tools to reduce interpretation risk*: Cambridge University Press.
- Barclay F., A. Bruun, K. B. Rasmussen, J. Camara-Alfaro, A. Cooke, D. Cooke, D. Salter, R. Godfrey, D. Lowden, S. McHugo, H. Özdemir, S. Pickering, F. Gonzalez-Pineda, J. Herwanger, S. Volterrani, A. Murineddu, A. Rasmussen, and R. Roberts, 2008, Seismic inversion reading between the lines: *Oilfield Review*, Spring, 42–63, accessed April 22, 2011; http://www.ocean.slb.com/Docs/PSIV-B1/Seismic_Inversion_ReadingBetween.pdf.
- Betanzos-Gallifa M. A., M. A. Cárdenas Sánchez, C. A. Cózar-Ángulo, B. P. Galindo-González, R. Guerra, J. H. Hernández-Arcos, M. Landeros-Flores, S. de A. Padilla-Ramos, M. A. Sánchez-Ríos, and H. Ruíz, 2010, *Internal biostratigraphy reports: PEMEX Exploración y Producción*, unpublished.
- Bird P., 2002, Stress direction history of the western United States and Mexico since 85 Ma: *Tectonics*, **21**, 5-1–12.

- Blumentritt C. H., K. J. Marfurt, and E. C. Sullivan, 2006, Volume-based curvature computations illuminate fracture orientations —Early to mid-Paleozoic, central Basin Platform, west Texas: *Geophysics*, **71**, B159–B166.
- Bolli, H. M., J. B. Saunders, and K. Perch-Nielsen, eds., 1985, *Plankton stratigraphy, Volume 1; planktic foraminifera, calcareous, nannofossil and calpionellids*, Cambridge University Press.
- Bosch M., T. Mukerji, and E. F. Gonzalez, 2010, Seismic inversion for reservoir properties combining statistical rock physics and geostatistics: A review: *Geophysics*, **75**, A165-A176, doi: 10.1190/1.3478209.
- Bouma A. H., 2000, Fine Grained, mud-rich turbidite systems: model and comparison with coarse-grained, sand-rich systems, *in* A. H. Bouma, and C. G. Stone, 2000, *Fine-grained turbidite systems: AAPG Memoir 72*, and Society for Sedimentary Geology Special Publication No. 68, 9–20.
- Chopra, S., and K. J. Marfurt., 2007a, Curvature attribute applications to 3D surface seismic data, *The Leading Edge*, **26**, 404–414, doi: 10.1190/1.2242449.
- Chopra, S., and K. J. Marfurt., 2007b, Seismic attributes for prospect identification and reservoir characterization: SEG, *Geophysical Developments Series No. 11*.
- Chopra, S., and K. J. Marfurt, 2010, Integration of coherence and volumetric curvatures images: *The Leading Edge*, **29**, 1092–1107.
- Connolly P., 1999, Elastic impedance: *The Leading Edge*, **18**, 438-452, accessed April 22, 2011, doi: 10.1190/1.1438307.
- Cruz-Helú P., R Verdugo V., R. Bárcenas P., 1977, Origin and Distribution of Tertiary conglomerates, Veracruz Basin, Mexico: *AAPG Bulletin*, **61**, 207–226.
- Davogustto, O. E., 2011, *Removing footprint from legacy seismic data volumes: M.S. Thesis*, The University of Oklahoma, Norman, Oklahoma, 78 p.
- Davogustto, O., and K. J. Marfurt, 2011, Footprint suppression applied to legacy seismic data volumes: GCSSEPM 31st Annual Bob. F. Perkins Research Conference on Seismic attributes—New views on seismic imaging: Their use in exploration and production, doi: 10.5724/gcs.11.31.0001.

- Davogustto, O., B. Dowdell, S. Guo, T. Kwiatkowski, K. J. Marfurt, A. Roy, S. Verma and B. Zhang, 2011, Running AASPI software with GUIs: Attribute-Assisted Seismic Processing & Interpretation consortium, Section 20, accessed February 22, 2012; <http://geology.ou.edu/aaspi/documentation.html>.
- De-Sansores, J. C. and C. Flores-Covarrubias, 1972, Atlas de foraminíferos bentónicos del Terciario Superior de la Cuenca Salina del Istmo de Tehuantepec, Mex.: Instituto Mexicano del Petróleo, Subdirección de Tecnología de Exploración.
- Eberli, G.P., G.T. Baechle, F.S. Anselmetti, and M. L. Incze, 2003, Factors controlling elastic properties in carbonate sediments and rocks: The Leading Edge, **22**, 654–660.
- Eguiluz-de-Antuñano S., M. Aranda-García, and R. Marett, 2000, Tectónica de la Sierra Madre Oriental, México: Boletín de la Sociedad Geológica Mexicana, **LIII**, 1–26, accessed October 10, 2010; <http://boletinsgm.igeolcu.unam.mx/epoca03/eguiluz.pdf>.
- Fehmers and Höecker, 2003, Fast structural interpretation with structure-oriented filtering Geophysics, **68**, 1286–1293, doi: 10.1190/1.1598121.
- Ferket H., N. Guilhaumou, F. Roure, and R. Swennen, 2010, Insights from fluid inclusions, thermal and PVT modeling for paleo-burial and thermal reconstruction of the Cordoba petroleum system (NE Mexico): Marine and Petroleum Geology, **28**, 936–58; accessed February 9, 2012; doi: 10.1016/j.marpetgeo.2010.01.020.
- Ferket, H., S. Ortuño-Arzate, F. Roure, and R. Swennen, 2002, Diagenesis and fluid flow history in reservoir carbonates of the Cordilleran foreland fold and thrust belt: The Cordoba Platform (eastern Mexico): AAPG Search and Discovery Article #90011©2002 AAPG Hedberg Conference, May 14-18, 2002, Palermo-Mondello, Sicily, Italy, accessed February 9, 2012; http://www.searchanddiscovery.com/abstracts/pdf/2002/hedberg_sicily/ndx_ferket.pdf.

- Ferrill D. A. and A. P. Morris, 2008, Fault zone deformation controlled by carbonate mechanical stratigraphy, Balcones fault system, Texas, AAPG Bulletin, **92**, 359–380.
- Folk, R. L., 1959, Practical petrographic classification of limestones: AMGP Bulletin, **43**, 1–39.
- Folk, R. L., 1962, Spectral subdivision of limestone types, *in* Ham, W. E., ed., Classification of Carbonate Rocks-A Symposium: AAPG Memoir, **1**, 62–84.
- Fossen H., 2010, Structural geology: Cambridge University Press.
- Goodway B., 2001, A tutorial on AVO and Lamé constants for rock parameterization and fluid detection, accessed October 27, 2011; http://gsa.seg.org/pdf_forms/RecorderJune2001LMRAVO_new2007july.pdf.
- Gray D., 2002, Elastic inversion for Lamé parameters, 72nd Annual International Meeting, SEG, Expanded Abstracts, 213–216.
- Gray G. G., and T. F. Lawton, 2011, New constraints on timing of Hidalgoan (Laramide) deformation in the Parras and La Popa basins, NE Mexico: Boletín de la Sociedad Geológica Mexicana, **63**, 333–343, accessed January 27 2012; [http://boletinsgm.igeolcu.unam.mx/epoca04/6302/\(13\)Gray.pdf](http://boletinsgm.igeolcu.unam.mx/epoca04/6302/(13)Gray.pdf).
- Gray G. G., R. J. Pottorf, D. A. Yurewicz, K. I. Mahon, D. R. Pevear, and R. J. Chuchla, 2001, Thermal and chronological record of syn- to post-Laramide burial and exhumation, Sierra Madre Oriental, Mexico, *in* C. Bartolini, R. T. Buffler, and A. Cantú-Chapa, eds., The western Gulf of Mexico Basin: Tectonics, sedimentary basins, and petroleum systems: AAPG Memoir, **75**, 159–181.
- Gutiérrez-Paredes, H. C., M. Martínez-Medrano, and H. L. Sessarego, 2009, Provenance for the middle and upper Miocene sandstones of the Veracruz Basin, Mexico, *in* C. Bartolini and J. R. Román Ramos eds., Petroleum systems in the southern Gulf of Mexico: AAPG Memoir, **90**, 397–407.

- Guzmán, E. J., and Z. De Cserna, 1963, Tectonic History of Mexico, *in* O. E. Childs, Beebe, B. W., eds., *Backbone of the Americas – tectonic history from pole to pole: AAPG Special Volumes, M 2*, 113–129, accessed February 9, 2012; <http://search.datapages.com/data/open/offer.do?target=%2Fspecpubs%2Fstructure%2Fdata%2Fa151%2Fa151%2F0001%2F0100%2F0113.htm>.
- Hampson and Russell, 2005, Simultaneous inversion of pre-stack seismic data, 75th Annual International Meeting, SEG, Expanded Abstracts, 1633-1638, doi: 10.1190/1.2148008.
- Hernández-Martínez, R., 2009, Modelo Geológico del Campo, Internal report and presentation: PEMEX Exploración y Producción, unpublished.
- Hjelt S., 1992, Pragmatic inversion of geophysical data: Springer-Verlag, Lecture Notes in Earth Sciences, vol. 39.
- International Commission on Stratigraphy, 2010, International stratigraphic chart, accessed, February 9, 2012; http://www.stratigraphy.org/ics%20chart/09_2010/StratChart2010.pdf.
- Jennette D. C., T. F. Wawrzyniec, K. Foud, J. Meneses-Rocha, M. H. Holtz, S. Sakurai, S. Talukdar, F. Grimaldo, R. Muñoz, J. E. Lugo, d. Barrera, c. Williams, A. Escamilla, S. P. Dutton, W. A. William, D. B. Dunlap, J. A. Bellian, and E. H. Guevara, 2002, Play-element characterization of the Miocene and Pliocene Veracruz basin, southeastern Mexico: *Gulf Coast Association of Geological Societies Transactions*, **52**, 441–453, accessed October 21 2011; ww.oilprognosis.com/Articles/Suhas_Paper%202.pdf.
- Jennette D., T. Wawrzyniec, K. Fouad, D. B. Dunlap, J. Meneses-Rocha, F. Grimaldo, R. Muñoz, D. Barrera, C. T. Williams-Rojas, and A. Escamilla-Herrera, 2003, Traps and turbidite reservoir characteristics from a complex and evolving tectonic setting, Veracruz Basin, southeastern Mexico: *AAPG Bulletin*, **87**, 1599–1622, doi: 10.1306/05130302010.
- Kennet J. P. and M. S. Srinivasan, 1983, Neogene planktonic foraminifera: A phylogenetic atlas, Hutchinson Ross Publishing Company.

- Latimer R. B., R. Davidson, and P. Van Riel, 2000, An interpreter's guide to understanding and working with seismic-derived acoustic impedance data: *The Leading Edge*, **19**, 242-256, doi: 10.1190/1.1438580.
- Magoon L. B., T. L. Hudson, and H. E. Cook, 2001, Pimienta-Tamabra (!)—A giant supercharged petroleum system in the southern Gulf of Mexico, onshore and offshore Mexico, *in* C. Bartolini, R. T. Buffler, and A. Cantú-Chapa, eds., *The western Gulf of Mexico Basin: Tectonics, sedimentary basins, and petroleum systems: AAPG Memoir*, **75**, 83–125.
- Marion D., and D. Jizba, 1997, Acoustic properties of carbonate rocks: use in quantitative interpretation of sonic and seismic measurements, *in* H. Palaz, and K. J. Marfurt, eds., *Carbonate seismology: SEG, Geophysical developments no. 6*, 75-93.
- Martínez-Medrano M., R Vega-Escobar, F. Flores-Cruz, D. Ángeles-Marín, and C. López-Martínez, 2009, Integrated seismic and petrographic analyses of the sandstone reservoirs of the Tertiary Veracruz Basin, Mexico, *in* C. Bartolini and J. R. Román Ramos eds., *Petroleum systems in the southern Gulf of Mexico: AAPG Memoir*, **90**, 217–235.
- Mavko G., T. Mukerji, and J. Dvorkin, 2009, *The rock physics handbook, second edition tools for seismic analysis of porous media: Cambridge University Press*. 28, 2011; doi: 10.1017/CBO9780511626753.001.
- Meju M. A., 1994, *Geophysical data analysis: Understanding inverse problem theory and practice: SEG, Course Series, no. 6*.
- Menke W., 1984, *Geophysical data analysis: Discrete inverse theory: Academic Press Inc.*
- Mitchell J., 2011, Horizontal drilling of deep granite wash reservoirs, Anadarko Basin, Oklahoma and Texas: Shale Shaker, *The Journal of the Oklahoma City Geological Society*, **62**, 118–167.

- Morán-Zenteno D., 1994, Geology of the central region of Mexico: Chapter 3: Section I. The Geology of the Mexican Republic: AAGP Special volumes, SG 39, 55–74, accessed February 9, 2012; <http://search.datapages.com/data/open/offer.do?target=%2Fspecpubs%2Fhistory1%2Fdata%2Fa121%2Fa121%2F0001%2F0050%2F0055.htm>.
- Mossman R. W. and F. Viniegra, 1976, Complex fault structures in Veracruz Province of Mexico: AAPG Bulletin, **60**, No. 3, 379–388.
- Ortuño-Arzate S., H. Ferket, M.-C. Cacas, R. Swennen, F. Roure, 2003, Late Cretaceous carbonate reservoirs in the Córdoba Platform and Veracruz Basin, eastern Mexico, *in* C. Bartolini, R. T. Buffler, and J. Blickwede, eds., The Circum-Gulf of Mexico and the Caribbean: Hydrocarbon habitats, basin formation, and plate tectonics: AAPG Memoir, **79**, 476–514.
- Padilla-y-Sánchez R. J., 2007, Evolución geológica del sureste mexicano desde el Mesozoico al presente en el contexto regional del Golfo de México: Boletín de la Sociedad Geológica Mexicana, **LIX**, 19–42, accessed, October 21, 2011; [http://boletinsgm.igeolcu.unam.mx/epoca04/5901/\(3\)Padilla.pdf](http://boletinsgm.igeolcu.unam.mx/epoca04/5901/(3)Padilla.pdf)
- Palaz H, and K. J. Marfurt, 1997, Carbonate seismology: An overview, *in* H. Palaz, and K. J. Marfurt, eds., Carbonate seismology: SEG, Geophysical developments no. 6, 1–7.
- PEMEX, 2009, Internal reports of the field of study: PEMEX E&P, Activo Integral Veracruz, non-published proprietary information.
- PEMEX, 2010, Las reservas de hidrocarburos de México 1 de Enero de 2010: PEMEX Exploración y Producción, accessed, February 9 2012; <http://www.ri.pemex.com/files/content/Libro%202010.pdf>.
- PEMEX, 2011, Las reservas de hidrocarburos de México 1 de Enero de 2011: PEMEX Exploración y Producción, accessed, February 9 2012; http://www.ri.pemex.com/files/content/reservas_hidrocarburos_2011.pdf.

- Pendrel J., 2006, Seismic inversion — A critical tool in reservoir characterization: Scandinavian Oil-Gas Magazine, **5/6**, 19–22, accessed October 27, 2011; <http://www.fugrojason.com/regpages/ff/techpaperrequest.php?sn=CriticalTool>; http://www.fugro-jason.ru/readingroom/articles/reprint_seismicinversion.pdf.
- Prost, G., and M. Aranda, 2001, Tectonics and hydrocarbon systems of the Veracruz Basin, Mexico, in C. Bartolini, R. T. Buffler, and Cantú-Chapa, eds., The western Gulf of Mexico Basin: Tectonics, sedimentary basins, and petroleum systems: AAPG Memoir, **75**, 271–291.
- Rai C. S., and C. H. Sondergeld, 2011, Seismic reservoir modeling: lectures and class notes, Mewbourne School of Petroleum and Geological Engineering, The University of Oklahoma.
- Roure, F., H. Alzaga-Ruiz, J. Callot, H. Ferket, D. Granjeon, G. E. Gonzalez-Mercado, N. Guilhaumou, M. Lopez, P. Mougín, S. Ortuño-Arzate and M. Séranne, 2009, Long lasting interactions between tectonic loading, unroofing, post-rift thermal subsidence and sedimentary transfers along the western margin of the Gulf of Mexico: Some insights from integrated quantitative studies: Tectonophysics, **475**, 169-189; doi:10.1016/j.tecto.2009.04.012.
- Roy A., V. Jayaram, T. Kwiatkowski, and D. Devegowda, 2012, Learning from Past Experience in Shale Gas Reservoirs: A Predictive Machine-Learning Tool Based on a Generative Topographic Model to Estimate EURs and Well Productivity, submitted to 2013 SPE Reservoir Simulation Symposium.
- Russell B., and D. Hampson, 2006, The old and the new in seismic inversion: CSEG Recorder, December, 5–11, accessed April 22, 2011; <http://www.cseg.ca/publications/recorder/2006/12dec/dec2006-seismicinversion.pdf>.
- Scholle P. A., and D. S. Ulmer-Scholle, 2003, A color guide to the petrography of carbonate rocks: grains, textures, porosity, diagenesis: AAPG Memoir, **77**.
- Shue R. T., 1985, A simplification of the Zoeppritz equations: Geophysics, **50**, no.4, 609-614, accessed October 30, 2011; doi: 10.1190/1.1441936.

- Singleton S., 2011, The effects of seismic data conditioning on prestack simultaneous impedance inversion: GCSSEPM 31st Annual Bob. F. Perkins Research Conference on Seismic attributes—New views on seismic imaging: Their use in exploration and production, doi: 10.5724/gcs.11.31.0035.
- Tucker M. E., and V. P. Wright, 2008, Carbonate sedimentology: Blackwell Science Ltd.
- Verma S., A. Roy, R. Perez, and K. J., Marfurt, 2012, Mapping high frackability and high TOC zones in the Barnett shale: Supervised probabilistic neural networks vs. unsupervised multi-attribute Kohonen SOM, 82nd Annual International Meeting, SEG, Expanded Abstracts.
- Wallet B. C., M. C. de Matos, J. T. Kwiatkowski, and Y. Suarez., 2009, Latent space modeling of seismic data: An overview: The Leading Edge, **28**, 1454-1459, doi: 10.1190/1.3272700.
- Wang Z, 1997, Seismic properties of carbonate rocks, *in* H. Palaz, and K. J. Marfurt, eds., Carbonate seismology: SEG, Geophysical developments no. 6, 29–52.
- Whitcombe D. N., P. A. Connolly, R. L. Reagan, and T. C. Redshaw, 2002, Extended elastic impedance for fluid and lithology: Geophysics, **67**, 63-67, doi: 10.1190/1.1451337.
- Yilmaz O., 2001, Seismic data analysis processing, inversion, and interpretation of Seismic data: SEG.
- Zhang K., 2010, Seismic attribute analysis of unconventional reservoirs stratigraphic patterns, PhD dissertation, The University of Oklahoma, 147 p.

APPENDIX A: PETROGRAPHIC DESCRIPTION OF CORE SAMPLES

The area of study has 22 well cores cut in four reservoir units, EOC-10, EOC-20, EOC-30 and EOC-50, besides two cores drilled in the water bearing unit EOC-40. From the total cores, ten have petrographic analysis of X-ray diffraction (XRD) and point counting over thin sections. Figure A-1 shows the distribution of wells with core data that I used to analyze the petrographic information from XRD and point counting.

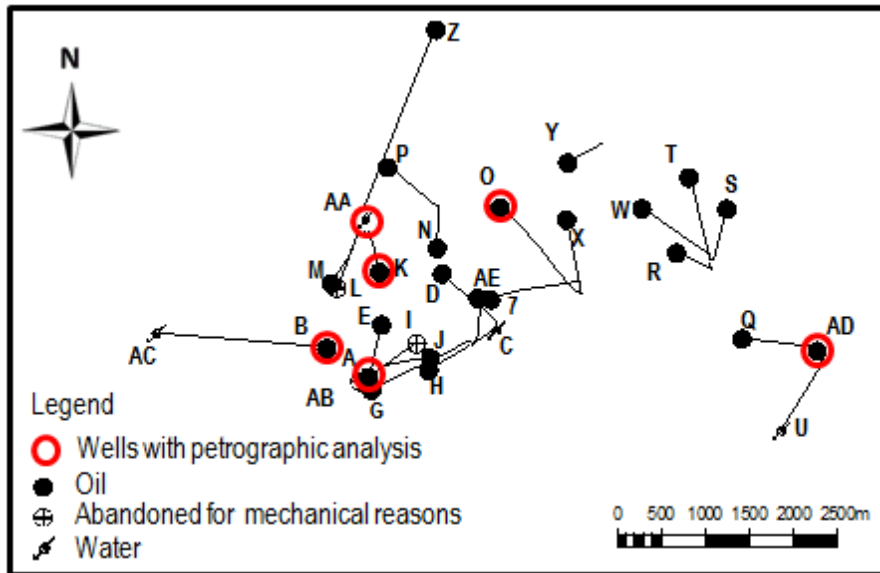


Figure A-1. Distribution of wells with petrographic analysis

Table A-1 summarizes the mineralogical composition in percentage of total weight of sampling resulted from X-ray diffraction analysis in addition to porosity, permeability and bulk density measurements at 800 psi of confining pressure. The average porosity obtained from cores measurements falls below the production cut-off value for the field which is 9%. This low porosity value is the result of core plug sampling in mostly cemented layers which are not representative of the producing intervals.

In Table A-2, I present the rock components from point counting analysis discretized in terms of porosity, allochemicals, calcareous clasts, detritus, cement, and matrix. Allochemical grains comprise pellets, fossils, ooids, and intraclasts (Folk, 1962). However, in my statistical analysis, I excluded all carbonate rock fragments counted as intraclasts from allochemical components, and I grouped those fragments under calcareous clasts category without differentiating between intraclasts or extraclasts. Considering the genesis of deposit, most of these rock fragments meet extraclasts characteristics. Extraclasts are defined as fragments of previous carbonates from out of the basin where they were deposited Folk (1962). I incorporate in the far right columns the Folk's and Dunham's classification of thin sections.

I used Table A-1 and Table A-2 to estimate the mineralogy and total components distribution for each reservoir unit: EOC-10, EOC-20, EOC-30, and EOC-50 and the water-bearing unit EOC-40. The joint distribution of mineralogy, rock components and porosity type for all units is shown in the main text of this thesis.

Figure A-2 shows the distribution of mineralogical components from XRD analysis in percentage of total sample weight for each unit. Note that units EOC-10, EOC-20 and EOC-30, which are Middle Eocene in age, present a similar calcite component from 80% to 85% in average, whereas EOC-50, the younger reservoir which is the only one producing heavy oil of 16 °API, has the highest calcite content of 95% in average. This difference in constitution suggest a difference in the source and may be in depositional environment.

Figure A-3 shows clay minerals distribution normalized to 100%. Note that reservoir units EOC-10 and EOC-20, producing in the crest of the anticlinal, have the

same clay minerals in similar proportion: illite/smectite ranging from 54 to 78%, illite/mica from 12 to 17%, kaolinite from 7 to 17% and chlorite from 3 to 12%. In contrast, EOC-50 contain the largest proportion of illite/mica (73%) and kaolinite is absent in EOC-30. Chlorite constitutes the smallest proportion of clay mineral in all the reservoirs. These differences in clay minerals may be link to degree of diagenesis.

Figure A-4 illustrates the distribution of total components from point counting analysis. Fossils are the most abundant grains under allochemical category. Pellets and ooids are present in trace quantities. Calcareous clasts are the second most predominant component in EOC-10 and EOC-20, while for EOC-30 and EOC-50 is matrix. Allochemical grains and calcareous clasts in combination with cement and matrix are responsible for the high calcite mineral content that XRD analysis reflects. All the reservoirs present small detritus content that ranges from 1 to 3.7% of the total, which is additionally supported by the mineralogy distribution from XRD analysis. Matrix, cement and porosity content varyies independently of depth and stratigraphical position. Note that the most porous reservoir is EOC-50 positioned immediately below the main unconformity in the east flank of the anticline.

I normalized the total porosity from point counting analysis to 100% in order to estimate the distribution of porosity types (Figure A-5). There is no correlation of porosity type from one reservoir to another. Microporosity is the predominant type in EOC-20 and EOC-30. Moldic and interparticle porosity dominates in EOC-10 while EOC-50 presents the most equally distribution of intraparticle, interparticle, microporosity and intercrystalline porosity types.

Semiquantitative petrographic description of the Eocene carbonate conglomerates

		Point counting (thin section analysis)																		
		Porosity (normalized to 100%)							Total components (allochemical, orthochemical and total porosity normalized to 100%)											
Well	Core Sample	Reservoir horizon	Depth	Interparticle	Intraparticle	Intercrystalline	Moldic	Microporosity	Fracture	Sum	Total porosity	Allochemical (fossils, ooids, pellets)	Calcareous clasts	Detritus (quartz feldspar, and lithics)	Cement	Matrix	Sum	Dunham classification	Folk classification	Reservoir quality
AD	3A	EOC-50	2891.29								39.3	11.7	15.0	30.3	3.7	100	Grainstone	Poorly washed intrasparite	Bad	
AD	7A	EOC-50	2893.03		100.0					2.7	38.7	10.0	12.0	30.7	6.0	100	Grainstone	Poorly washed intrasparite	Regular	
AD	11A	EOC-50	2896.47								36.0	12.0	17.0	30.0	5.0	100	Packstone – Grainstone	Poorly washed intrasparite	Bad	
AD	15A	EOC-50	2898.18								33.3	15.0	14.3	32.3	5.0	100	Grainstone	Unsorted intrasparite	Bad	
AD	16A	EOC-50	2937								22.3	4.3	2.0	6.7	64.7	100	Wackestone – Packstone	Packed biomicrite	Bad	
AD	17A	EOC-50	2937.82								58.7	15.0	10.0	7.0	9.3	100	Packstone	Packed biomicrite	Bad	
AD	21A	EOC-50	2938.81		100.0						0.3	60.0	8.3	2.7	26.3	2.3	100	Grainstone	Rounded biosparite	Bad
AD	25A	EOC-50	2939.94		100.0						0.3	63.3	17.0	4.7	7.3	7.3	100	Packstone – Grainstone	Poorly washed biosparite	Bad
O	N1H1	EOC-50	2809.11					100.0			5.0	40.0	14.0	3.0	18.0	20.0	100	Packstone – Grainstone	Poorly washed intrasparite	Bad
O	N1H2	EOC-50	2810.5					100.0			4.0	40.0	12.0	3.0	24.0	17.0	100	Packstone – Grainstone	Poorly washed intrasparite	Bad
O	N1H3	EOC-50	2811.08	53.8	7.7	23.1	0.0	15.4		100	13.0	58.0	5.0	1.0	23.0		100	Grainstone	Poorly sorted biosparite	Good
O	N1H5	EOC-50	2812.23	42.9		35.7	14.3	7.1		100	14.0	51.0	5.0	0.0	17.0	13.0	100	Packstone – Grainstone	Poorly washed biosparite	Good
O	N1H8	EOC-50	2813.08	43.5	26.1	13.0	8.7	8.7		100	23.0	58.0	4.0	3.0	8.0	4.0	100	Packstone – Grainstone	Poorly washed biosparite	Good
O	N1H11	EOC-50	2813.96	36.4	36.4	9.1		18.2		100	11.0	63.0	2.0	1.0	11.0	12.0	100	Packstone	Packed biomicrite	Regular-bad
O	N1H14	EOC-50	2815.45																No thin section	
O	N1H17	EOC-50	2816.25	12.0	24.0	12.0	48.0	4.0		100	25.0	40.0	2.0	1.0	7.0	25.0	100	Packstone – Grainstone	Poorly washed biosparite	Good
A	N4-H2	EOC-40	2513.60		72.5	24.1	3.4			100	9.7	35.0	4.0	5.3	24.7	21.3	100	Packstone – Grainstone	Poorly washed biosparite	Bad
A	N4-H5	EOC-40	2516.00	3.9	46.1	30.7	15.4		3.8	100	17.3	33.7	8.3	6.3	16.7	17.7	100	Packstone – Grainstone	Poorly washed intrasparite	Bad
A	N4-H6	EOC-40	2516.30	73.2	18.3	4.2	4.2			100	23.6	16.0	19.3	16.7	14.3	10.0	100	Packstone – Grainstone	Poorly washed intrasparite	Poor
A	N4-H9	EOC-40	2520.80	33.9	37.1	20.9	8.1			100	20.7	33.3	13.3	9.3	17.3	6.0	100	Packstone – Grainstone	Poorly washed intrasparite	Poor
O	N2H1	EOC-30	2970.22	7.7	30.8	15.4		46.2		100	13.0	63.0	3.0	4.0	4.0	13.0	100	Packstone – Grainstone	Packed biomicrite	Regular-bad
O	N2T6	EOC-30	2971.92					100.0		100	4.0	63.0	1.0	3.0	25.0	4.0	100	Grainstone	Poorly sorted biosparite	Bad
O	N2H7	EOC-30	2972.17					100.0		100	5.0	12.0		3.0	8.0	72.0	100	Wackestone	Poorly washed biosparite	Bad
O	N2H8	EOC-30	2972.76					100.0		100	5.0	46.0	8.0	2.0	14.0	25.0	100	Wackestone – Packstone	Biomicrite	Bad
O	N2T12	EOC-30	2974.52															Wackestone	Sparse intramicrite	Bad
O	N2H16	EOC-30	2975.58					100.0		100	11.0	57.0	3.0	3.0	13.0	13.0	100	Packstone	Packed biomicrite	Bad
O	N2H17	EOC-30	2975.9					100.0		100	5.0	56.0	2.0	6.0	19.0	12.0	100	Grainstone	Poorly sorted biosparite	Bad
O	N2H20	EOC-30	2977.04					100.0		100	5.0	36.0	9.0	2.0	21.0	27.0	100	Packstone – Grainstone	Packed intramicrite	Bad
O	N2H23	EOC-30	2978.27																No thin section	
A	N5-H1	EOC-20	2592.80		50.0	25.0	25.0			100	4.0	36.7	19.0	2.3	36.0	2.0	100	Grainstone	Poorly sorted intrasparite	Bad
A	N5-H4	EOC-20	2594.07		44.4		55.6			100	3.0	37.7	12.0	2.3	41.3	3.7	100	Grainstone	Poorly sorted intrasparite	Bad
A	N5-H8	EOC-20	2596.94	48.9	6.4	14.9	29.8			100	15.7	43.0	15.0	3.0	21.3	2.0	100	Grainstone	Poorly sorted biosparite	Excellent
A	N5-H10	EOC-20	2597.47	7.7	38.5	19.2	34.6			100	8.7	48.3	11.0	2.0	27.0	3.0	100	Grainstone	Poorly sorted biosparite	Good
B	N1H1	EOC-20	3330.06					100.0		100	5.0	25.0	55.0	3.0	12.0		100	Grainstone	Poorly sorted intrasparite	Bad
B	N1H2	EOC-20	3330.23					100.0		100	5.0	54.0	21.0	7.0	13.0		100	Grainstone	Poorly sorted intrasparite	Bad
B	N1T3	EOC-20	3330.73																No thin section (too argillaceous)	
B	N1H4	EOC-20	3331.20					100.0		100	4.0	45.0	20.0	5.0	26.0		100	Grainstone	Poorly sorted biosparite	Bad
AD	30A	EOC-20	3170.57								55.3	22.7	3.0	17.3	1.7	100	Grainstone	Poorly sorted biosparite	Bad	
AD	35A	EOC-20	3172.29								54.3	20.3	1.3	6.3	17.7	100	Grainstone	Poorly sorted biosparite	Bad	
AD	44A	EOC-20	3174.85								49.0	20.0	7.7	17.7	5.7	100	Grainstone	Poorly sorted intrasparite	Bad	
AD	47A	EOC-20	3175.78								58.3	15.3	6.0	5.0	15.3	100	Packstone – Grainstone	Poorly washed biosparite	Bad	
AD	53A	EOC-20	3178.25		100.0					100	3.0	41.3	21.3	4.3	0.7	29.3	100	Packstone – Grainstone	Poorly washed intrasparite	Bad
K	F1	EOC-10	2662.11								29.0	43.0	0.3	8.0	19.7	100	Packstone – Grainstone	Poorly washed intrasparite	Bad	
K	F2	EOC-10	2662.6		64.0		36.0			100	3.7	13.3	40.0	0.0	6.0	37.0	100	Packstone	Packed intramicrite	Poor
K	F3	EOC-10	2663.98	8.0	40.2		51.8			100	8.4	24.0	30.7	1.3	6.0	29.7	100	Packstone	Poorly washed biosparite	Excellent
K	F4	EOC-10	2665.36								32.0	35.7	1.0	6.3	25.0	100	Packstone	Packed intramicrite	Bad	
K	F5	EOC-10	2666.94	100.0						100	0.3	23.3	55.0	6.3	4.3	10.7	100	Packstone – Grainstone	Poorly washed intrasparite	Bad
AA	N4-H1	EOC-10	2556.6								30.7	17.7	6.0	35.3	10.3	100	Packstone – Grainstone	Poorly washed intrasparite	Bad	
AA	N4-H4	EOC-10	2557.1								41.0	18.0	1.3	15.3	24.3	100	Packstone	Packed intramicrite	Bad	
AA	N4-H7	EOC-10	2560								32.0	17.7	0.3	7.0	43.0	100	Packstone	Packed intramicrite	Bad	
AA	N4-H9	EOC-10	2562.15								30.3	26.3	3.7	15.0	24.7	100	Packstone	Packed intramicrite	Bad	
AA	N4-H11	EOC-10	2563.62								32.0	17.3	1.7	12.3	36.7	100	Packstone	Packed intramicrite	Bad	
AA	N5-H1	EOC-10	2572			und					29.0	29.7	1.0	17.0	23.3	100	Packstone – Grainstone	Poorly washed intrasparite	Bad	
AA	N5-H3	EOC-10	2572			und	und				36.0	23.3	1.3	8.7	30.7	100	Packstone	Packed intramicrite	Bad	
AA	N5-H5	EOC-10	2572			und					35.7	11.0	3.7	9.7	40.0	100	Packstone	Packed intramicrite	Bad	
AA	N5-H11	EOC-10	2572	0.0	21.7		78.3			100	7.7	26.3	18.7	2.0	24.0	21.3	100	Packstone – Grainstone	Poorly washed intrasparite	Poor
AA	N5-H14	EOC-10	2572	0.0		und					32.0	21.7	3.7	35.3	7.3	100	Grainstone	Poorly sorted intrasparite	Bad	

Table A–2. Semiquantitative petrographic description from point counting analysis. Gray boxes indicates zero, n/a are non-available, and und means undetermined values.

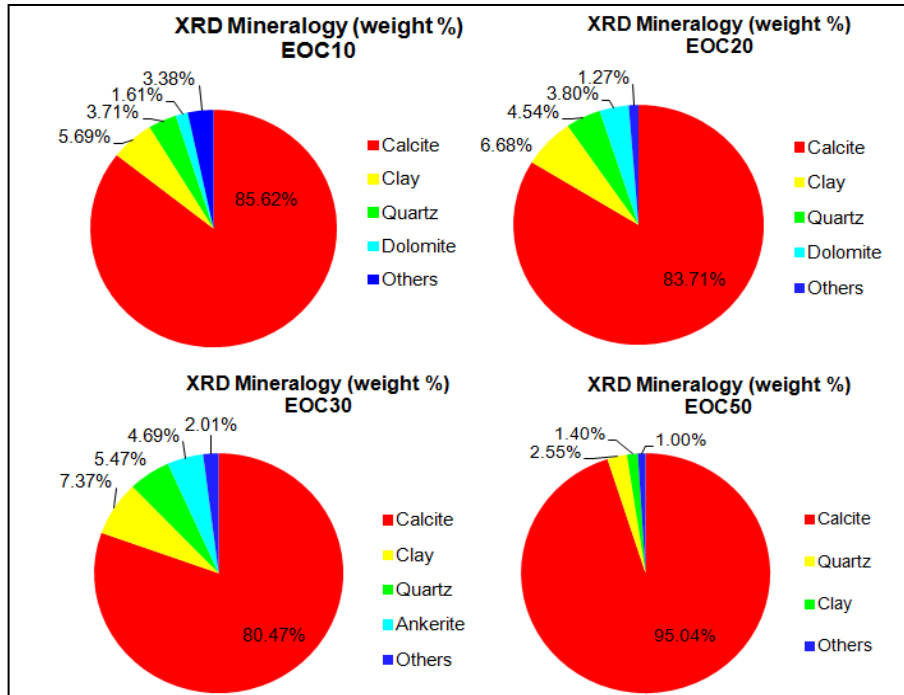


Figure A-2. Mineralogical content in weight percent from XRD analysis for reservoir units EOC-10, EOC-20, EOC-30 and EOC-50.

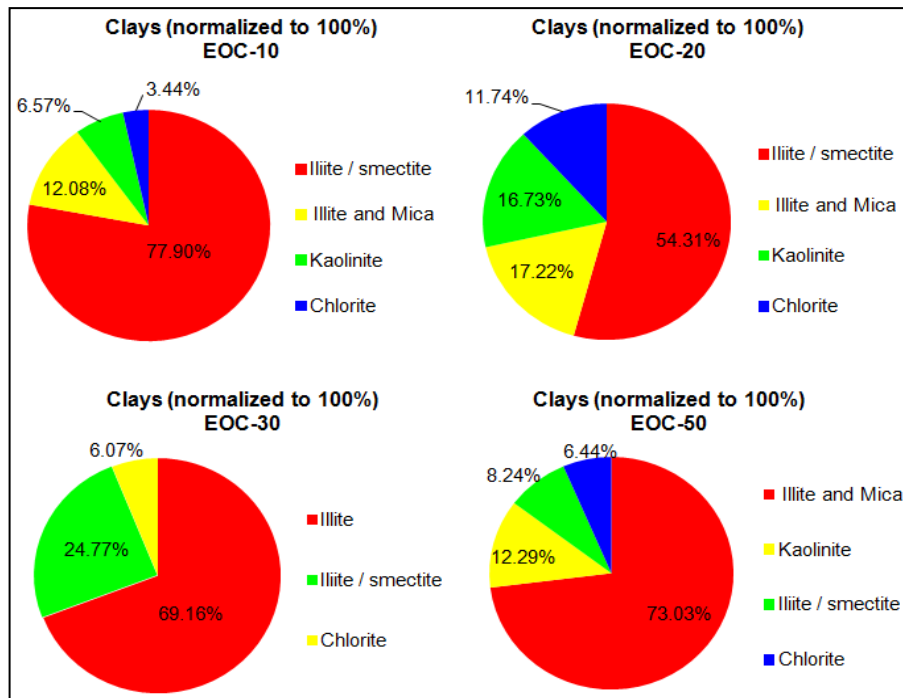


Figure A-3. Clay minerals, normalized to 100% from XRD analysis, for reservoir units EOC-10, EOC-20, EOC-30 and EOC-50.

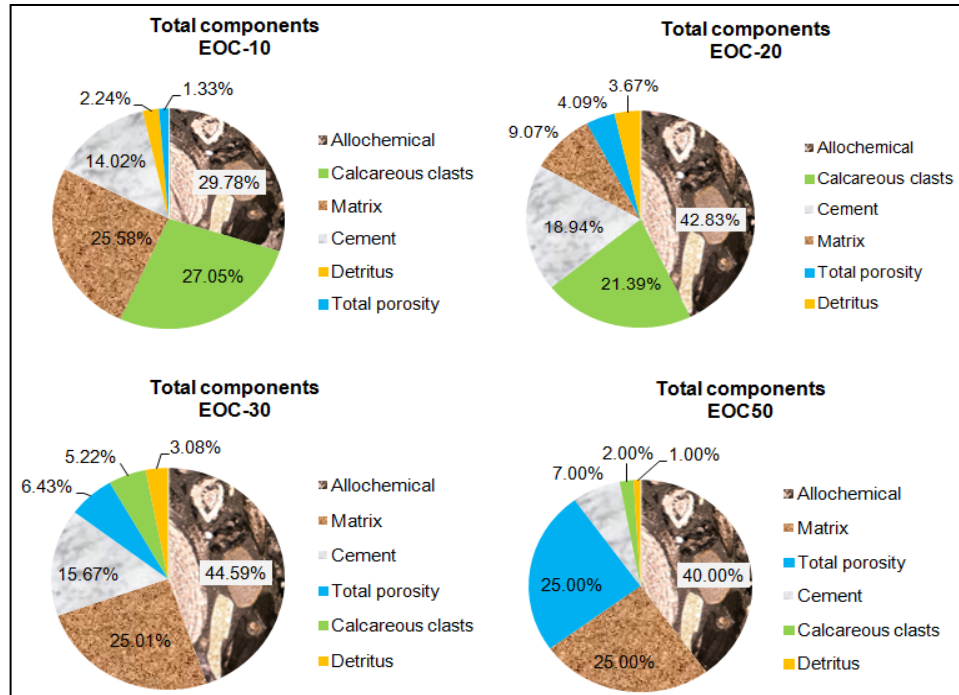


Figure A-4. Total components distribution from point counting analysis for reservoir units EOC-10, EOC-20, EOC-30 and EOC-50.

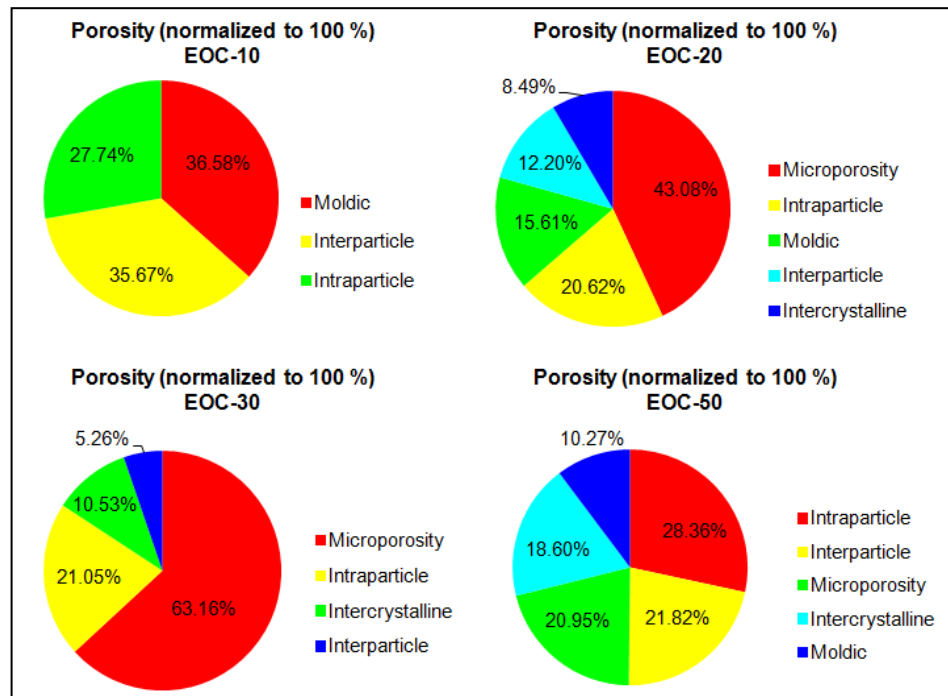


Figure A-5. Distribution of types of porosity normalized to 100% of the 4 reservoir units with core data: EOC-10, EOC-20, EOC-30 and EOC-50.

Figure A-6 shows the mineralogy and total components distribution for the water-bearing unit EOC-40. The age of this unit is uncertain. It was first dated as Late Miocene; however, this age may be anomalous since the same unit was dated as Middle Eocene; however, this age may be anomalous since the same unit was dated as Middle Eocene in other well just 100 m apart, and the mineral content is similar to the confirmed Middle Eocene reservoir units EOC-10, EOC-20 and EOC-30.

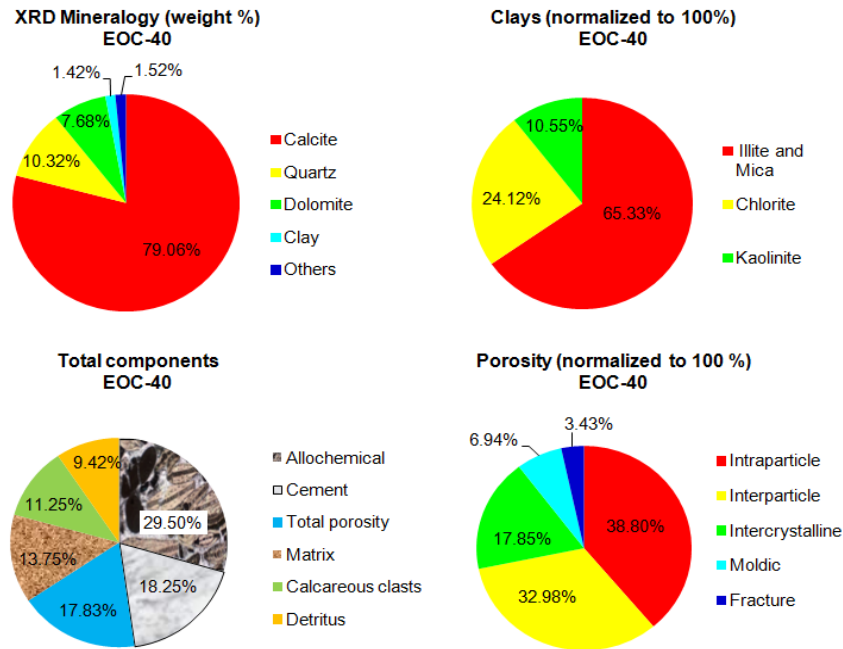


Figure A-6. Distribution of mineralogy and clays normalized to 100% from XRD analysis, and total components and porosity normalized to 100% from point counting analysis of water bearing unit EOC-40.

Figures A-7 to A-16 correspond to slabbed core photographs and thin sections described quantitatively in Table A-1 and A-2. Note that changes in color and texture on slabbed cores are directly related to variation in reservoir quality. Dark brown intervals corresponds to oil impregnated porous intervals (Figures A-11 and A-14) which contrast with the light-gray highly cemented (Figures A-12 and A-13). Observed in Figures A-8, A-13 and A-16 large clasts, ranging from subangular to rounded, which provide evidence of high energy transportation over long distance.

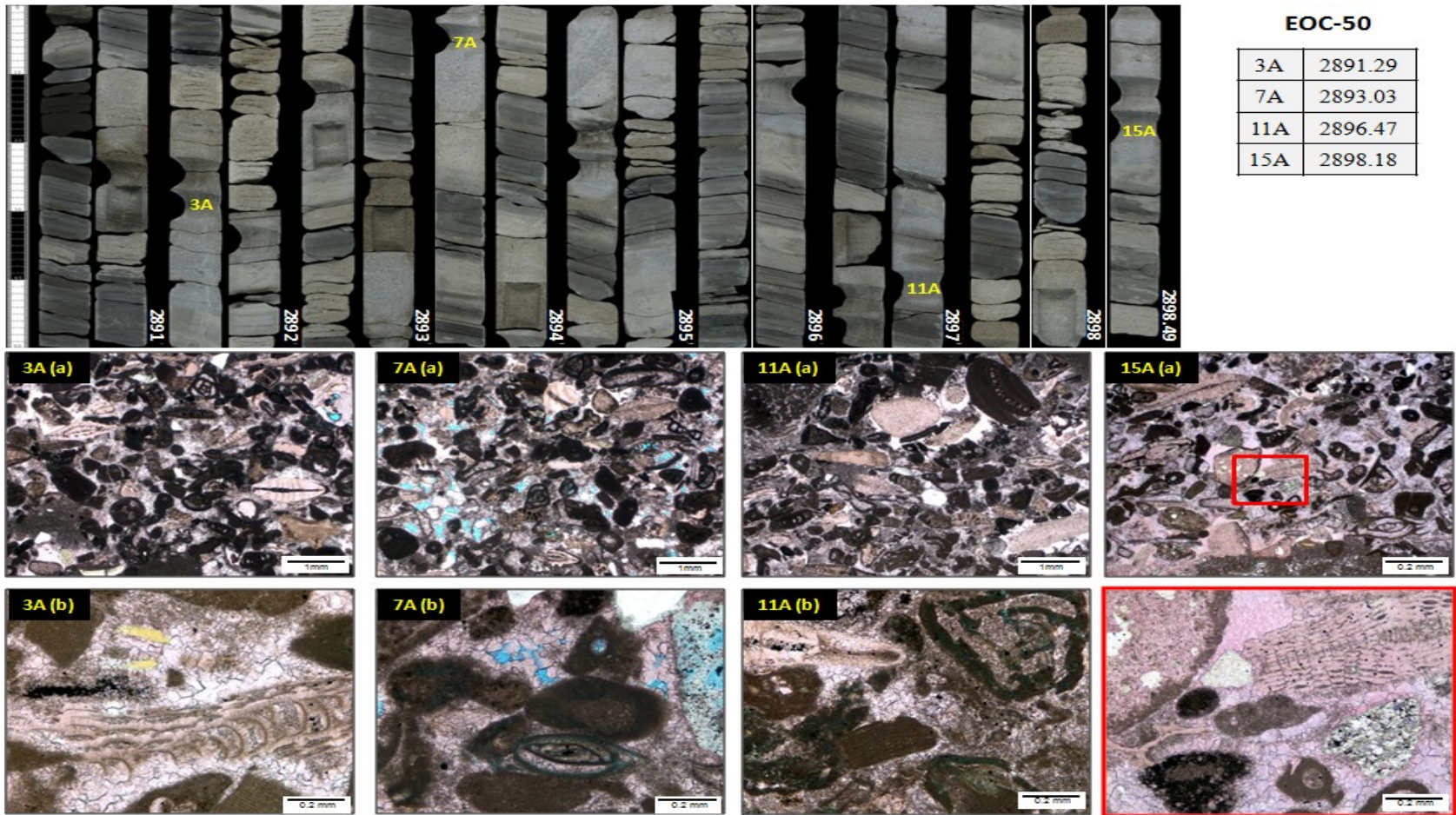


Figure A-7. Slabbed core and two thin sections at different scale (a) and (b) for each depth position of well AD, in EOC-50. Red box indicates magnification of sample 15A. Fossils are the dominant grain component of this grainstone. Dissolution increased the porosity in 74A. (Data courtesy of PEMEX E&P).

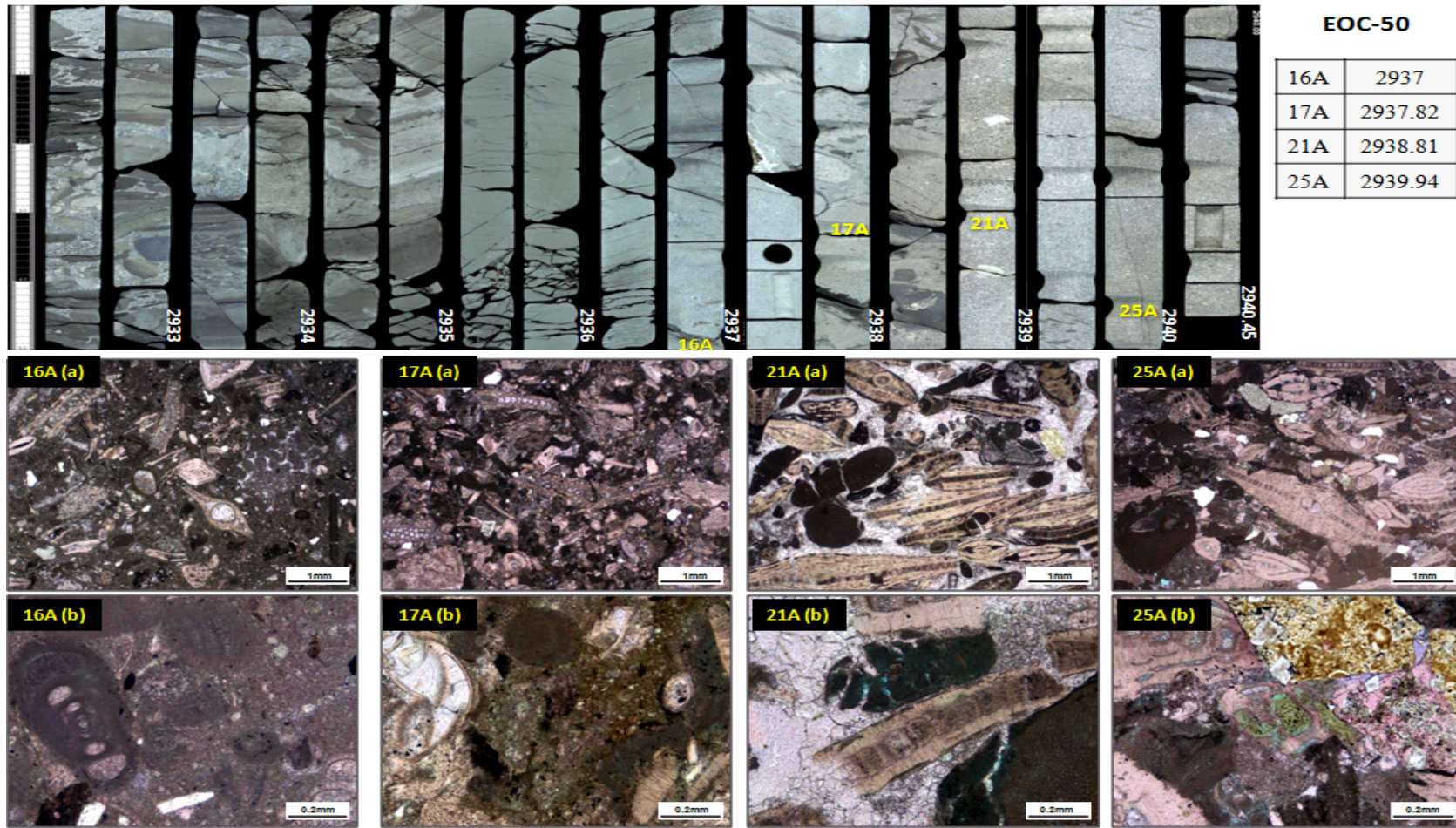
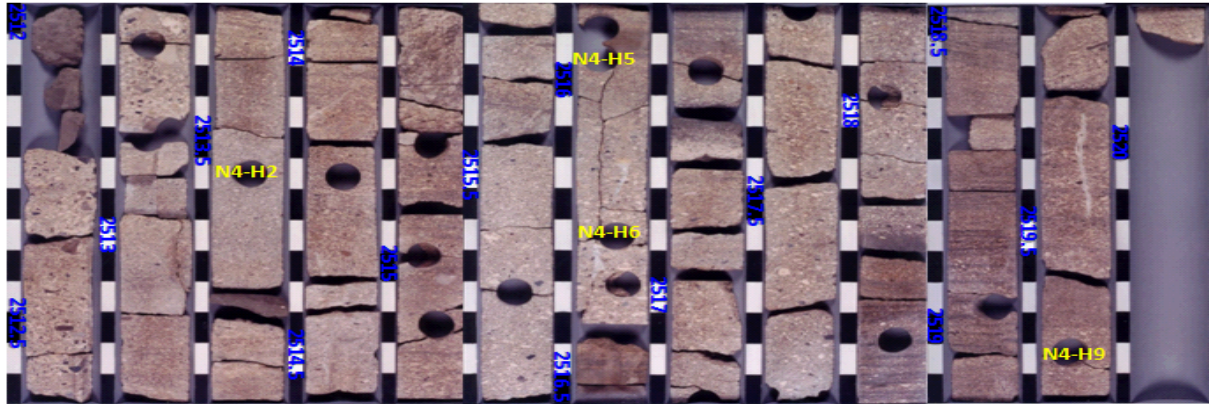


Figure A-8. Slabbed core and two thin sections at different scale (a) and (b) for each depth position of well AD, in EOC-50. Textures varies from packstone to grainstone. Note in slabs subrounded to rounded clasts at the top of the core and above first thin section 17A. Fossils are the dominant grain component. (Data courtesy of PEMEX E&P).



EOC-40

N4-H2	2513.60
N4-H5	2516.00
N4-H6	2516.30
N4-H9	2519.80

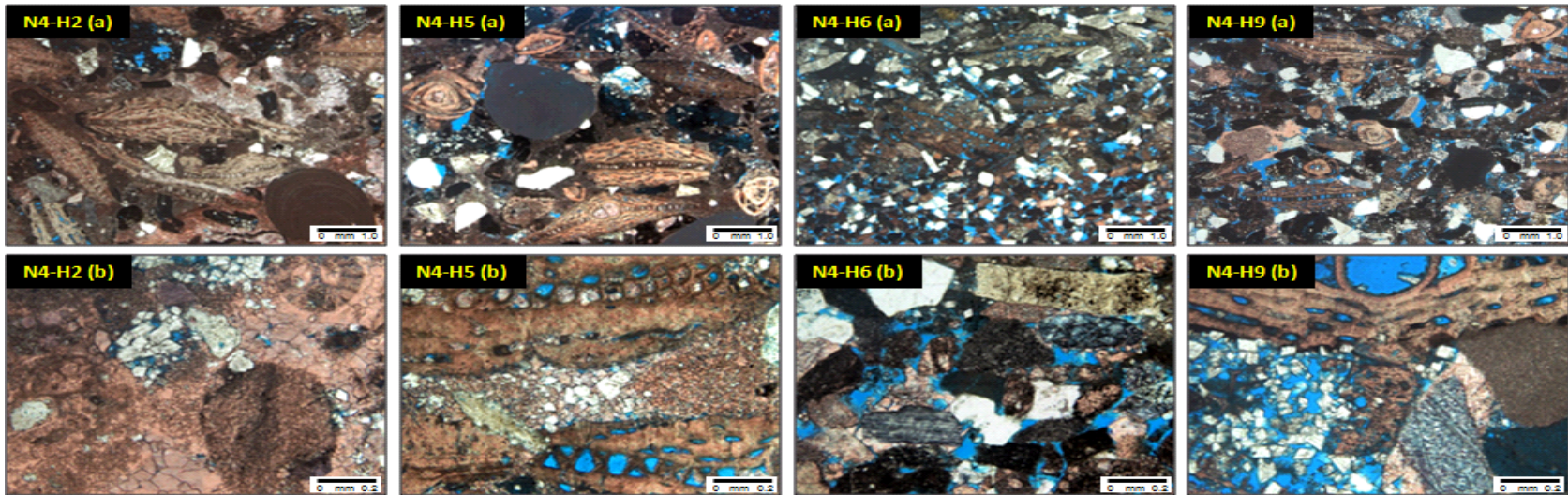


Figure A-9. Slabbed core and two thin sections at different scale (a) and (b) for each depth position of well A, in EOC-40. Textures vary from packstone to grainstone. Note that fossils are the dominant grain component in N4-H2 and N4-H5. Dolomitization has increased porosity in samples N4-H6 and N4-H9. Note angular and sub-angular clasts presence. (Data courtesy of PEMEX E&P).

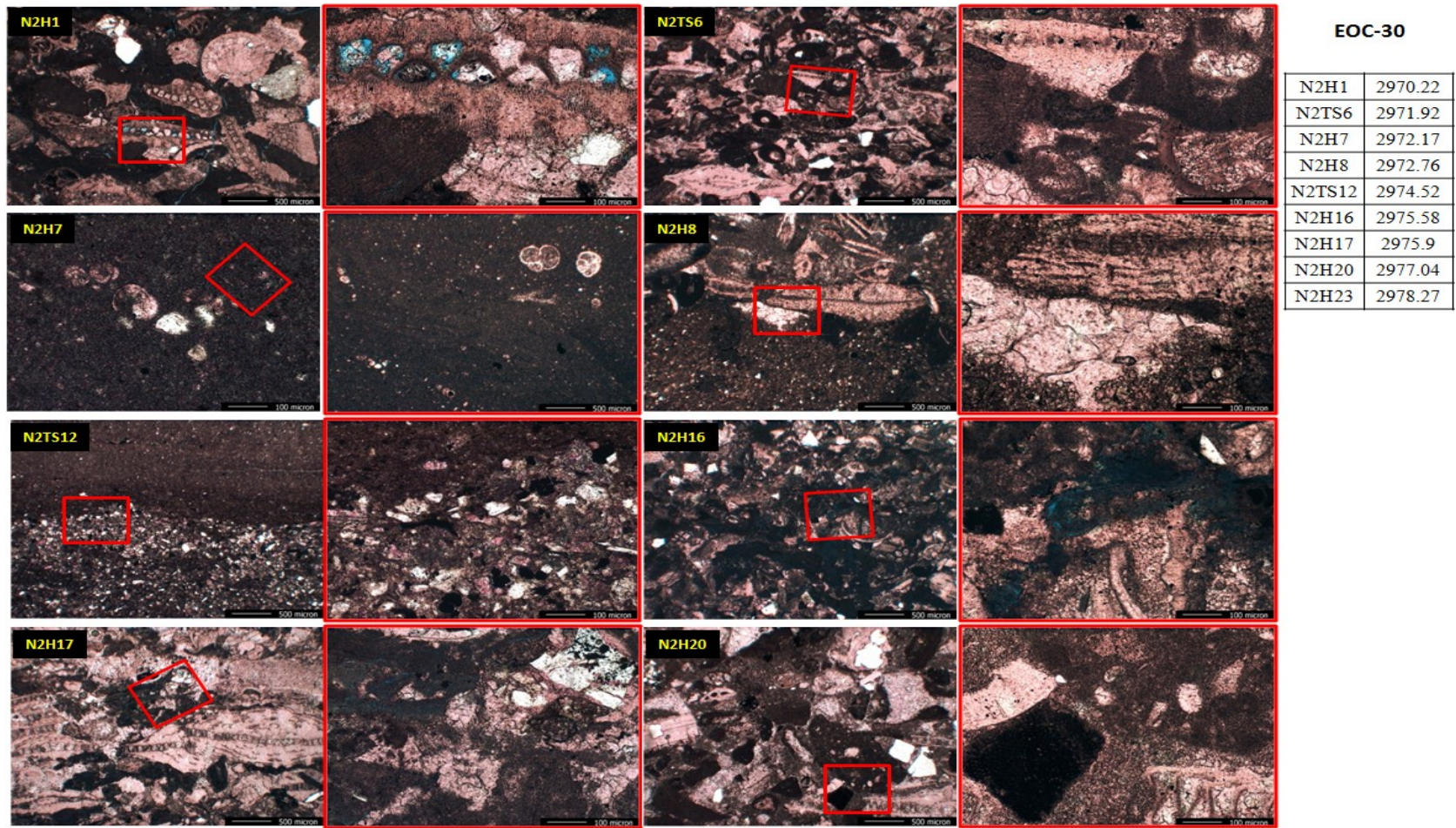


Figure A-10. Thin sections of well C in EOC-30. Red boxes indicate position of magnifications of each section at the right. Textures vary from mudstone to wackestone with fragmented fossils and crystals of dolomite, calcite and quartz. (Data courtesy of PEMEX E&P).



EOC-20

N5-H1	2592.80
N5-H4	2594.07
N5-H8	2596.94
N5-H10	2597.47

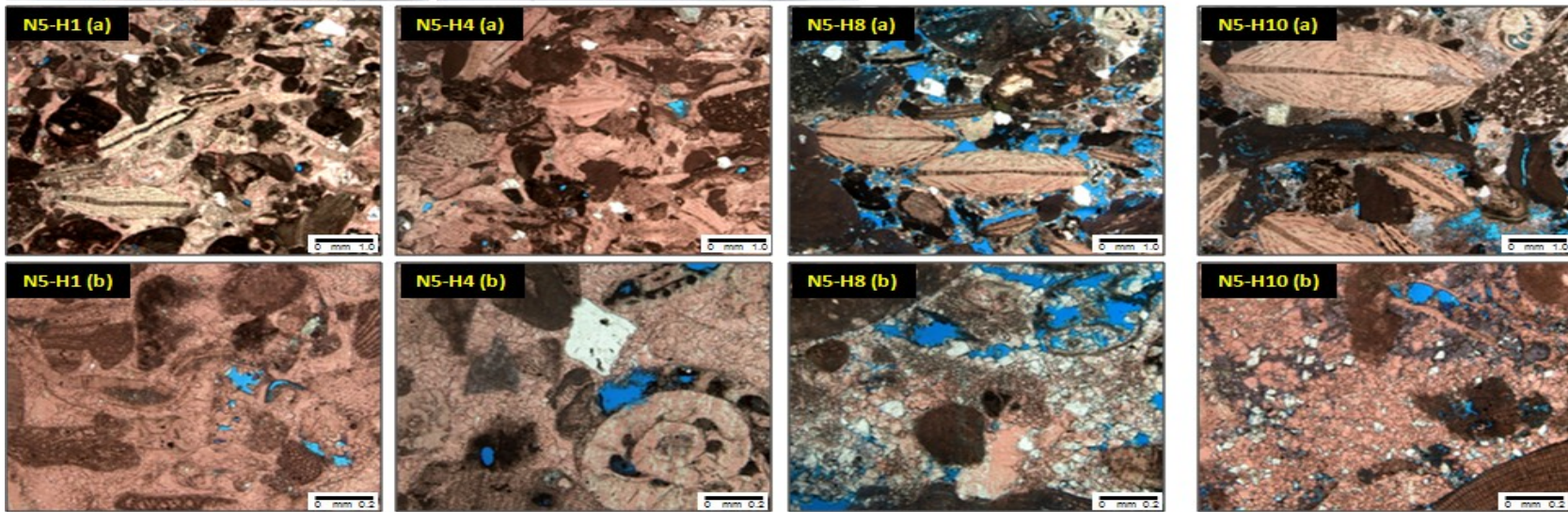
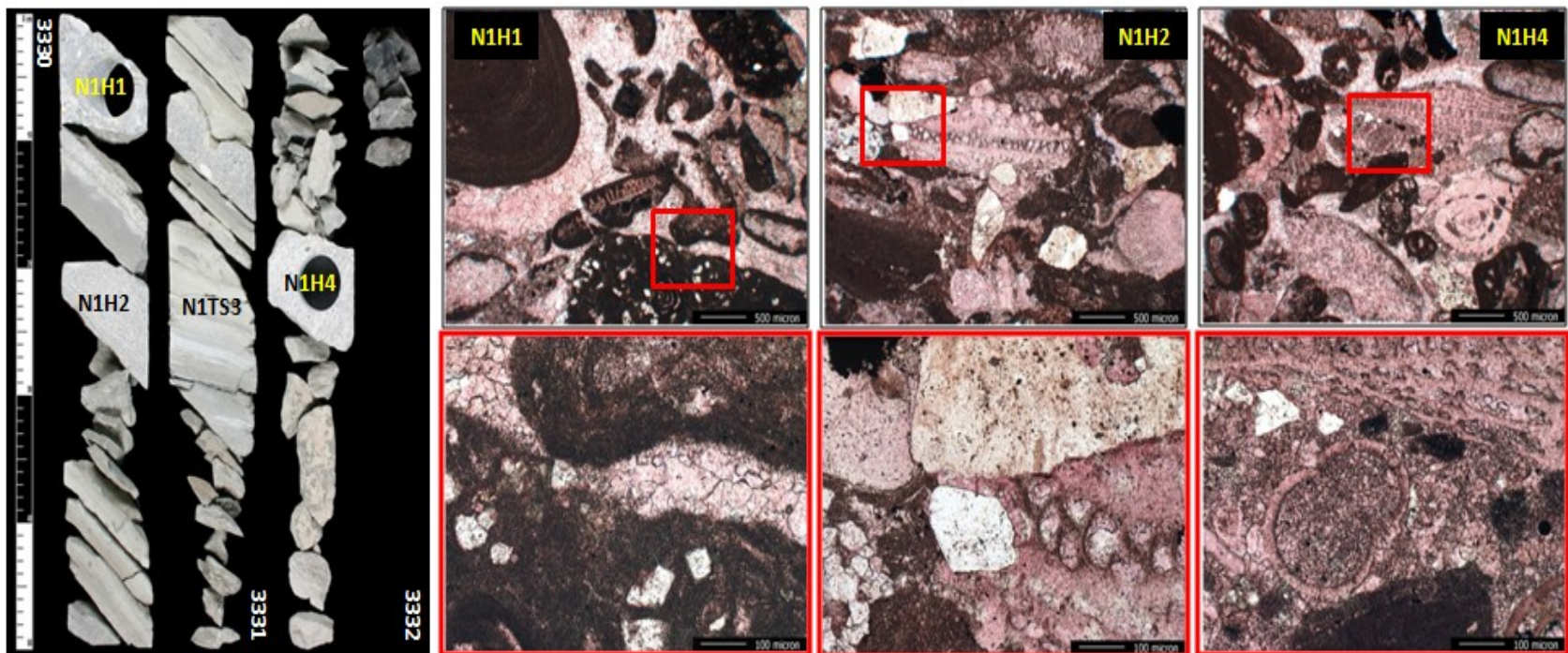


Figure A-11. Slabbed core and two thin sections at different scale (a) and (b) for each depth position of well A in EOC-20. Fossils are the dominant grain component of this grainstone. Note dissolution and dolomitization in N5-H8 and N5-H10 increasing porosity besides subrounded to rounded carbonate clasts. Brown intervals are oil impregnated. (Data courtesy PEMEX E&P).



EOC-20

N1H1	3330.06
N1H2	3330.23
N1TS3	3330.73
N1H4	3331.20

Figure A-12. Core slab and thin sections of well B in EOC-20. Red boxes indicate position of magnifications of each section in the bottom. Fossiliferous grainstone with minor calcite-filled fractures, subangular to subrounded carbonate clasts. Cementation has occluded all pores. (Data courtesy of PEMEX E&P).

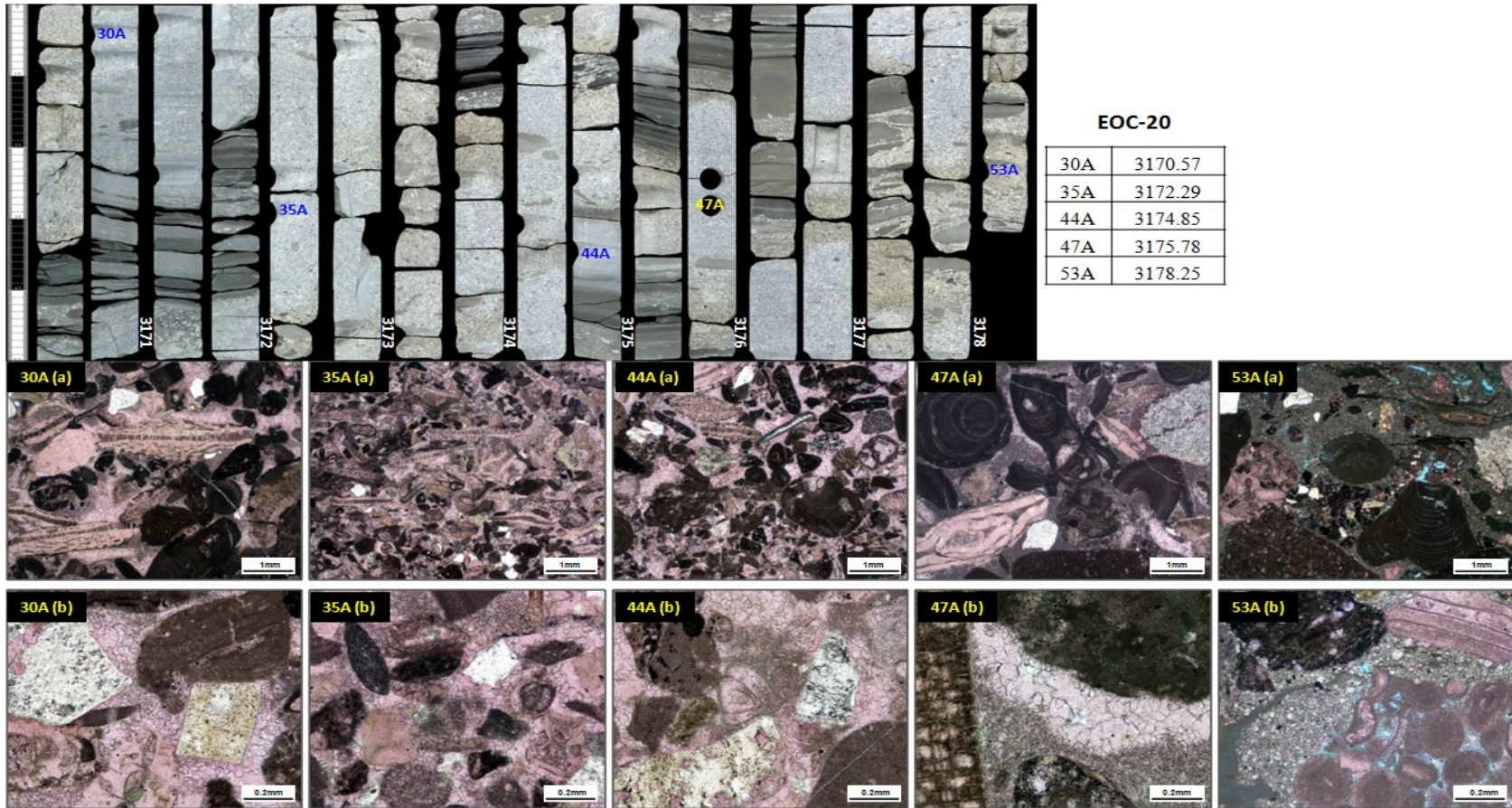


Figure A-13. Slabbed core and two thin sections at different scale (a) and (b) for each depth position of well AD in EOC-20. Fossils, red algae and benthic foraminifers, are the dominant grain component of this grainstone. Note redeposited sub-angular to sub-rounded carbonate clasts in section 53A(b) and slabs. There are minor calcite-filled fractures in 30A, 44A and 47A. (Data courtesy of PEMEX E&P).

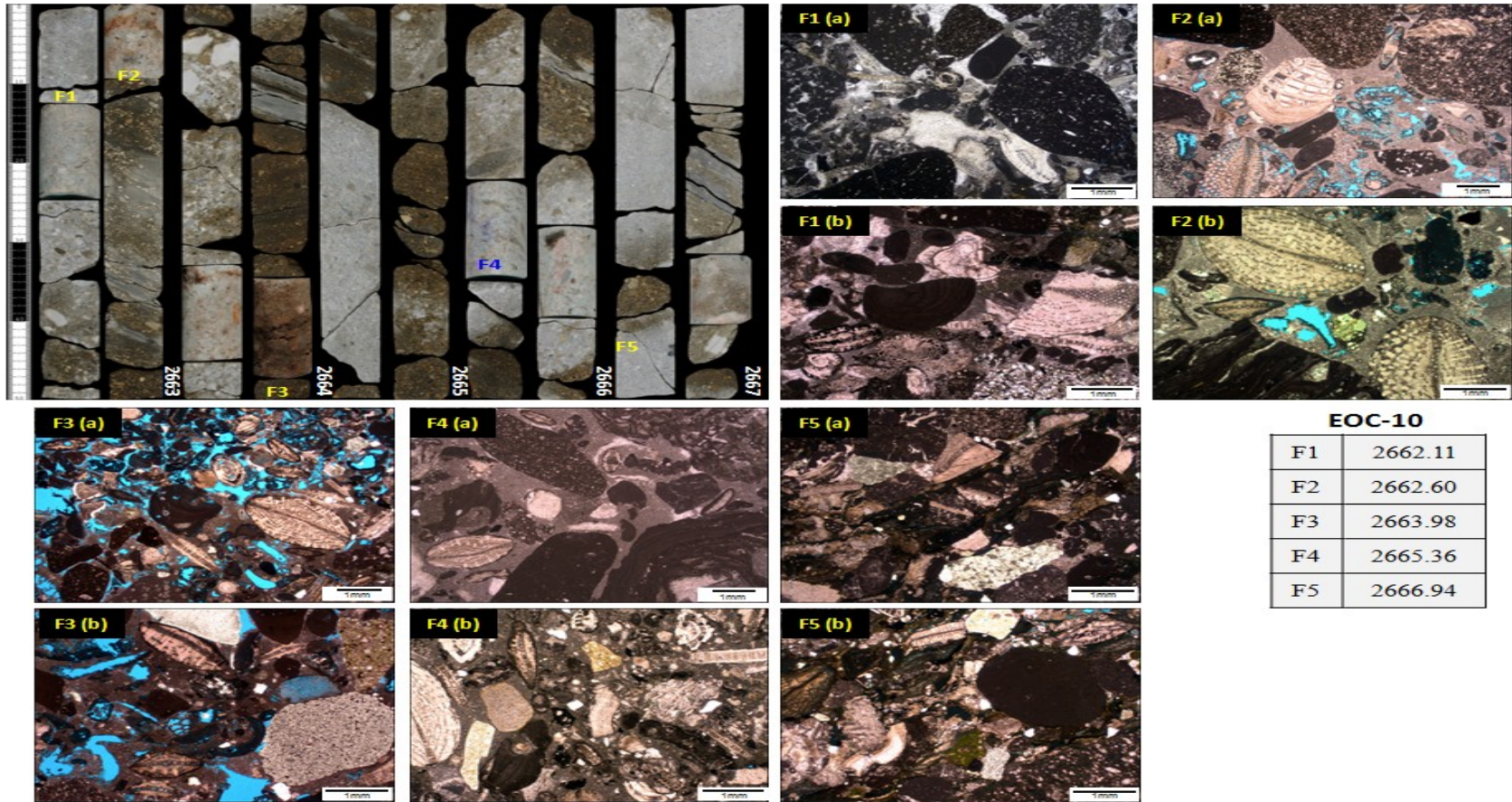
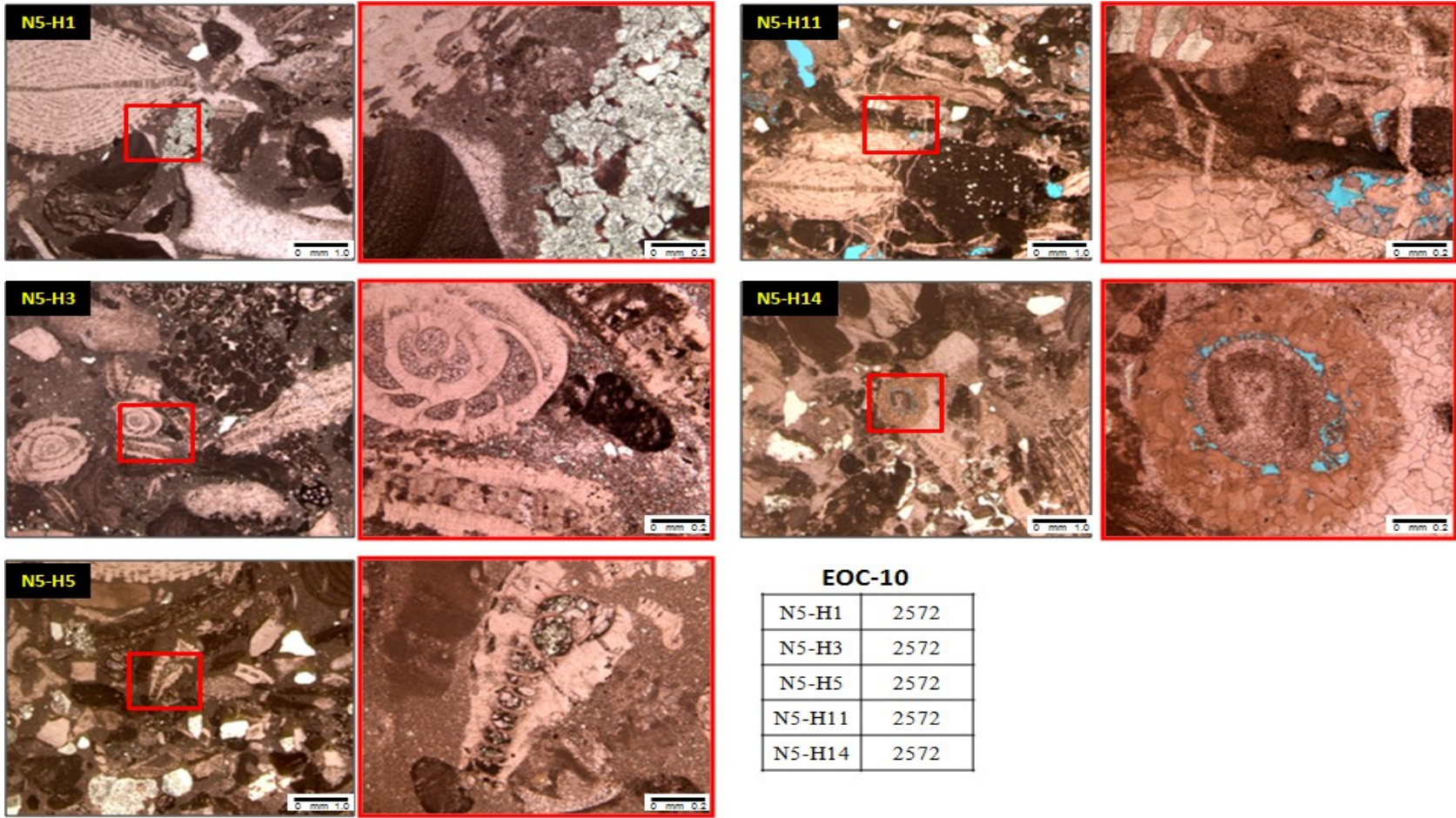


Figure A-14. Slabbed core and two thin sections at different scale (a) and (b) for each depth position of well K, the most productive well in EOC-10. Textures vary from wackestone to grainstone. Dissolution has increased porosity in F3 while cementation and micritization has reduce it in the others. Note in all sections and slabs the presence of subrounded carbonate clasts. (Data courtesy of PEMEX E&P).



EOC-10

N5-H1	2572
N5-H3	2572
N5-H5	2572
N5-H11	2572
N5-H14	2572

Figure A-15. Thin sections of well AA in EOC-10. Red boxes indicate position of magnifications of each section at the right. Fossiliferous packstone affected by different diagenetic processes such as cementation (N5-H14), dolomitization (N5-H1), fracturing (N5-H11) and dissolution (N5-H11). No photos available of the slabbled core. (Data courtesy of PEMEX E&P).

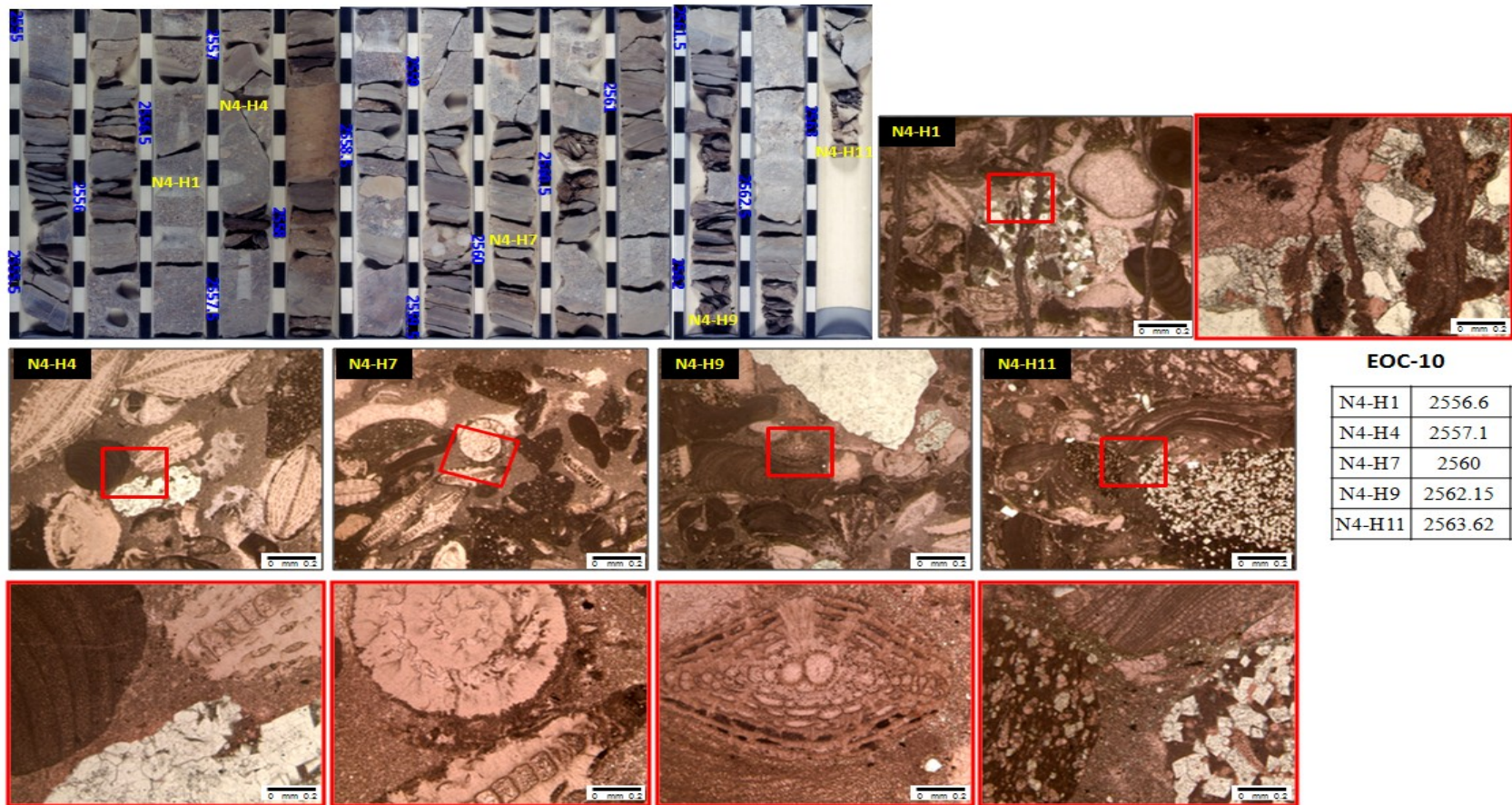


Figure A-16. Core slab and thin sections of well AA, in EOC-10. Red boxes indicate position of magnifications of each section at the right (N4-H1) and in the bottom. This poorly washed biomicrite is affected by diagenetic processes such fracturing (N4-H1), micritization (N4-H1, N4-H4), dolomitization (N4-H11) and calcite replacement (N4-H17). Note clasts in slabs and sections. (Data courtesy of PEMEX E&P).

I present in Tables A–3 and A–4 diagenesis interpretation of the thin sections previously shown in Figures A–8 to A–16. I compiled and verified this interpretation from the reports of core well analysis in PEMEX, (2009).

Well	Core Sample	Reservoir horizon	Depth	Porosity (%)	Permeability (md)	Compaction	Micritization	Piritization	Dissolution	Cementation (calcite)	Replacement by dolomite	Fracturing	Fracture filling	Neomorphism	Observations
AD	3A	EOC50	2891.29	4.2	0.001	X				X					Autigenic calcite (slightly ferrous)
AD	7A	EOC50	2893.03	4.8	0.070	X				X					Autigenic calcite (slightly ferrous)
AD	11A	EOC50	2896.47	5.5	0.280	X		X		X					Autigenic calcite (slightly ferrous)
AD	15A	EOC50	2898.18	3.7	0.015	X		X		X					Autigenic calcite (slightly ferrous)
AD	16A	EOC50	2937.00	6.0	0.001	X		X		X					Autigenic calcite (slightly ferrous)
AD	17A	EOC50	2937.82	3.5	0.001	X		X		X					Autigenic calcite (slightly ferrous), pyrite.
AD	21A	EOC50	2938.81	6.7	0.260	X		X		X					Autigenic calcite (slightly ferrous), calcite-filled minor fractures
AD	25A	EOC50	2939.94	6.9	0.033	X		X		X					Autigenic calcite (slightly ferrous) and illite.
O	N1H1	EOC50	2809.11	0.4	n/d	X	X	X		X	X				Early calcite cement precipitation followed by micritization of calcareous mud. Pyrite and dolomite. Microporosity is associated with micritized grains and partially recrystallized matrix
O	N1H2	EOC50	2810.50	0.8	0.009		X			X		X	X		Equant calcite cement precipitation and grain dissolution. Minor fractures calcite-filled.
O	N1H3	EOC50	2811.08	10.5	77.458		X		X	X					Micritization and calcite cement precipitation
O	N1H5	EOC50	2812.23	11.5	0.005		X		X						Micritization, calcite cement, partial dissolution increasing porosity.
O	N1H8	EOC50	2813.08	22.3	1.625	X	X		X	X		X			Minor compaction and recrystallization of edges around grain contacts, precipitation of calcite cement and dissolution of grains and cement.
O	N1H11	EOC50	2813.96	26.7	34.552	X	X		X	X					Compaction of grains during deposition closed intergranular porosity. Early cementation partially closed intergranular porosity. The carbonate mud was micritized forming abundant microporosity.
O	N1H14	EOC50	2815.45	20.6	0.376										No thin section
O	N1H17	EOC50	2816.25	20.6	36.112		X		X	X					Micritic matrix recrystallized and minor quantities of calcite cement. Precipitation of calcite cement and dissolution of bioclasts and other grains.
A	N4-H2	EOC40	2513.60	9.5	0.059	X			X	X	X				compaction > dissolution > cementation with ferrous and non ferrous sparry calcite cement > dolomite cementation.
A	N4-H5	EOC40	2516.00	16.9	6.350	X			X	X	X	X	X		Compaction > dissolution > cementation with ferrous and non ferrous spatic calcite cement > fracturing > filling fracture. Open fractures cutting some grains and matrix. Minor fractures filled with dolomite.
A	N4-H6	EOC40	2516.30	23.3	212.000	X			X	X	X				compaction > dissolution > cementation with ferrous and non ferrous sparry calcite cement > dolomite cementation.
A	N4-H9	EOC40	2520.80	21.4	26.600	X			X	X	X				compaction > dissolution > cementation with ferrous and non ferrous sparry calcite cement > dolomite cementation.
O	N2H1	EOC30	2970.22	13.2	15.546	X				X		X			Compaction followed by precipitation of calcite cement. Presence of opened fractures cutting several grains.
O	N2TS6	EOC30	2971.92	n/d	n/d	X				X					Moderate compaction followed by precipitation of calcite cement.
O	N2H7	EOC30	2972.17	8.0	0.113	X	X			X					Compaction followed by moderated precipitation of calcite cement.
O	N2H8	EOC30	2972.76	2.3	0.002	X	X	X		X					Compaction followed by moderated precipitation of calcite cement.
O	N2TS12	EOC30	2974.52	n/d	n/d	X	X	X				X			Compaction and filling of bioclasts by calcite and pyrite.
O	N2H16	EOC30	2975.58	1.8	0.024	X	X	X		X					Deformation due to recrystallization under compaction, calcareous cement precipitation and piritization.
O	N2H17	EOC30	2975.90	7.2	0.077	X	X	X		X					
O	N2H20	EOC30	2977.04	1.5	0.001		X			X					Slight compaction, micritization of matrix and precipitation of coarse calcite.
O	N2H23	EOC30	2978.27	0.6	0.001										No thin section

Table A–3. Diagenetic description of thin sections for reservoir units EOC–50, EOC–40 and EOC–30. Light yellow boxes indicate the more significant events that affect reservoir quality. Gray boxes indicate absence of diagenetic process. (Data courtesy of PEMEX E&P).

Well	Core Sample	Reservoir horizon	Depth	Porosity (%)	Permeability (md)	Compaction	Micritization	Piritization	Dissolution	Cementation (calcite)	Replacement by dolomite	Fracturing	Fracture filling	Neomorphism	Observations
A	N5-H1	EOC20	2592.80	4.3	0.003	X			X	X	X				compaction > dissolution > cementation of sparry calcite cement > cementation and precipitation of dolomite.
A	N5-H4	EOC20	2594.07	3.4	0.002	X			X	X	X				compaction > dissolution > cementation of ferrous and no ferrous sparry calcite cement > cementation and precipitation of dolomite.
A	N5-H8	EOC20	2596.94	12.6	8.170	X			X	X	X				compaction > dissolution > cementation of sparry calcite cement > precipitation of dolomite cement.
A	N5-H10	EOC20	2597.47	12.8	26.000	X			X	X	X				compaction > dissolution > cementation with ferrous and nonsparry calcite cement > cementación menor con dolomita
B	N1H1	EOC20	3330.06	0.8	0.001					X	X		X		Equant cement. Minor fractures calcite-filled. Calcite cement precipitation.
B	N1H2	EOC20	3330.23	5.3	0.082					X	X		X		Calcite cement precipitation. Recrystallization and dolomitization. Equant cement. Minor fractures calcite-filled.
B	N1TS3	EOC20	3330.73	n/d	n/d										No thin section
B	N1H4	EOC20	3331.20	0.4	0.001	X				X	X				Initial compaction. At least two events of calcite precipitation.
AD	30A	EOC20	3170.57	SD	SD	X	X	X		X			X		Calcite cement. Micritization is mainly due by illite/smectite combination. Minor calcite filled fractures.
AD	35A	EOC20	3172.29	2.7	0.001	X	X	X		X					Presence of authigenic calcite.
AD	44A	EOC20	3174.85	4.4	0.009	X	X	X		X			X		Presence of authigenic calcite.
AD	47A	EOC20	3175.78	3.1	0.001	X	X	X					X		Presence of authigenic calcite.
AD	53A	EOC20	3178.25	NSA	NSA										Authigenic clay (illite/smectite)
K	F1	EOC10	2662.11	1.9	0.035	X	X		X					X	Micritization includes Illite/smectate combination. Detrital clay recrystallized. Calcite cement precipitation. The matrix is mainly micrite. Fossils has been dissolved resulted in intraparticle and moldic porosity.
K	F2	EOC10	2662.60	3.3	0.020	X	X		X					X	Glauconite, ferroicite calcite, micritization. Argillaceous recrystallized matrix.
K	F3	EOC10	2663.98	9.5	43.190	X	X		X					X	Micrite and calcite sparite. Calcite cement precipitation and micritization. Intraparticle and moldic porosity resulted from dissolution.
K	F4	EOC10	2665.36	1.1	0.016	X	X	X	X					X	Micrite and spatic cement. Calcite cement precipitation. Organic matter and micrite.
K	F5	EOC10	2666.94	1.7	0.050	X	X	X	X					X	Glauconite in itraparticle pores. Calcite cement precipitation and micritization.
AA	N4-H1	EOC10	2556.60	4.1	1.530	X	X	X	X	X	X	X	X		Compaction > micritization > piritization > dissolution > calcite cementation > dolomitization > fracturing > fracture filling with micrite and spatic cement
AA	N4-H4	EOC10	2557.10	1.7	0.001	X	X	X	X	X	X	X	X		Compaction > micritization > piritization > dissolution > calcite cementation > dolomitization > fracturing > fracture cementation (micrite)
AA	N4-H7	EOC10	2560.00	3.3	0.006	X	X	X	X	x	X				Compaction > micritization > piritization > dissolution > calcite cementation > dolomitization
AA	N4-H9	EOC10	2562.15	3.4	0.004	X	X	X	X	X	X				Compaction > micritization > piritization > dissolution > calcite cementation > dolomitization
AA	N4-H11	EOC10	2563.62	2.9	0.013	X	X	X	X	X	X				Compaction > micritization > piritization > dissolution > calcite cementation > dolomitization
AA	N5-H1	EOC10	2572.00	1.7	0.001	X	X	X	X	X	X				Compaction > micritization > piritization > dissolution > calcite precipitation > dolomitization . Fossils replaced by calcite, micrite and dolomite crystals.
AA	N5-H3	EOC10	2572.00	2.4	0.002	X	X	X	X	X	X		X		Compaction > micritización > piritización > dissolution > calcite precipitation > dolomitization > fracturing > fracture filling with calcite
AA	N5-H5	EOC10	2572.00	5.3	0.284	X	X	X	X	x					Compaction > micritization > piritization > dissolution > calcite precipitation > dolomitization
AA	N5-H11	EOC10	2572.00	5.5	0.148	X	X	X	X	X	X	X	X		Compaction > micritization > piritization > dissolution > calcite precipitation > dolomitization > fracturing > fracture filling with calcite
AA	N5-H14	EOC10	2572.00	2.1	0.002	X	X	X	X	X	X	X	X		Compaction > micritization > piritization > dissolution > calcite precipitation > dolomitization > fracturing > fracture filling with calcite

Table A–4. Diagenetic description of thin sections for reservoir units EOC–20 and EOC–10. Light yellow boxes indicate the more significant events that affect reservoir quality. Gray boxes indicate absence of diagenetic process. (Data courtesy of PEMEX E&P).

APPENDIX B: BIOSTRATIGRAPHIC DATA

The reservoir age was dated with biostratigraphic analysis of drill cuttings and cores within the reservoir units by PEMEX's paleontological team. The analysis includes determination of relative age, according to fossil content and range of living, and paleobathymetry inferred from foraminifera based on Bolli et al. (1985), De-Sansores and Flores-Covarrubias (1972), and Kennet and Srinivasan, (1983) (Tables B–1 and B–2).

Relative age	Well	Unit	Fossil	Paleobathymetry	Observations
Upper Eocene	AD	EOC-50	Turborotalia cerroazulensis, Globigerinathea sp.	Middle bathyal	Redeposited foraminifera from internal neritic.
	O	EOC-50	Catapsydrax dissimilis, Turborotalia cerroazulensis cerroazulensis, Globigerina pseudoampliapertura, Pseudohastigerina micra, Morozovella spinuloinflata, Vulvulina pennatula, Turborotalia centralis, Hantkenina alabamensis, Bulimina alazanensis, Globigerina ampliapertura, Siphonina tenuicarinata.	Middle to upper bathyal and outer neritic in the lower part	There is a maximum flooding surface, the environment is reported as lower bathyal.
	AB	EOC-40 and EOC-20	Turborotalia cerroazulensis	No reported	A lot of reworked fossils in this unit. Uncertainty in dating.
	B	EOC-40	Morozovella spinulosa, Acarinina spinuloinflata, Truncorotaloides topilensis, Globigerinathea sp., Hantkenina sp., Anomalina dorri, Catapsydrax dissimilis, Turborotalia cerroazulensis frontosa, Chilostomella oolina, Cibicides sp.	No reported	This unit is 175 m thick. The upper part of this unit was dated as Upper Eocene, while the middle and lower part was dated as Middle Eocene.
	AC	Above EOC-10	Turborotalia cerroazulensis, Hantkenina alabamensis	No reported	Well on the contiguous western fold. It is not in the field structure.
Middle Eocene	AD	EOC-30	Truncorotaloides rohri, Truncorotaloides topilensis, Morozovella spinulosa, Morozovella spinuloinflata	Middle bathyal	Most of the macroforaminifera redeposited showed to be from internal neritic environment.
	O	EOC-30	Morozovella spp., Morozovella cf. spinulosa,	Ranges from outer neritic to upper bathyal	Dating on core. Early Eocene foraminifera is likely reworked. Top of Eocene is undetermined because of lack of amplex above core.
	A	EOC-20	Morozovella spinulosa, Acarinina spinuloinflata, Morozovella formosa, Morozovella quetra, Morozovella aequa reworked inside middle Eocene	Upper bathyal	Dating on core. Some Middle Eocene macroforaminifera redeposited. There are inner to outer neritic bentic foraminifera from evaporitic environments.
	D	EOC-20	Lepidocyclina spp, Truncorotaloides topilensis, Globigerinathea spp., Truncorotaloides rohri.	No reported	Late Cretaceous reworked fossils (Globotruncana spp.).
	G	EOC-20	Turborotalia cerroazulensis frontosa, Morozovella spinulosa, Acarinina bullbrookii.	Lower bathyal	
	C	EOC-10 and EOC-20	Morozovella spp	No reported	Late Cretaceous reworked fossils (Globotruncana spp. y una Pseudotextularia spp.). The intervalled with samples was very short, from 2790 to 2870 m.

Table B–1. Biostratigraphic interpretation of units EOC–50, EOC–40, EOC–30 and EOC–20 in drill cuttings and cores (Betanzos-Gallifa et al., 2010). (Data courtesy of PEMEX E&P, Laboratory of Paleontology in Veracruz).

Relative age	Well	Unit	Fossil	Paleobathymetry	Observations
Middle Eocene	Z	Below EOC-10	Truncorotaloides rohri, T. topilensis, Morozovella lehneri, Morozovella spinulosa, Morozovella lehneri, Morozovella aragonensis, and Acarinina broedermanni.	Middle bathyal	Dating on core and drilled cuttings.
	AA	EOC-10	Calcareous nanoplankton, Acarinina spinuloinflata, Morozovella spinulosa and calcareous nanoplacton.	Middle bathyal	The core was dated with calcareous nanoplankton ,and the drill cutting with foraminifera. A lot of inner to external neritic reeeposited fossils. There are several redeposited fossils in the upper part of the unit.
	AC	EOC-10	Globigerinatheka mexicana, H. lenheri	No reported	Well on the contiguous western fold. It is not in the field structure.
	B	EOC-10	Morozovella spinulosa, Acarinina spinuloinflata, Truncorotaloides topilensis, Globigerinatheka sp., Hantkenina sp., Anomalina dorri, Catapsydrax dissimilis, Turborotalia cerroazulensis frontosa, Chilostomella oolina, Cibicides sp	No reported	Globotruncana spp. reworked from late Cretaceous, abundant calcite fragments.
	K	EOC-10	Morozovella spinulosa, Acarinina spinuloinflata	Upper bathyal	constant and well preserved
	L	EOC-10	Morozovella cf. quetra, Morozovella spinulosa, Morozovella lehneri, Turborotalia cerroazulensis frontosa, Lepidocyclina sp.	No reported	The mayority of fauna is from middle Eocene, however, Globigerina ampliapertura y G. pseudoampliapertura ranging from Middle Oligocene to Late Eocene are present, so the reworked fossils may be Middle Eocene instead. Several Cretaceous reworked fossils.
	M	EOC-10	Globigerina ampliapertura, Turborotalia topilensis.	Middle bathyal	
	N	EOC-10	Morozovella espinulosa, Morozovella aragonensis.	Middle bathyal	
Lower Eocene	AA	Below reservoir units	Morozovella subbotinae, Morozovella quetra, Morozovella aequa	Middle bathyal	
	AC	Below reservoir units	Morozovella formosa, Morozovella quetra, Morozovella aequa.	From inner neritic to upper bathyal	A lot of reworked fossils. Presence of macroforaminifera, coral fragments, spines and equinoderms. This well is outside the field structure in the western edge.
	O	Below reservoir units	Orbulinoides spp., Morozovella quetra, Acarinina soldadoensis angulosa, Anomalinoides capitatus, Catapsydrax dissimilis, Morozovella aragonensis, Acarinina broedermanni.	Middle bathyal	

Table B–2. Biostratigraphic interpretation of unit EOC–10 and deeper intervals in drill cuttings and cores (Betanzos-Gallifa et al., 2010). (Data courtesy of PEMEX E&P, Laboratory of Paleontology in Veracruz).

Note that reservoir unit EOC–50 corresponds to Upper Eocene while units EOC–30, EOC–20 and EOC–10 are Middle Eocene. EOC–40 age is uncertain. The correlation of reservoir units is lithostratigraphic, based on well logs character, rather than chronostratigraphic because paleontology does not provide enough resolution to distinguish each reservoir unit.

APPENDIX C. STRUCTURE ORIENTED FILTERING

First introduced by Fehmers and Höecker (2003), structure-oriented filters (SOF) provide a means to minimize random and coherent noise that is inconsistent with the dominant dip. Most modern implementations (summarized by Davogustto and Marfurt, 2011) not only smooth along reflector strike and dip but also preserve or even enhance major discontinuities. The presence of such discontinuities is measured using either coherence (used in this application and summarized in Figure C–1) or chaos (used in Fehmers and Höecker, 2003 and many commercial software implementations).

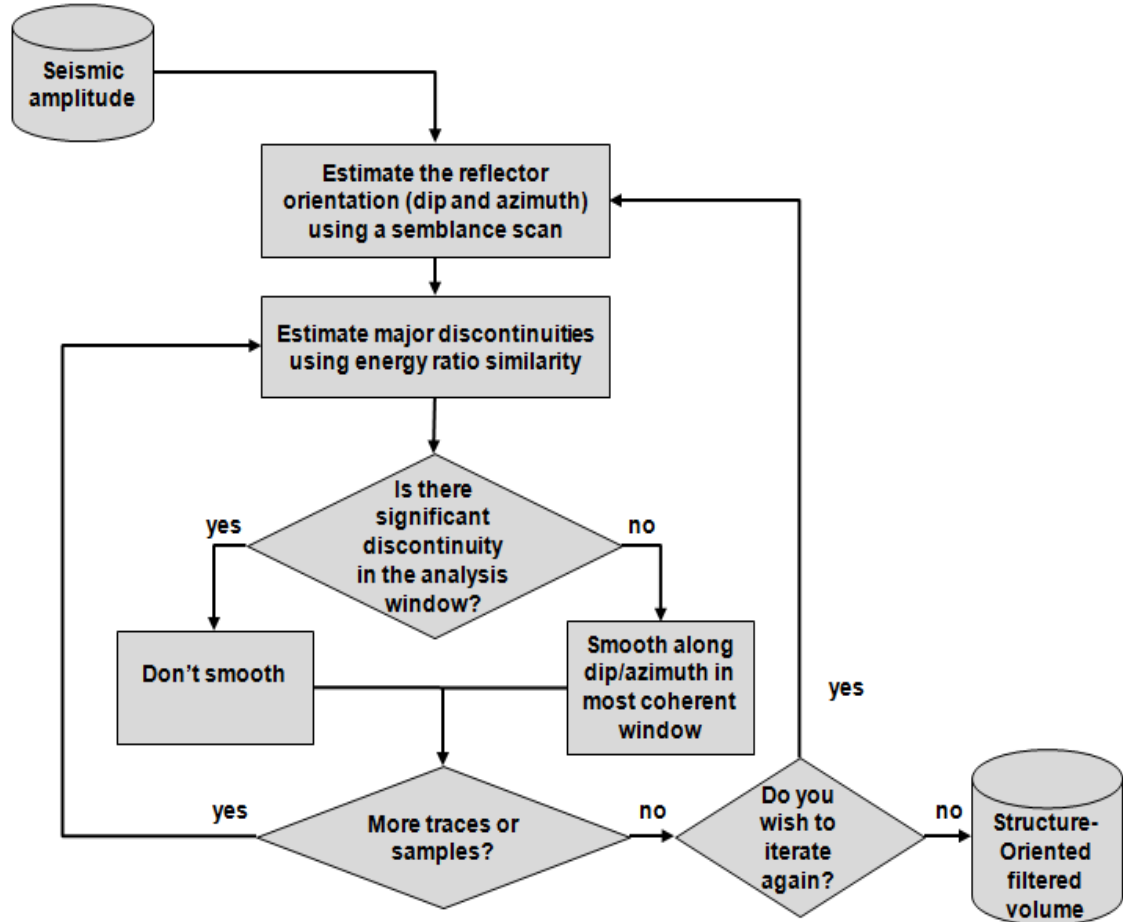


Figure C–1. Workflow for structure-oriented filtering of poststack seismic amplitude volume. (Adapted from Davogustto and Marfurt, 2011).

The input volume is the poststack seismic amplitude volume, from which I extracted volumetric dip and azimuth using a semblance scan technique (Davogustto and Marfurt (2011)). After that, I compute coherence to determine the location of the major discontinuities patterns. If the data are relatively coherent along the analysis window, then it is smoothed. In contrast, if the data are relatively incoherent, then the original data are preserved. I use energy ratio similarity as the coherence attribute to determine whether smoothing or not. For this data volume, the energy ratio similarity provides sharper discontinuities than Sobel filter similarity or semblance-based similarity. The response of the coherence family of attributes depends on the data quality and geological features of interest. I find Sobel-filter similarity works better on other data volumes and in mapping thin channels. The smoothing was applied where reflectors were continuous, preserving the discontinuities indicated by the coherence attribute.

The filtering process is iterative; I obtained satisfactory results with two iterations of SOF. After each iteration, I estimated a coherence volume to quality control the filtering results. Other quality control is analyzing the rejected noise after each iteration of SOF by calculating the difference between the original and the filtered volume, making sure that the rejected traces corresponds to noise instead of signal. The seismic amplitude volume from the final iteration of structure-oriented filtering serves as input to subsequent geometric attributes calculations used for structural interpretation. Two iterations provided improved attribute images with less noise and fewer artifacts. An additional third iteration did not provide any significant improvement.

Prestack SOF works in much the same way (Figure C-2). In this case, the input consists of prestack time migrated common reflection point amplitude gathers. First, the gathers are stacked. This stacked volume is used to compute coherence, dip and azimuth volumes that will be used to constrain the structure-oriented filtering applied to each common-offset or common-azimuth gather (Davogustto et al., 2011). Depending on the data quality of the input gathers, we can choose principal component (PC), alpha-trimmed mean, lower upper middle- (LUM), and mean filters (Davogustto et al., 2011). Results of these filters are shown in the main text of this thesis.

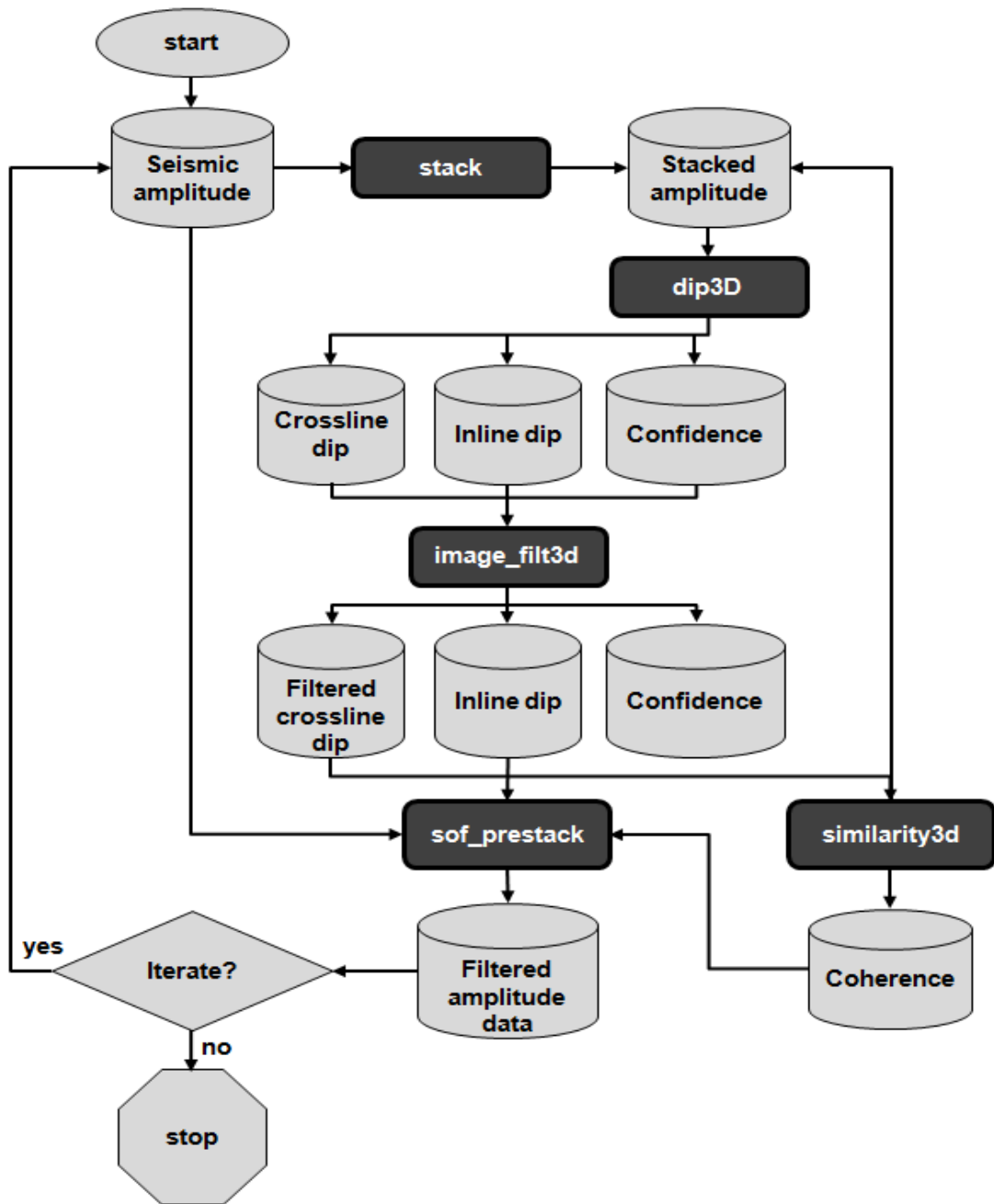


Figure C-2. Workflow for pre-stack structure oriented filtering. (Davogustto et al., 2011). In my software environment “stack” simply stacks the data, program “dip3D” computes the value and confidence of inline and crossline dip components, program “image_filt3d” removes artifacts in the dip volumes using nonlinear filters, program “similarity3d” computes similarity (coherence) attribute volumes, and program “sof3d” applies structure-oriented filter to each common-offset prestack time migrated data volume.